

# Mode-locking of Thulium-doped and Erbium-doped Fiber Lasers

by

Lynn Elizabeth Nelson

Submitted to the Department of Electrical Engineering and  
Computer Science

in partial fulfillment of the requirements for the degree of

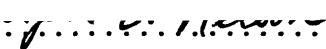
Doctor of Philosophy in Electrical Engineering

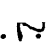
at the


MASSACHUSETTS INSTITUTE OF TECHNOLOGY

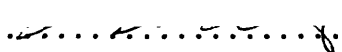
May 1997

© Massachusetts Institute of Technology 1997. All rights reserved.

Author .....  .....  
Department of Electrical Engineering and Computer Science  
February 12, 1997

Certified by .....  .....  
Hermann A. Haus  
Institute Professor  
Thesis Supervisor

Certified by ...  .....  
Erich P. Ippen  
Elihu Thompson Professor of Electrical Engineering  
Thesis Supervisor

Accepted by .....  .....  
Arthur C. Smith  
Chairman, Departmental Committee on Graduate Students

JUL 24 1997

ARCHIVES

LIBRARIES

# Mode-locking of Thulium-doped and Erbium-doped Fiber Lasers

by

Lynn Elizabeth Nelson

Submitted to the Department of Electrical Engineering and Computer Science  
on February 12, 1997, in partial fulfillment of the  
requirements for the degree of  
Doctor of Philosophy in Electrical Engineering

## Abstract

This thesis reports work on passive mode-locking of thulium-doped and erbium-doped fiber ring lasers using the technique of polarization additive pulse mode-locking (P-APM). A self-starting, mode-locked  $\text{Tm}^{+3}$ -doped fiber laser was demonstrated with 360 to 500 fsec pulses tunable from 1.8 to 1.9  $\mu\text{m}$ , the largest tuning range demonstrated from a rare-earth doped fiber. This laser operated in the soliton regime due to the large negative group-velocity dispersion (GVD) of the fiber at 1.8  $\mu\text{m}$ . A possible application to optical coherence tomography on biomedical tissue was explored.

A stretched-pulse  $\text{Er}^{+3}$ -doped laser at 1.55  $\mu\text{m}$  was optimized for the application of frequency-doubling to 775 nm where the pulses can be used as a seed for a Ti:Sapphire regenerative amplifier. This laser incorporated segments of fiber with positive and negative GVD to avoid operation in the soliton regime. Compressed fundamental pulses of 100 fsec and 2.7 nJ were obtained, and three nonlinear crystals,  $\beta\text{-BaB}_2\text{O}_4$  (BBO),  $\text{KNbO}_3$  (potassium niobate), and  $\text{LiB}_3\text{O}_5$  (LBO), were evaluated for frequency doubling. Near transform-limited pulses at 771 nm with average powers of 8.7 mW were obtained with a 1-cm BBO crystal, corresponding to conversion efficiencies of up to 10%. Frequency resolved optical gating (FROG) measurements were performed on both the fundamental and doubled pulses to better characterize the laser.

The effect of linear birefringence on P-APM was explored through numerical simulations for the case of standard fibers, where the two are of the same order. Although reduced by the birefringence, pulse shaping still occurred and there was no inherent periodicity due to the fiber beat-length. Measurements of birefringence and temperature sensitivity of both standard and polarization maintaining (PM) fibers were also performed.

Experimental work toward an environmentally stable  $\text{Er}^{+3}$ -doped fiber laser included two different schemes. The first design was comprised of only PM-fiber, but stable mode-locking was prevented by the temperature dependence of the PM-fiber birefringence. The second scheme, the sigma laser, was a traveling-wave cavity which used both non-PM and PM-fiber. Environmental stability was achieved by canceling changes in linear phase bias in the non-PM fiber and using linear polarization along one of the axes in the PM fiber. Stretched-pulse operation of the sigma laser was achieved with sub-110 fsec,  $> 1$  nJ pulses generated directly from the cavity.

Thesis Supervisor: Hermann A. Haus

Title: Institute Professor

Thesis Supervisor: Erich P. Ippen

Title: Elihu Thompson Professor of Electrical Engineering

## Acknowledgments

I have many people to thank for their help in the completion of this thesis and my Ph.D. First of all I thank Professor Erich Ippen and Professor Hermann Haus for the opportunity to work in the ultrafast optics group at MIT. I have enjoyed many discussions with Professor Ippen about nonlinear optics and fiber lasers and was impressed each time with his ability to explain things simply and intuitively. I appreciated the opportunity to work independently, with the confidence that he was available to discuss technical issues when I needed to. On many occasions he patiently listened to my ideas and problems and then helped me to ask the right questions and focus on what was important. I have also appreciated his interest in my future career and the many times he talked with me about various decisions.

I am grateful to Professor Haus for his guidance, enthusiasm, and encouragement during my years at MIT. He was always willing to discuss my experiments and would patiently answer my questions and sometimes explain things more than once. Professor Haus is truly an inspiration with his variety of outside interests and bike rides to MIT from Lexington. I have enjoyed many group dinners in the homes of both Professor Haus and Professor Ippen and several wonderful group ski trips to New Hampshire, chaperoned by the Ippens.

I thank Professor Shaol Ezekiel for agreeing to be the third reader for thesis. I have enjoyed talking with him about some of my research, and I also enjoyed taking his class, 16.302. His interest and encouragement along the way were helpful.

I was very fortunate to have been supported by a number of outside organizations while at MIT. I thank the Office of Naval Research for financial support through a National Defense Science and Engineering Graduate Fellowship for my first three years, and I have appreciated the financial and mentoring support of AT&T Bell Labs through my participation in the Graduate Research Program for Women. I also thank General Electric for a GE Fund Faculty for the Future Fellowship which supported my graduate studies from January to June 1995. Most recently I sincerely thank the Joint Services Electronics Program for the JSEP Fellowship which has supported my studies since June 1995.

I thank Ursula Keller, my first mentor from AT&T Bell Labs, for her tutelage and counsel before I began my studies at MIT, and Keith Goossen who graciously stepped in as my mentor in 1992. I also thank Professor N. Lawandy and Professor T.F. Morse at Brown University for encouraging my initial interest in optics.

The ultrafast optics group has been a home away from home for the past five and a half years. Along the way, I have been fortunate to interact with great people from the group, many of whom I saw graduate and have missed these last years. John Moores and Farzana Khatri were the first people I worked with at MIT and taught me about the world of computer simulations. They were great about answering all my questions. I feel very fortunate to have had the opportunity to work with Kohichi Tamura during my first three years at MIT. He taught me much about working in the lab and working with others in the group and was never too busy to listen to my concerns about research, classes, qualifying exams, or life in general. I have appreciated his perspective, support, and friendship over the years. I was also

fortunate to get to know Keren Bergman and Katie Hall during my first two years at MIT. They are true examples to me of women who are making it without giving up the rest of their lives. I have sincerely appreciated their support and encouragement.

Gadi Lenz, Dave Dougherty, and Siegfried Fleischer have been great sources of technical advice and stamina over the past three years. As my office mates and pseudo-office mate (Siegfried), they have always taken the time to deal with my questions about the lab and physics, and have helped me to try to ask the right questions about my research. I have enjoyed many lively discussions with them and have been impressed each time with each of their knowledge, understanding, and patience in explaining to me. I also enjoyed being included in their trips for dinner or coffee.

During my first three years at MIT I enjoyed meeting Chris Doerr, who inspired me by newly defining the words "working hard," while still taking time to help me or answer my questions. More recently, I have enjoyed the opportunity to work with David Jones in the lab. David is someone else who inspires me with his determination and willingness to work hard, while still trying to maintain some balance in life. He has always been ready to discuss my ideas and has helped me on numerous occasions with presentations and proof-reading. I thank Michelle and him for their friendship over the last three years.

I enjoyed working with Brett Bouma and Gary Tearney on the Thulium OCT experiment and have appreciated their interest in my work and rare-earth doped fibers. It has been great to talk with Brett about lasers and life in general; I admire how he treats others and his ability to be a team player. I thank Brett, Siegfried, and Boris Golubovic for including me in their adventure to Joshua Tree, CA last June before CLEO. It was a great break when I really needed one, and my rappelling experience has provided a good story.

I thank Shu Namiki and William Wong for some interesting technical discussions and for donations/loans of fiber components. And I have enjoyed interacting with Erik Thoen and Pat Chou over the last two years. I thank our group secretaries Cindy Kopf, Donna Gayle, and Mary Aldridge, for the many times they helped me navigate MIT and Boston. I also thank the rest of the optics group for technical advice, equipment loans, and encouragement during my years at MIT.

Outside of the optics group at MIT I am grateful to Marilyn Pierce for her consistent interest and encouragement. My friends from KEYs and the Public Service Center have also been a great source of support over the last three years.

Finally I am very grateful to my friends and family. Their continued interest in my work and emotional support have pulled me through the difficult times and given me much needed confidence. I thank Ann Jansen (my MIT-Wisconsin friend) for her perspective and constant encouragement. I especially thank Susan Voss for her continued friendship and for sharing many of the happy and hard times with me. Most of all, I thank my parents, Paul, Eric, and Wendy for their unwavering love, support, and understanding. Their strength, belief in me, and willingness to always listen has helped me more than they can know. This thesis is dedicated to my parents.

# Contents

<b>1</b>	<b>Introduction</b>	<b>17</b>
1.1	Thesis Organization . . . . .	19
<b>2</b>	<b>Fiber Laser Background</b>	<b>20</b>
2.1	Erbium-doped silica fiber . . . . .	20
2.2	Thulium-doped silica fiber . . . . .	22
2.2.1	Photodarkening in $\text{Tm}^{+3}$ -doped fibers . . . . .	23
2.3	Double-clad doped-fibers . . . . .	26
2.4	Self-Phase Modulation . . . . .	26
2.5	Group Velocity Dispersion . . . . .	28
2.6	Polarization APM . . . . .	30
2.6.1	Master equation for P-APM in a fiber laser . . . . .	31
2.6.2	Matrix formulation of P-APM parameters . . . . .	32
2.7	Self-Starting . . . . .	35
<b>3</b>	<b>Thulium-doped fiber soliton laser</b>	<b>37</b>
3.1	Experimental Setup . . . . .	37
3.2	Mode-locked operation . . . . .	39
3.3	Tuning characteristics . . . . .	42
3.4	Dispersion measurement . . . . .	44
3.5	Soliton behavior . . . . .	44
3.6	Spectral modulation . . . . .	46
3.7	Limitations of soliton lasers . . . . .	49
3.8	Possible improvements to the $\text{Tm}^{+3}$ -doped fiber laser . . . . .	50
3.8.1	Filtering . . . . .	50
3.8.2	Rejection Port . . . . .	51
3.8.3	Stretched-pulse operation . . . . .	52
3.9	Optical Coherence Tomography using a $1.8 \mu\text{m}$ source . . . . .	55
3.9.1	OCT background . . . . .	56
3.9.2	$\text{Tm}^{+3}$ -doped fiber ASE source . . . . .	58
3.9.3	OCT source comparison . . . . .	60
<b>4</b>	<b>Frequency-doubling of a stretched-pulse erbium-doped fiber laser</b>	<b>61</b>
4.1	Stretched-pulse laser optimization . . . . .	62
4.2	Frequency-doubling results . . . . .	65

4.3	Frequency-resolved optical gating measurements . . . . .	69
4.4	Noise measurements . . . . .	75
4.5	Technology transfer . . . . .	78
4.6	Comparison of doubling with different net dispersions of stretched-pulse lasers . . . . .	80
4.7	Summary . . . . .	80
<b>5</b>	<b>Effect of Linear Birefringence on P-APM</b>	<b>83</b>
5.1	Measurement of fiber birefringence . . . . .	84
5.1.1	Cutback measurement of beat-length for non-PM fiber . . . . .	85
5.1.2	Birefringent filter measurement for PM-fiber . . . . .	85
5.2	Temperature dependence of fiber birefringence . . . . .	89
5.2.1	Standard fiber versus PM fiber . . . . .	89
5.2.2	Measurement of birefringence temperature dependence in Panda fiber . . . . .	90
5.3	Simulations of the effect of linear birefringence on P-APM . . . . .	92
5.3.1	Regimes of birefringence versus nonlinearity . . . . .	95
5.3.2	Does birefringence cause periodicity of P-APM? . . . . .	101
5.3.3	Optimum starting polarization state for maximum polarization rotation . . . . .	105
<b>6</b>	<b>Work toward an environmentally stable mode-locked fiber laser</b>	<b>108</b>
6.1	Comparison of P-APM in PM fiber versus non-PM fiber . . . . .	109
6.1.1	P-APM in PM fiber . . . . .	110
6.1.2	P-APM in non-PM fiber . . . . .	112
6.2	Mode-locking of an all PM-fiber laser . . . . .	113
6.3	Stretched-Pulse Sigma Laser . . . . .	120
6.3.1	Further work on the stretched-pulse sigma laser . . . . .	125
<b>7</b>	<b>Conclusions and Suggestions for Future Work</b>	<b>126</b>
7.1	Summary . . . . .	126
7.1.1	Mode-locked thulium-doped fiber laser . . . . .	126
7.1.2	Stretched-pulse laser and frequency doubling . . . . .	127
7.1.3	Linear birefringence on P-APM . . . . .	128
7.1.4	Environmentally stable mode-locked fiber laser . . . . .	128
7.2	Further Work . . . . .	129
7.2.1	Co-doped and cladding-pumped fibers . . . . .	129
7.2.2	Bragg gratings . . . . .	129
7.2.3	Semiconductor saturable absorbers . . . . .	130
7.2.4	Mode-locked fiber laser applications . . . . .	131
<b>A</b>	<b>Comparison of Forward and Backward Pumping Configurations in Fiber Ring Lasers</b>	<b>133</b>

<b>B Numerical Simulations</b>	<b>137</b>
B.1 Normalization of simulation equations . . . . .	137
B.2 Sample data file for simulations . . . . .	138



# List of Figures

1-1	Diagram of wavelength ranges which can be obtained by rare-earth dopants in silica fibers. The approximate bandwidth for each rare-earth ion is also indicated . . . . .	18
2-1	Energy levels of $\text{Er}^{+3}$ in silica-glass fiber. Possible pump bands are at 800 nm, 980 nm, and 1.48 $\mu\text{m}$ , with broadband emission near 1.55 $\mu\text{m}$ . (Energy levels above the ${}^4F_{9/2}$ level are not shown) . . . . .	21
2-2	Energy levels of $\text{Tm}^{+3}$ in a silica-glass fiber. Possible pump bands are at 670 nm, 785 nm, and 1.06 $\mu\text{m}$ . Emission typically occurs between 1.8 and 2.0 $\mu\text{m}$ , but also at $\sim 370$ nm and 460 nm when pump excited-state absorption occurs . . . . .	24
2-3	Flourescence spectrum of thulium-doped silica fiber when pumped with 500 mW of cw power at 785 nm . . . . .	25
2-4	Cross-sectional view of neodymium-doped double-clad fiber. The 7.5 $\mu\text{m}$ -diameter circular core is surrounded by a region of pure silica that is rectangular with dimensions 100 $\mu\text{m} \times 300 \mu\text{m}$ . The second cladding is a fluoropolymer with a low refractive index and low optical loss. The rectangular region serves as the cladding for confining laser light in the single-mode core and as the multimode core for the 807 nm pump light within the hard polymer outer cladding [52] . . . . .	27
2-5	Diagram of how pulse shortening occurs in a laser through Polarization APM. An initial pulse is linearly polarized and then made elliptical with a quarter-wave plate. The light then passes through an optical fiber where ellipse rotation occurs and the peak of the pulse rotates more than the pulse wings. At the output of the fiber, the waveplates orient the pulse so that the peak of the pulse passes through the polarizer while the wings of the pulse are extinguished, thus achieving pulse shortening . . . . .	31
2-6	Schematic diagram of a ring laser with saturable gain, linear loss, filtering (gain-bandwidth limiting), self-amplitude modulation for mode-locking, self-phase modulation, group velocity dispersion, and isolator for unidirectional operation. The Master equation includes each of these effects in determining the pulse envelope . . . . .	33

3-1	Experimental set-up for the mode-locked thulium-doped fiber ring laser. PBS: polarizing beam splitter, Tuning plate: quartz plate of thickness 10T . . . . .	38
3-2	Calculated transmission versus wavelength for a quartz birefringent tuning plate filter of thickness 10T at Brewster's angle in the cavity. Solid curve: c-axis at 40 deg from TE polarization (for maximum extinction). Dashed curve: c-axis at 50 deg from TE polarization . . . . .	39
3-3	Pulse autocorrelation (fit with a sech) and spectrum of typical single-pulse operation. The pulse FWHM is 480 fsec, and the spectrum is centered at 1850 nm . . . . .	40
3-4	Laser output power vs. coupled pump power for the $Tm^{+3}$ -doped fiber laser with a spectrum centered near $1.8 \mu m$ . . . . .	41
3-5	Minimum pulse width vs. center wavelength for single-pulse operation of the mode-locked thulium-doped fiber laser . . . . .	42
3-6	Mode-locked spectra from the thulium-doped fiber laser showing a continuous tuning range of $> 50$ nm when only the birefringent filter is adjusted . . . . .	43
3-7	A second set of mode-locked spectra from the thulium-doped fiber laser showing the continuous tuning range after the isolator was modified for lower loss at $1.8 \mu m$ allowing pulsed operation at shorter wavelengths. The pump power was also adjusted along with the birefringent tuning plate . . . . .	43
3-8	Measurement of $T_{rep}$ vs. wavelength for the $Tm^{+3}$ -doped fiber laser with 10.3 meters of SMF-28 and 1.3 meters of $Tm^{+3}$ -doped fiber. The slope $D \ell_{cav} = +0.355$ ps/nm, corresponding to a net dispersion $k'' \ell_{cav} = -0.645$ ps <sup>2</sup> . . . . .	45
3-9	Plot of the propagation constant $k$ vs. angular frequency $\Delta\omega$ which shows the phase-matching condition for sidebands occurring when the laser is periodically perturbed. The soliton-like pulse has a constant $k_s$ , while the dispersive waves have $k_{lin}$ with a quadratic dependence on $\Delta\omega$ . Phase-matching occurs at the particular frequencies where the periodic perturbation (with $k_p$ ) makes up the difference between $k_s$ and $k_{lin}$ . . . . .	48
3-10	Spectrum of the mode-locked thulium-doped fiber laser showing sidebands due to periodicity and modulation due to an etalon in the cavity. Sidebands located more than 7 nm from the center of the spectrum corresponded to the order 2, 3, and 4 resonant sidebands, while the modulation near the spectral peak is due to an intracavity etalon . . . . .	49
3-11	Calculated transmission versus wavelength for a multiple plate filter of quartz plates with thickness 2T, 4T, and 8T at Brewster's angle in the cavity. The filter angle is set for maximum extinction (with c-axis at 40 degrees from TE) . . . . .	51

3-12	Comparison of pulses which exit the 5% output coupler (OC) with the pulses which exit the rejected port (RP). a) Autocorrelation of OC pulse with 450 fsec FWHM (fit with a sech) and average power 640 $\mu$ W. b) Autocorrelation of RP pulse with 420 fsec FWHM (fit with a sech) and average power 5.9 mW. c) Spectrum of OC pulse centered at 1792 nm. d) Spectrum of RP pulse centered at 1794 nm . . . . .	53
3-13	Diagram of pulse evolution in an stretched-pulse $\text{Er}^{+3}$ -doped fiber laser. The strong positive GVD of the $\text{Er}^{+3}$ -doped fiber is approximately balanced by the negative GVD of the passive fiber, causing the pulse to stretch and compress as it travels around the fiber ring . . . . .	54
3-14	Plot of group-velocity dispersion $k''$ versus wavelength for the dispersion-compensating (DC) fiber from Corning. The dispersion is +162 $\text{ps}^2/\text{km}$ at 1.55 $\mu\text{m}$ and is extrapolated to be $\approx +330 \text{ps}^2/\text{km}$ at 1.85 $\mu\text{m}$ . . . . .	56
3-15	Experimental setup for Optical Coherence Tomography from [87] . . . . .	57
3-16	$\text{Tm}^{+3}$ -doped fiber ASE versus absorbed pump power for 1.3 meters of CTm-158 and cw pump power at 785 nm . . . . .	58
3-17	ASE output power versus pump wavelength for a constant incident pump power of 840 mW . . . . .	59
3-18	First moment of ASE spectrum versus absorbed pump power at 785 nm. The wavelength shifts due to self-absorption in the fiber . . . . .	59
3-19	Two dimensional OCT image of calcified aortic plaque taken in vitro with the $\text{Tm}^{+3}$ -doped fiber ASE source and with a 1.3 $\mu\text{m}$ source of comparable resolution . . . . .	60
4-1	Experimental set-up of a stretched-pulse fiber laser optimized for frequency doubling. BFP: 5T quartz birefringent plate. PBS: polarizing beam splitter . . . . .	63
4-2	Plot of pulse energy and pulse width versus net dispersion for a stretched-pulse fiber laser, after Ref. [86] which used a 5% output coupler . . . . .	64
4-3	Autocorrelation of the 1.55 $\mu\text{m}$ pulse (dashed) and the frequency-doubled pulse (solid). A sech fit of the frequency-doubled pulse is also shown (dotted) . . . . .	65
4-4	Spectrum of 1.55 $\mu\text{m}$ pulse with spectral width of $\approx 67 \text{nm}$ (top) and spectrum of frequency-doubled pulse at 771 nm with spectral width of $\approx 7.3 \text{nm}$ . . . . .	66
4-5	Plot of the Type I phase-matching angle for second harmonic generation in BBO . . . . .	67
4-6	Experimental setup for frequency doubling the stretched-pulse (SP) fiber laser. Two other crystals, $\text{KNbO}_3$ and LBO, were also tested in place of the BBO . . . . .	68
4-7	Comparison of frequency-doubled spectra from the 10 mm BBO crystal (solid) and the 1.5 mm BBO crystal (dashed) . . . . .	68
4-8	Frequency-doubled spectra from the 10 mm BBO crystal (solid) and from the 1.5 mm $\text{KNbO}_3$ and 7.0 mm LBO crystals (dashed). The spectra from the $\text{KNbO}_3$ and LBO were essentially identical . . . . .	69

4-9	Experimental setup for measurement of SHG FROG. The spectrum of the SHG is measured as the pulse delay is changed in a background free autocorrelator . . . . .	71
4-10	Numerical SHG FROG traces of an unchirped gaussian pulse (left) and a chirped gaussian pulse (right). The SHG intensity is plotted versus time delay and frequency offset, where zero frequency offset corresponds to the peak of the spectrum . . . . .	71
4-11	SHG FROG traces of the 1.55 $\mu\text{m}$ pulse which was compressed to 72 fsec with gratings. The contour plot on the left shows the experimentally-measured trace, while the right-hand plot shows the calculated fit using the method of generalized projections . . . . .	73
4-12	Derived 1.55 $\mu\text{m}$ pulse intensity and phase profile based on the FROG fit from Fig. 4-11 . . . . .	73
4-13	Comparison of the 1.55 $\mu\text{m}$ pulse intensity and phase profiles from the derived fit of the experimental pulse (dashed) and when dispersion of $-0.0008 \text{ ps}^2$ was numerically added to obtain the optimally compressed pulse (solid) . . . . .	74
4-14	Plot of 1.55 $\mu\text{m}$ pulse width versus (numerically) added dispersion, which shows that the minimum pulse width of 67 fsec occurs for an added dispersion of $-0.0008 \text{ ps}^2$ . . . . .	74
4-15	Comparison of the experimentally measured 1.55 $\mu\text{m}$ spectrum (dashed) with the derived spectrum from the SHG FROG measurement (solid) . . . . .	75
4-16	Autocorrelation of the fundamental pulse plotted on a log scale to show the peak-to-background ratio of $\approx 10^5$ for time delays $> 2 \text{ psec}$ . . . . .	76
4-17	Autocorrelation of the frequency-doubled pulse plotted on a log scale to show the reduction in pulse wings from the fundamental pulse . . . . .	76
4-18	SHG FROG traces of the frequency-doubled pulse. The contour plot on the left shows the experimentally-measured trace, while the right-hand plot shows the calculated fit . . . . .	77
4-19	Low frequency RF spectrum (10 Hz to 100 kHz) of the frequency-doubled pulses compared to a commercial argon-pumped mode-locked Ti:sapphire laser. The y-axis is in units of dBc/Hz . . . . .	79
4-20	Pulsed operation of the stretched-pulse laser with net dispersion of $+0.041 \text{ ps}^2$ . Top: Autocorrelation trace (solid) and sech fit (dashed) showing pulse wings which extended to $> 2 \text{ psec}$ with 32% of the pulse energy contained in the non-sech wings, as compared to 20% for the laser with net dispersion of $+0.041 \text{ ps}^2$ as shown in Fig. 4-3 . Bottom: Pulse spectrum with spectral width of $\approx 70 \text{ nm}$ . . . . .	82
5-1	Experimental set-up for cut-back measurement of non-PM fibers. A circularly polarized source is launched into the fiber, and the polarization state is monitored at the end of the fiber as a function of fiber length . . . . .	86

5-2	Results of cutback measurement for the beat-length of fiber CTm-158 with a launched $1.3 \mu\text{m}$ source. At $1.85 \mu\text{m}$ the beat-length is approximately $35 \text{ cm}$ . . . . .	86
5-3	Experimental set-up for birefringent filter measurement of the beat-length of a PM fiber. A broadband $1.3 \mu\text{m}$ source is launched into the fiber at $45$ degrees from the birefringent axes, and the output polarizer is also set at $45$ degrees to the fiber axes. The optical spectrum of the output then shows the filtering effect and free spectral range from which the beat-length can be determined . . . . .	88
5-4	Results of a beat-length measurement with $1.157$ meters of PM $\text{Er}^{+3}$ -doped fiber in a birefringent filter configuration with a $1.3 \mu\text{m}$ broadband source. The free spectral range is $2.90 \text{ nm}$ , corresponding to $\ell_b = 2.6 \text{ mm}$ at $1.3 \mu\text{m}$ and $\ell_b \approx 3.1 \text{ mm}$ at $1.55 \mu\text{m}$ . . . . .	88
5-5	Plot of the output polarization state (described in terms of aspect ratio $c$ ) versus temperature for a $5.1$ -meter length of SMF-28 fiber with a launched circularly-polarized $1.55 \mu\text{m}$ source . . . . .	90
5-6	Plot of the output polarization state (described in terms of aspect ratio $c$ ) versus temperature for a $5.1$ meter length of PM Panda fiber with a launched circularly-polarized $1.55 \mu\text{m}$ source. Note that the x-axis range is only $5 \text{ deg C}$ compared with $120 \text{ deg C}$ in the measurement of the SMF-28 fiber in Fig. 5-5 . . . . .	91
5-7	Plot of free spectral range versus temperature for the measurement of Panda PM fiber set up as a birefringent filter, as in Fig. 5-3 . using a $93\text{-cm}$ fiber length and a $1.55 \mu\text{m}$ source . . . . .	93
5-8	Evolution of the polarization state in the presence of only birefringence. $\ell_b = 8$ meters (normalized $\ell_b = 1.12$ ) and $\ell_{npr} = \infty$ . The distance of propagation is $z$ . $I_+ =  E_+ ^2$ (solid), $I_- =  E_- ^2$ (dot-dash), $I_x =  E_x ^2$ (solid), and $I_y =  E_y ^2$ (dot-dash). The phase differences are indicated by $P_{+-} = \phi_+ - \phi_-$ (solid) and $P_{xy} = \phi_x - \phi_y$ (dot-dash) . . . . .	96
5-9	Evolution of the polarization state in the presence of only nonlinearity. $\ell_{npr} = 6.97$ and $\ell_b = \infty$ . Axis labels are the same as those of Fig. 5-8 . . . . .	97
5-10	Evolution of the polarization state in the presence of nonlinearity $\eta = 1.0$ and birefringence $\delta = 0.15$ . ( $\ell_{npr} = 6.97$ and $\ell_b = 21$ ). Axis labels are the same as those of Fig. 5-8 . . . . .	98
5-11	Evolution of the polarization state in the presence of nonlinearity $\eta = 1.0$ and birefringence $\delta = 0.25$ . ( $\ell_{npr} = 6.97$ and $\ell_b = 12.6$ ). Axis labels are the same as those of Fig. 5-8 . . . . .	99
5-12	Evolution of the polarization state in the presence of nonlinearity $\eta = 1.0$ and birefringence $\delta = 0.35$ . ( $\ell_{npr} = 6.97$ and $\ell_b = 8.98$ ). Axis labels are the same as those of Fig. 5-8 . . . . .	100
5-13	Evolution of the polarization state for different intensities: (solid) $100\text{W}$ , (dashed) $80\text{W}$ , (dot-dash) $60\text{W}$ , (dotted) $40\text{W}$ , and (solid) $20\text{W}$ . Parameters are from [21] with normalized $\eta = 1.0$ and $\delta = 2.8$ and initial state with $ E_x ^2 = 0.36$ and $P_{xy} = \phi_x - \phi_y = 30 \text{ deg}$ . Axis labels are the same as those of Fig. 5-8 . . . . .	102

5-14	Dot-product of polarization states at different intensities with the polarization state at the peak of the pulse. Parameters are from [21] with normalized $\eta = 1.0$ and $\delta = 2.8$ and initial state with $ E_x ^2 = 0.36$ and $P_{xy} = \phi_x - \phi_y = 30$ deg. Curves: (dashed) dot-product of 80W and 100W, (dot-dash) dot-product of 60W and 100W, (dotted) dot-product of 40W and 100W, and (solid) dot-product of 20W and 100W	103
5-15	Dot-product of polarization state at the peak of the pulse with the polarization state of cw for fiber with birefringence (dashed) and without birefringence (solid). Parameters are from [21] with normalized $\eta = 1.0$ and $\delta = 2.8$ for the dashed curve. Both curves are sinusoidal, although the period of the dot-product with birefringence is longer because the birefringence reduces the nonlinear polarization rotation	104
5-16	Diagram of elliptical polarization state. The azimuthal angle $\Psi$ is the angle of the major axis of the ellipse from the x-axis (slow-axis) and is defined in eqn. (5.29). The ellipticity of the polarization state is defined by $\mathcal{X}$ in eqn. (5.30)	105
5-17	Contour plot of intensity discrimination versus azimuthal angle $\Psi$ and ellipticity $\mathcal{X}$ which occurs for the simulation length of 10 meters. The optimum initial elliptical states have intensity discriminations which approach 1.0	107
6-1	Diagram of the nonlinear Mach-Zehnder interferometer which is equivalent to light traveling in two polarizations down a fiber	110
6-2	Plot of $r\sqrt{1-r^2}$ (dash-dot), $(2r^2-1)$ (dashed), and $r\sqrt{1-r^2}(2r^2-1)$ (solid) versus $r^2$	114
6-3	Experimental setup of an all-PM Er <sup>+3</sup> -doped fiber laser. WDM: wavelength-division multiplexing coupler, PBS: polarizing beam splitter, and BFP: birefringent tuning plate. In the PM Er-doped fiber section, the light is linearly polarized along one of the PM axes, so no APM action occurs in this fiber. The section of passive PM fiber is repeatedly cross-spliced so that the pulses stay overlapped and both SPM and XPM occur, aiding the pulse shortening	115
6-4	Diagram of the offset angle $\rho$ between fast and slow axes at a cross-splice. $x_1$ and $y_1$ are the slow and fast axes, respectively, of the first fiber, while $x_2$ and $y_2$ are the slow and fast axes of the second fiber. For an optimum cross-splice, $y_2$ would overlap $x_1$ . An offset angle $\rho$ between $y_2$ and $x_1$ decreases the transmitted power by a factor of $(\cos \rho)^2$ due to walkoff from uncompensated linear birefringence	117
6-5	Spectrum of pulses from all-PM fiber laser with one cross-splice	118
6-6	Experimental setup for the stretched-pulse sigma laser. FR: Faraday rotator, WDM: wavelength-division-multiplexing coupler, BFP: birefringent tuning plate, and AM: amplitude modulator	121
6-7	Spectrum (a) and autocorrelations of the same pulse from the stretched-pulse sigma laser after compression with gratings (b) or prisms (c). The autocorrelations are fit with a sech (dashed)	124

6-8	Transmission versus nonlinear phase shift $\phi_{nl}$ for eqn. (6.26 ) with $r^2 = 0.85$ , $\sin 2\theta = 1$ , and $\phi_{nl} = 2\kappa a ^2(2r^2 - 1)$ . For the solid curve, the phase bias $\phi = \pi$ , while for the dashed curve $\phi = 2\pi/3$ . Transmission is $ b ^2/ a ^2$ . . . . .	125
7-1	Possible design for a mode-locked $\text{Er}^{+3}$ -doped fiber laser which uses a saturable Bragg reflector and P-APM. The percentage of the intracavity intensity which impinges on the SBR can be adjusted from 0% to 100% so that the effect of the SBR on the mode-locking can be studied	131
A-1	Experimental setup for measuring output power at $1.55 \mu\text{m}$ and unabsorbed pump power at $980 \text{ nm}$ versus input pump power in the backward-pumping scheme . . . . .	135
A-2	Plot of output power versus input pump power for backward pumping ( $\diamond$ ) and forward pumping ( $\bullet$ ) . . . . .	136
A-3	Plot of unabsorbed pump power versus input pump power for both lasing and non-lasing operation. Backward pumping is indicated by closed and open diamonds for lasing and non-lasing, respectively, while forward pumping is indicated by closed and open circles . . . . .	136

# List of Tables

2.1	Comparison of the Kerr coefficients $\delta$ and the second- and third-order group velocity dispersions for the fibers used in this thesis. $\lambda$ : wavelength, and MFD: mode-field diameter. The values shown for $k''$ were calculated and then verified experimentally, while those for $k'''$ were only calculated. . . . .	30
4.1	Comparison of the frequency-doubling results obtained with the BBO, KNbO <sub>3</sub> , and LBO crystals. . . . .	70
4.2	Comparison of the 1.55 $\mu\text{m}$ pulse characteristics and frequency-doubling results (using a 1-cm, uncoated BBO crystal) for the stretched-pulse lasers with net dispersion of +0.041 ps <sup>2</sup> and +0.013 ps <sup>2</sup> . . . . .	81



# Chapter 1

## Introduction

In the late 1960's the incorporation of trivalent rare-earth ions such as neodymium, erbium, and thulium into glass hosts [1] in the cores of glass fiber waveguides [2,3] made fiber lasers possible. Due to the high efficiency of the  $\text{Nd}^{+3}$  ion as a laser, early work focused on  $\text{Nd}^{+3}$ -doped silica fiber lasers which operated at  $1.06 \mu\text{m}$  [4]. The advantages of these lasers included simple doping procedures, low loss, and optical power confinement over extended interaction lengths. Doping of silica fibers with  $\text{Er}^{+3}$ -ions was not achieved until the 1980's [5,6]. Since that time  $\text{Er}^{+3}$ -doped fiber lasers have received much attention and research effort because the lasing wavelength at  $1.55 \mu\text{m}$  falls within the low-loss window of optical fibers and thus is suitable for optical fiber communications. Thulium ( $\text{Tm}^{+3}$ ) is a third rare-earth ion which has been successfully incorporated into optical fibers [7]. Initial interest in  $\text{Tm}^{+3}$ -doped fiber lasers arose because its emission covers gaps between the bands of  $\text{Nd}^{+3}$  and  $\text{Er}^{+3}$  in the 1400 to 2700 nm range. With silica as the glass host,  $\text{Tm}^{+3}$ -doped fiber lasers have operated from 1.7 to  $2.1 \mu\text{m}$  [8,9]. In fluoride-glass hosts, additional transitions of the  $\text{Tm}^{+3}$ -ion are available due to an increase in the number of metastable upper states. Continuous-wave  $\text{Tm}^{+3}$ -doped fluoride fiber lasers have been demonstrated around 0.82, 1.48, 1.9, and  $2.3 \mu\text{m}$  [10]. Rare-earth ions such as  $\text{Ho}^{+3}$  [11,12] and  $\text{Yb}^{+3}$  [13,14] have also been used as dopants or co-dopants in silica or fluoride fibers allowing new lasing or pumping wavelengths, while  $\text{Pr}^{+3}$  has been incorporated into fluoride fiber providing emission at  $1.3 \mu\text{m}$  [15,16]. Fig. 1-1 shows the wavelength ranges accessible from the different rare-earth dopants in silica glass fibers. Interest in compact, diode-pumped, fiber-compatible optical sources at various wavelengths has been the motivation for much of this fiber laser research over the last ten years.

In addition to continuous-wave operation, fiber lasers can be operated in a pulsed mode (mode-locked) with an output of one or more pulses per round-trip time. Mode-locked lasers have a number of potential applications, depending on the wavelength and pulse width. They could be used as sources in communications systems, spectroscopic tools in the laboratory for time-resolved studies of fast nonlinear phenomena in semiconductors, or as a source in eye-safe laser radar (LIDAR). Short pulses could also be used as a source for a pulsed optical-fiber gyroscope or as a seed pulse for another laser in medical applications. Applications such as Optical Coherence Tomography could take advantage of the broad bandwidth of a mode-locked fiber laser

rather than the temporal ultrashort pulse width.

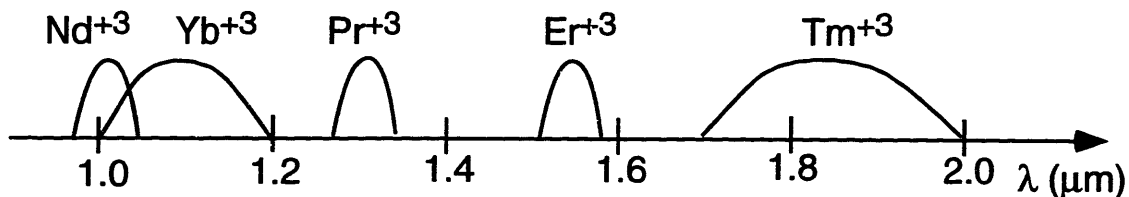


Figure 1-1: Diagram of wavelength ranges which can be obtained by rare-earth dopants in silica fibers. The approximate bandwidth for each rare-earth ion is also indicated.

Fiber lasers can be mode-locked actively, where a modulator controls the cavity losses and induces pulsed operation, or passively, where an intensity fluctuation acts in conjunction with a nonlinear medium inside the cavity to modulate the cavity loss without external control. The shortest pulses which can be obtained from active mode-locking tend to be limited to approximately 1 psec by the speed of the electronics used to drive the modulators, and so passive mode-locking is the preferred technique for obtaining the shortest pulses. (Active mode-locking, though, allows operation at frequencies much higher than the fundamental repetition rate, which is important for communications applications.) Passive mode-locking of fiber lasers has been achieved using three methods: nonlinear amplifying loop mirrors [17,18], nonlinear polarization rotation [19,20,21], and semiconductor saturable absorbers [22]. Both the nonlinear amplifying loop mirror and nonlinear polarization rotation use the Kerr effect in a length of optical fiber in conjunction with an interferometer geometry to form an artificial saturable absorber and achieve pulse shortening. (Nonlinear polarization rotation will be explained in more detail in Section 2.6.) In the semiconductor saturable absorber experiments, a multiple-quantum well sample on a high reflector is bleached by high intensities. The loss of the cavity decreases as intensity increases, thus favoring pulsed operation. These three techniques have resulted in the demonstration of subpicosecond pulses at a number of different wavelengths. Neodymium-doped silica fiber lasers have produced pulses as short as 42 fsec at 1.06  $\mu\text{m}$  [23], while 620 fsec pulses at 1.3  $\mu\text{m}$  have been generated by praseodymium-doped fluoride fiber lasers [24]. Erbium-doped fiber lasers have produced pulses as short as 63 fsec at 1.55  $\mu\text{m}$ , corresponding to spectral widths greater than 60 nm and close to the gain-bandwidth of erbium [25].

Although significant research has been done on lasers at longer wavelengths in  $\text{Tm}^{+3}$ -doped and  $\text{Ho}^{+3}$ -doped fibers, work has primarily focused on obtaining tunable and high-power continuous-wave operation [11,26,27]. Pulsed sources at wavelengths between 1.8 and 2.0  $\mu\text{m}$  have a number of interesting applications because they are eye-safe: water strongly absorbs light in this wavelength region, preventing these wavelengths from reaching the retina. In eye-surgery and other types of surgery, water absorption in this wavelength region prevents the laser light from penetrating the tissue too deeply. Therefore, two potential applications for a mode-locked fiber laser at 1.8 to 2.0  $\mu\text{m}$  are as a tunable seed for  $\text{Tm}:\text{YAG}$  or  $\text{Ho}:\text{YAG}$  lasers for short-pulse medical applications and as a source for eye-safe laser radar (LIDAR). Thulium-doped silica fiber is a natural choice for the laser gain material, since the smooth fluorescence spectrum of thulium is the widest of all the rare-earth ions, indicating that tunable ultrashort pulse generation should be possible. Thulium-doped fiber also has the advantage of strong absorption at 785 nm, where  $\text{AlGaAs}$  laser diodes have provided sufficient pump power for cw operation [9] and potentially could pump a mode-locked laser. Previously reported work on mode-locking of a thulium-doped fiber laser was an actively mode-locked and passively Q-switched thulium-doped fluoride fiber laser operating at 810 nm [28]. The authors obtained mode-locked pulses of 6 nsec and 0.54 W peak power under a 400 nsec Q-switched window. More recently, a group at Raytheon has reported work on a mode-locked thulium-doped fiber laser using a semiconductor saturable absorber [29]. Pulses of 190 fsec and with average powers up to 1 mW were obtained, but the laser was not tunable.

## 1.1 Thesis Organization

This thesis is organized as follows. Chapter two discusses  $\text{Er}^{+3}$ - and  $\text{Tm}^{+3}$ -doped fibers and also reviews the Kerr effect and group-velocity dispersion in fibers as these are the two components most important in building a mode-locked fiber laser. Passive mode-locking employing nonlinear polarization rotation (also called polarization additive pulse mode-locking, P-APM) is reviewed. Chapter three discusses a mode-locked  $\text{Tm}^{+3}$ -doped fiber laser at 1.8  $\mu\text{m}$  and explores an application for this new source. As a continuation of previous research in our group on mode-locked  $\text{Er}^{+3}$ -doped fiber lasers, chapter four discusses work on the optimization of a stretched-pulse fiber laser for a new application of frequency doubling the 1.55  $\mu\text{m}$  pulses to 775 nm.

Measurements of the birefringence and temperature sensitivity of standard and PM-fiber are discussed in chapter five, as well as simulation and analysis of the effects of linear birefringence in a fiber laser mode-locked by P-APM. Work towards achieving environmental stability of a mode-locked fiber laser is the topic of chapter six. An analysis of mode-locking in a laser constructed of PM fiber as well as two designs for environmentally-stable mode-locked fiber lasers are discussed. Conclusions and suggestions for further work are discussed in chapter seven.

# Chapter 2

## Fiber Laser Background

Doped optical fibers are an attractive gain material for lasers and amplifiers. They are solid-state and do not have to be water-cooled, and they can be pumped easily with wavelength-division-multiplexing fiber couplers. Doped fibers provide both the gain and the cavity since the light is guided by the single-mode core. Fiber lasers can also be made compact when packaged efficiently, and silica-based fibers are reliable and are not hygroscopic. In order to achieve passive mode-locking in a fiber laser, certain effects in the optical fiber are exploited such as group-velocity dispersion and self-phase modulation. This chapter contains short descriptions of the characteristics of thulium-doped and erbium-doped silica fibers, which are the two rare-earth doped fibers used in this thesis, as well as descriptions of the effects in a fiber which are important for mode-locking. Pulse shortening via nonlinear polarization rotation is also explained.

### 2.1 Erbium-doped silica fiber

Due to current interest in all-optical communications, erbium-doped fiber is probably the most well-known of all the rare-earth doped fibers.  $\text{Er}^{+3}$ -doped fiber amplifiers are beginning to replace repeaters in undersea transmission systems, and  $\text{Er}^{+3}$ -doped fiber lasers may someday have a role as a pulsed source in a communications network. Many excellent references exist on the characteristics of  $\text{Er}^{+3}$ -doped fiber including [30,31,32], and so only brief comments are included here.

Erbium-doped silica fiber is a three-level system with pump absorption bands at 800 nm, 980 nm, and 1480 nm and broadband emission near 1.55  $\mu\text{m}$  as shown in Fig. 2-1. Common oxide glasses doped with  $\text{Er}^{+3}$  only have this one metastable state ( $^4\text{I}_{13/2}$ ) at room temperature leading to gain at the 1500 nm  $^4\text{I}_{13/2} \rightarrow ^4\text{I}_{15/2}$  emission band. Fluoride glasses, on the other hand, can provide gain at a number of other wavelengths (1.0  $\mu\text{m}$  [33] and 2.7  $\mu\text{m}$  [34]). The difference in emission wavelengths is due to the difference of non-radiative decay rates between the two glasses. Oxide glasses have larger nonradiative rates because their strong covalent bonds result in higher phonon frequencies. The weaker ionic bonds in halide glasses lead to a much lower nonradiative decay rate as well as higher transparency in the mid-infrared (2 to

8  $\mu\text{m}$ ). The low effective phonon frequencies in fluorides enable additional metastable states and thus allow more transitions. (In general, glasses have much larger non-radiative rates than crystals of similar composition because of the larger effective phonon frequencies and stronger electron-phonon coupling.)

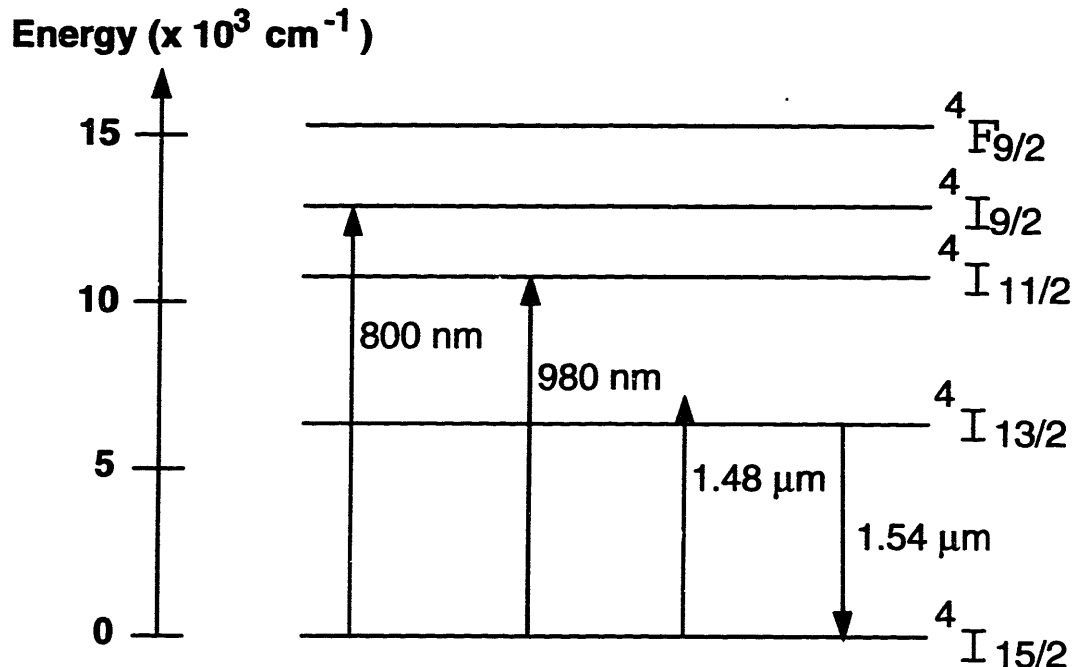


Figure 2-1: Energy levels of  $\text{Er}^{+3}$  in silica-glass fiber. Possible pump bands are at 800 nm, 980 nm, and 1.48  $\mu\text{m}$ , with broadband emission near 1.55  $\mu\text{m}$ . (Energy levels above the  ${}^4F_{9/2}$  level are not shown).

For erbium-doped silica fiber, the most convenient pump wavelength would be 800 nm due to the availability of high power AlGaAs diodes, but pump excited-state absorption occurs which seriously degrades the pumping efficiency. 980 nm and 1480 nm are then the preferred pump wavelengths, and diode lasers are available at both wavelengths: strain-layer InGaAs diodes at 980 nm and InGaAsP diodes at 1480 nm. Pumping at 980 nm has shown higher gains and better noise performance [35], and so in this thesis, a commercial Master Oscillator Power Amplifier (MOPA) at 980 nm was used as the pump source. The MOPA output power is 1 Watt single-mode, of which 60 to 70% can be coupled into a single-mode fiber.

The lasing transition in  $\text{Er}^{+3}$ -doped silica fiber is primarily homogeneously broadened at room temperature, although rare-earth doped fibers exhibit both homogeneous and inhomogeneous broadening mechanisms. The underlying splitting mechanism is Stark splitting due to the local electric field. The degenerate energy levels of each active ion are split into a series of levels called a manifold. Also, homogeneous and inhomogeneous broadening mechanisms smear out each of the levels within the manifold. In solids, inhomogeneous broadening results from the fact that the laser ions

see different environments (different local crystal structure, defects, dislocations, and lattice impurities) [36]. These defects and random strains can change the local crystal fields seen by the laser ions, resulting in shifts of the exact resonance frequencies of these ions. The different energy levels created within the manifolds are essentially independent of temperature (and thus inhomogeneous). Homogeneous broadening is caused by phonon broadening due to lattice vibrations. There are rapid phonon-induced transitions between the Stark components within a given multiplet, and this broadening mechanism is reduced by decreasing the temperature. There have been a number of studies on broadening mechanisms in erbium-doped fiber [37,38] which revealed that by cooling the fiber to liquid helium temperatures (4.2 K), the gain changed from primarily homogeneous to primarily inhomogeneous. But at room temperature (where the experiments of this thesis were performed), this inhomogeneous strain broadening in the fiber is masked by the larger phonon-broadening effects, and the erbium-doped fiber appears to be homogeneously broadened and shows predominantly homogeneous saturation characteristics [39]. (Even the highest components of the  ${}^4I_{15/2}$  and  ${}^4I_{13/2}$  multiplets have some thermal occupation, and the emission and absorption near  $1.55\ \mu\text{m}$  is a composite of 56 largely unresolved Stark transitions.) The radiative lifetime of the upper state is  $\approx 10$  msec in erbium-doped fiber [40].

## 2.2 Thulium-doped silica fiber

Thulium is the rare-earth element next to erbium on the periodic table (atomic number 69) and has the same stable trivalent (3+) level of ionization due to the removal of the  $6s^2$  and  $5d$  electrons. Although Gandy and coworkers [41] reported the first  $\text{Tm}^{+3}$ -doped glass laser at 1900 nm using a Li-Mg-Al silicate glass in 1967, significant work on  $\text{Tm}^{+3}$ -doped glasses did not occur until the late 1980's when interest in doped fiber lasers heightened [7,42]. The energy level diagram for  $\text{Tm}^{+3}$ -doped silica fiber is shown in Fig. 2-2 and shows emission at 1.8 to  $2.0\ \mu\text{m}$  which occurs in a region of the optical spectrum not covered by  $\text{Nd}^{+3}$  or  $\text{Er}^{+3}$ . Similar to erbium, when thulium is incorporated into fluoride fibers, additional transitions are available (at 0.82, 1.48, 1.88, and  $2.35\ \mu\text{m}$  [10,27] and  $2.25$  to  $2.5\ \mu\text{m}$  [43]) due to lower multiphonon relaxation rates which enable a larger number of metastable upper states. In silica fiber, the energy gaps below the  ${}^3H_5$ ,  ${}^3F_3$ , and  ${}^3F_2$  levels are so small that multiphonon emission causes them to have extremely short lifetimes, so it would be unlikely to achieve a population inversion for any of these states regardless of host or temperature [30]. The host glass thus has a greater effect on the emission wavelengths for  $\text{Tm}^{+3}$  compared to  $\text{Er}^{+3}$  or  $\text{Nd}^{+3}$  because of the small effective energy gaps. Like  $\text{Er}^{+3}$ ,  $\text{Tm}^{+3}$  is primarily homogeneously broadened at room temperature. The individual Stark transitions cannot be resolved except at temperatures close to absolute zero, and composition-to-composition variations of the room-temperature homogeneous line widths cannot be fully explained yet.

The  ${}^3H_4$  level is metastable in  $\text{Tm}^{+3}$ -doped silica glass, resulting in a three-level lasing system when the  ${}^3H_4$  to  ${}^3H_6$  transition is pumped with 785 nm into the  ${}^3H_4$  level. Fig. 2-3 shows the  ${}^3H_4 \rightarrow {}^3H_6$  emission spectrum of a  $\text{Tm}^{+3}$ -doped silica fiber

(CTm158). The transition is significantly broader than the  ${}^4I_{13/2} \rightarrow {}^4I_{15/2}$  transition in  $\text{Er}^{+3}$  due to a larger number of Stark components in the  $\text{Tm}^{+3}$  manifolds and slightly larger splittings. Relaxation of the  ${}^3H_4$  level is predominately non-radiative, leading to low quantum efficiencies of 5 to 15% for silica, where the measured lifetime  $\tau_{\text{obs}} \approx 0.2$  msec and estimated radiative lifetime  $\tau_{\text{rad}} \approx 3.4$  msec [8]. The low quantum efficiency results in a high threshold for these lasers, but should not impair the slope efficiency since the stimulated emission dominates nonradiative relaxation once threshold is reached [26]. Because the transition is three-level in nature,  $\text{Tm}^{+3}$  also has a problem with self-absorption: the absorption due to thermally populated Stark levels in the ground state multiplet which pushes the lasing to longer wavelengths. Cooling the fiber to depopulate the upper Stark levels results in reduced self-absorption [7] as does using shorter fiber lengths. The tuning ranges of continuous-wave  $\text{Tm}^{+3}$ -doped lasers have been adjusted by using the appropriate fiber lengths to control self-absorption [8].

As shown in Fig. 2-2  $\text{Tm}^{+3}$ -doped silica fiber can be pumped at 670 nm, 785 nm, and in the extreme wing of the  ${}^3H_6 \rightarrow {}^3H_5$  transition at 1064 nm. Dye lasers and even laser diodes are available at 670 nm, however, pump excited-state absorption from the  ${}^3F_2$   ${}^3F_3$  level to the  ${}^1D_2$  lowers the pumping efficiency. Emission at  $\approx 460$  nm and  $\approx 370$  nm have been observed with 670 nm pumping [30]. The  ${}^3H_6 \rightarrow {}^3H_4$  transition at 785 nm has exhibited no excited-state absorption and has a relatively large absorption cross-section ( $\approx 3.2 \times 10^{-21}$  cm<sup>2</sup> at 785 nm compared to  $\approx 5.2 \times 10^{-21}$  cm<sup>2</sup> at 670 nm). Thus, for the experiments reported in this thesis, the pump source was a cw Ti:Sapphire laser at 785 nm using a Schwarz Electro Optic crystal which provided up to 600 mW of pump power inside the fiber. (The laser was also tunable from 770 nm to 810 nm with a quartz birefringent tuning plate.) It is also possible to pump  $\text{Tm}^{+3}$  with a Nd:YAG laser at 1064 nm, as demonstrated in a number of experiments [42,44]. Although decent lasing can be obtained [26], excited-state absorption of the pump is still a problem, leading to considerable blue emission at 460 nm which involves a three-photon process [44].

### 2.2.1 Photodarkening in $\text{Tm}^{+3}$ -doped fibers

An interesting phenomenon which has been observed in some  $\text{Tm}^{+3}$ -doped fibers is photodarkening, the increase in attenuation coefficient over a broad spectral region induced by exposure to certain pump wavelengths. Photodarkening had previously been observed in Ge-containing fibers with no rare-earth ions when the fiber was exposed to 488 nm light [45]. The process generally involves two-photon absorption (TPA), which can break Ge-Si bonds, creating free electrons and Ge(3) color centers. The free electrons can fall into Ge-related traps, creating Ge(1) and Ge(2) centers, which are broadly absorbing. Although the photodarkening is decreased by single-photon absorption, spontaneous recombination, and thermal bleaching, permanent changes in loss were induced by pumping sufficiently so that TPA dominated. On the other hand, photodarkening in  $\text{Tm}^{+3}$ -doped fibers has occurred without Ge as a co-dopant, indicating that the thulium ions and  $\text{Al}_2\text{O}_3$  co-dopant were important [46]. (Photodarkening was not observed in an undoped aluminosilicate fiber [47].)

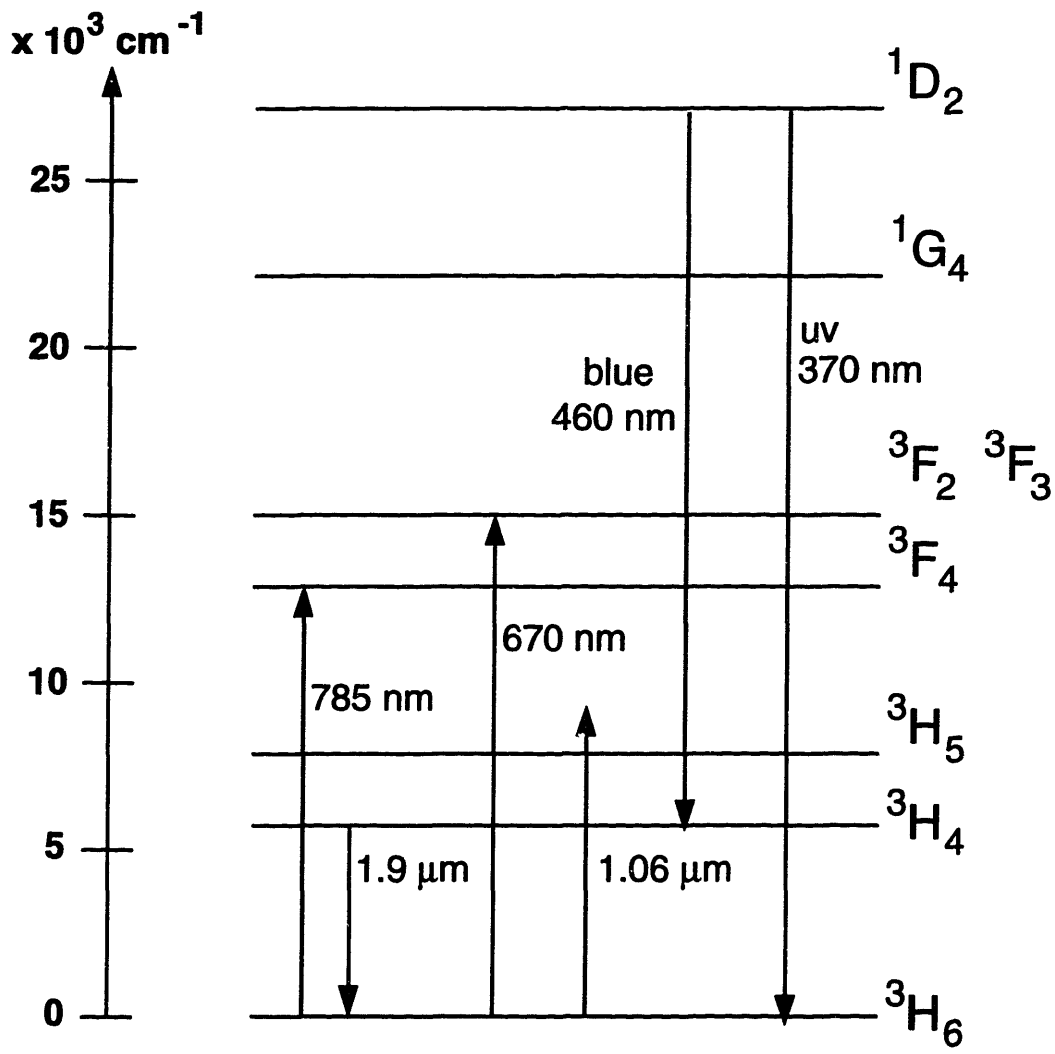


Figure 2-2: Energy levels of  $Tm^{+3}$  in a silica-glass fiber. Possible pump bands are at 670 nm, 785 nm, and  $1.06 \mu\text{m}$ . Emission typically occurs between  $1.8$  and  $2.0 \mu\text{m}$ , but also at  $\sim 370 \text{ nm}$  and  $460 \text{ nm}$  when pump excited-state absorption occurs.



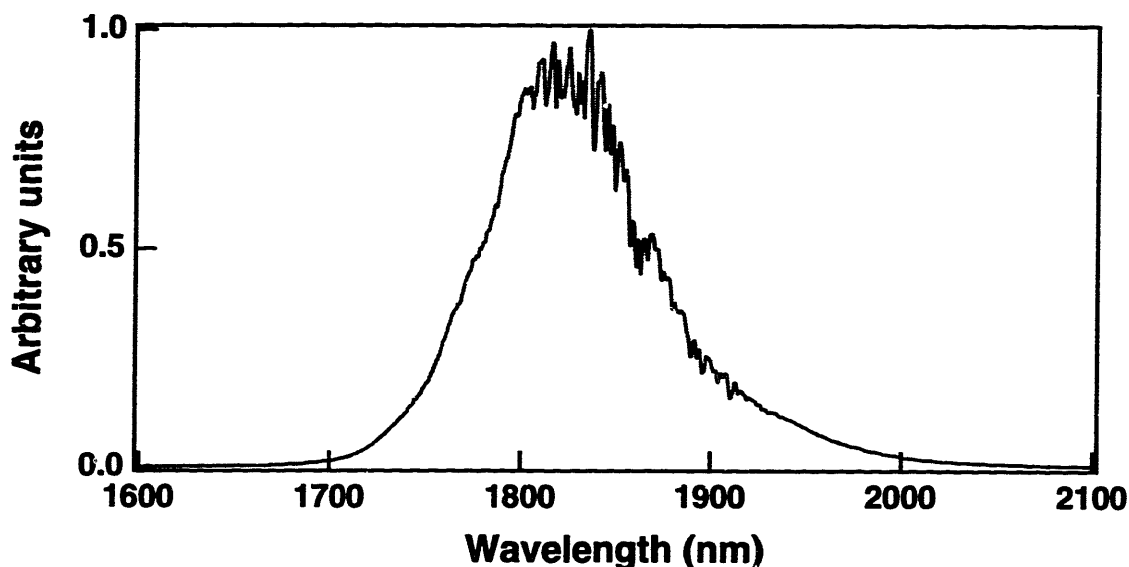


Figure 2-3: Fluorescence spectrum of thulium-doped silica fiber when pumped with 500 mW of cw power at 785 nm.

Exposure to near-resonance mode-locked 1064-nm radiation at 300 K induced permanent photodarkening with a rate that followed a  $\approx 5$  power dependence on the pump intensity. The results in [46] showed that absorption of infrared radiation led to photoionization in the  $\text{Tm}^{+3}$ -doped fiber through a multiphoton (5 photon) step-wise excitation channel.

I observed photodarkening in a  $\text{Tm}^{+3}$ -doped fiber from AT&T which had  $\text{Al}_2\text{O}_3$  as a co-dopant and an absorption of 50-60 dB at 790 nm. In the experiment, a 1 meter piece of fiber was pumped with about 500 mW of cw 785 nm light from a Ti:Sapphire laser. The transmitted pump power was at first 100 mW, but decayed within 2 minutes to the  $\mu\text{W}$  level. Then when the fiber was left unpumped for 3 - 4 minutes, the fiber seemed to recover completely, at least in terms of absorption at the pump wavelength. Although I did not investigate this photodarkening behavior extensively, I did observe that the photodarkening rate was highly dependent on the intensity of the 785 nm pump power. With 200 mW at 785 nm in the fiber, darkening was very slow ( $\sim$  hours). The pump wavelength also affected the photodarkening rate. Our hypothesis was that the photodarkening was caused by photo-ionization of  $\text{Tm}^{+3}$  to  $\text{Tm}^{+4}$  (through absorption of four photons) and trapping of the free electrons in the defects in the glass, forming broadly absorbing color centers. The recovery is due to thermal recombination of the free electrons with the  $\text{Tm}^{+4}$  to form  $\text{Tm}^{+3}$  again. Similar experiments with other  $\text{Tm}^{+3}$ -doped fibers from Rutgers University (with higher  $\text{Tm}^{+3}$  doping and only Ge as a co-dopant) did not reveal any photodarkening, providing further evidence that both  $\text{Tm}^{+3}$  and  $\text{Al}_2\text{O}_3$  are important for the process. These non-darkening fibers (CTm119 and CTm158) were used in the mode-locked laser reported in this thesis. A more detailed study of photodarkening in  $\text{Tm}^{+3}$ -doped fibers with different co-dopants would be an interesting subject for further

research, in particular, because photodarkening has also recently been observed in  $\text{Yb}^{+3}$ -doped fibers [48,49].

## 2.3 Double-clad doped-fibers

Recently there has been considerable work on rare-earth doped double-clad fibers, which allow inexpensive and high-power multi-mode diodes to be used as the pump source. Fig.2-4 shows a double-clad fiber with a rectangularly shaped second cladding. The double-clad fiber is single-mode at the lasing wavelength and multi-mode at the pump wavelength, but the second cladding confines the pump wavelength. The pump light basically undergoes total internal reflection at the interface between the second cladding and outermost cladding and is guided around and through the core to excite the lasing ions (which are doped only in the single-mode core). Certain shapes for the second cladding optimize the frequency with which a ray of pump light passes through the core as it travels down the fiber, i.e. a rectangular outer cladding is better than a circular one [50]. Although the pumping efficiency is lower, requiring longer fiber lengths for equivalent gain to a standard doped fiber, the double-clad geometry allows the use of multi-mode pump diodes which can have high powers and can be inexpensive. Both amplifiers and lasers have been demonstrated in double-clad  $\text{Nd}^{+3}$ -doped fibers [51,52] and in double-clad  $\text{Yb:Er}$ -doped fibers [53,54,55,56].

Unfortunately cladding-pumping is, at this time, not feasible in  $\text{Tm}^{+3}$ - or  $\text{Er}^{+3}$ -doped fibers, because they are three-level systems, whereas  $\text{Nd}^{+3}$  is a four-level system. The high pump rate required for inversion in three-level systems can not be reached in cladding-pumped fibers.  $\text{Tm}^{+3}$ -doped silica fibers are sometimes called quasi-three-level because the lower laser level is a Stark component of the ground state manifold with a small thermal population of the total ground state population. But the transition is not sufficiently close to four-level for efficient cladding-pumping, which was verified in recent experiments with a double-clad  $\text{Tm}^{+3}$ -doped fiber [57] pumped at 785 nm and 1064 nm. (Too much self-absorption occurs: ions in the ground state reabsorb emission at the shorter wavelengths.) Efficient cladding-pumping can be achieved for  $\text{Er}^{+3}$  when the co-dopant  $\text{Yb}^{+3}$  is used.  $\text{Yb}^{+3}$  is a four-level system, has a high absorption cross-section centered at 980 nm band, and can be pumped over a wavelength range extending from 800 - 1100 nm, whereupon energy transfer occurs to excite the erbium ions. The pump absorption and population inversion of the  $\text{Er}^{+3}$  system can be dominated by the concentration of  $\text{Yb}^{+3}$  ions when concentration ratios of 10:1 to 30:1 are employed. Disadvantages of these  $\text{Yb:Er}$ -doped fibers include lower  $\text{Er}^{+3}$ -doping concentrations than in conventional  $\text{Er}^{+3}$ -doped fibers, requirement of long fiber lengths, and limited availability of the  $\text{Yb:Er}$ -doped fiber itself.

## 2.4 Self-Phase Modulation

Dispersion and self-phase modulation are two effects which occur in mode-locked lasers due to the refractive index of the glass. Self-phase modulation (SPM) is the intensity dependent phase shift and resulting spectral broadening which arises when

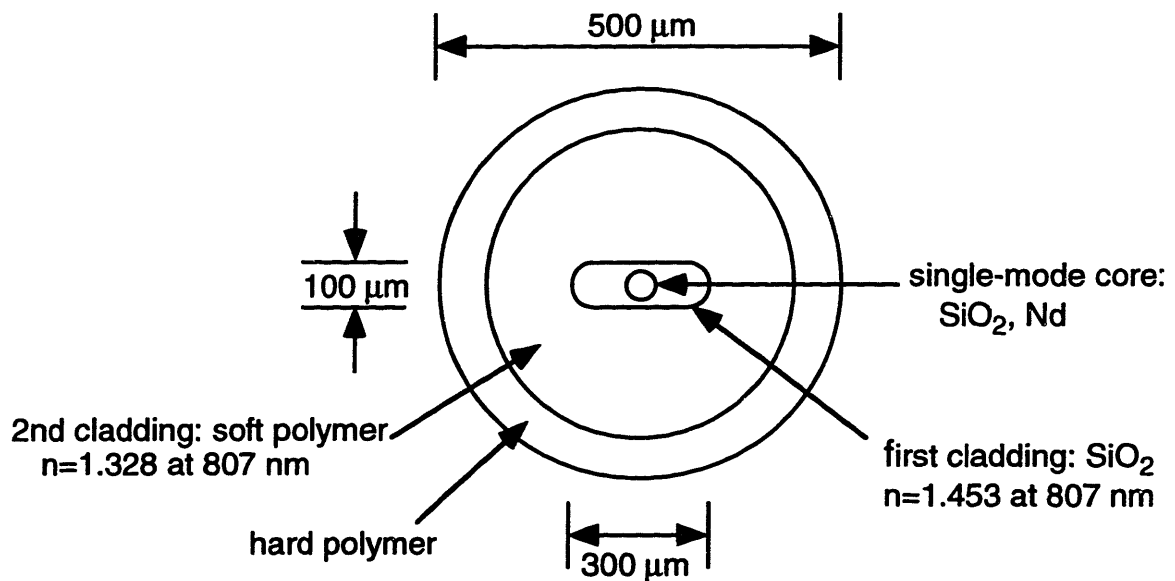


Figure 2-4: Cross-sectional view of neodymium-doped double-clad fiber. The 7.5  $\mu\text{m}$ -diameter circular core is surrounded by a region of pure silica that is rectangular with dimensions  $100 \mu\text{m} \times 300 \mu\text{m}$ . The second cladding is a fluoropolymer with a low refractive index and low optical loss. The rectangular region serves as the cladding for confining laser light in the single-mode core and as the multimode core for the 807 nm pump light within the hard polymer outer cladding [52].

a pulse passes through a medium with an intensity dependent index of refraction. The index  $n$  is expressed as

$$n(I(t)) = n_0 + n_2 I(t) \quad (2.1)$$

where  $n_0$  is the linear index,  $n_2$  is the nonlinear index, and  $I(t)$  is the pulse intensity. The index is assumed to respond instantaneously to changes in intensity. When a pulse propagates through a medium with nonzero nonlinear index  $n_2$  and length  $\ell_K$ , the pulse magnitude is unchanged, while the pulse acquires a nonlinear phase proportional to its intensity:

$$u_{out}(t) = u_{in}(t) \exp(-j\delta\ell_K|u_{in}(t)|^2) \quad (2.2)$$

where the SPM or Kerr coefficient

$$\delta = \frac{2\pi n_2}{\lambda A_{eff}} \quad (2.3)$$

with  $A_{eff}$  the effective cross-section of the mode inside the medium and  $\lambda$  the wavelength of light in vacuum. The phase of the optical pulse becomes a function of time such that the instantaneous frequency across the pulse,  $(\omega(t) = -\frac{\partial\phi}{\partial t})$ , is also time dependent. A time-dependent instantaneous frequency is called chirp and for  $n_2 > 0$ , the higher frequency or blue components are in the trailing edge of the pulse while the lower frequency or red components are in the leading edge of the pulse. The pulse spectrum is broadened so that the pulse now includes more frequencies. Although SPM broadens the pulse spectrum, SPM alone does not result in temporal pulse shortening. The new frequency components travel in the leading and trailing edges of the pulse, resulting in a chirped pulse which is not transform-limited.

The Kerr coefficient is enhanced in optical fibers because of the small effective mode area  $A_{eff} \sim 8 \times 10^{-11} \text{ m}^2$  and the ability to use lengths of fiber on the order of meters. The nonlinear index  $n_2 = 2.36 \times 10^{-16} \text{ cm}^2/\text{W}$  in silica fiber, as recently measured and reported in [58]. Table 2.1 lists the Kerr coefficients for the various fibers used in the experiments of this thesis at the wavelengths of interest.

## 2.5 Group Velocity Dispersion

Group velocity dispersion results from the frequency dependence of the index of refraction,  $n(\omega)$ . Because of the frequency dependence of the index, different frequency components of the pulse will travel at different speeds and the temporal pulse shape will broaden as it propagates. The propagation constant  $k = \frac{n(\omega)\omega}{c}$  can be expanded in a Taylor series about the pulse center frequency  $\omega_0$ :

$$k(\omega) = k(\omega_0) + k'(\omega_0)(\omega - \omega_0) + \frac{1}{2}k''(\omega_0)(\omega - \omega_0)^2 + \frac{1}{6}k'''(\omega_0)(\omega - \omega_0)^3 + \dots \quad (2.4)$$

where the primes indicate differentiation with respect to frequency.  $k'(\omega_0)$  is the inverse group velocity of the pulse, and  $k''(\omega_0)$  is called the group-velocity dispersion

(GVD) since it is responsible for pulse broadening.  $k'''(\omega_0)$  is the third derivative of  $k$  with respect to frequency and is called the third-order dispersion. By normalizing out the inverse group velocity, the effects of GVD and third-order dispersion on the pulse envelope after propagating through a medium of length  $L_D$  is expressed as

$$u_{out}(\omega) = u_{in}(\omega) \exp \left\{ -j \frac{1}{2} k'' L_D (\omega - \omega_0)^2 - j \frac{1}{6} k''' L_D (\omega - \omega_0)^3 \right\}. \quad (2.5)$$

When a pulse propagates through a medium with nonzero GVD, or  $k''(\omega_0) \neq 0$ , the pulse magnitude broadens, while the spectrum remains unchanged. Also, the pulse acquires a time dependent instantaneous frequency or chirp which depends on the sign of  $k''(\omega_0)$ . For positive GVD, or  $k''(\omega_0) > 0$ , the lower frequency or red components travel faster and are in the leading edge of the pulse while the higher frequency or blue components are in the trailing edge of the pulse. And for negative GVD, or  $k''(\omega_0) < 0$ , the higher frequency components travel faster and are in the leading edge of the pulse, with the lower frequency components in the pulse trailing edge. The chirp from negative GVD is opposite to the chirp induced from SPM. When the effects of SPM and GVD are balanced, the pulse does not acquire a net chirp as it propagates, and so the pulse propagates without changing temporal or spectral shape. This is called a soliton and has a normalized pulse amplitude envelope of the form  $u(t) = \text{sech}(t)$ .

Optical fibers have group-velocity dispersion composed of both material dispersion and waveguide dispersion. The material dispersion is due to the frequency dependence of the refractive index of the silica (and co-dopants such as  $\text{GeO}_2$ ) and can be determined by simply taking the second derivative of the Sellmeier equation for the refractive index. For pure, undoped silica, the material GVD is negative (or anomalous) for wavelengths above  $1.3 \mu\text{m}$ , and is  $-25 \text{ ps}^2$  at  $1.55 \mu\text{m}$  and  $-65 \text{ ps}^2$  at  $1.8 \mu\text{m}$ . Waveguide dispersion reflects the dependence of the effective mode index on the core diameter, index difference between core and cladding ( $\Delta n$ ), and fiber structure. For step-index geometries and wavelengths in the infrared, waveguide dispersion is positive (or normal). It is then possible to shift the zero-dispersion wavelength to  $1.55 \mu\text{m}$  or greater by using the appropriate core size (4 to  $5 \mu\text{m}$  core diameter) and index difference ( $\approx 0.006$ ).

In 1991 Kohichi Tamura, a graduate student in our group, wrote a Mathematica program to calculate the GVD of the silica fibers he was using in his experiments. The program uses a Sellmeier equation for pure, undoped  $\text{SiO}_2$  from the Physics Handbook to determine the material dispersion. The waveguide dispersion calculation involves finding the propagation constant  $\beta$  over the wavelength range of interest by using the small index difference approximation,  $\Delta n \ll 1$ , and assuming an ideal, step-index circular waveguide. For the  $\text{LP}_{01}$  mode, the field solutions are Bessel functions and lead to a mode condition which can be solved numerically for  $\beta$  as a function of wavelength [59]. The program has been used to calculate the GVD of a variety of fibers, and results for standard single-mode fibers have been found to be within  $\approx 5\%$  of specified measured values. When  $\Delta n > 0.03$  the waveguide dispersion has a significant contribution, and the program may not be as accurate. Frequently the specialty doped fibers have small cores and large  $\Delta n$ , and the GVD

Fiber type	$\lambda$ ( $\mu\text{m}$ )	MFD ( $\mu\text{m}$ )	$\delta$ (1/W-m)	$k''$ ( $\text{ps}^2/\text{km}$ )	$k'''$ ( $\text{ps}^3/\text{km}$ )
SMF 28	1.55	8.9	$1.5 \times 10^{-3}$	-22	+0.126
Flexcor	1.55	5.4	$4.2 \times 10^{-3}$	-7	+0.102
Er <sup>+3</sup> (1128)	1.55	3.9	$8.0 \times 10^{-3}$	+70	-0.108
Er <sup>+3</sup> (1128-2)	1.55	3.1	$12.8 \times 10^{-3}$	+105	-0.235
SMF 28	1.85	8.7	$1.3 \times 10^{-3}$	-60	+0.53
Tm <sup>+3</sup> (CTm119)	1.85	4.5	$5.0 \times 10^{-3}$	+3.3	+0.032
Tm <sup>+3</sup> (CTm158)	1.85	4.7	$4.6 \times 10^{-3}$	-12	+0.135

Table 2.1: Comparison of the Kerr coefficients  $\delta$  and the second- and third-order group velocity dispersions for the fibers used in this thesis.  $\lambda$ : wavelength, and MFD: mode-field diameter. The values shown for  $k''$  were calculated and then verified experimentally, while those for  $k'''$  were only calculated.

is usually not specified. The calculated dispersion can be checked by measuring the GVD experimentally using the method of Knox [60] as shown in section 3.4. Co-dopants in the fiber core such as GeO<sub>2</sub> and Al may significantly raise the refractive index; reference [61] contains a useful table of Sellmeier coefficients for silica glass doped with various amounts of co-dopants which can be used in the program to more accurately calculate the material dispersion. Table 2.1 shows values for the second- and third-order dispersion of the various fibers used in this thesis.

## 2.6 Polarization APM

Additive Pulse Mode-locking (APM) is a passive mode-locking technique that employs a nonlinear interferometer to achieve pulse shortening. The pulse is split into the two arms of the interferometer with a nonlinear element in one arm. The pulses recombine back at the beam splitter and pulse shortening occurs through the coherent addition of the self-phase modulated pulses. One advantage of APM is that it is extremely fast because it is based on the self-phase modulation (SPM) from the Kerr effect and thus should not put a limit on the shortest pulses which can be achieved. The technique has been extensively studied both experimentally and theoretically in several solid-state lasers [62,63,64], and the reader is encouraged to check these references for further details. APM can be extended to fiber lasers, where SPM is easy to achieve. As discussed in the following, pulse shortening is achieved with SPM and polarization control.

Nonlinear polarization rotation occurs in an optical fiber when an initial elliptical polarization state rotates as it propagates because of the intensity dependence of the refractive index ( $n = n_0 + n_2 I$ ) [65]. The ellipse can be resolved into right- and left-hand circular polarization components of different intensities. The circular components accumulate different nonlinear phase shifts when propagating in a nonlinear medium (optical fiber) which leads to a rotation of the polarization ellipse,

while maintaining the ellipticity and handedness of the ellipse. An optical fiber is particularly well-suited for nonlinear polarization rotation because long fiber lengths can be used and the small mode diameter leads to high intensities and thus to a large nonlinear index change. Fig. 2-5 shows how nonlinear polarization rotation can be used in conjunction with bulk polarization optics to obtain an artificial saturable absorber (an element which absorbs low intensities but is bleached by and transmits high intensities) and mode-lock the laser. The mode-locking technique is called Polarization Additive Pulse Mode-locking (P-APM) since the right- and left-hand circular polarization components acquire a differential nonlinear phase shift and are added together at the final polarizer. P-APM has been successfully employed to mode-locked  $\text{Er}^{+3}$ - and  $\text{Nd}^{+3}$ -doped fiber lasers [19,20,21,66]; a natural extension is to employ the technique in a  $\text{Tm}^{+3}$ -doped fiber laser, as reported in chapter 3.

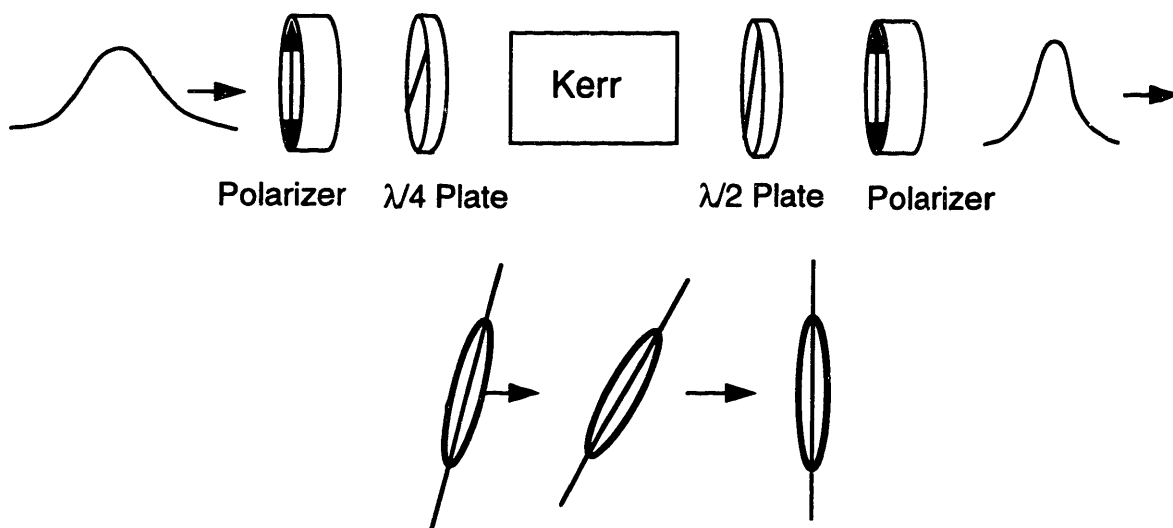


Figure 2-5: Diagram of how pulse shortening occurs in a laser through Polarization APM. An initial pulse is linearly polarized and then made elliptical with a quarter-wave plate. The light then passes through an optical fiber where ellipse rotation occurs and the peak of the pulse rotates more than the pulse wings. At the output of the fiber, the waveplates orient the pulse so that the peak of the pulse passes through the polarizer while the wings of the pulse are extinguished, thus achieving pulse shortening.

### 2.6.1 Master equation for P-APM in a fiber laser

The pulse in a laser which is mode-locked by APM can be described using a steady-state analysis which treats mode-locking in the time domain, as in [64]. The method analyzes the action of each component of the laser system on the pulse and assumes that the net modification of the pulse envelope upon return to the starting reference plane is zero. The main assumption is that the mode-locked pulse experiences only small changes per pass (less than 10%), so that the effects can be treated as distributed

throughout the laser. The electric field for the radiation inside the laser cavity has the form:

$$E(t) = u(t) \exp(j\omega_0 t) \quad (2.6)$$

where  $u(t)$  is the complex amplitude of the slowly-varying temporal envelope of frequency  $\omega_0$ . Fig. 2-6 shows the possible effects in a mode-locked laser which are taken into account in the following Master equation:

$$\left\{ -j\psi + g - \ell + \left( \frac{g}{\Omega_g^2} + j\frac{1}{2}k''L_D \right) \frac{\partial^2}{\partial t^2} + (-j\delta L_K + \gamma)|u|^2 \right\} u = 0. \quad (2.7)$$

where  $\psi$  is the net linear phase shift,  $\ell$  is the linear loss per pass, and  $g$  is the laser gain. The gain is assumed to be slow, saturable gain, which means that as the pulse energy increases, the gain saturates but on a time scale much longer than the pulse width. The second term proportional to  $g$  is due to the finite bandwidth of the gain.  $k''L_D$  represents the contribution of the group velocity dispersion  $k''$  in a material of length  $L_K$ , while  $\delta L_K$  is the SPM contribution with Kerr coefficient  $\delta$  in a material of length  $L_K$ . The last term on the right-hand side represents the artificial saturable absorber action of the P-APM, which is also called self-amplitude modulation (SAM).  $\gamma$  is inversely proportional to the saturation intensity and must be positive so that higher intensities see lower loss.

The Master equation has an exact solution [64],

$$u(t) = A_0 \left( \operatorname{sech}\left(\frac{t}{\tau}\right) \right)^{[1+j\beta]} \quad (2.8)$$

where  $\tau$  is the normalized pulse width ( $\tau = 0.567\tau_{FWHM}$ ) and  $\beta$  is the chirp parameter. In the negative GVD regime, it is possible to obtain chirp-free pulses ( $\beta = 0$ ), such that the contributions from SPM and GVD balance and the filtering and saturable absorber action also balance. The mode-locked pulse is then transform-limited (having the shortest temporal width for a given spectral width) and has the same shape as a soliton, which was previously described. These are the optimum pulses which can be produced by lasers which are passively mode-locked by FSA-like mechanisms, and in chapter 3, the pulses from the  $\text{Tm}^{+3}$ -doped fiber laser will be compared to unchirped secant hyperbolic pulses. The "solitons" predicted by the Master equation for zero chirp are similar to the "average solitons" which occur in periodically amplified transmission systems [67,68]. Although the attenuation and amplification within one round trip can be considerable, an important requirement on these "solitons" is that the nonlinear phase shift per round trip must be small ( $\ll 2\pi$ ), as will be explained in more detail in section 3.6.

## 2.6.2 Matrix formulation of P-APM parameters

By using a Jones Matrix formulation, P-APM as shown in Fig. 2-5 can be modeled theoretically. The goal is to find expressions for the SPM ( $\delta|u|^2$ ), SAM ( $\gamma|u|^2$ ), and linear loss  $\ell$  in terms of the P-APM parameters, by comparing the output field after P-APM with a general form of the output field:

$$a_{(out)} \simeq (T + (\gamma + j\delta) |a_{(in)}|^2) a_{(in)}. \quad (2.9)$$



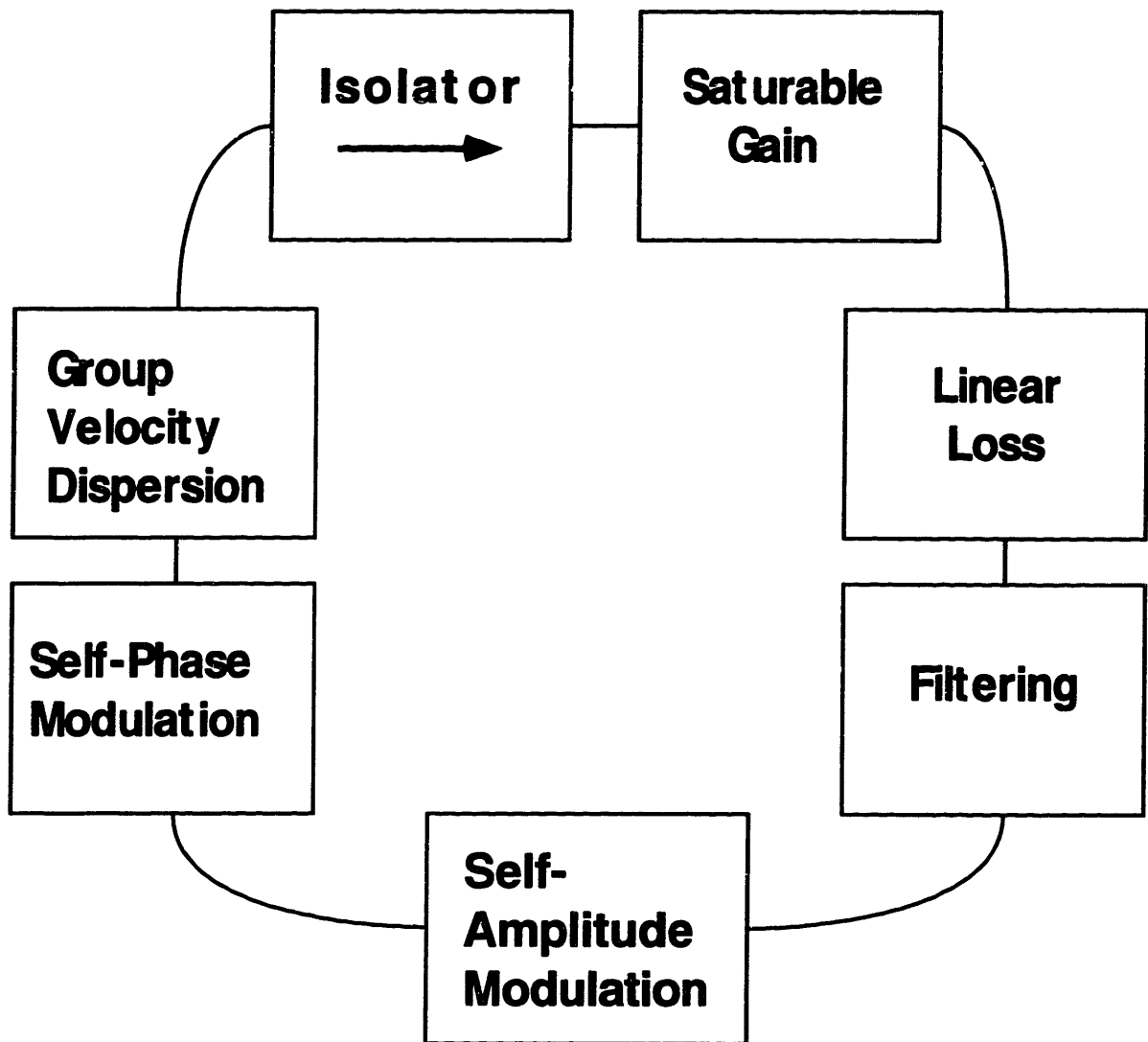


Figure 2-6: Schematic diagram of a ring laser with saturable gain, linear loss, filtering (gain-bandwidth limiting), self-amplitude modulation for modelocking, self-phase modulation, group velocity dispersion, and isolator for unidirectional operation. The Master equation includes each of these effects in determining the pulse envelope.

The analysis here follows that reported in [69] and [70].

The input field in the basis of linearly polarized modes  $E_x$  and  $E_y$  is represented by a vector

$$\mathbf{E} = \begin{bmatrix} E_x \\ E_y \end{bmatrix} \quad (2.10)$$

The action of each component (waveplates, Kerr medium, and polarizers) in the P-APM scheme can then be represented by a matrix which multiplies the input field. We assume in this analysis that the Kerr medium (fiber) is isotropic, and so it is simpler to describe the Kerr effect in the basis of circular polarization. (The case of non-isotropic, or birefringent, fiber will be examined in chapter 5.) The linear modes  $E_x$  and  $E_y$  can be converted to the circular basis through the unitary transformation  $\mathbf{U}$ :

$$\begin{bmatrix} E_+ \\ E_- \end{bmatrix} = \frac{1}{\sqrt{2}} \begin{bmatrix} 1 & j \\ 1 & -j \end{bmatrix} \begin{bmatrix} E_x \\ E_y \end{bmatrix} = \mathbf{U} \begin{bmatrix} E_x \\ E_y \end{bmatrix}. \quad (2.11)$$

The entire expression for the output field becomes:

$$\begin{bmatrix} E_x \\ E_y \end{bmatrix}_{(out)} = [\mathbf{X}_{pol}] [\mathbf{HWP}(\theta)] [\mathbf{U}_{xy}] [\mathbf{KERR}] [\mathbf{U}] [\mathbf{QWP}(\alpha)] [\mathbf{X}_{pol}] \begin{bmatrix} E_x \\ E_y \end{bmatrix}_{(in)} \quad (2.12)$$

where the Jones matrices for the different elements are familiar and listed here for convenience. The  $\mathbf{X}$  polarizer is

$$[\mathbf{X}_{pol}] = \begin{bmatrix} 1 & 0 \\ 0 & 0 \end{bmatrix} \quad (2.13)$$

while the quarter-wave plate at angle  $\alpha$  is defined as

$$[\mathbf{QWP}(\alpha)] = \frac{(1-j)}{2} \begin{bmatrix} j + \cos(2\alpha) & \sin(2\alpha) \\ \sin(2\alpha) & j - \cos(2\alpha) \end{bmatrix} \quad (2.14)$$

and  $\mathbf{U}$  is defined in equation (2.11). The Kerr effect in the circular basis is expressed as

$$[\mathbf{KERR}] = e^{j\Phi} \begin{bmatrix} e^{j\Delta\phi} & 0 \\ 0 & e^{-j\Delta\phi} \end{bmatrix} \quad (2.15)$$

where

$$\Phi = \frac{\kappa}{2}(|E_+|^2 + |E_-|^2) = \frac{\kappa}{2}|E_x|^2 \quad (2.16)$$

is the common nonlinear phase shift and

$$\Delta\phi = \frac{\kappa}{6}(|E_+|^2 - |E_-|^2) \quad (2.17)$$

is the differential nonlinear phase shift with  $\kappa = \frac{4\pi n_2 \ell_K}{\lambda A_{eff}} = 2\delta\ell_K$ . When the input state is linear,  $\Delta\phi = 0$  because  $|E_+|^2 = |E_-|^2$  and there will be no polarization rotation.

The matrix  $\mathbf{U}_{xy}$  is the unitary transformation which converts the circular basis back to the linear ( $xy$ ) basis,

$$[\mathbf{U}_{xy}] = \frac{1}{\sqrt{2}} \begin{bmatrix} 1 & 1 \\ -j & j \end{bmatrix}. \quad (2.18)$$

And the matrix for the half-wave plate at angle  $\theta$  is

$$[\mathbf{HWP}(\theta)] = \begin{bmatrix} \cos(2\theta) & \sin(2\theta) \\ \sin(2\theta) & -\cos(2\theta) \end{bmatrix}. \quad (2.19)$$

When the multiplication of the matrices is carried out, the output field is then

$$E_x^{(out)} = \frac{E_x}{2} e^{j\Phi} [e^{j\Gamma}(c_\alpha + s_\alpha) + e^{-j\Gamma}(c_\alpha - s_\alpha)] \quad (2.20)$$

where  $\Gamma = \alpha + \Delta\phi - 2\theta$ ,  $c_\alpha$  represents  $\cos \alpha$ , and  $s_\alpha$  represents  $\sin \alpha$ . The intensity  $|E_x^{(out)}|^2$  is then

$$|E_x^{(out)}|^2 = \frac{|E_x^{(in)}|^2}{2} (1 + c_{2\alpha} c_{2\Gamma}). \quad (2.21)$$

Now equation (2.20) can be cast in the general output field form of equation (2.9). The linear transmission  $T$  can be determined by setting the nonlinearity equal to zero ( $\Delta\phi = 0$ ) in equation 2.21, such that  $E_x^{(out)} = T E_x^{(in)}$ . The linear transmission is then

$$T = \frac{1}{\sqrt{2}} \sqrt{1 + c_{2\alpha} c_{2(\alpha-2\theta)}}. \quad (2.22)$$

Finally, by assuming small nonlinearity and ignoring terms which are higher than first order, the SPM and SAM parameters can be determined as:

$$\delta|E|^2 = \frac{1}{2} \kappa |E|^2 \left[ T - \frac{1}{6} \frac{s_{2\alpha}^2}{T} \right] \quad (2.23)$$

$$\gamma|E|^2 = \frac{1}{24} \kappa |E|^2 \frac{s_{4\alpha} s_{2(\alpha-2\theta)}}{T} \quad (2.24)$$

As shown in [64], it is best to operate with a large ratio of  $\gamma/\delta$  in order to optimize the pulse width, chirp, and stability.

## 2.7 Self-Starting

Ideally, a passively mode-locked laser will evolve into a pulsed state on its own, without external perturbation or trigger. This is called self-starting, meaning that the pulses start up from an initial noise fluctuation formed by mode beating of the multiple axial modes in the laser. In general, systems mode-locked by fast saturable absorbers have difficulty with self-starting due to the weak pulse shaping for long pulses [71]. Random mode-beating fluctuations decay within a characteristic time (the lifetime of the fluctuation) due to competing scattering processes [72]. A mode-locked state can only be established if the excess round-trip gain experienced by

the initial fluctuation is large enough to complete the mode-locking process within the lifetime of the fluctuation. The lifetime is related to the linewidth of the first beat-note of the power spectrum of the free-running laser [72].

Lasers in a unidirectional ring configuration have been shown to self-start more easily, which has also been explained theoretically in references [73] and [74]. Both papers point out that mode-pulling will decrease the mode coherence time (decreasing the lifetime of a fluctuation). Reference [73] explains that spurious reflections (off bulk elements or polished fiber ends) and etalons in the cavity create a multiple Fabry-Perot structure with unevenly spaced axial modes. Larger injection signals (higher powers) are then needed to start the pulses. In a linear cavity, a single reflection surface can cause mode pulling. In a unidirectional ring cavity, though, the effect of reflections is reduced since two reflecting surfaces must occur in order to form an etalon. (A first-order reflection is attenuated in the isolator.) As reported in [73] low self-starting thresholds appear to be possible for a ring cavity, whereas significantly more power (a factor of  $\sim 10-100$ ) may be required for self-starting in a linear cavity.

A second explanation for mode-pulling and reduction in the mode coherence time is based on spatial hole burning in the gain medium which occurs in a linear cavity [74]. The forward and backward propagating waves form a standing wave pattern of the electric field which induces a spatial modulation of the complex refractive index in the gain medium. This grating then causes a change in the mode-beating frequencies which differs for different pairs of adjacent axial modes, and thus causes mode-pulling. Consequently, the linewidth of the first beat-note is broadened, resulting in a higher self-starting threshold for linear cavities versus unidirectional ring cavities where spatial hole burning does not occur. Reference [74] also points out that since there is a finite build-up time for the population grating in the gain medium, sudden perturbations or periodic variations of the cavity length partially can erase the grating and enable self-starting which explain why moving mirrors or "tapping the optical table" are helpful starting mechanisms. Due to the enhanced self-starting of the ring geometry, the laser designs reported in this thesis are unidirectional ring lasers or at least have a ring as part of the geometry.

# Chapter 3

## Thulium-doped fiber soliton laser

As discussed in the first chapter,  $\text{Tm}^{+3}$ -doped silica fiber is an attractive gain medium for a fiber laser because it has a broad and smooth gain profile and can provide gain between 1.8 and 1.9  $\mu\text{m}$ , a region not covered by the more common rare-earth dopants  $\text{Nd}^{+3}$  and  $\text{Er}^{+3}$ . This chapter contains a discussion of a passively mode-locked  $\text{Tm}^{+3}$ -doped fiber laser using P-APM, which demonstrates that the P-APM technique is not limited to  $\text{Er}^{+3}$ -doped fiber lasers at 1.55  $\mu\text{m}$  [21], but can be applied to lasers at any wavelength. The motivation for this work was to determine the shortest pulses which could be generated from the  $\text{Tm}^{+3}$ -doped fiber laser and the factors limiting the pulse width. With the broad gain bandwidth of  $\sim 100$  nm, transform-limited (sech) pulses could potentially be as short as 40 fsec. A 1.8  $\mu\text{m}$  pulsed source could open up new applications such as LIDAR, medical surgery, Optical Coherence Tomography (OCT), or spectroscopy on intersubband transitions in quantum wells, which take advantage of either the time resolution or the spectral bandwidth at 1.8  $\mu\text{m}$ . The application of a 1.8  $\mu\text{m}$  broadband source to OCT was explored and is also discussed. Initial experimental results from this laser were reported in [75]. Subsequently, important work on a passively mode-locked  $\text{Tm}^{+3}$ -doped fiber laser was reported in [29].

### 3.1 Experimental Setup

The laser was mode-locked using nonlinear polarization rotation in the unidirectional ring configuration shown in Fig. 3-1. The thulium-doped silica fiber (CTm-158) was donated by Rutgers University and had a core diameter of 4  $\mu\text{m}$ , numerical aperture of 0.23, and cutoff wavelength of 1.16  $\mu\text{m}$ . The fiber was doped with 31,000 ppm  $\text{Tm}^{+3}$ -ions concentrated in the center 1/7th of the core area. The purpose of this unique geometry was to have a sufficient  $\text{Tm}^{+3}$  concentration to enable an increased pumping efficiency, yet allow the pump absorption to be distributed along one to two meters of fiber. When the  $\text{Tm}^{+3}$  concentration is sufficiently large, a cross-relaxation process can occur between an excited thulium ion and a neighboring thulium ion in the ground state, resulting in two lasing photons from a single pump photon [76]. Due to the high losses of our laser cavity, it could not be determined if an increased pump efficiency occurred due to this doping geometry. Although the small signal absorption

was measured to be approximately 100 dB/m at 785 nm, at the typical pump powers (300 to 500 mW in the fiber) used in our experiment, bleaching of the absorption occurred. The fiber was tested by monitoring the fluorescence when pumping a piece of the fiber at the peak of the absorption at 785 nm. Fluorescence spectra of more than 100 nm were observed as shown in Fig. 2-3. The optimum length of  $Tm^{+3}$ -doped fiber was estimated to be 1.3 - 1.4 meters. This length was determined by pumping a piece of  $Tm^{+3}$ -doped fiber with 500 mW at 785 nm and cutting back the fiber until maximum fluorescence was achieved at the end.

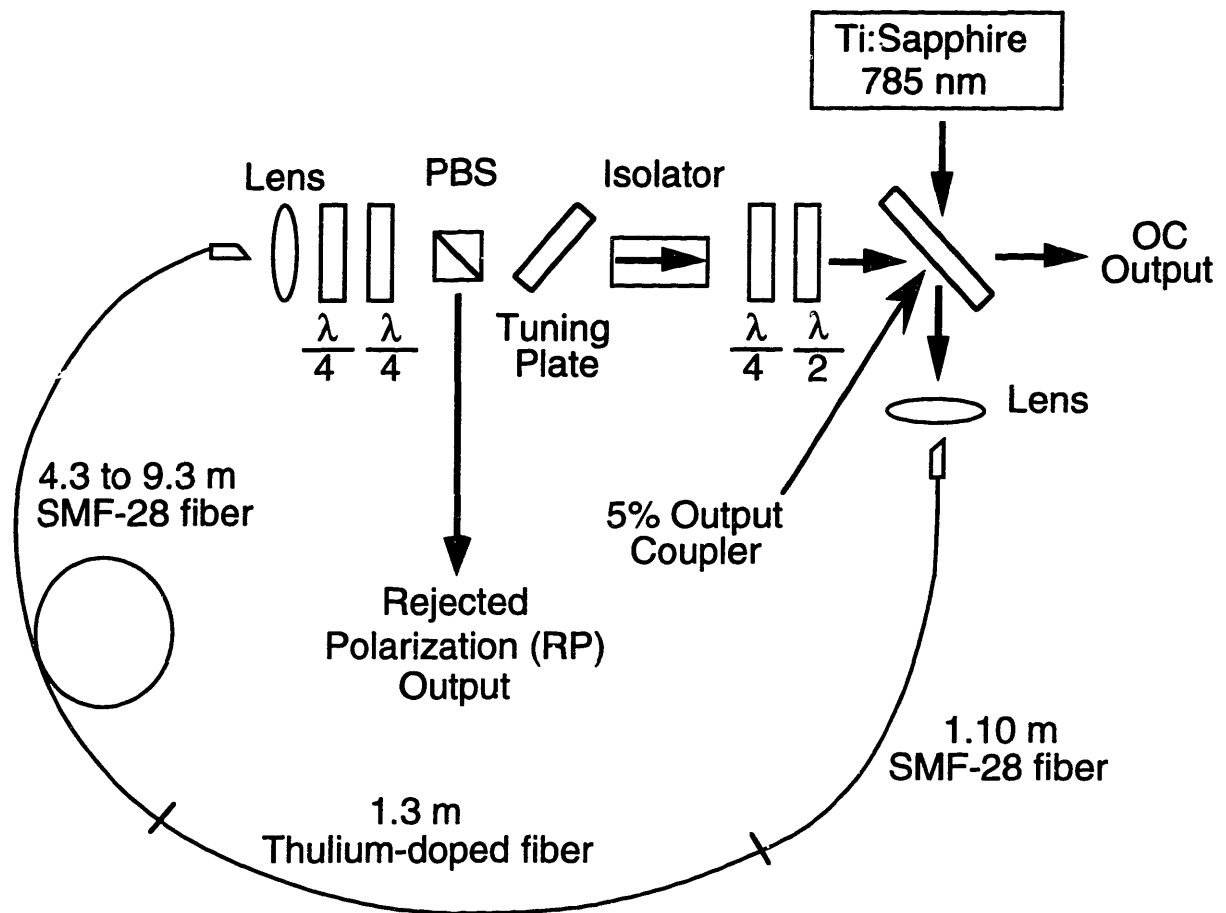


Figure 3-1: Experimental set-up for the mode-locked thulium-doped fiber ring laser. PBS: polarizing beam splitter, Tuning plate: quartz plate of thickness 10T.

The pump coupling and output coupling were done in the air gap with a dichroic mirror, because standard single-mode fiber couplers and wavelength-division-multiplexing couplers are not yet commercially available at the required wavelengths. A Ti:sapphire laser operating at 783 nm was coupled into the fiber laser through the input/output coupler with an efficiency of  $\approx 50\%$  of the incident pump power. The output coupling was  $\approx 5\%$  at 1.9  $\mu m$ . Waveplates and an isolator in the air gap achieved the artificial saturable absorber action described in Fig. 2-5 which allowed self-starting, mode-locked operation. Polarization control was achieved through the use of the bulk

zero-order waveplates instead of fiber polarization controllers because of the higher bending loss in standard single-mode fiber at wavelengths longer than  $1.5 \mu\text{m}$  and the better mode-locking repeatability obtained with bulk waveplates. A commercial Ho:YAG optical isolator designed for  $2.0$  to  $2.2 \mu\text{m}$  was used to enforce unidirectional operation, which was important for self-starting operation [21]. Insertion of a 10T ( $T=0.512 \text{ mm}$ ) quartz birefringent plate at Brewster's angle between the isolator and the polarizing beam-splitter allowed smooth tuning and bandwidth control. This filter had a free spectral range of  $74 \text{ nm}$  and FWHM bandwidth of  $35.5 \text{ nm}$ , as shown in Fig. 3-2. The length of passive single-mode fiber (SMF-28) in the laser was initially  $9.3$  meters in order to have sufficient nonlinear polarization rotation to achieve mode-locking. In later experiments, this SMF-28 length was cut back to  $4.3$  meters to adjust the cavity length and net dispersion. Unless indicated, the results reported in this chapter used the  $9.3$ -meter length of SMF-28.

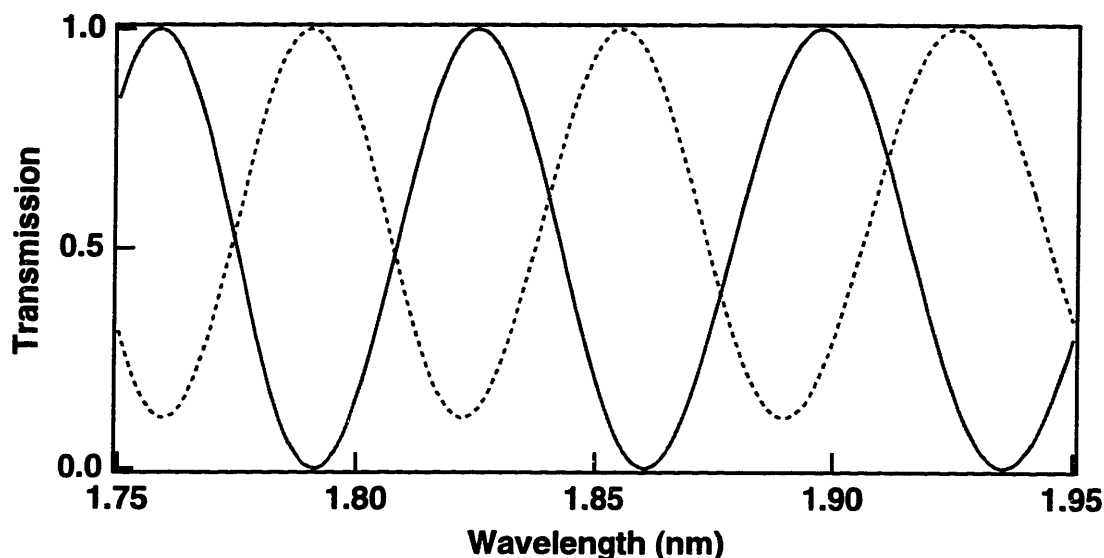


Figure 3-2: Calculated transmission versus wavelength for a quartz birefringent tuning plate filter of thickness 10T at Brewster's angle in the cavity. Solid curve:  $c$ -axis at  $40^\circ$  from TE polarization (for maximum extinction). Dashed curve:  $c$ -axis at  $50^\circ$  from TE polarization.

## 3.2 Mode-locked operation

By properly adjusting the waveplates and birefringent filter, mode-locking was achieved with spectra centered between  $1.8 \mu\text{m}$  and  $1.9 \mu\text{m}$ , depending on the waveplate positions. An example of typical mode-locked operation at  $1.85 \mu\text{m}$  with a single pulse per round-trip is shown in Fig. 3-3. The pulse FWHM was  $480 \text{ fsec}$ , assuming a sech, and the average output power was  $280 \mu\text{W}$  with  $350 \text{ mW}$  of coupled pump power. The spectrum is centered at  $1850 \text{ nm}$  with a bandwidth of approximately  $8 \text{ nm}$  (again assuming a sech), corresponding to a time-bandwidth product of  $0.34$

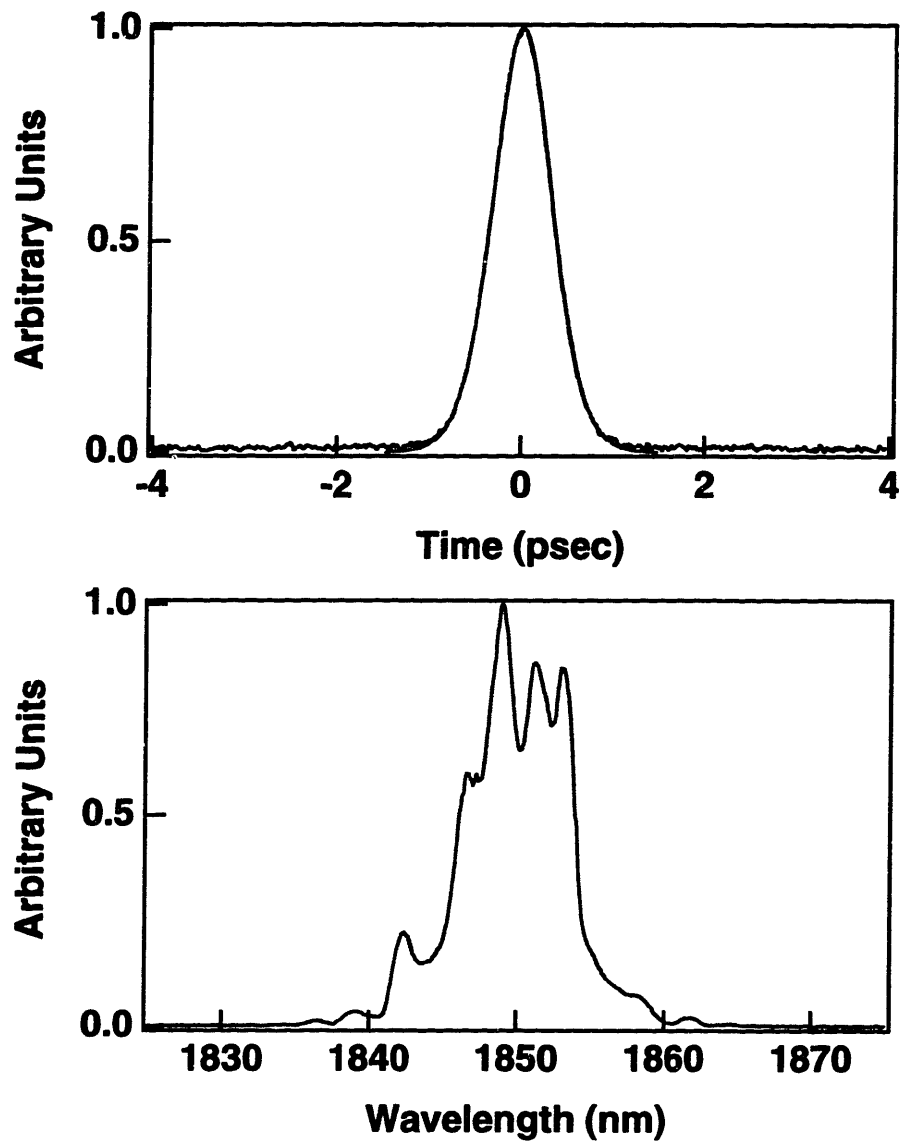


Figure 3-3: Pulse autocorrelation (fit with a sech) and spectrum of typical single-pulse operation. The pulse FWHM is 480 fsec, and the spectrum is centered at 1850 nm.



The cw threshold was 225 mW, while the input pump threshold for mode-locking varied with the pulse wavelength and was a minimum of 325 mW near the peak of the gain at 1.8  $\mu\text{m}$ . Fig. 3-4 is a plot of output power vs. coupled pump power which shows the different states of the laser. The high mode-locking threshold is due to reflections and large cavity losses in the air gap. The laser was self-starting (i.e. the pulses started from noise without external perturbation) over the entire tuning range, but at certain operating points the laser self-started to multiple pulses rather than to single pulses. (Multiple pulse operation will be discussed further in section 3.7). After obtaining mode-locking, single-pulse operation could then be obtained by attenuating the pump. (Single-pulse operation was determined both by fast-detector monitoring and by taking long autocorrelation scans.) Mode-locking could be maintained with input pump powers as low as 250 mW, which is lower than the self-starting threshold and indicative of internal reflections. Self Q-switching of the thulium-doped fiber laser was never observed, as opposed to erbium-doped fiber lasers [21]. This may be related to the shorter upper-state lifetime of thulium, which is  $\approx 250 \mu\text{sec}$  and 40 times shorter than the upper-state lifetime of erbium [32]. The laser would remain stably mode-locked for hours.

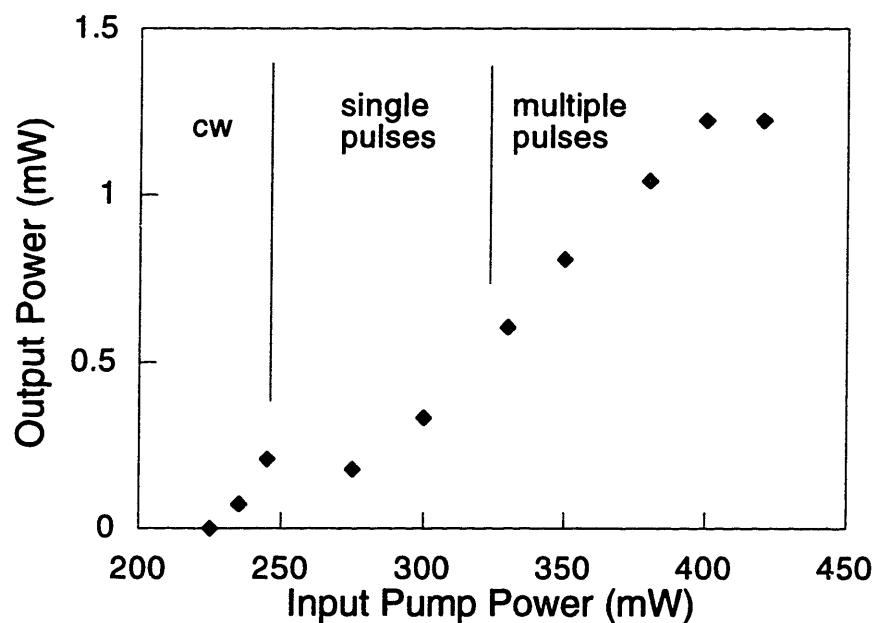


Figure 3-4: Laser output power vs. coupled pump power for the  $\text{Tm}^{+3}$ -doped fiber laser with a spectrum centered near 1.8  $\mu\text{m}$ .

### 3.3 Tuning characteristics

Tuning of the laser was easily achieved by adjusting the waveplates and birefringent tuning plate in the cavity. As shown in Fig.3-5, the laser could be tuned over the range from 1.8  $\mu\text{m}$  to 1.9  $\mu\text{m}$  with pulse durations between 350 and 500 fsec. Tuning below 1.8  $\mu\text{m}$  was limited not by the gain, but by the commercial Ho:YAG optical isolator which was optimized for 2.0 to 2.1  $\mu\text{m}$  and introduced  $\geq 15\%$  loss for wavelengths less than 1.8  $\mu\text{m}$ . With a particular setting of the waveplates, continuous tuning over 50 nm was possible with adjustment of only the birefringent tuning plate at constant pump power. This range of continuous tuning was limited by the 70-nm free spectral range of the single birefringent plate as shown in Fig. 3-2. With the larger free spectral range of a multiple-plate filter, continuous tuning may be possible over a larger bandwidth. Fig. 3-6 shows a set of continuously tuned spectra with constant coupled pump power at 400 mW and output power of approximately 250  $\mu\text{W}$ . The second set of spectra shown in Fig. 3-7 were taken after the isolator was modified for lower loss at 1.8  $\mu\text{m}$ , allowing pulsed operation down to 1.78  $\mu\text{m}$ . For this second tuning range the coupled pump power was adjusted between 350 mW and 480 mW with more pump power required at the shorter wavelengths. The pulse widths over this tuning range were between 400 and 500 fsec.

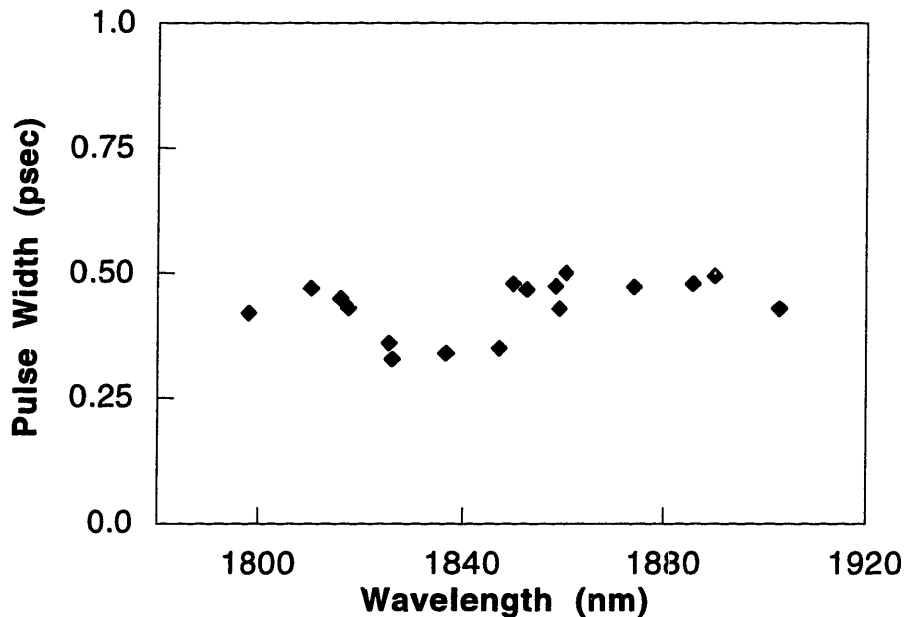


Figure 3-5: Minimum pulse width vs. center wavelength for single-pulse operation of the mode-locked thulium-doped fiber laser.

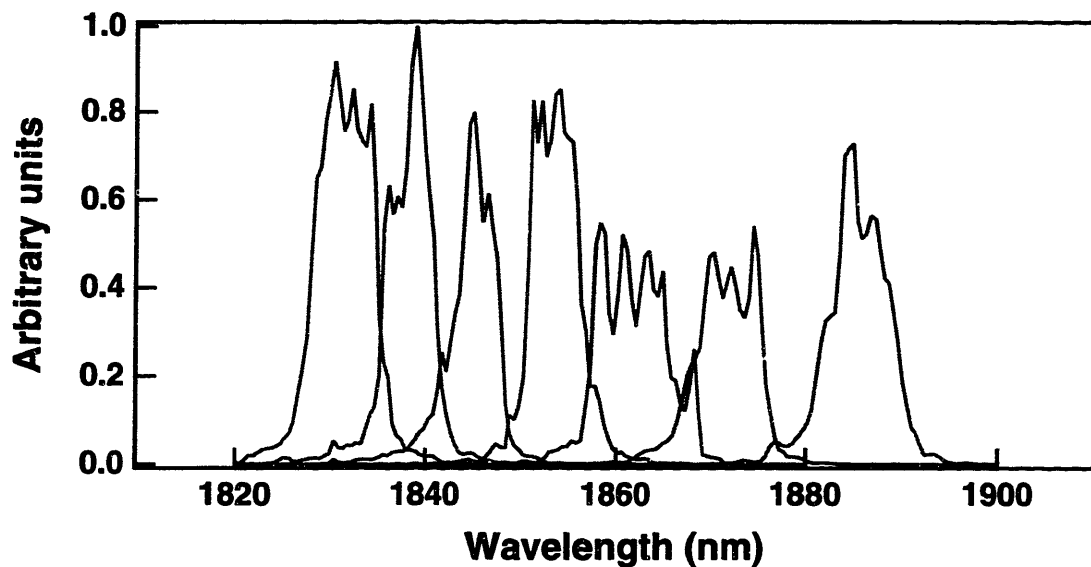


Figure 3-6: Mode-locked spectra from the thulium-doped fiber laser showing a continuous tuning range of  $> 50$  nm when only the birefringent filter is adjusted.

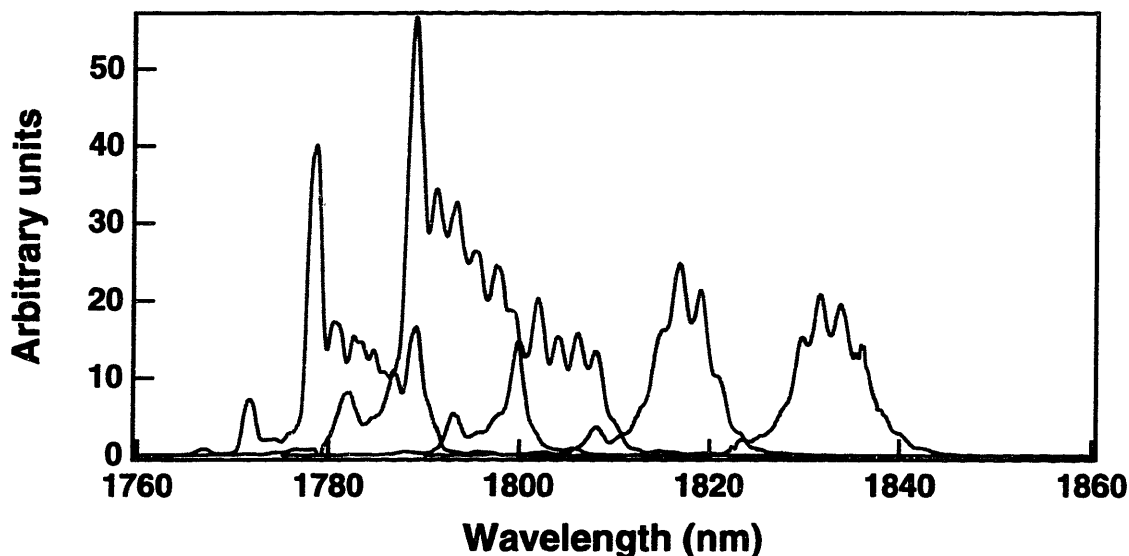


Figure 3-7: A second set of mode-locked spectra from the thulium-doped fiber laser showing the continuous tuning range after the isolator was modified for lower loss at  $1.8 \mu\text{m}$  allowing pulsed operation at shorter wavelengths. The pump power was also adjusted along with the birefringent tuning plate.

### 3.4 Dispersion measurement

The dispersions of the thulium-doped fiber and SMF-28 fiber at 1.85  $\mu\text{m}$  were calculated to be  $\approx -12 \text{ ps}^2/\text{km}$  and  $-60 \text{ ps}^2/\text{km}$ , respectively, as shown in table 2.1. These calculations were confirmed by experimentally measuring the total cavity dispersion using a technique developed by Knox [60]. This method involves tuning the laser while it is mode-locked and measuring the round-trip time at each wavelength. The slope of  $T_{rep}(\lambda)$  is then the net dispersion  $D \ell_{cav}$  in units of psec/nm which can be converted to more conventional units by

$$k'' \ell_{cav} (\text{ps}^2) = -\frac{\lambda^2}{2\pi c} D \ell_{cav} \quad (3.1)$$

Third order dispersion can also be determined by taking the second derivative of  $T_{rep}(\lambda)$ . The large tuning range of the  $\text{Tm}^{+3}$ -doped fiber laser (1.8  $\mu\text{m}$  to 1.9  $\mu\text{m}$ ) facilitates this measurement of the net dispersion. The individual fiber dispersions can be determined by changing the length of either the  $\text{Tm}^{+3}$ -doped fiber or the SMF-28 fiber and repeating the measurement. The net dispersion of the cavity for the 1.30 meters of  $\text{Tm}^{+3}$ -doped fiber and 10.30 meters of SMF-28 fiber was measured to be  $-0.645 \text{ ps}^2$  at 1.850  $\mu\text{m}$ , as shown in Fig. 3-8. The total cavity length was 12.0 meters, giving an average dispersion of  $k'' = -0.0538 \text{ ps}^2/\text{m}$ . The birefringent beat length of the thulium-doped fiber was measured to be  $\approx 35 \text{ cm}$  at 1.85  $\mu\text{m}$ , while the beat length of the SMF-28 fiber was 4 to 8 meters. These measurements were made by launching circularly polarized 1.3  $\mu\text{m}$  light into a short length of fiber and measuring the output polarization state as a function of fiber length. Beat-length measurements will be discussed in more detail in chapter 5.

### 3.5 Soliton behavior

The mode-locked pulses in the laser represent a balance between the negative group velocity dispersion and the self-phase modulation occurring in the fiber, and thus are solitons. Propagation of solitons is described by the Nonlinear Schrödinger Equation (NLSE),

$$\frac{\delta u}{\delta z} = -j\eta|u|^2u + jk''\frac{\delta^2 u}{\delta t^2} \quad (3.2)$$

where  $\eta$  is the nonlinear Kerr coefficient  $\eta = \frac{2\pi n_2}{\lambda}$  and  $n_2 = 1.2 \times 10^{22} \text{ m}^2/\text{V}^2$ ,  $k''$  is the group velocity dispersion, and  $u(t, z)$  is the complex amplitude of the slowly-varying envelope of the electric field (in V/m). (Note that the NLSE is written in a retarded coordinate frame which moves at the group velocity of the pulse, determined by  $k'$ , the first derivative of the propagation constant  $k(\omega)$  with respect to frequency.) The solution has a secant hyperbolic shape which is constant with distance. Only the phase accumulates with distance:

$$u(t, z) = A_0 \text{sech}(t/\tau) \exp(-j\frac{z}{2Z_c}) \quad (3.3)$$

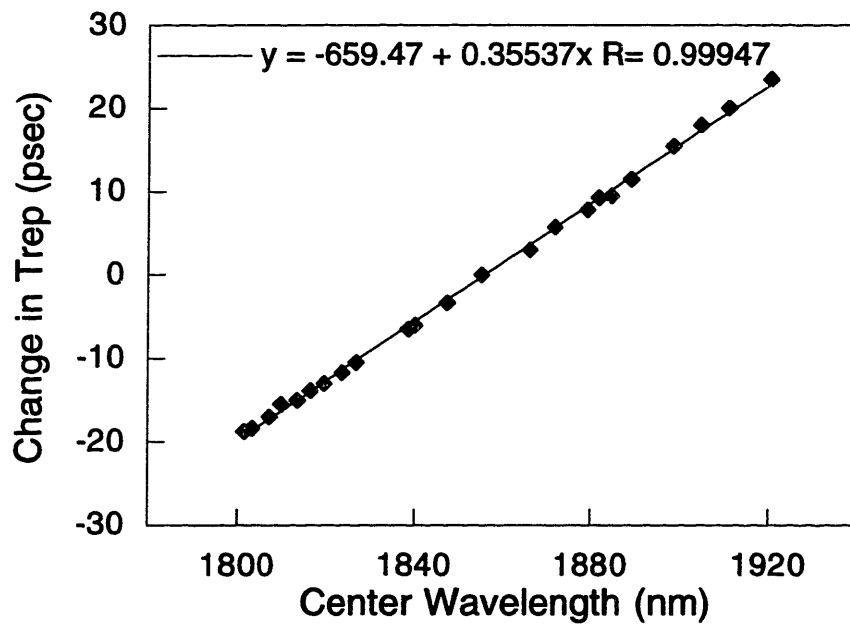


Figure 3-8: Measurement of  $T_{rep}$  vs. wavelength for the  $Tm^{+3}$ -doped fiber laser with 10.3 meters of SMF-28 and 1.3 meters of  $Tm^{+3}$ -doped fiber. The slope  $D \ell_{cav} = +0.355$  ps/nm, corresponding to a net dispersion  $k'' \ell_{cav} = -0.645$  ps<sup>2</sup>.

where  $\tau = 0.567\Delta T$  ( $\Delta T$  is the pulse full-width at half-maximum intensity) and  $Z_c = \frac{\tau^2}{|k''|}$ . By substituting the solution in eqn. (3.3) back into the NLSE in eqn. (3.2), we obtain the relation:

$$\frac{|k''|}{\tau^2} = \eta|A_0|^2. \quad (3.4)$$

The soliton energy is then found by integrating  $|u(t, z)|^2$  over all time:

$$E_{\text{sol}} = \int_{-\infty}^{\infty} |A_0|^2 \text{sech}^2(t/\tau) dt = 2|A_0|^2\tau. \quad (3.5)$$

Using eqn. (3.4), the energy can be expressed as

$$E_{\text{sol}} = \frac{2|k''|}{\eta\tau}. \quad (3.6)$$

Therefore, by knowing the average dispersion  $|k''|$  in the laser and the Kerr coefficient  $\eta$ , we can verify how well a pulse with peak power  $|A_0|^2$  and width  $\tau$  obeys the soliton condition. The soliton spectrum should also have a secant hyperbolic shape and the time-bandwidth product ( $\Delta\nu\Delta T$ ) will be equal to 0.314 for a transform-limited pulse.

As discussed above, the dispersions of the thulium-doped fiber and passive single-mode fiber at 1.85  $\mu\text{m}$  were calculated and experimentally verified to be  $\approx -12$  ps<sup>2</sup>/km and  $-60$  ps<sup>2</sup>/km, respectively. The average dispersion  $k''$  in the cavity of 1.30 meters of thulium-doped fiber and 10.30 meters of SMF-28 was  $-0.0538$  ps<sup>2</sup>/m. For a pulse width of 400 fsec and a Kerr coefficient  $\eta = 1.47 \times 10^{-3}$ /m-W, the peak power inside the laser should have been 710 W for a soliton, according to eqn. (3.4). The typical output power from the laser at the 5% output coupler was 300  $\mu\text{W}$ , which corresponded to an intracavity pulse energy of 340 pJ at 17.47 MHz repetition rate and peak power of 750 W. The close agreement between the theoretical and experimental intracavity peak powers verified that the pulse was indeed a soliton. Additionally, pulse autocorrelations and spectra fit well with a secant hyperbolic, and typical time-bandwidth products were  $\approx 0.35$ .

### 3.6 Spectral modulation

The mode-locked pulse spectra of the Tm<sup>+3</sup>-doped fiber laser show significant spectral modulation which is related to the fact that the pulses are soliton-like. Work in long-distance soliton transmission [77,67] and in fiber soliton lasers [78,79,80,81] has shown that a resonant instability exists when the period (the amplifier spacing or the laser length)  $Z_p$  approaches  $4\pi Z_c$ , where  $Z_c$  is defined as before as  $\tau^2/|k''|$ . This can be explained by a simple phase-matching argument. When a soliton propagates in a fiber laser, it encounters various periodic perturbations such as gain, filtering, and loss due to splices or output couplers. The perturbed soliton does not obey the NLSE and sheds dispersive radiation as it reshapes back to a soliton. These linear dispersive waves are generated over the broad spectrum of the soliton and have a dispersion relation:

$$k_{lin} = -\frac{|k''|}{2} \Delta\omega^2, \quad (3.7)$$

where  $\Delta\omega$  is the frequency offset from the peak of the soliton spectrum.

Each frequency component then propagates at its own phase velocity. The dispersive waves generated each period  $Z_p$  will interfere destructively except for the dispersive waves at frequencies which are phase-matched to the soliton. This phase-matching condition is expressed by

$$Z_p(k_s - k_{lin}) = 2\pi m \quad (3.8)$$

where

$$k_s = \frac{|k''|}{2\tau^2} \quad (3.9)$$

is the propagation constant of the soliton from eqn. (3.3),  $m$  is an integer, and  $Z_p$  is the perturbation length (length of the laser). The phase-matching condition is shown in Fig. 3-9. By using eqn. (3.7) in the above relation, we can solve for the frequency offset  $\Delta\omega$  at which phase-matching occurs:

$$\Delta\omega = \pm \frac{1}{\tau} \sqrt{4\pi m \frac{Z_c}{Z_p} - 1}. \quad (3.10)$$

At these phase-matched frequencies, the dispersive radiation builds up and causes sidebands of order  $m$  on the pulse spectrum as shown in Fig. 3-10. For long pulses,  $Z_c = \tau^2/|k''|$  is large, so the sidebands are located far from the peak of the soliton. If the average dispersion and laser length are kept constant as the pulse width decreases, then  $Z_c$  will decrease, and the sidebands will be located closer to the peak of the soliton. The resonant instability occurs when the pulse width is such that  $Z_p/Z_c = 4\pi$ , and the frequency offset of the sideband  $\Delta\omega = 0$ . Note that the amount of continuum that is generated at a certain frequency is proportional to the amplitude of the soliton at that frequency [79]. Sidebands which are very near to the soliton peak can produce a significant amount of energy between the pulses.

Although it might appear that we could avoid the resonant instability by decreasing the average dispersion  $|k''|$  as the pulse width  $\tau$  decreases, the soliton energy is proportional to  $|k''|$  (see eqn. (3.6)), so this is not an optimal solution. Experimentally it has been found that the shortest pulses satisfy the condition  $Z_p \leq \frac{3\pi}{2} Z_c$  in mode-locked  $\text{Er}^{+3}$ -doped fiber lasers. This implies that for the  $\text{Er}^{+3}$ -doped fiber soliton laser, the total nonlinear phase shift per pass is limited to  $\frac{3\pi}{2}$  from eqn. (3.4). The limited nonlinear phase shift leads to small peak powers and long pulse widths, and thus low pulse energies.

The  $\text{Tm}^{+3}$ -doped fiber laser spectrum of Fig. 3-10 corresponds to the shortest single-pulse operation observed from this laser. The pulse FWHM was 360 fsec with output power of 240  $\mu\text{W}$ , corresponding to a peak power of 670 W inside the cavity following the output coupler. Considering the amplification in the loop, this is consistent with an average intracavity peak power on the order of the theoretical soliton peak power of 860 W. By fitting the spectrum with a sech on a log scale, the spectral width was determined to be  $\approx 10$  nm, resulting in a time-bandwidth product of 0.32. The spectral modulation shown in Fig. 3-10 has two causes: periodic perturbations and an intracavity Fabry-Perot etalon. When the laser was operating in this short

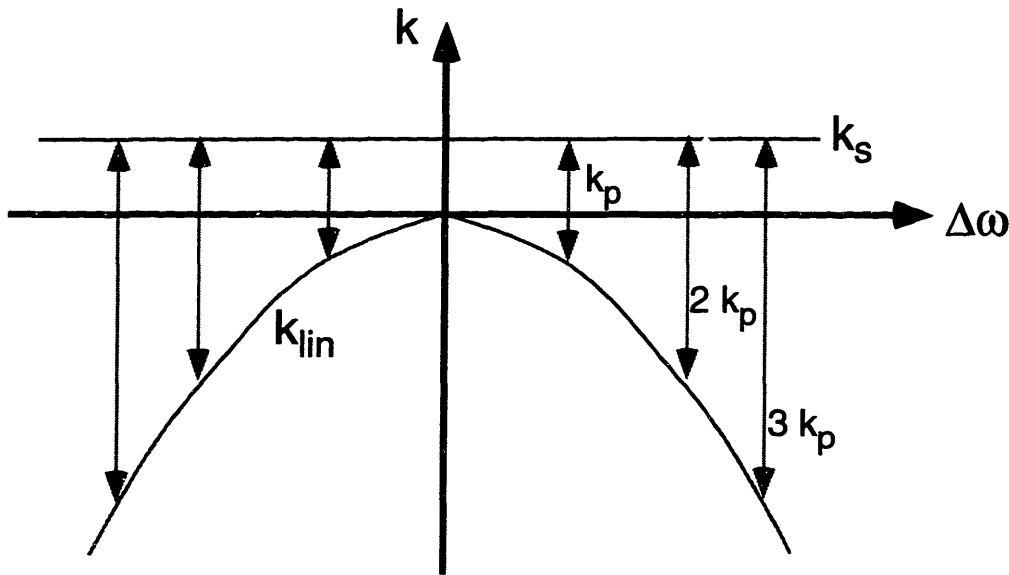


Figure 3-9: Plot of the propagation constant  $k$  vs. angular frequency  $\Delta\omega$  which shows the phase-matching condition for sidebands occurring when the laser is periodically perturbed. The soliton-like pulse has a constant  $k_s$ , while the dispersive waves have  $k_{lin}$  with a quadratic dependence on  $\Delta\omega$ . Phase-matching occurs at the particular frequencies where the periodic perturbation (with  $k_p$ ) makes up the difference between  $k_s$  and  $k_{lin}$ .

pulse state, the cavity length  $Z_p$  was on the order of  $4\pi Z_c$ . Therefore, significant continuum generation occurred in the laser. This result differs from erbium-doped fiber soliton lasers which, in the past, have operated with  $Z_p$  of not more than  $\frac{3\pi}{2} Z_c$  [21]. The erbium-doped fiber lasers typically had shorter cavity lengths, smaller average dispersion, and smaller perturbations due to an all-fiber cavity design. The  $Tm^{+3}$ -doped fiber laser may have been able to operate in this regime because of the high net (negative) dispersion of the cavity ( $k''l_{cav} = -0.645 \text{ ps}^2$  compared to  $k''l_{cav} = -0.091 \text{ ps}^2$  for the  $Er^{+3}$ -doped fiber laser of [21]) which should help to disperse the broadband continuum before it can build up to excessive levels in the sidebands and make the pulse unstable.

In Fig.3-10, the sidebands located more than 7 nm from the center of the spectrum corresponded to the order 2, 3, and 4 resonant sidebands, and their positions agreed well with theory. The further away from the center of the spectrum, the more closely the sideband positions matched the theory. (The locations of the first order sidebands could not be simply predicted by the theory of [81] when  $Z_p$  is close to  $4\pi Z_c$ .) The structure near the center of the spectrum can be attributed to the first order sidebands due to resonant dispersive radiation as well as Fabry-Perot fringes due to intracavity etalon effects. A modulation with period  $\approx 2 \text{ nm}$  was consistently observed near the center of the different pulse spectra. After significant investigation it was determined that this modulation was due to an etalon in the commercial isolator in the laser cavity. The Faraday rotator in this isolator was anti-reflection coated for 2.0 to 2.2  $\mu\text{m}$  which resulted in a reflectivity of  $> 2\%$  at 1.8  $\mu\text{m}$ . This small reflectivity was sufficient



to cause the modulation depth of  $\approx 8\%$  which appeared on the spectrum. The optical thickness of the rotator ( $\approx 1$  mm) also corresponded well to the modulation period. Another indication that both periodic perturbations and an intracavity etalon contributed to the spectral modulation was that modulation due to the etalon had a consistent period of 2 nm, while the sidebands due to periodic perturbations changed position with pulse width, as predicted by eqn. 3.10.

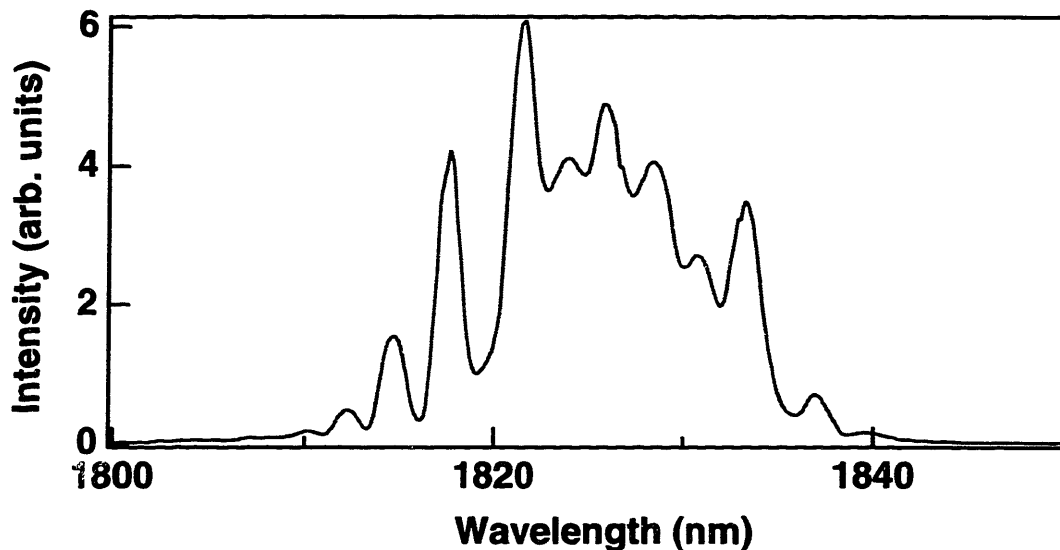


Figure 3-10: Spectrum of the mode-locked thulium-doped fiber laser showing sidebands due to periodicity and modulation due to an etalon in the cavity. Sidebands located more than 7 nm from the center of the spectrum corresponded to the order 2, 3, and 4 resonant sidebands, while the modulation near the spectral peak is due to an intracavity etalon.

### 3.7 Limitations of soliton lasers

The mode-locked thulium-doped fiber laser discussed in the previous section has an impressive tuning range but also has a number of disadvantages due to its operation in the soliton regime. The sidebands due to periodic perturbations and the resulting continuum generation are an important limitation on all soliton lasers. For a fixed cavity dispersion, the continuum generation limits the shortest obtainable pulse width. This long pulse width then limits the pulse peak power due to the soliton area theorem, which states that the soliton area is fixed by the average dispersion and nonlinearity:

$$\text{Soliton Area} = A_0\tau = \sqrt{\frac{-k''}{\eta}}. \quad (3.11)$$

A small peak power then implies low average output power in single-pulse per round-trip operation. Even without the pulse width limitation imposed by periodic perturbations, a soliton laser would eventually have a limited pulse peak power due to

the finite bandwidth of the gain material. Once the shortest pulse width is reached ( $\tau_{min} \propto 1/\Delta\nu_{gain}$ ), the peak power is fixed by the area theorem, implying limited pulse energies. But, generally the limit due to periodic perturbations occurs before the gain bandwidth becomes important.

Soliton lasers also have the problem of multiple-pulse operation due to APM saturation in a system with excessive gain [82]. As discussed in the previous paragraph, because of the soliton area theorem, the energy of a soliton is limited when either the peak power or pulse width is limited. Although the self-amplitude modulation (APM action) is generally represented by  $\gamma|u|^2$  as in eqn. (2.7), it may be more accurate to represent it by  $\sin(\gamma|u|^2)$  since the APM action is interferometric. A pulse which passes through this APM structure has an energy gain of

$$\int_{-\infty}^{\infty} dt |u|^2 \sin(\gamma|u|^2) \quad (3.12)$$

with

$$u(t) = A_0 \operatorname{sech}\left(\frac{t}{\tau}\right) \quad (3.13)$$

as defined by eqn. (2.8). The maximum of eqn. (3.12) is found to be at  $\gamma|A_0|^2 \simeq 0.6\pi$  through substitution of eqn. (3.13), differentiation, and numerical solution. Now the peak power of the soliton is limited, implying a limited pulse energy from the area theorem. If the pump power is increased to obtain high powers, the peak power of the soliton will eventually reach the limit imposed by the APM saturation. Then the single pulse per cavity round trip will break up into multiple, uncontrollable (untimed) pulses.

## 3.8 Possible improvements to the $\text{Tm}^{+3}$ -doped fiber laser

This section includes suggestions for improving the operation of the mode-locked  $\text{Tm}^{+3}$ -doped fiber laser in terms of smoother spectra, larger continuous tuning, and higher output powers.

### 3.8.1 Filtering

Although it is not possible to avoid the nonlinear phase shift limit in soliton lasers, filtering in the cavity can reduce the spectral sidebands without significantly increasing the pulse width as shown by Tamura [83] in an  $\text{Er}^{+3}$ -doped fiber laser. The spectrum of the  $\text{Tm}^{+3}$ -doped fiber laser from the previous section shows the spectral sidebands due to the periodicity, as well as other modulation, as shown in Fig. 3-10. This laser did contain a birefringent filter, but the bandwidth of 35 nm at 1.85  $\mu\text{m}$  was too large to significantly decrease the sidebands from the spectra, which had bandwidths of only 10 nm. Using a birefringent plate of greater thickness would decrease the bandwidth, but would also decrease the free spectral range of the filter. The continuous tuning range of the laser would then be smaller. A birefringent filter composed of

multiple plates (with thicknesses that are integer multiples of each other such as 1T, 2T, and 4T) can be designed to achieve both the desired bandwidth and free spectral range. Fig. 3-11 shows the transmission curve of a filter designed for the  $Tm^{+3}$ -doped fiber laser. The plate thicknesses are 2T, 4T, and 8T, resulting in a bandwidth of  $\approx 20$  nm and free spectral range of  $> 70$  nm. The spectral modulation may also be reduced by finding an optical isolator which will not exhibit an etalon effect. A Faraday rotator which is anti-reflection-coated for  $1.85 \mu m$  as well as a thicker, wedged rotator component would reduce the etalon effect.

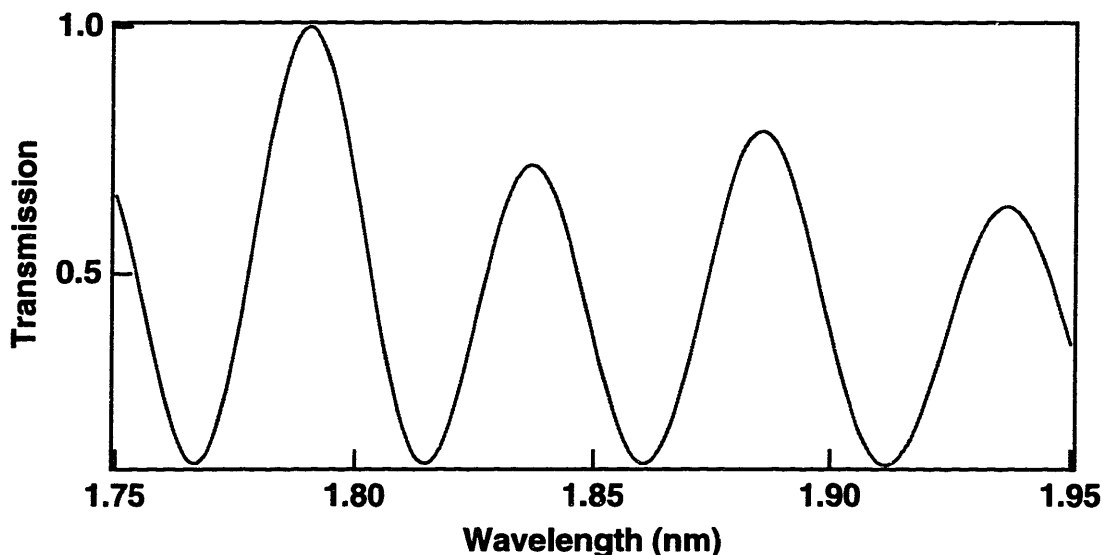


Figure 3-11: Calculated transmission versus wavelength for a multiple plate filter of quartz plates with thickness 2T, 4T, and 8T at Brewster's angle in the cavity. The filter angle is set for maximum extinction (with c-axis at 40 degrees from TE).

### 3.8.2 Rejection Port

Higher output powers may be obtained from the  $Tm^{+3}$ -doped fiber laser by using the rejection port as the output coupler in addition to the normal output coupler. As shown in Fig. 2-5, after the pulse exits the Kerr medium (fiber), it passes through a half-wave plate to bias it so that the peak will pass through the polarizer, and the orthogonal polarization, which contains the pulse wings, will be extinguished. This orthogonal polarization contains the power which is rejected in order to achieve pulse shortening. Although one might expect the power exiting this port to have poor pulse quality, as demonstrated in [84], the rejected pulse can be of high quality if the differential nonlinear phase shift required for mode-locking is small ( $< \pi/2$ ). The rejected pulse is usually longer than the intracavity pulse, but the rejected output power can be as much as 50% of the intracavity power when the laser is biased to a point where there is large loss for low intensities.

In the  $Tm^{+3}$ -doped fiber laser shown in Fig. 3-1, the rejected power leaves the cavity through the PBS before the birefringent tuning plate. In some preliminary

experiments, the output from this rejected port (RP) was compared with the pulses from the 5% output coupler (OC). Fig.3-12 shows a set of autocorrelations and spectra from the two ports when the laser consisted of 1.25 meters of  $\text{Tm}^{+3}$ -doped fiber and 4.95 meters of SMF-28 and when a multiple-plate birefringent filter (2T, 4T, and 8T) was used in the cavity. The pulse widths were approximately the same: the OC pulse FWHM was 450 fsec compared to 420 fsec from the RP.<sup>1</sup> As expected, the output power from the RP was significantly higher, 5.9 mW versus 640  $\mu\text{W}$  from the OC, indicating that a large fraction of the intracavity power was rejected. (Unfortunately this fraction can not be calculated exactly since the laser power immediately before the PBS is not known.)

The larger pulse wings on the RP autocorrelation are very apparent as well as the larger continuous-wave spikes on the spectrum. A quantitative way to compare the pulses is to calculate what fraction of the pulse energy lies in the wings of the pulse which are larger than the sech fit. For the OC pulse, 9% of the pulse energy is contained in the non-sech wings, compared to 23% for the RP pulse. This indicates a fairly poor quality pulse, particularly in the case of the RP pulse, compared to the pulse of Fig. 3-3 which had only 3.6% of the pulse energy in the non-sech wings. This cavity with shorter fiber length tended to operate with larger pulse wings, which is not completely understood but may have a number of possible causes. The shorter cavity has a smaller net negative dispersion which may reduce the dispersing of the broadband continuum so that it builds up more significantly before it can build up in the sidebands. Secondly, the multiple-plate birefringent filter may have an etalon effect or may provide a larger perturbation to the pulse as it circulates in the cavity. Further comparison of the output from the OC and RP may provide more insight into the operation of the laser. This brief investigation, though, showed that if optimal pulse quality is not important, the RP pulses should be used since the output power is an order of magnitude larger than the pulses from the output port.

### 3.8.3 Stretched-pulse operation

A possible way to obtain higher output powers and shorter pulses from the  $\text{Tm}^{+3}$ -doped fiber laser is to avoid operating in the soliton regime, as first demonstrated in our group with the stretched-pulse fiber laser [85]. The stretched-pulse technique involves using segments of positive- and negative-dispersion fiber in the laser with a net dispersion that is slightly positive. The pulses are alternately stretched and compressed as they circulate in the cavity, as shown in Fig. 3-13, resulting in a lower total net nonlinear phase shift per round trip. Spectral broadening occurs in the doped fiber due to the action of the positive dispersion with self-phase modulation. At the output, the pulses have high energy, a broad bandwidth, and a large positive chirp. Because the pulses are at a minimum for only a very small portion of the cavity round trip, the nonlinear phase shift is limited, and the alternating dispersion is the dominant effect. This results in output pulses which have a large chirp that is

---

<sup>1</sup>This state of operation with a shorter RP pulse than OC pulse was somewhat unusual. Generally the RP pulse width was  $\approx 10\%$  larger than the OC pulse width. This state was chosen for Fig. 3-12 for its higher output powers.

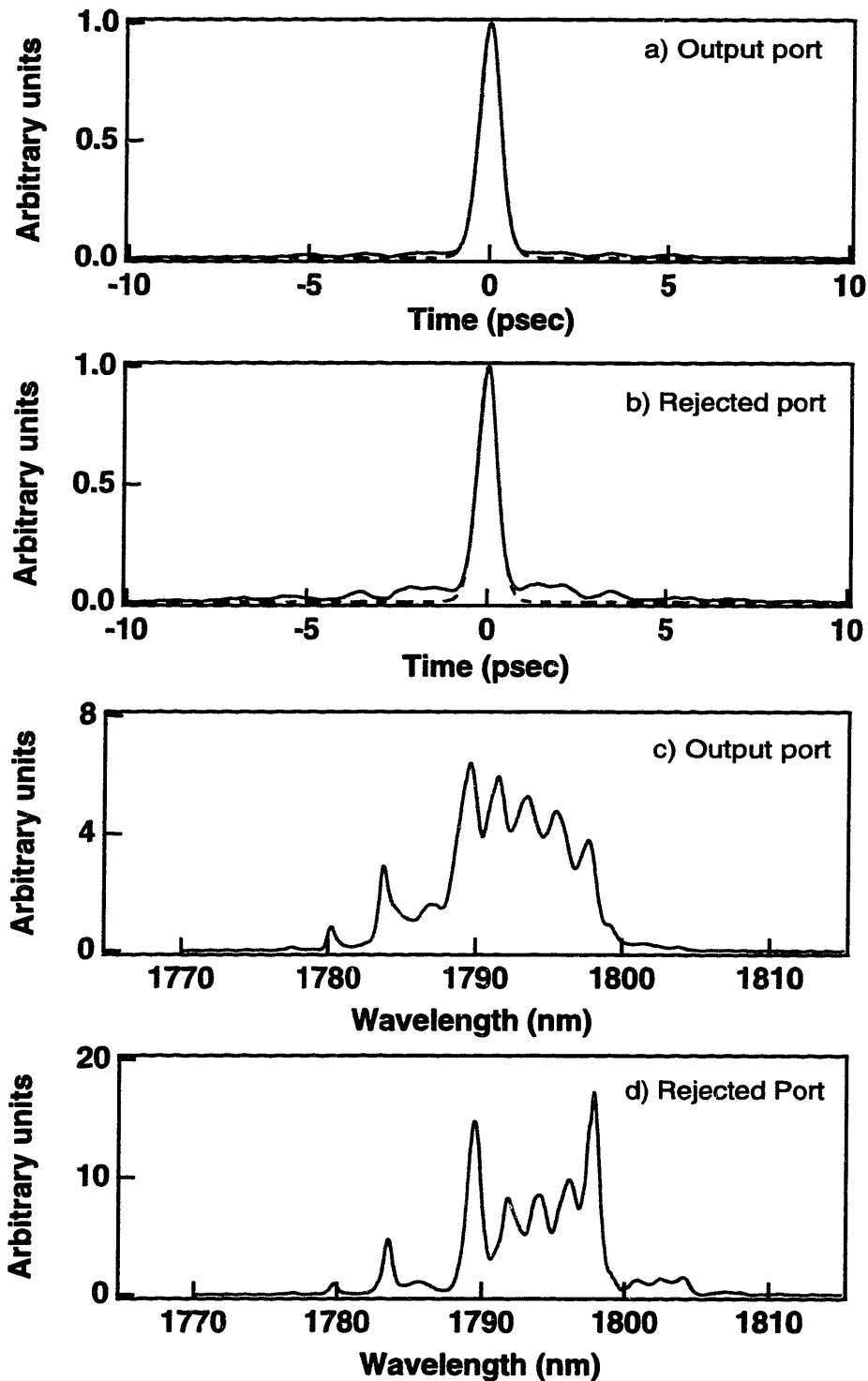


Figure 3-12: Comparison of pulses which exit the 5% output coupler (OC) with the pulses which exit the rejected port (RP). a) Autocorrelation of OC pulse with 450 fsec FWHM (fit with a sech) and average power 640  $\mu$ W. b) Autocorrelation of RP pulse with 420 fsec FWHM (fit with a sech) and average power 5.9 mW. c) Spectrum of OC pulse centered at 1792 nm. d) Spectrum of RP pulse centered at 1794 nm.

highly linear. The chirp can then be compressed with prisms or gratings to achieve sub-100 fsec pulses. Another important aspect of the stretched-pulse technique is that the alternating dispersion causes a periodically varying  $k(\omega)$  (instead of a constant  $k_s = \frac{|k''|}{2\tau^2}$  as in the soliton laser) which reduces phase-matched coupling to resonant sidebands [86]. Thus the spectra are cleaner and there is less dispersive radiation between pulses.

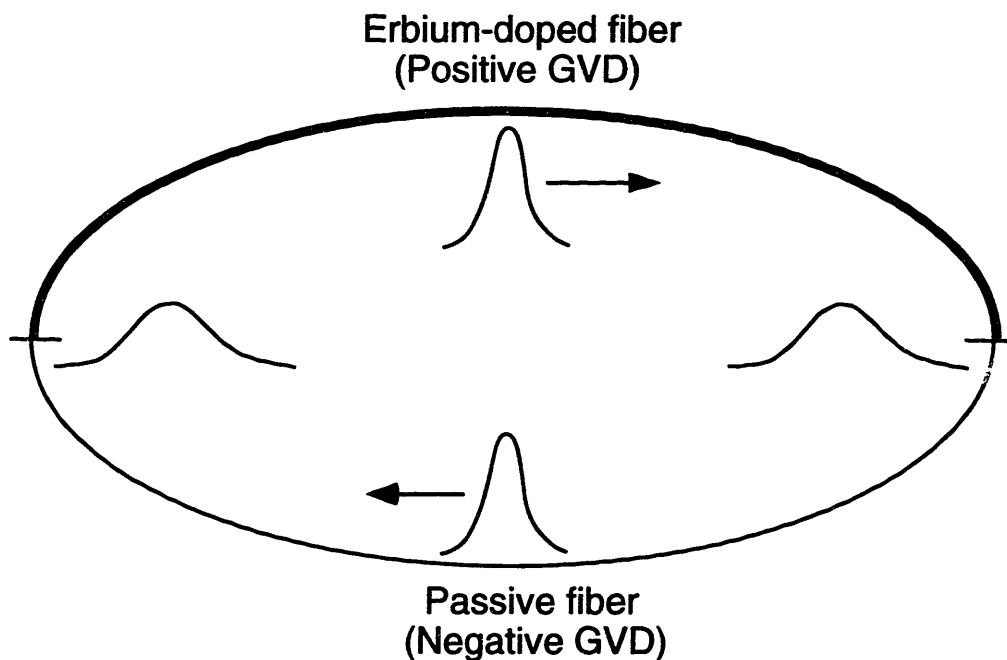


Figure 3-13: Diagram of pulse evolution in an stretched-pulse  $\text{Er}^{+3}$ -doped fiber laser. The strong positive GVD of the  $\text{Er}^{+3}$ -doped fiber is approximately balanced by the negative GVD of the passive fiber, causing the pulse to stretch and compress as it travels around the fiber ring.

The application of the stretched-pulse technique is unfortunately more difficult in the thulium system at  $1.8 \mu\text{m}$ . In the  $\text{Er}^{+3}$ -doped fiber laser discussed above, the positive dispersion fiber was the doped fiber, while the passive fiber had negative dispersion. At  $1.55 \mu\text{m}$  the material dispersion of silica is  $-28 \text{ ps}^2/\text{km}$ , but the waveguide dispersion in the doped fiber (due to a small core and large index difference between core and cladding) is sufficiently positive to shift the net dispersion of the fiber to  $+75 \text{ ps}^2/\text{km}$ . (The dispersion of the passive fiber is  $-23 \text{ ps}^2/\text{km}$  at  $1.55 \mu\text{m}$ .) At  $1.8 \mu\text{m}$ , the material dispersion of silica is significantly more negative than at  $1.55 \mu\text{m}$ ,

resulting in a dispersion of  $-60 \text{ ps}^2/\text{km}$  for the passive fiber and  $-12 \text{ ps}^2/\text{km}$  for the  $\text{Tm}^{+3}$ -doped fiber. It is unlikely at this time that any positive-dispersion  $\text{Tm}^{+3}$ -doped fiber will be available, since few universities or research laboratories even make this type of doped fiber. Therefore, constructing a stretched-pulse thulium-doped fiber laser with positive dispersion in the gain fiber is not feasible.

In order to still achieve some stretching in the laser, there may be other ways of introducing positive dispersion into the cavity. Bulk mono-crystalline silicon has high positive dispersion ( $+0.9 \text{ ps}^2/\text{m}$ ) at  $1.8 \mu\text{m}$ , but a very long piece ( $\simeq 70 \text{ cm}$ ) would be required in order to compensate the net dispersion of the  $-0.645 \text{ ps}^2$  in the  $\text{Tm}^{+3}$ -doped fiber laser of section 3.1. This is completely impractical, of course. Another option for positive dispersion would be to use a set of prisms with lenses in the air-gap of the laser cavity. Unfortunately the alignment of a cavity with prisms would be very difficult because the  $1.8 \mu\text{m}$  beam is essentially invisible (even infrared cards are not sensitive beyond  $1.7 \mu\text{m}$ ).

The most practical way to introduce positive dispersion into the cavity is to use a piece of (passive) dispersion-compensating (DC) fiber which has positive dispersion at  $1.8 \mu\text{m}$ . DC fiber was designed to compensate the large negative dispersion in present long-haul communications systems which have zero dispersion at  $1.3 \mu\text{m}$  but operate at  $1.55 \mu\text{m}$  where there is negative dispersion of  $k'' \approx -22 \text{ ps}^2/\text{km}$ . I was recently able to obtain a piece of DC fiber from Corning which has a dispersion of  $+162 \text{ ps}^2/\text{km}$  at  $1.55 \mu\text{m}$ , as shown in Fig. 3-14, and an extrapolated dispersion of  $+330 \text{ ps}^2/\text{km}$  at  $1.85 \mu\text{m}$ . This fiber was tested in a stretched-pulse  $\text{Er}^{+3}$ -doped fiber laser, and two possible problems were identified. First, the refractive index profile of the DC fiber consists of concentric higher-index rings around the core which causes splice loss of  $\geq 20\%$  when DC fiber is spliced to SMF-28 or other more standard fiber. Secondly, the stretching factors and spectral bandwidth may be smaller than when the positive-dispersion fiber has gain (as in the laser of Fig. 3-13) because there will be lower peak power and thus less spectral broadening due to the action of the positive dispersion with self-phase modulation. An interesting future experiment would be to try to use this fiber in the  $\text{Tm}^{+3}$ -doped fiber laser to determine if the laser will mode-lock and if stretching occurs in this cavity configuration to allow higher output powers.

### 3.9 Optical Coherence Tomography using a $1.8 \mu\text{m}$ source

As discussed in the introduction, Optical Coherence Tomography (OCT) is a possible application for a mode-locked fiber laser which takes advantage of the broad spectrum. This section includes an investigation of this application using a  $\text{Tm}^{+3}$ -doped fiber amplified-spontaneous emission (ASE) source to evaluate the use of the  $1.8$  to  $1.9 \mu\text{m}$  wavelength range for OCT. A description of the ASE source is also included.

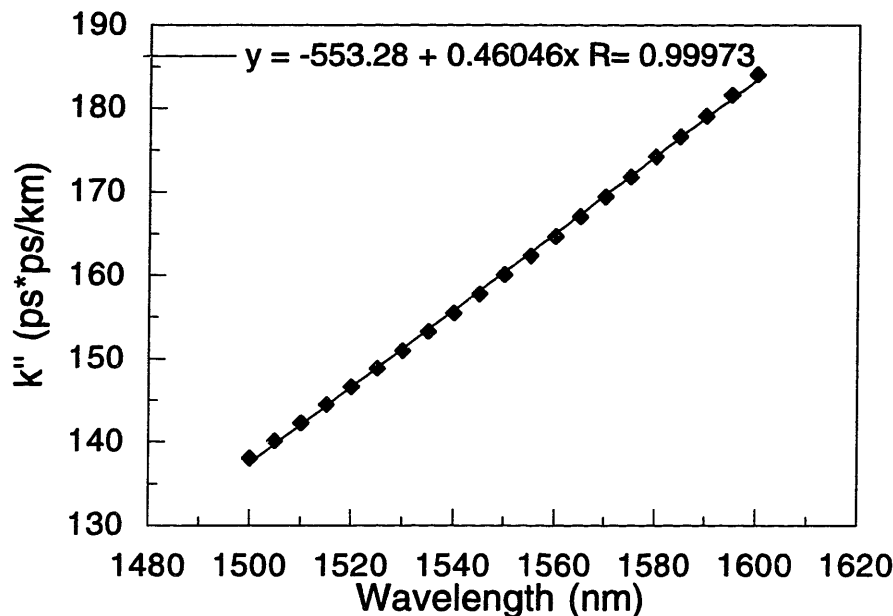


Figure 3-14: Plot of group-velocity dispersion  $k''$  versus wavelength for the dispersion-compensating (DC) fiber from Corning. The dispersion is  $+162 \text{ ps}^2/\text{km}$  at  $1.55 \mu\text{m}$  and is extrapolated to be  $\approx +330 \text{ ps}^2/\text{km}$  at  $1.85 \mu\text{m}$ .

### 3.9.1 OCT background

Optical Coherence Tomography is a medical imaging diagnostic technique which uses low coherence light to do high resolution optical ranging [87,88]. Cross-sectional images of biological tissues are obtained non-invasively by measuring the optical reflections from the internal structures. These reflections give time-of-flight information which can be used to obtain spatial information about the tissue microstructure [87]. The incident optical ranging beam is scanned in the transverse direction(s) to obtain the cross-sectional image. Retro-reflection OCT is a form of Optical Coherence Domain Reflectometry (OCDR) using a fiber-optic Michelson interferometer and a low-coherence or mode-locked source, as shown in Fig. 3-15. All four ports of the coupler are used: the two input ports for the source and detector, and the two output ports for the sample and reference. Light which exits the sample arm is collimated and directed into the specimen. Some of this light is retro-reflected and interferes in the fiber-optic beamsplitter with light that arrives after reflecting off the scanning mirror at the end of the reference arm. The detector then measures coherent interference only when the distance of the reflection from the specimen is matched to the reference arm length within a coherence length of the source. By using low coherence light, sub- $20 \mu\text{m}$  resolutions can be achieved.

The coherence length (spectral bandwidth) and wavelength of the source deter-



mine the ranging resolution of OCT. This resolution can be expressed as:

$$\Delta L = \ln(2) \frac{2 \lambda^2}{\pi \Delta \lambda} \quad (3.14)$$

where  $\Delta \lambda$  is the FWHM spectral bandwidth, and it is clear that a broad bandwidth source is desirable. Resolutions of  $3.7 \mu\text{m}$  have been demonstrated with the  $> 100 \text{ nm}$  bandwidth of a Ti:Sapphire mode-locked source at  $830 \text{ nm}$  [89]. The wavelength of the source is also important in OCT because absorption and scattering can significantly decrease the amplitude of the detected signal. Absorption is of course highly wavelength dependent and will vary with the type of tissue being measured. Performing OCT at multiple wavelengths would allow the measurement of spectral properties of tissues such as hydration or the size of the light-scattering particles. Rayleigh scattering is a loss mechanism which is inversely proportional to the fourth power of the wavelength, implying that a longer wavelength source is better. High incident power is also desirable for an OCT source because it enables shorter data acquisition times or an increase in the signal level and penetration range.

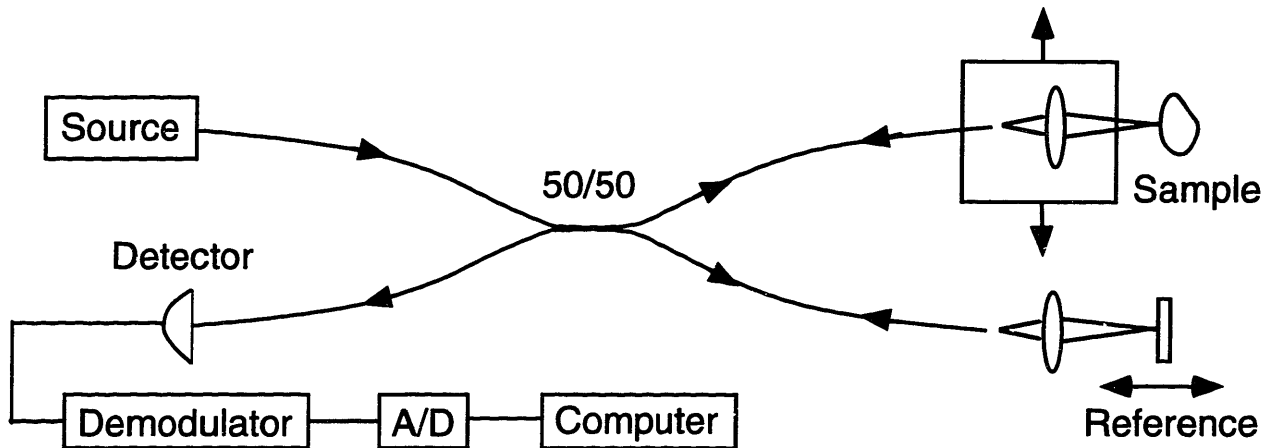


Figure 3-15: Experimental setup for Optical Coherence Tomography from [87].

Professor J. Fujimoto's group at MIT has used a number of sources for OCT experiments including a super-luminescent diode (SLD) at  $830 \text{ nm}$  [87], mode-locked Ti:Sapphire laser at  $830 \text{ nm}$  [89], and a mode-locked Cr:Fosterite laser at  $1.3 \mu\text{m}$  [90]. A natural extension of their work is use of a longer wavelength source, possibly near  $1.8 \mu\text{m}$  where the loss due to Rayleigh scattering is low. Another interesting aspect of this wavelength is that water has an absorption peak in this region, which may provide information about the tissue hydration, especially when comparing the depth of penetration to that of other wavelengths. At the present time the mode-locked  $\text{Tm}^{+3}$ -doped fiber laser has a resolution of only  $140 \mu\text{m}$  with its small spectral bandwidth of  $10 \text{ nm}$ . But the fluorescence spectrum of the  $\text{Tm}^{+3}$ -doped fiber is as large as  $100 \text{ nm}$  and has a very smooth shape as shown in Fig. 2-3, indicating that an ASE source from this  $\text{Tm}^{+3}$ -doped fiber could potentially have an OCT resolution of  $14 \mu\text{m}$  at  $1.8 \mu\text{m}$ . A  $\text{Tm}^{+3}$ -doped fiber ASE source was therefore constructed and optimized, as described in the following section.

### 3.9.2 Tm<sup>3+</sup>-doped fiber ASE source

The ASE source consisted of the same Tm<sup>3+</sup>-doped fiber (CTm-158) and was pumped with a maximum of 500 mW at 785 nm from the cw Ti:Sapphire laser. Both fiber ends were angle-polished to prevent lasing, and a cutback measurement was taken while measuring the ASE output at the unpumped fiber end under constant pump power. The optimal fiber length for this configuration was 1.3 meters, and output ASE powers as high as 7 mW were achieved. Fig. 3-16 shows a plot of output power versus absorbed pump power when pumping at 785 nm. With maximum output power of 7 mW, the ASE spectrum was centered at 1808 nm with a 70 nm spectral FWHM. The dependence of absorbed pump power on pump wavelength was also tested (with constant incident pump power), as shown in Fig. 3-17, and the optimum pump wavelength was between 784 and 788 nm. (This measurement is important for determining the pump tolerance in the interest of eventually diode-pumping the Tm<sup>3+</sup>-doped fiber.) Finally, the dependence of the spectral first moment on level of pump power at 785 nm was also measured, as shown in Fig. 3-18. The center wavelength increased from 1800 nm to 1820 nm as the absorbed pump power was decreased from 320 mW to 150 mW, which was due to self-absorption in the Tm<sup>3+</sup>-doped fiber. The 70 nm bandwidth at 1808 nm corresponded to an OCT resolution of 20  $\mu\text{m}$ .

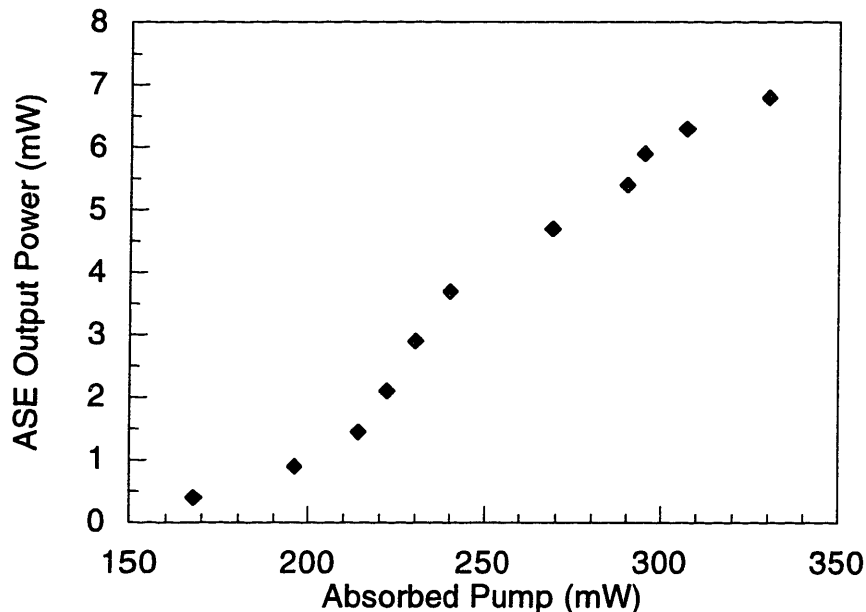


Figure 3-16: Tm<sup>3+</sup>-doped fiber ASE versus absorbed pump power for 1.3 meters of CTm-158 and cw pump power at 785 nm.

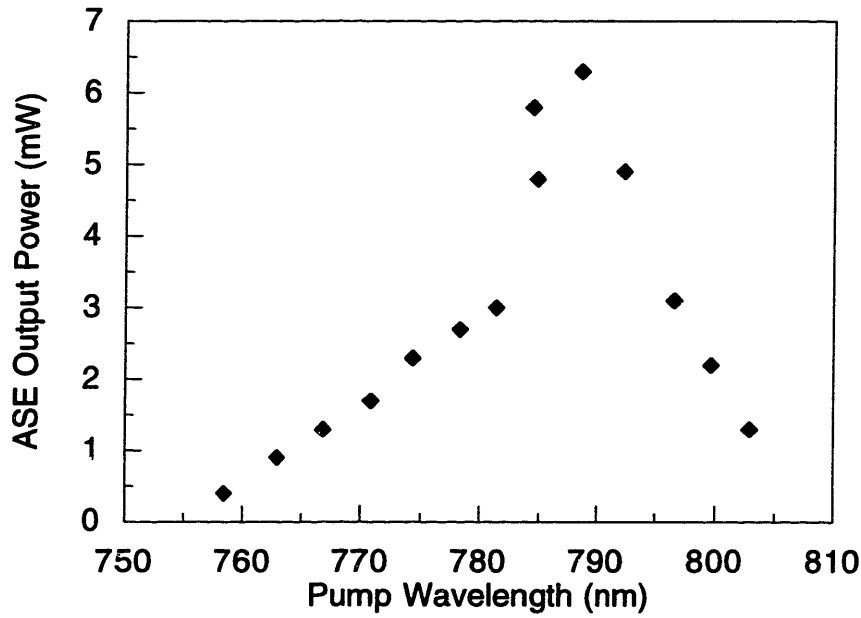


Figure 3-17: ASE output power versus pump wavelength for a constant incident pump power of 840 mW.

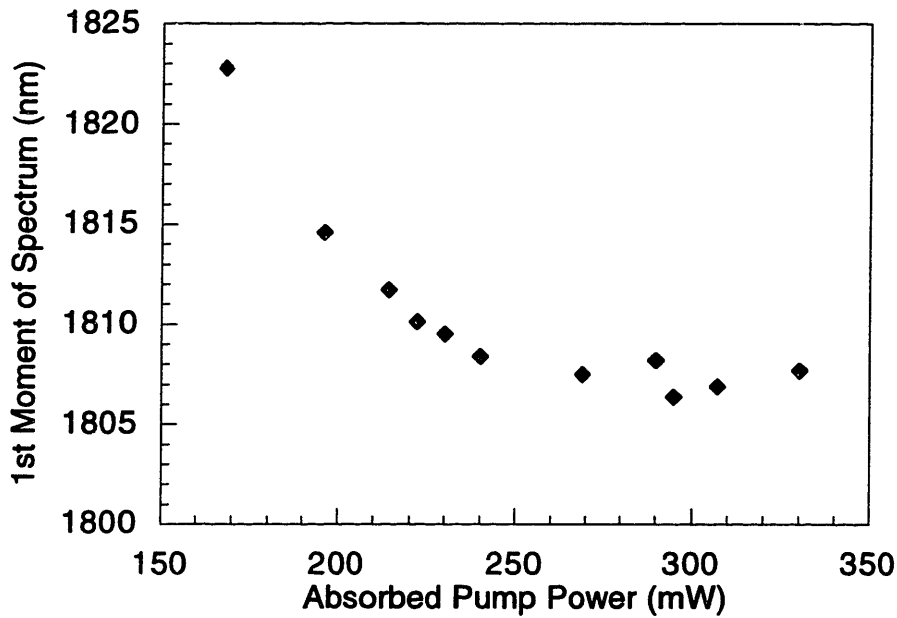


Figure 3-18: First moment of ASE spectrum versus absorbed pump power at 785 nm. The wavelength shifts due to self-absorption in the fiber.

### 3.9.3 OCT source comparison

In collaboration with Prof. Fujimoto's group, the  $\text{Tm}^{+3}$ -doped fiber ASE source was used to take an image of a biological tissue in vitro. The same tissue was then imaged with a commercially available  $1.3 \mu\text{m}$  super-fluorescent source. The resolutions of the two sources were comparable ( $20 \mu\text{m}$  at  $1.8 \mu\text{m}$  versus  $15 \mu\text{m}$  at  $1.3 \mu\text{m}$ ), and the power levels of the sources were matched. Fig. 3-19 shows a comparison of the two images taken with the sources. The results were promising; the images obtained with the  $1.8 \mu\text{m}$  source had a slightly larger penetration depth compared with the images taken at  $1.3 \mu\text{m}$ , and the resolution was comparable. An additional advantage of thulium source are that it is eye-safe and could be used clinically. The OCT group is currently continuing to examine the feasibility of using a thulium-doped fiber source for imaging.

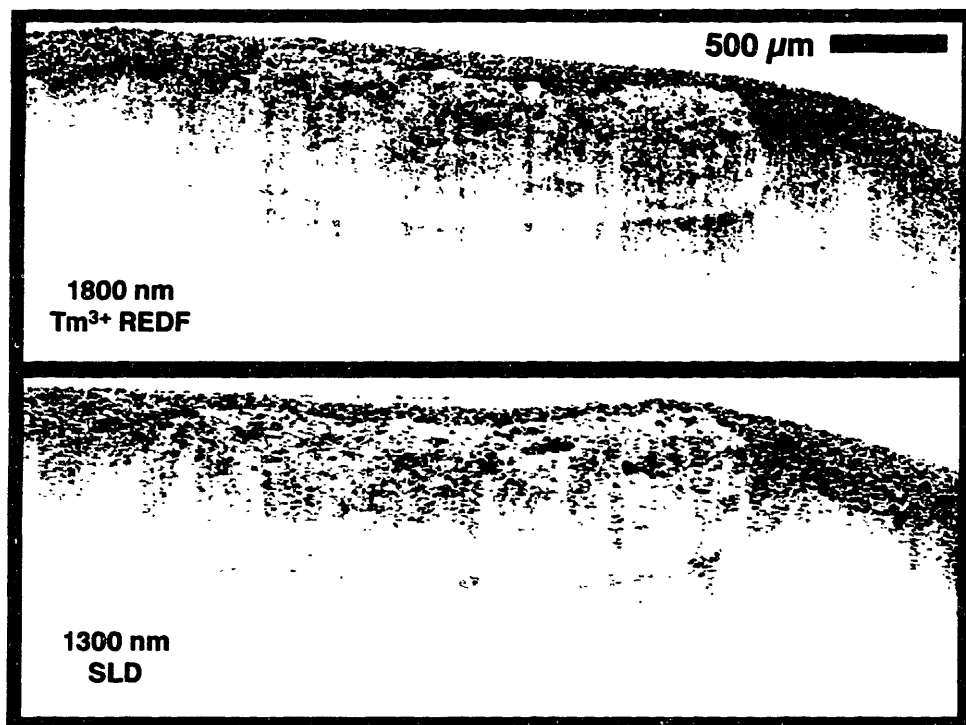


Figure 3-19: Two dimensional OCT image of calcified aortic plaque taken in vitro with the  $\text{Tm}^{+3}$ -doped fiber ASE source and with a  $1.3 \mu\text{m}$  source of comparable resolution.

# Chapter 4

## Frequency-doubling of a stretched-pulse erbium-doped fiber laser

The stretched-pulse technique was discussed in section 3.8.3 as a possible way to obtain higher output powers and broader spectra by operating in the non-soliton regime [85]. An analytical theory of stretched-pulse operation was developed by Haus, et. al. [91] which describes the mode-locked pulses for this case when the pulse undergoes large changes per pass due to dispersion. Pulse lengthening due to dispersion leads to a reduction of the excessive nonlinear effects and improved output pulse characteristics. This chapter includes a discussion of the stretched-pulse technique for a new application: frequency doubling of the 1.55  $\mu\text{m}$  output of the  $\text{Er}^{+3}$ -doped fiber laser to achieve 770 nm pulses for amplifier seeding. Portions of this work were published in [92].

Stretched-pulse erbium-doped fiber lasers have generated ultra-short pulses (100 fsec) with energies comparable to those of color-center lasers [84]. By employing the APM rejection port as the output port, pulse energies of over 2 nJ have been achieved with average powers of  $> 90$  mW [93]. The laser has several key features which have led to a number of applications at 1.55  $\mu\text{m}$ . The broad bandwidth of  $> 40$  nm can be used for wavelength-division multiplexing (WDM) by slicing the bandwidth into channels which are individually modulated [94]. A tunable psec source for WDM has also been demonstrated by passing the broad bandwidth output through an interference filter [95]. Additionally, the broad bandwidth could be used for optical characterization between 1.5 and 1.6  $\mu\text{m}$ . Pulses from this 1.55  $\mu\text{m}$  low-noise source can also be used in time-resolved spectroscopy and as a seed for a  $\text{KCl:Tl}^+$  color-center amplifier. The amplified pulses can then be compressed and focussed into a material with a large nonlinear index of refraction  $n_2$  to generate continuum for spectroscopy [96]. Optical coherence tomography [97] at 1.55  $\mu\text{m}$  is a possible application which would utilize the low coherence of the SP-APM laser.

An additional feature of the laser is the high peak power ( $> 15$  kW) of the compressed 1.55  $\mu\text{m}$  pulses which allows efficient second harmonic generation (SHG) to 775 nm near the peak of gain for Ti:Sapphire. A potential application for these

frequency-doubled pulses is as a seed for a Ti:Sapphire regenerative amplifier. The frequency-doubled stretched-pulse fiber laser would be an inexpensive and compact replacement for the argon-pumped mode-locked Ti:Sapphire oscillator which is normally used as a seed. Dominance over amplified spontaneous emission has been demonstrated with 100 pJ seed pulses in a Ti:Sapphire amplifier [98] and with 3 pJ seed pulses in an alexandrite amplifier [99]. In this chapter, experimental results for frequency-doubling of a SP-APM fiber laser will be presented where near transform-limited pulses of over 270 pJ at 771 nm were achieved. Another advantage of the system is the  $> 30$  MHz repetition rate which results in an easily visible red beam and simplifies alignment of the amplifier system. First we consider optimization of a SP-APM fiber laser for this application in section 4.1. Then frequency-doubling results are discussed including the evaluation of three different nonlinear crystals. In order to more fully characterize the laser, frequency resolved optical gating measurements were made and are discussed in section 4.3. Finally amplitude noise measurements were made on the frequency doubled pulses and compared with an argon-ion pumped Ti:Sapphire laser.

## 4.1 Stretched-pulse laser optimization

As discussed previously, the SP-APM fiber laser is a unidirectional ring laser with segments of positive-dispersion (erbium-doped) fiber and negative-dispersion (passive) fiber with an overall dispersion that is slightly positive [85]. The full experimental set-up is shown in Fig. 4-1. Several optimizations were made to this laser compared to that reported in [93], including net dispersion, erbium-doped fiber length, and pumping geometry. The net dispersion  $D_T$  of the SP-APM laser affects the pulse width and pulse energy as shown in [86] and in Fig. 4-2. As  $D_T$  is increased from negative to positive, the pulse energy increases due to higher pulse stretching factors and avoidance of nonlinear saturation. Although operating with  $D_T$  at zero or slightly positive results in the shortest compressed pulses, the pulse energies are significantly higher for  $D_T > +0.01$  ps<sup>2</sup> while the pulse widths remain around 100 fsec. Therefore, for frequency-doubling applications where fundamental peak power is most important for obtaining high efficiencies, it is advantageous to operate the laser with large positive  $D_T \geq +0.02$  ps<sup>2</sup>.

In order to obtain higher efficiencies and peak power, the erbium-doped fiber was longer than in previous stretched-pulse lasers (1.7 meters), resulting in a longer cavity and thus a larger single pulse energy. The erbium-doped fiber was backwards pumped with a 980 nm commercially available master oscillator power amplifier (MOPA) diode laser. Backwards pumping gives higher gain than forward pumping because the fiber is pumped hardest where signal and signal saturation are strongest, thus maximizing power conversion efficiency and signal gain. Significant research on erbium-doped fiber amplifiers has shown that in saturated fiber amplifiers, backwards pumping results in higher gain [100,101]. Appendix A reports an experimental comparison of forward and backward pumping in a continuous-wave erbium-doped ring fiber laser using the highly-doped Er1128-2 fiber.

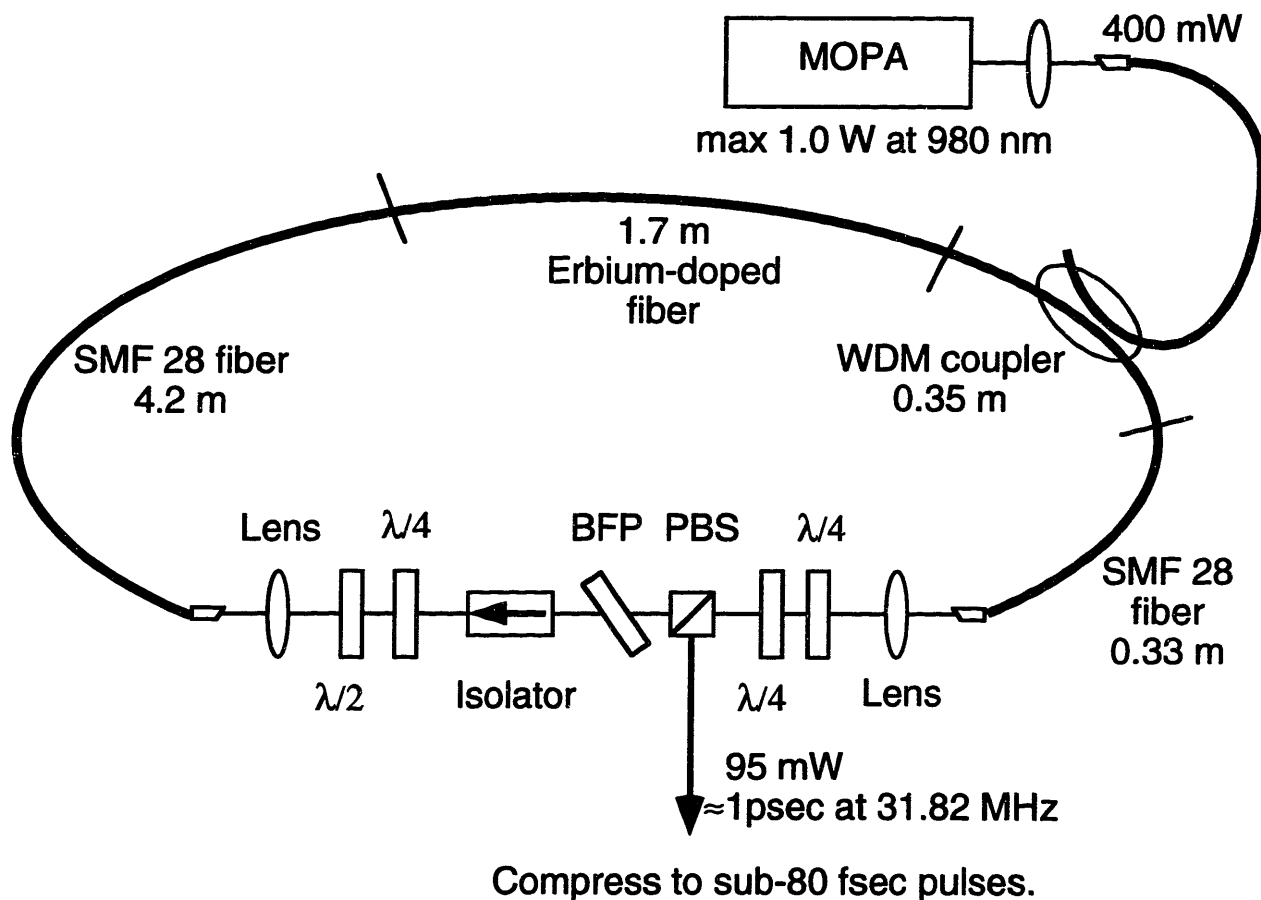


Figure 4-1: Experimental set-up of a stretched-pulse fiber laser optimized for frequency doubling. BFP: 5T quartz birefringent plate, PBS: polarizing beam splitter.

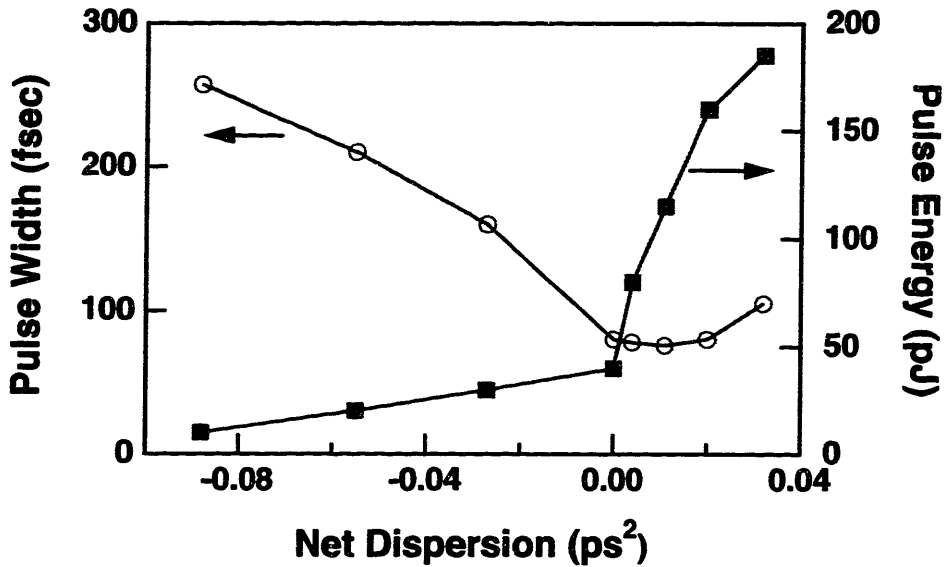


Figure 4-2: Plot of pulse energy and pulse width versus net dispersion for a stretched-pulse fiber laser, after Ref. [86] which used a 5% output coupler.

An additional optimization was the use of the APM rejection port as the output port in order to maximize the output power [84]. One might expect the pulse from the rejection port to be of poor quality since it contains the pulse wings which are rejected in order to shorten the intracavity pulse. But because the nonlinear phase shift per pass is small ( $< \pi/2$ ), this pulse can still be of acceptable quality, especially for this application of SHG, since the nonlinear process "cleans up" the frequency-doubled pulse. High output powers can be achieved by setting the waveplates to bias the cavity for large loss at low intensities, so approximately 50% of the intracavity power is actually rejected as the output. The strong pumping and nonlinear output coupling at the APM rejection port do cause the fundamental pulses to have excess energy in the pulse wings and larger time-bandwidth products than when the SP-APM laser is optimized for minimum pulse width. But the frequency-doubling results presented in this chapter show that the SHG conversion efficiency is still significantly enhanced by this higher power operation without comparable conversion of the pulse wing energy. The frequency-doubled pulses were clean with less than 1% of the pulse energy in the non-sech wings.

The SP-APM laser had a mode-locking threshold of approximately 200 mW of coupled pump power and average output powers of  $> 95$  mW at 31.82 MHz with 400 mW of coupled pump power. (Pumping with higher power was possible but led to multiple pulsing.) With the fiber lengths shown in Fig. 4-1, the net dispersion of the laser was  $+0.013$  ps<sup>2</sup>. (Additional experiments were performed with a net dispersion of  $+0.042$  ps<sup>2</sup> and will be discussed in section 4.6). Even though the laser was not packaged for environmental stability, it operated with the same pulse characteristics for days without readjustment of the waveplate settings. The highly-stretched  $\sim 1$  psec pulses were compressed in a four silicon Brewster prism sequence with prism



separation of approximately 12 cm and total transmission of up to 90%. Silicon is highly dispersive at  $1.55 \mu\text{m}$  which allows a very compact compression geometry even when providing large negative dispersion  $\sim -0.015 \text{ ps}^2$ . The resulting compressed pulses at  $1.55 \mu\text{m}$  were 100 to 110 fsec with 85 mW of average power and pulse energy of 2.7 nJ. Fig. 4-3 shows the autocorrelation of a typical compressed pulse while the spectrum is shown in Fig. 4-4. The spectral width of approximately 67 nm and pulse width of 106 fsec result in a time-bandwidth product of  $\sim 0.89$  assuming a sech.

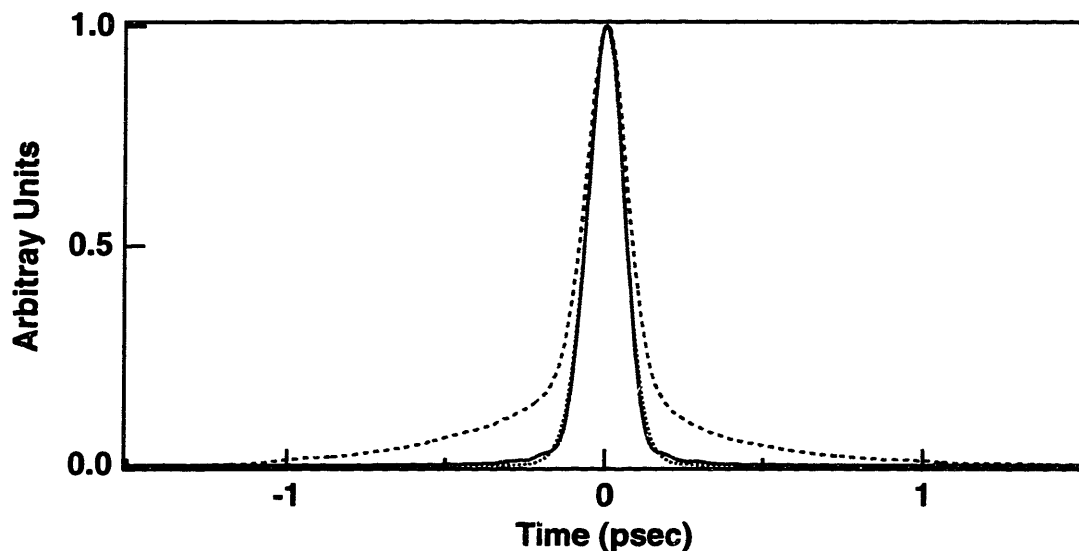


Figure 4-3: Autocorrelation of the  $1.55 \mu\text{m}$  pulse (dashed) and the frequency-doubled pulse (solid). A sech fit of the frequency-doubled pulse is also shown (dotted).

A 150 lines/mm grating (blazed at  $2.0 \mu\text{m}$ ) was also used for compression in a single grating geometry. Grating compression was easily aligned and fundamental pulse widths as short as 70 fsec were achieved. Due to the lower efficiency of grating compression ( $\approx 30\%$  transmission with four reflections off the grating), all doubling results reported here were obtained with silicon prisms, and gratings were used only for diagnostics.

## 4.2 Frequency-doubling results

Several nonlinear crystals for frequency-doubling the SP-APM laser were evaluated including  $\beta\text{-BaB}_2\text{O}_4$  (BBO),  $\text{KNbO}_3$  (potassium niobate), and  $\text{LiB}_3\text{O}_5$  (LBO). Calculations indicate that BBO should be an excellent nonlinear crystal for doubling  $1.55 \mu\text{m}$ . The phase-matching angle, as shown in Fig. 4-5, varies by  $< 0.3$  degree between  $1.5$  and  $1.6 \mu\text{m}$ , according to [102] which reports index data from 400 nm to  $1.061 \mu\text{m}$ . Although the Sellmeier equations are not strictly valid at  $1.55 \mu\text{m}$ , they indicate that the group-velocity mismatch between the fundamental and second harmonic generation (SHG) approaches zero near  $1.5 \mu\text{m}$ . The frequency-doubling

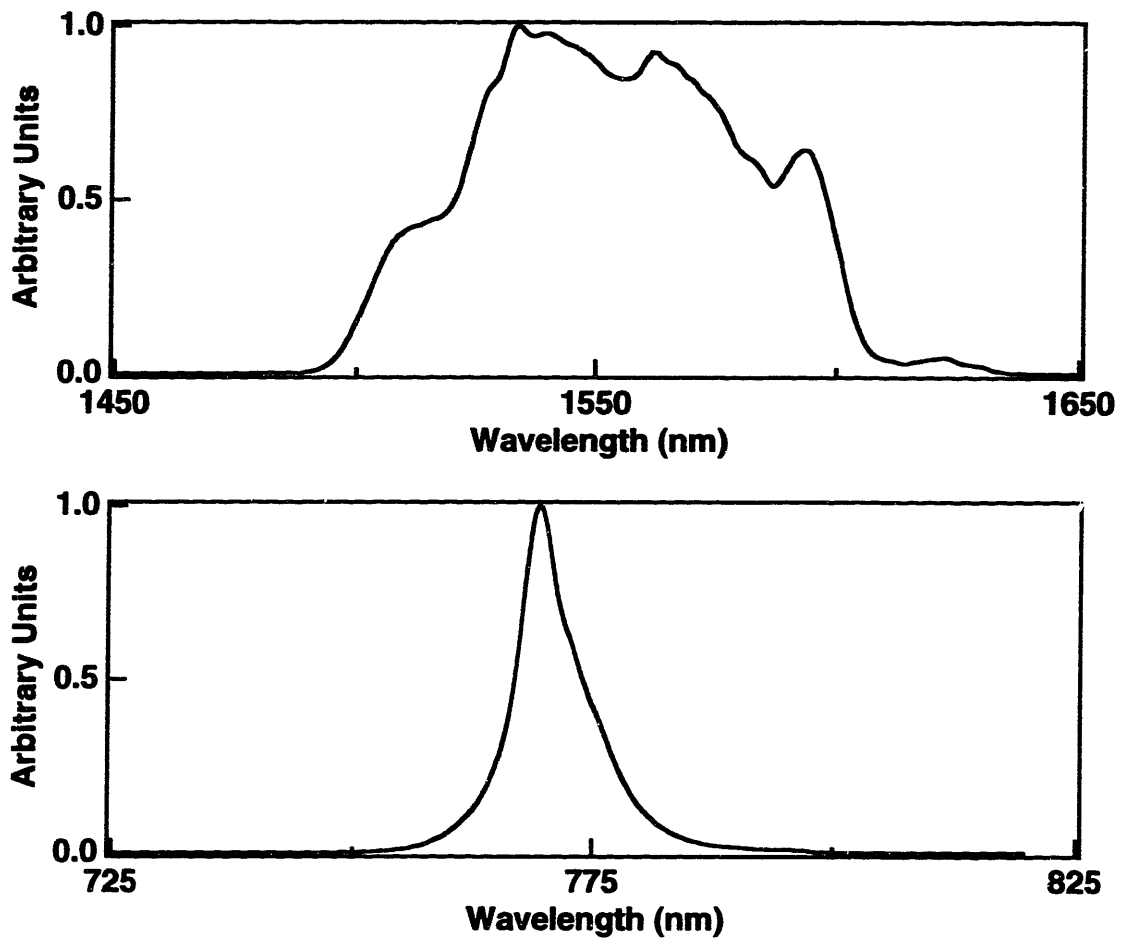


Figure 4-4: Spectrum of 1.55  $\mu\text{m}$  pulse with spectral width of  $\approx 67$  nm (top) and spectrum of frequency-doubled pulse at 771 nm with spectral width of  $\approx 7.3$  nm.

setup is shown in Fig. 4-6. With 85 mW of compressed fundamental power focused onto a 1-cm AR-coated BBO crystal with an AR-coated 75-mm focal-length lens, frequency-doubled powers as high as 8.7 mW were achieved, corresponding to 10% conversion efficiency and pulse energies of 270 pJ. Fig. 4-3 shows the autocorrelation of the 86 fsec frequency-doubled pulse (assuming a sech). The frequency-doubled spectrum, shown in Fig. 4-4, is 7.3 nm wide and centered at 771 nm, resulting in a time-bandwidth product of  $\approx 0.32$ . Efficient frequency-doubling thus results in a large reduction of excess bandwidth to generate near transform-limited red pulses.

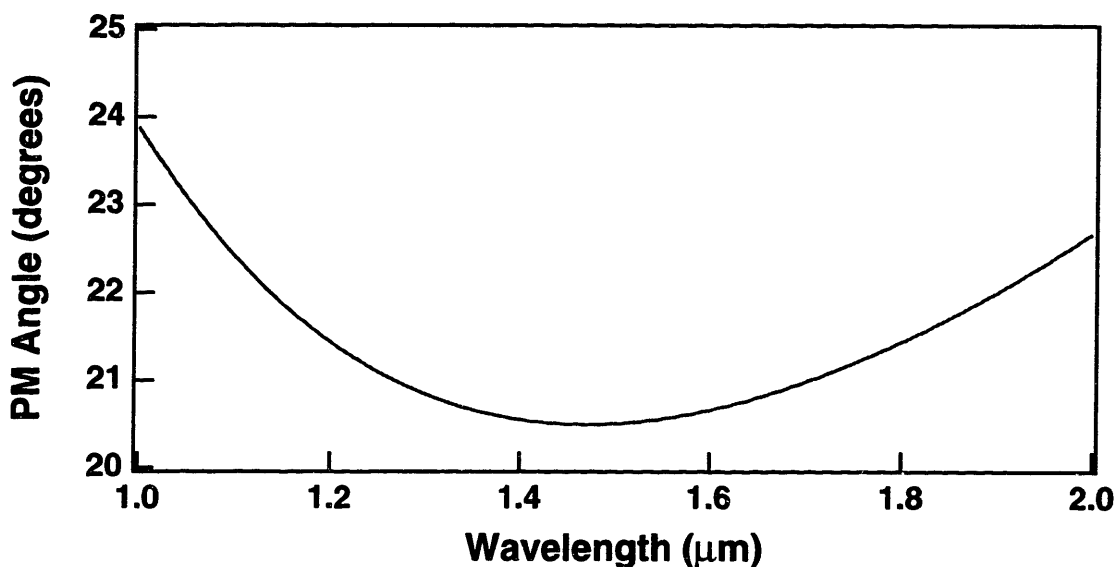


Figure 4-5: Plot of the Type I phase-matching angle for second harmonic generation in BBO.

Although the 1 cm BBO crystal was relatively long, spectral narrowing did not occur due to the  $> 40$  nm phase-matching bandwidth at  $1.55 \mu\text{m}$ . (Phase-matching bandwidth is defined here as a single-sided bandwidth and is the wavelength offset from the peak of the spectrum at which the SHG conversion efficiency is zero; i.e.  $\lambda$  at which  $\Delta k(\lambda) = 2\pi/\ell_c$  where  $\ell_c$  is the crystal length.) This was verified by comparing the spectrum of the frequency-doubled pulses generated in the 1 cm BBO crystal with that from a 1.5 mm crystal using the same 75-mm lens (confocal parameter  $2z_0 = 5.6$  mm). The frequency-doubled pulses from the 1 cm and 1.5 mm BBO crystals had the exact same spectrum as shown in Fig. 4-7. Although the SHG beam exiting the crystal was slightly astigmatic and elliptical due to spatial walkoff, the astigmatism and ellipticity had opposite signs and thus could be compensated by placing a single cylindrical lens at approximately 50 cm from the crystal where the beam profile was circular. In working with the system, it was observed that due to the high index of silicon, the compressed pulse beam quality and SHG conversion efficiency depended critically on matched prisms and prism alignment.

Frequency doubling was also performed with a 1.5 mm  $\text{KNbO}_3$  (potassium niobate) crystal, which has a larger nonlinear coefficient than BBO, and with a 7 mm  $\text{LiB}_3\text{O}_5$  (LBO) crystal, which can be temperature tuned for 90-degree phase matching

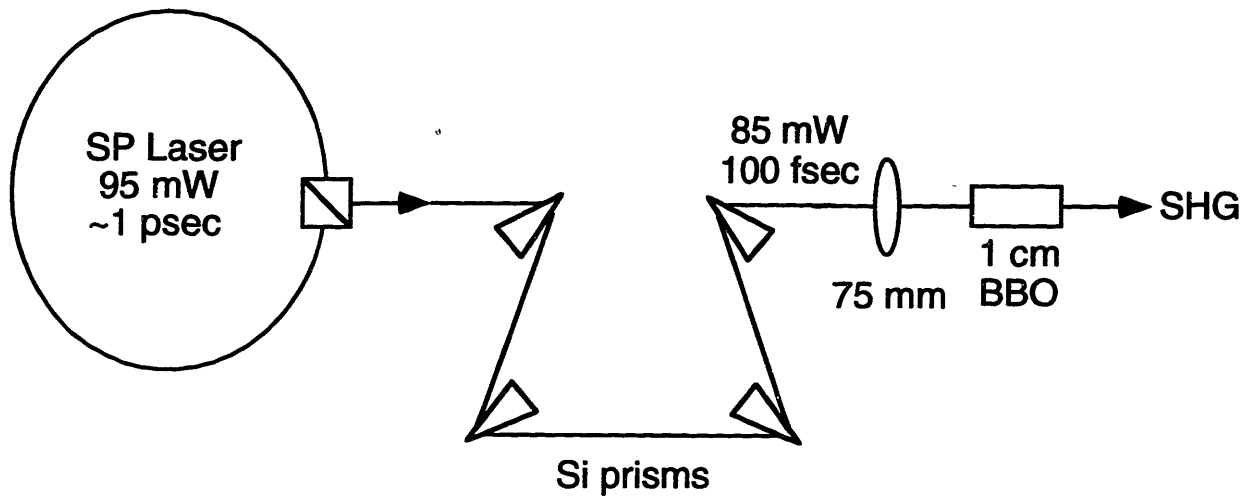


Figure 4-6: Experimental setup for frequency doubling the stretched-pulse (SP) fiber laser. Two other crystals,  $\text{KNbO}_3$  and LBO, were also tested in place of the BBO.

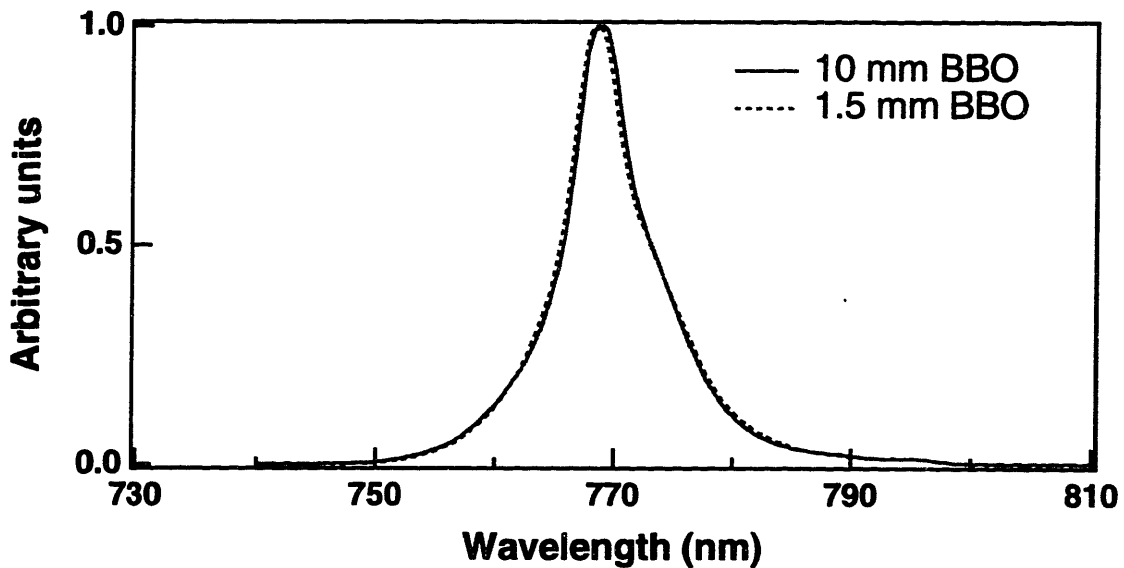


Figure 4-7: Comparison of frequency-doubled spectra from the 10 mm BBO crystal (solid) and the 1.5 mm BBO crystal (dashed).

with no spatial walkoff. Although conversion efficiencies of 3% and 6% were achieved for the LBO and potassium niobate, respectively, spectral narrowing occurred in both crystals due to group-velocity mismatch. For potassium niobate the phase-matching bandwidth at  $1.55 \mu\text{m}$  is only  $\approx 14 \text{ nm}$  for a  $1.5 \text{ mm}$  crystal length [103]. SHG pulses from this crystal were  $180 \text{ fsec}$  with spectral width of  $4.6 \text{ nm}$ . The LBO crystal was found to be 90-degree phase-matched at temperatures between  $14$  and  $18$  degrees Celsius (depending on alignment), a result that differs significantly from predictions of the temperature for frequency doubling of  $1.55 \mu\text{m}$  based on index data from [104]. The frequency-doubled pulses from LBO were  $170 \text{ fsec}$  and had spectral width of  $4.9 \text{ nm}$ . The doubled spectra from the different crystals are compared in Fig. 4-8, while Table 4.1 summarizes the doubling results from the three different crystals.

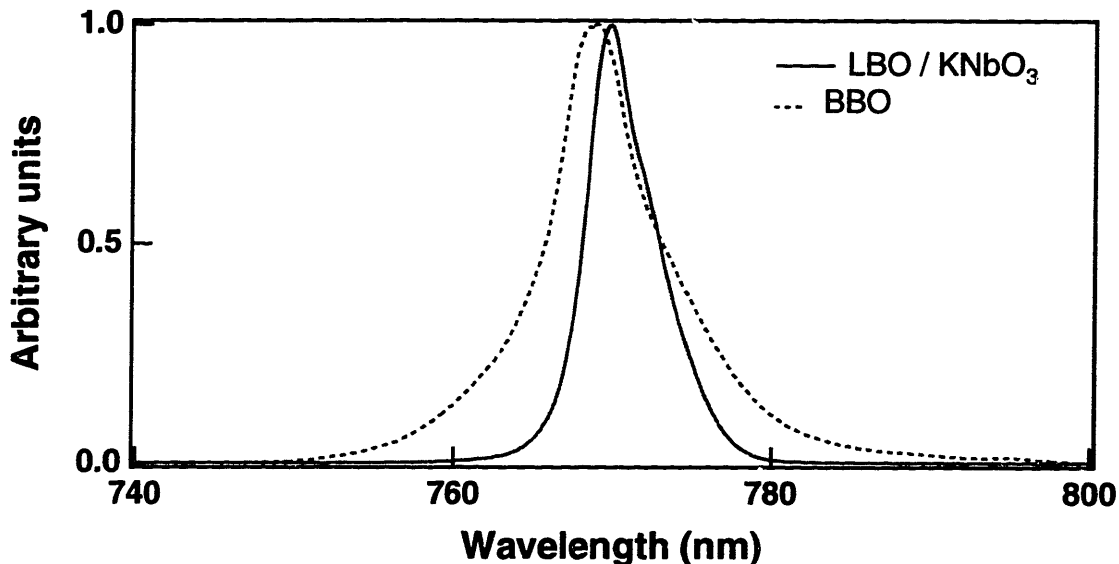


Figure 4-8: Frequency-doubled spectra from the  $10 \text{ mm}$  BBO crystal (solid) and from the  $1.5 \text{ mm}$   $\text{KNbO}_3$  and  $7.0 \text{ mm}$  LBO crystals (dashed). The spectra from the  $\text{KNbO}_3$  and LBO were essentially identical.

### 4.3 Frequency-resolved optical gating measurements

As shown in Fig. 4-4 the doubled pulse spectrum is offset from the center of the fundamental spectrum. This offset was explored by performing frequency-resolved optical gating (FROG) measurements [105,106] on both the fundamental and frequency-doubled pulses. FROG allows the direct determination of the intensity and phase profile of an ultrashort pulse. In traditional FROG measurements, the output pulse of the laser is split into two with a variable delay and then intersected in a  $\chi^{(3)}$  nonlinear medium to use the Kerr effect [107]. The signal-pulse electric field is then

$$E_{\text{sig}}(t, \tau) \propto E(t)|E(t - \tau)|^2, \quad (4.1)$$

Crystal	BBO	KNbO <sub>3</sub>	LBO
Phase-Matching	Type I (angle)	Type I (angle)	90 degree (temp.)
$d_{eff}$	$\approx 0.056$ pm/V	$\approx 9.0$ pm/V	$\approx 1.2$ pm/V
Length	10 mm	1.5 mm	7.0 mm
Conversion Efficiency	10%	6%	4%
770 nm Pulse Width	86 fsec	180 fsec	170 fsec
770 nm $\Delta\lambda$	7.3 nm	4.6 nm	4.9 nm
770 nm $\Delta\nu\Delta\tau$	0.32	0.42	0.42

Table 4.1: Comparison of the frequency-doubling results obtained with the BBO, KNbO<sub>3</sub>, and LBO crystals.

and the FROG trace is obtained by taking the spectrum of the signal pulse as a function of delay  $\tau$  between the two input pulses:

$$I_{\text{FROG}}(\omega, \tau) \propto \left| \int_{-\infty}^{\infty} E_{\text{sig}}(t, \tau) \exp(-i\omega t) dt \right|^2. \quad (4.2)$$

When displayed as a contour plot of intensity versus time delay  $\tau$  and frequency  $\omega$ , the FROG trace is essentially a plot of instantaneous frequency as a function of time and thus explicitly shows the chirp across the pulse. By using an iterative fast-Fourier-transform algorithm, the pulse amplitude and phase profile can be derived from the FROG trace.

When the pulse energy is less than  $\sim 50$  nJ, as is the case for the stretched-pulse laser, third-order nonlinearities generate insufficient signal strength for FROG measurements. A  $\chi^{(2)}$  material, though, can be used in place of the  $\chi^{(3)}$  material to obtain Second Harmonic Generation (SHG) FROG measurements. The SHG FROG trace is taken by measuring the spectrum of the SHG as the pulse delay is changed in a background-free autocorrelation configuration, as shown in Fig. 4-9. The electric field of the signal-pulse is

$$E_{\text{sig}}(t, \tau) \propto E(t)E(t - \tau), \quad (4.3)$$

as opposed to eqn. (4.1), and the FROG trace can be found by substituting the appropriate  $E_{\text{sig}}$  for SHG into eqn. (4.2). Fig. 4-10 shows contour plots of two SHG FROG traces which were numerically calculated. The first trace shows an unchirped gaussian pulse, while the second trace shows a gaussian pulse which is linearly chirped. One should note that by integrating along the frequency axis, we obtain the autocorrelation of the pulse. The frequency scan at  $\tau = 0$  is the spectrum of

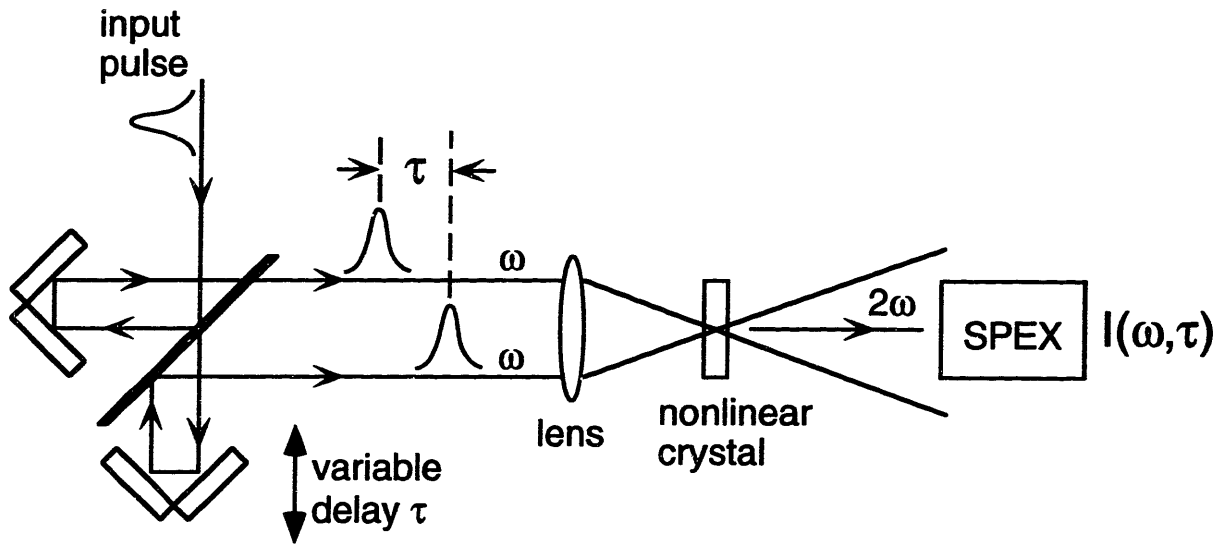


Figure 4-9: Experimental setup for measurement of SHG FROG. The spectrum of the SHG is measured as the pulse delay is changed in a background free autocorrelator.

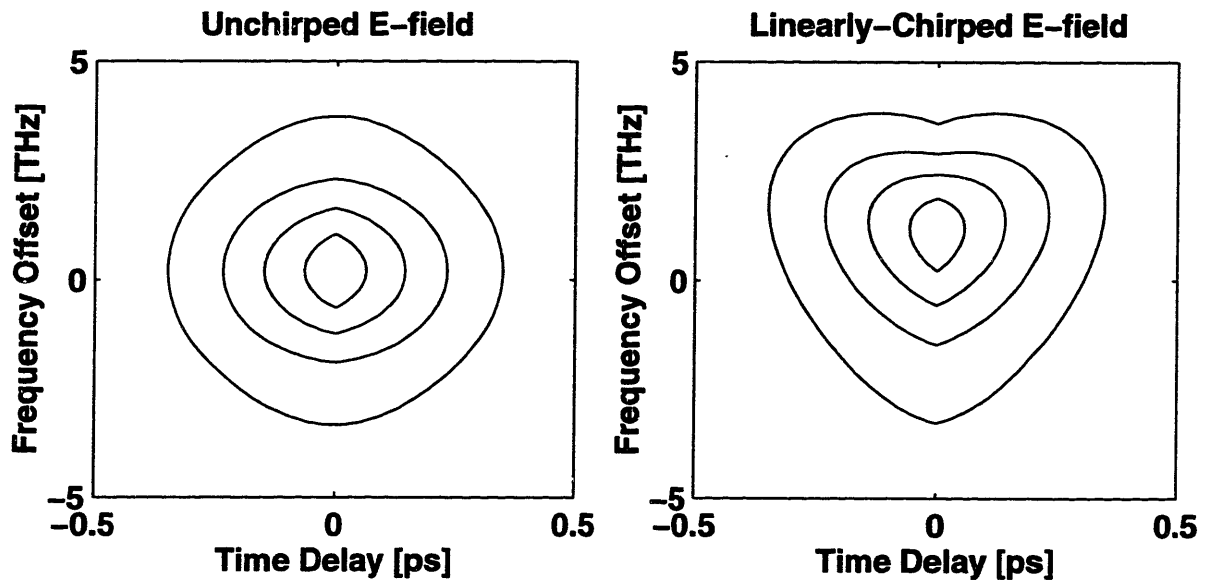


Figure 4-10: Numerical SHG FROG traces of an unchirped gaussian pulse (left) and a chirped gaussian pulse (right). The SHG intensity is plotted versus time delay and frequency offset, where zero frequency offset corresponds to the peak of the spectrum.

the SHG produced in the nonlinear crystal. The SHG FROG trace must be symmetric about the time axis.

A disadvantage of SHG FROG is that the trace is symmetric about the time axis  $\tau$ :  $I_{\text{FROG}}(\omega, \tau) = I_{\text{FROG}}(\omega, -\tau)$ . This symmetry causes an ambiguity in the direction of time in the derived electric field, so  $E(t)$  and  $E^*(-t)$  yield the same FROG trace. For example, a pulse with positive linear chirp has the same SHG FROG trace as a pulse with an equal negative linear chirp, and so when the fitting algorithm is applied, we will not know whether we have derived the pulse amplitude and phase profile  $E(t)$  or its time-reversed replica  $E(-t)$ . The ambiguity is less of a problem in cases where we have some knowledge about the pulse chirp or when we can make a second SHG FROG measurement after adding a known phase distortion to the pulse.

Fig. 4-11 shows experimental SHG FROG data for a 72-fsec fundamental pulse with grating compression (150 lines/mm grating) along with the best calculated fit, obtained using the generalized projections algorithm [108,109]. A full description of the algorithm appears in [108,109] and will not be reproduced here.<sup>1</sup> The experimental data was obtained using a 0.1 mm BBO crystal in the autocorrelator with a 50 mm lens. The wavelength span was from 740 nm to 810 nm with 0.05 nm increments, and the time delay was scanned from -1 psec to + 1 psec in 6.7 fsec steps. Wavelength data was then interpolated in the frequency domain and the final grid size was 256 points in frequency by 256 points in time. The algorithm was run on a SUN Sparc Station 4 and converged in  $\approx 100$  iterations, depending on the initial guess.

The SHG FROG trace in Fig. 4-11 indicates that the lower frequency components are contained in the pulse wings, and thus efficient frequency doubling occurs at shorter wavelengths. This explains why the SHG spectrum is centered at 771 nm rather than at 776 nm, which would be predicted based on the first moment of the fundamental spectrum. The calculated pulse intensity and phase profiles in Fig. 4-12 show that the phase is nearly flat across the central region of the pulse, indicating that the linear chirp was almost completely compensated in this region. Next, to check if all the linear chirp had been compensated with the grating compression, group-velocity dispersion was numerically added (and subtracted) to the derived pulse phase. With an added dispersion of  $-0.0008 \text{ ps}^2$ , the pulse phase profile was flat across the pulse and the pulse width was shortened to 67 fsec compared to the 72-fsec pulse width which was experimentally obtained. Fig. 4-13 compares this (numerically) optimally compressed pulse with the derived pulse from the experiment. A plot of the pulse width as a function of the (numerically) added dispersion is shown in Fig. 4-14. This analysis confirmed that the SHG FROG data was taken when the pulse was quite close to being optimally compressed.

An important consideration in SHG FROG measurements is the possibility that significant group-velocity mismatch (GVM) between the fundamental and SHG beams may occur in the doubling crystal. GVM will result in incomplete conversion of the entire fundamental spectrum to SHG, and thus the SHG FROG trace will not accurately represent the actual fundamental pulse. Fig. 4-15 compares the experimental 1.55  $\mu\text{m}$  spectrum with the Fourier transform of the calculated pulse intensity and

---

<sup>1</sup>The author is grateful to Siegfried Fleischer for his work on the SHG FROG fitting programs.



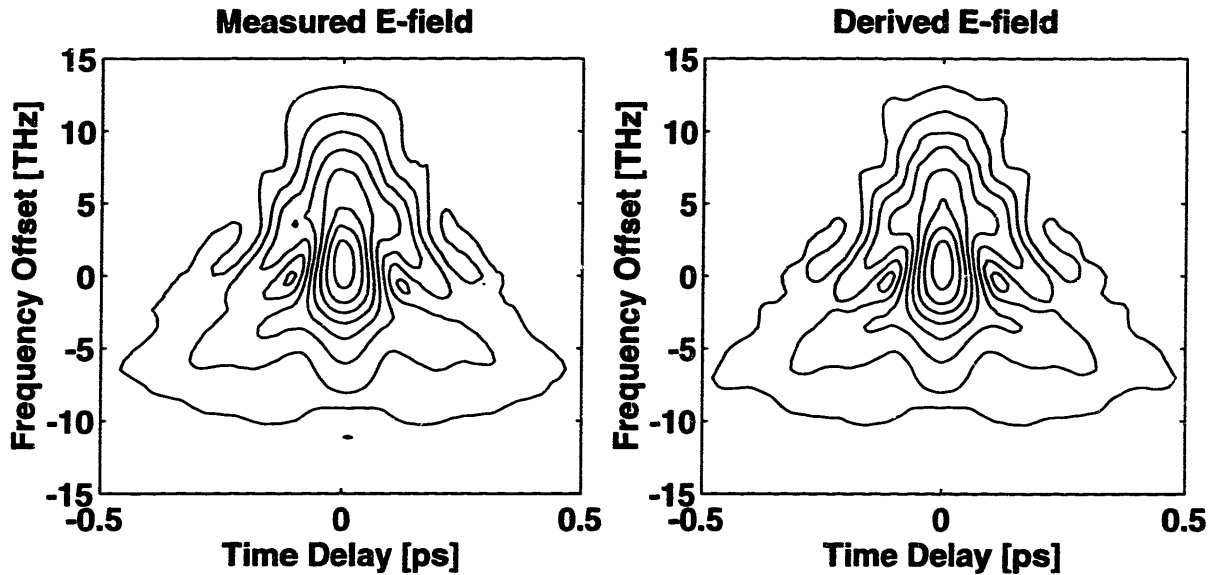


Figure 4-11: SHG FROG traces of the 1.55  $\mu\text{m}$  pulse which was compressed to 72 fsec with gratings. The contour plot on the left shows the experimentally-measured trace, while the right-hand plot shows the calculated fit using the method of generalized projections.

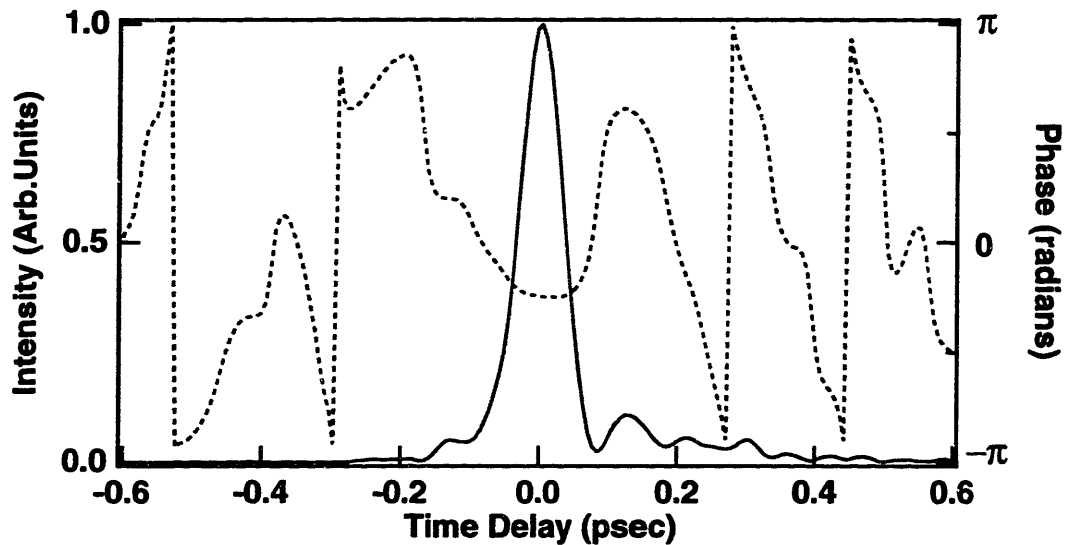


Figure 4-12: Derived 1.55  $\mu\text{m}$  pulse intensity and phase profile based on the FROG fit from Fig. 4-11.

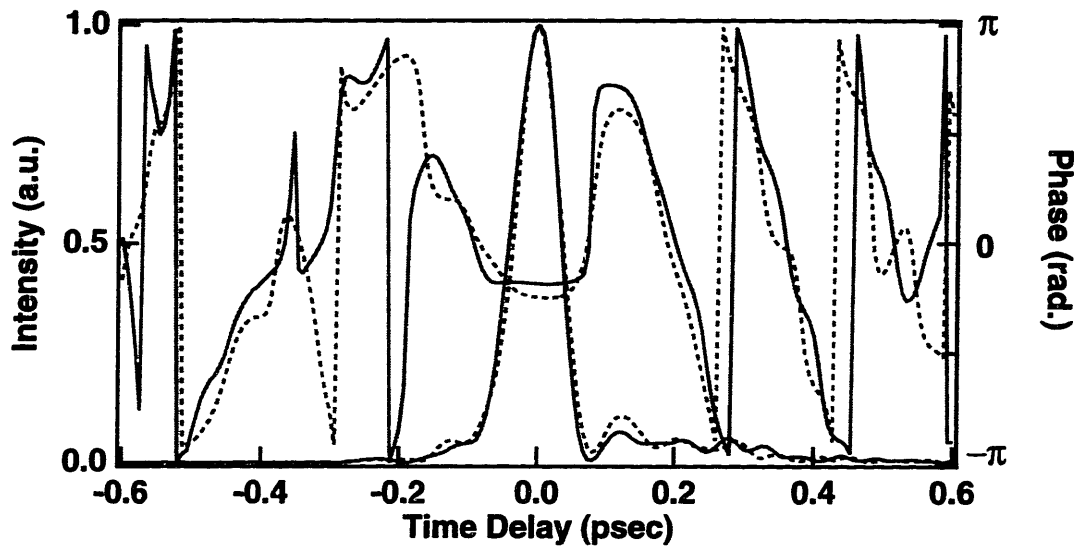


Figure 4-13: Comparison of the  $1.55 \mu\text{m}$  pulse intensity and phase profiles from the derived fit of the experimental pulse (dashed) and when dispersion of  $-0.0008 \text{ ps}^2$  was numerically added to obtain the optimally compressed pulse (solid).

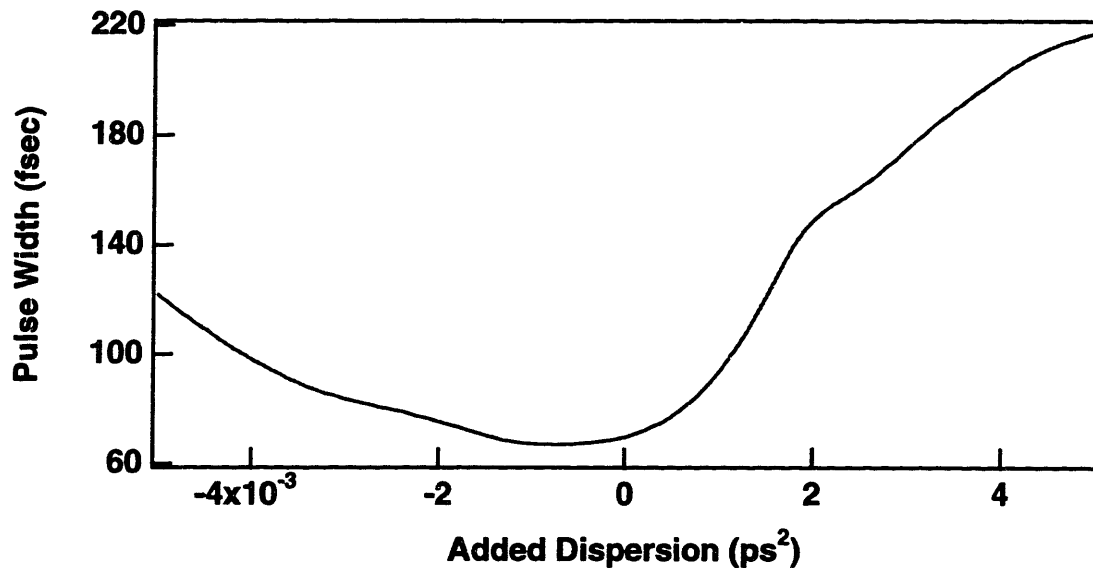


Figure 4-14: Plot of  $1.55 \mu\text{m}$  pulse width versus (numerically) added dispersion, which shows that the minimum pulse width of 67 fsec occurs for an added dispersion of  $-0.0008 \text{ ps}^2$ .

phase from Fig. 4-12. There was excellent agreement indicating that no filtering occurred in the grating compressor or BBO crystal.

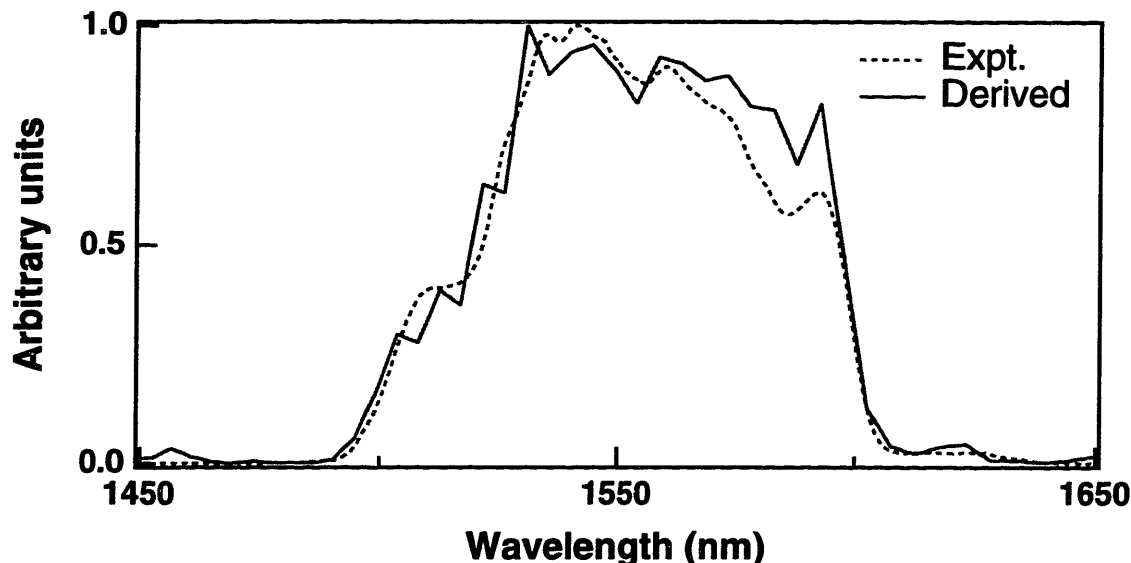


Figure 4-15: Comparison of the experimentally measured  $1.55 \mu\text{m}$  spectrum (dashed) with the derived spectrum from the SHG FROG measurement (solid).

Although the fundamental pulses had as much as 25% of the total energy in the uncompressed wings, the corresponding frequency-doubled pulses had less than 1% of the total pulse energy in the non-sech wings. Fig. 4-16 shows the fundamental pulse autocorrelation on a log-scale while Fig. 4-17 shows the frequency-doubled pulse autocorrelation. Both traces were obtained by double chopping in a background-free autocorrelator and detecting the difference frequency. The autocorrelation of the frequency-doubled pulses showed that the pulse followed a sech for more than two orders of magnitude, and for delays greater than 1 psec, the pulse wings were smaller than our measurement background of  $10^{-5}$ . The peak-to-background contrast ratio of  $\approx 10^5$  for both the fundamental and frequency-doubled pulses is one of the advantages of the stretched-pulse laser over soliton lasers, which typically have backgrounds at  $10^{-3}$  below the peak due to continuum generation. To further confirm the high pulse quality of the frequency-doubled output, an SHG FROG measurement was performed on the frequency-doubled pulses. The measurement was taken in a similar background-free autocorrelator setup as in Fig. 4-9 with a 1.5 mm BBO crystal and 15 cm lens. The FROG trace as shown in Fig. 4-18 was nearly round and smooth, and the calculated phase profile was flat across the entire pulse.

#### 4.4 Noise measurements

The pulse-to-pulse energy and timing fluctuations of a mode-locked laser can be characterized by measuring the power spectrum of the laser intensity as first proposed by von der Linde [110]. If the output fluctuations are assumed to be slowly varying

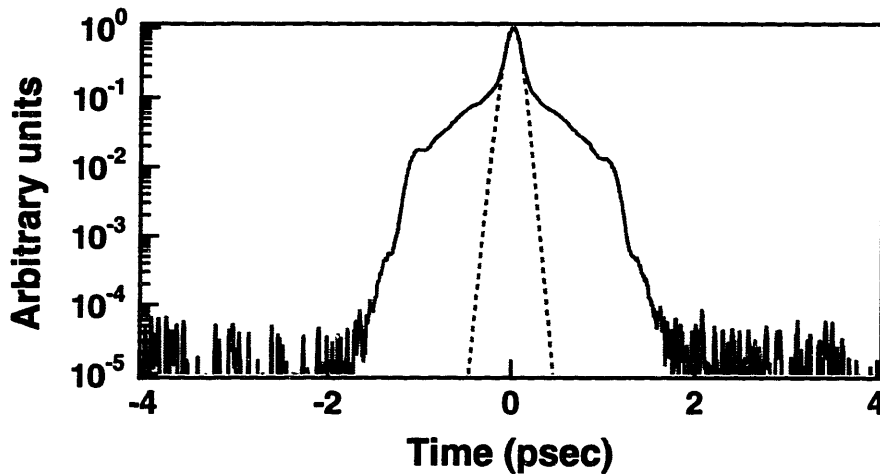


Figure 4-16: Autocorrelation of the fundamental pulse plotted on a log scale to show the peak-to-background ratio of  $\approx 10^5$  for time delays  $> 2$  psec.

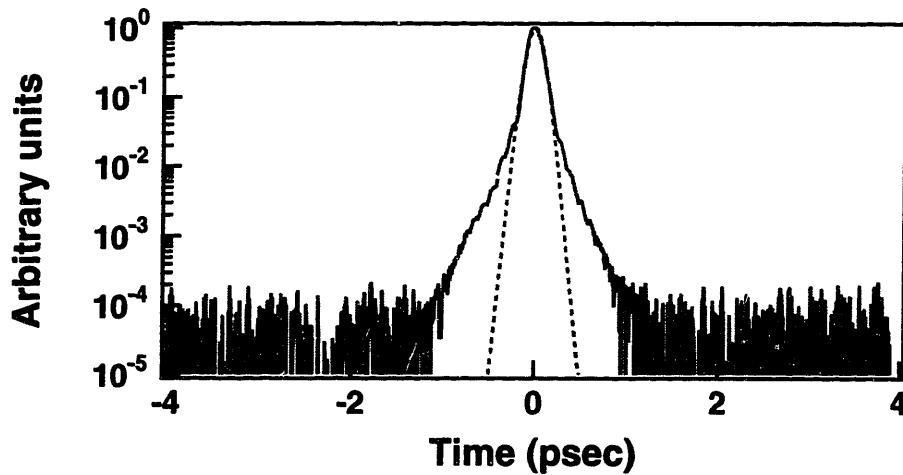


Figure 4-17: Autocorrelation of the frequency-doubled pulse plotted on a log scale to show the reduction in pulse wings from the fundamental pulse.

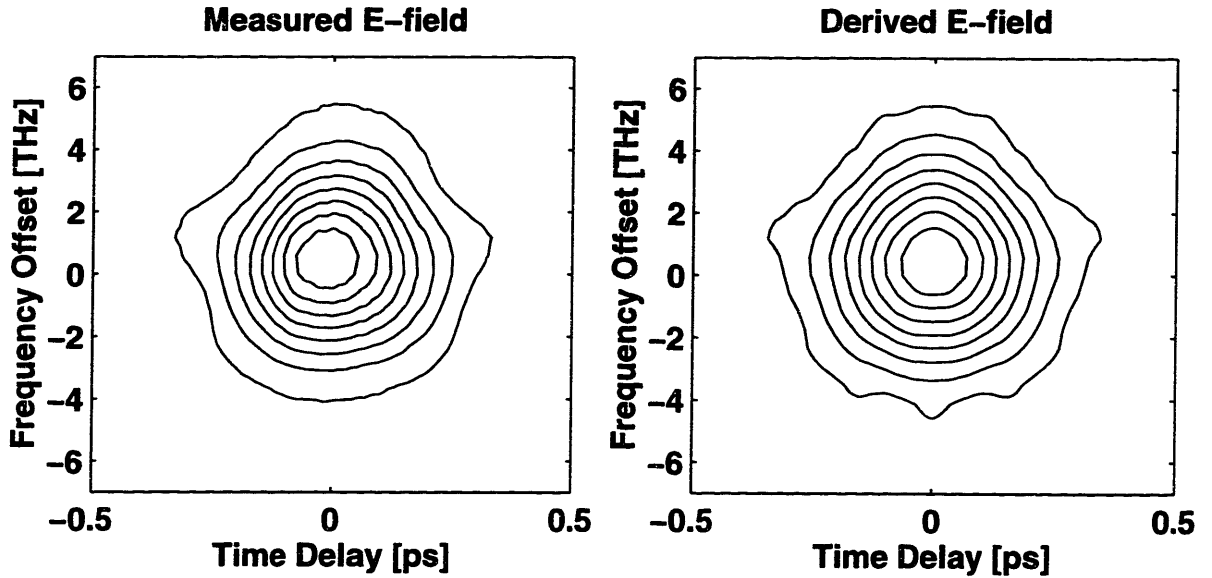


Figure 4-18: SHG FROG traces of the frequency-doubled pulse. The contour plot on the left shows the experimentally-measured trace, while the right-hand plot shows the calculated fit.

in comparison to the pulse intensity  $f(t)$ , the noisy laser intensity can be expressed as

$$F(t) = F_0(t) + F_0(t)A(t) + \dot{F}_0(t)TJ(t) \quad (4.4)$$

where  $F_0(t)$  is the output intensity of a perfectly mode-locked laser. The coefficient  $A(t)$  is a random function which represents the relative deviation from the average pulse energy, and so the second term represents amplitude noise, while the third term represents fluctuations in the repetition time of the pulses. ( $\dot{F}_0(t)$  is the time derivative of the laser intensity in the absence of noise, and  $J(t)$  is a random function of time representing the relative deviation from the average pulse repetition time  $T$ .) We can find the power spectrum of the laser intensity  $F(t)$  by taking the Fourier transform of the autocorrelation function:

$$P_F(\omega) = P_{F_0}(\omega) * [\delta(\omega) + P_A(\omega)] + [(\omega T)^2 P_{F_0}(\omega)] * P_J(\omega) \quad (4.5)$$

where  $P_A(\omega)$  and  $P_J(\omega)$  are the power spectra of  $A(t)$  and  $J(t)$ , respectively. Substituting the power spectrum of a perfectly mode-locked pulse train for  $P_{F_0}$ , the power spectrum of the noise laser intensity is finally given by

$$P_F(\omega) = (2\pi/T)^2 |f(\omega)|^2 \sum_{\mu} [\delta(\omega_{\mu} + P_A(\omega_{\mu})) + (2\pi\mu)^2 P_J(\omega_{\mu})] \quad (4.6)$$

where  $\omega_{\mu} = (\omega - 2\pi\mu/T)$  and  $\mu$  is an integer running from minus to plus infinity.

The noise power spectrum in eqn. (4.6) is a series of frequency bands centered at  $\omega_{\mu}$  with constant spacing  $\Delta\omega = 2\pi/T$ . The first term in the sum represents the

perfect noise-free pulse train, while the second term is the frequency-shifted power spectrum of the amplitude noise. The third term represents the timing jitter and is proportional to  $\mu^2$  where  $\mu$  is the harmonic. It is then clear that the amplitude noise can be directly determined by measuring the power spectrum around  $\omega = 0$ , where  $\mu = 0$  and the timing jitter is zero.

The Relative Intensity Noise (RIN) spectrum of the frequency-doubled pulses from the stretched-pulse laser was measured using a spectrum analyzer and a fast photo-diode, and is defined as

$$\text{RIN (dBc/Hz)} = 10 \log \left( \frac{N}{P_s} \right) \quad (4.7)$$

where  $N$  is the noise spectral density and  $P_s$  is the signal power. The RF spectrum was measured between 10 Hz and 100 kHz and compared with a similar measurement made in our lab on a commercial mode-locked Ti:Sapphire laser which was pumped by an argon-ion laser. As shown in Fig. 4-19, under normal laboratory conditions, the RF spectra showed that the amplitude fluctuations on the frequency-doubled pulses roll off more quickly and were at -138 dBc/Hz at 100 kHz. The Ti:Sapphire noise is typically at least 40 dBc/Hz higher over the range from 3 kHz to 100 kHz, and our measurement corresponded well with that reported in [111]. The difference in noise spectra is caused by the different upper state lifetimes of the two gain media. (The medium's response to amplitude modulation rolls off rapidly for frequencies greater than the inverse upper-state lifetime of the gain medium.) Erbium has a relatively long lifetime of  $\approx 10$  msec, implying that the noise of the frequency-doubled pulses should roll off around 100 Hz, as shown in Fig. 4-19. Ti:sapphire, on the other hand, has a 3.2  $\mu$ sec so the noise will not roll off until the frequencies are as high as 300 kHz. Pumping the Ti:Sapphire laser with an all-solid-state green source may reduce the amplitude noise. Nevertheless, the SP-APM laser's excellent amplitude noise characteristics reported in this thesis and phase noise characteristics reported in [112] are an added benefit to its use in high-repetition-rate amplifier seeding and pump-probe measurements.

## 4.5 Technology transfer

Due to the high power, low noise, and diode-pumped operation of the stretched-pulse laser and the efficient frequency doubling which can be achieved, Clark MXR, Inc. (a laser company in Dexter, MI) licensed the technology from MIT in 1995. With funding from a Small Business Innovation Research (SBIR) grant from NIST, the company developed a commercial product in collaboration with our group at MIT. This involved working with the engineer at Clark to optimize the laser mount design and doubling crystal. A prototype was built at MIT and eventually sent to Clark for final testing and packaging. The commercial product based on the stretched-pulse laser (ErF) is specified to deliver 120 fsec pulses at 1.55  $\mu$ m with  $> 50$  nm bandwidth and average powers  $> 50$  mW, while the frequency-doubled version (SErF) is specified to deliver 100 fsec pulses at 775 nm with average powers  $> 5$  mW. Both

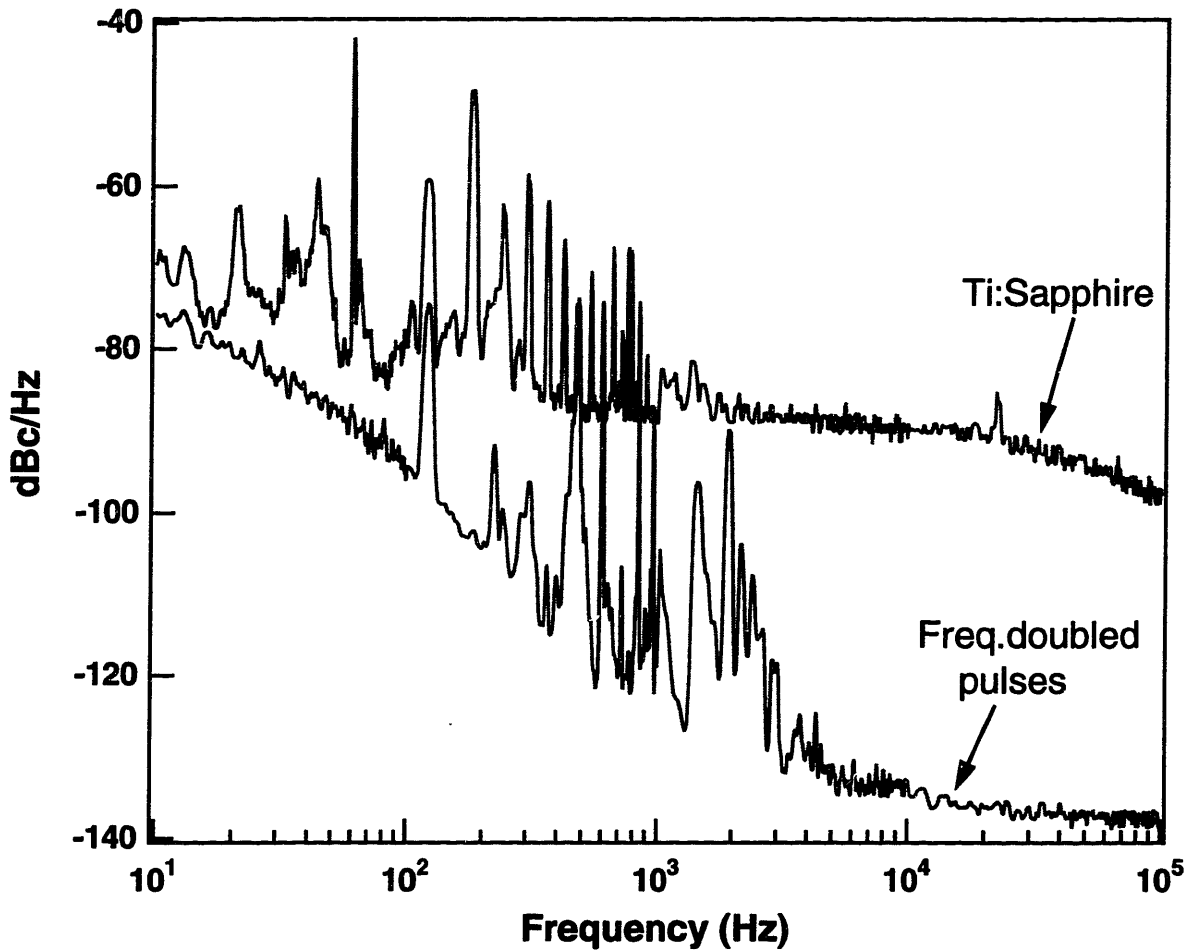


Figure 4-19: Low frequency RF spectrum (10 Hz to 100 kHz) of the frequency-doubled pulses compared to a commercial argon-pumped mode-locked Ti:sapphire laser. The y-axis is in units of dBc/Hz.

products are packaged in a 24" L × 12" D × 8" H case which is wall-plug and requires no water. Clark has demonstrated use of the SErF as a seed source for their commercial Ti:Sapphire regenerative amplifier system. The SErF sells for ≈ \$60,000 which is considerably less expensive than a commercial argon-pumped, mode-locked Ti:Sapphire laser at > \$100,000.

## 4.6 Comparison of doubling with different net dispersions of stretched-pulse lasers

Initial experiments of frequency doubling the stretched-pulse laser were performed with a net dispersion  $(k''\ell)_{net}$  of +0.042 ps<sup>2</sup> using a 1.72-meter piece of Er<sup>3+</sup>-doped fiber and 3.72 meters of SMF-28 fiber (versus 4.53 meters for the experiments reported in this chapter with  $(k''\ell)_{net} = +0.013$  ps<sup>2</sup>). This laser was operating with a higher net dispersion than that shown in Fig. 4-2 in an attempt to achieve the highest pulse energies. Self-starting mode-locking was achieved with output powers and compressed pulse widths which were similar to the laser with  $(k''\ell)_{net} = +0.013$  ps<sup>2</sup>. Table 4.2 compares the 1.55 μm pulse characteristics and frequency-doubling results of the two lasers (using a 1-cm, uncoated BBO crystal). As shown in the Table, although the average output power at 1.55 μm is the same, the lower repetition rate of the laser with  $(k''\ell)_{net} = +0.013$  ps<sup>2</sup> results in a higher 1.55 μm pulse energy and thus higher frequency-doubled powers. The SHG conversion efficiency was also affected by greater energy in the compressed pulse wings for the laser with  $(k''\ell)_{net} = +0.042$  ps<sup>2</sup>, as shown in Fig. 4-20 which should be compared to the 1.55 μm autocorrelation in Fig. 4-3. Higher  $(k''\ell)_{net}$  causes increased nonlinear chirp and a poorer pulse spectrum (as compared to Fig. 4-4) which results in a larger fraction of the compressed pulse energy in the non-sech wings and lower doubling efficiencies. These results indicate that operating with  $(k''\ell)_{net} \approx +0.1$  (slightly positive) will result in higher-quality 1.55-μm pulses and better SHG conversion.

## 4.7 Summary

In summary, a stretched-pulse erbium-doped fiber laser was optimized for frequency doubling and three nonlinear crystals were evaluated. Compressed fundamental pulses of 100 fsec and 2.7 nJ were generated. Sub-100 fsec pulses at 771 nm were generated with average powers of 8.7 mW at 31.8 MHz, corresponding to conversion efficiencies of up to 10%. SHG FROG measurements showed that frequency-doubling selects the part of the fundamental pulse which is un-chirped, resulting in an easily visible red beam of near transform-limited pulses which can be used for aligning and seeding a Ti:Sapphire regenerative amplifier. Amplitude noise measurements performed on the frequency-doubled pulses show significant improvement over a commercial argon-pumped mode-locked Ti:Sapphire laser.



Stretched-Pulse Laser Net Dispersion	+0.041 ps <sup>2</sup>	+0.013 ps <sup>2</sup>
$F_{rep}$	35.2 MHz	31.8 MHz
Self-starting Threshold	$\geq 300$ mW	200 mW
Output Power	95 mW	95 mW
Pulse Energy	2.7 nJ	3.0 nJ
at Pump Power	500 mW	500 mW
Spectral Width	$\approx 70$ nm	$\approx 61$ nm
Compressed Pulse Width (grating)	83 fsec	72 fsec
$\Delta\nu\Delta\tau$	0.73	0.55
Compressed Pulse Width (prism)	102 fsec	108 fsec
$\Delta\nu\Delta\tau$	0.89	0.82
$E_{wing}/E_{pulse}$	0.32	0.20
Power after Prisms	88 mW	89 mW
SHG Power	7.5 mW	8.3 mW
SHG Pulse Energy	210 pJ	260 pJ
Conversion Efficiency	8.5%	9.3%
SHG Pulse Width	73 fsec	86 fsec
SHG Spectral Width	8.5 nm	7.3 nm
SHG $\Delta\nu\Delta\tau$	0.31	0.32

Table 4.2: Comparison of the 1.55  $\mu\text{m}$  pulse characteristics and frequency-doubling results (using a 1-cm, uncoated BBO crystal) for the stretched-pulse lasers with net dispersion of +0.041 ps<sup>2</sup> and +0.013 ps<sup>2</sup>

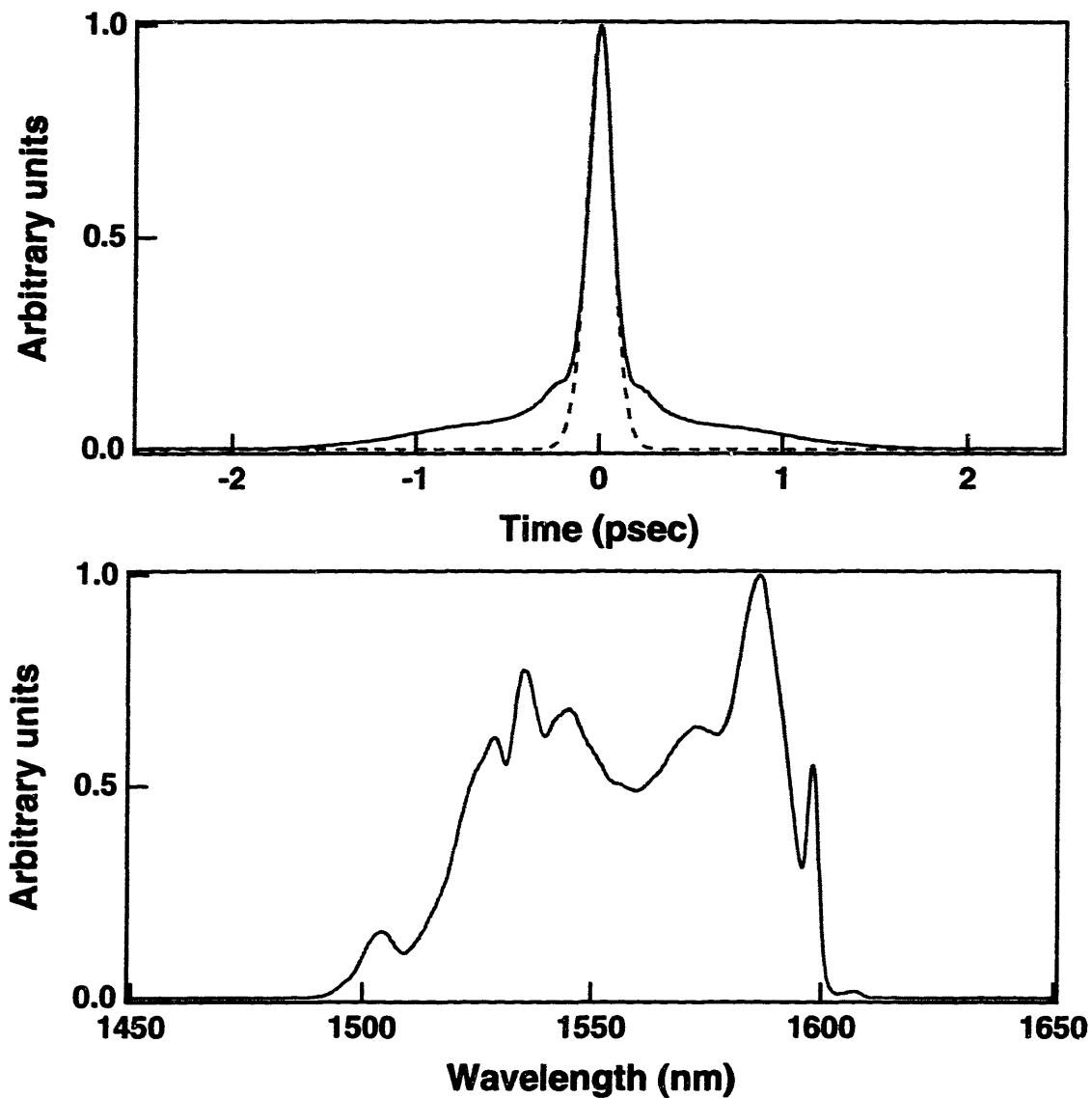


Figure 4-20: Pulsed operation of the stretched-pulse laser with net dispersion of  $+0.041 \text{ ps}^2$ . Top: Autocorrelation trace (solid) and sech fit (dashed) showing pulse wings which extended to  $> 2 \text{ psec}$  with 32% of the pulse energy contained in the non-sech wings, as compared to 20% for the laser with net dispersion of  $+0.041 \text{ ps}^2$  as shown in Fig. 4-3. Bottom: Pulse spectrum with spectral width of  $\approx 70 \text{ nm}$ .

## Chapter 5

# Effect of Linear Birefringence on P-APM

The lasers discussed in chapters 3 and 4 work well under standard laboratory conditions with no special precautions for temperature or humidity (the fiber is basically set out on the optical table). Once the bias settings for the waveplates are found, the laser will reliably start to pulsed operation for days at a time and will remain stably mode-locked for hours. The bulk components (waveplates, isolators, etc.) can be "hermetically sealed" to withstand demanding environmental conditions, and the recent surge in fiber-optic communications work has made these types of hermetic products inexpensive and available. Maintaining stable alignment of the cavity over long periods of time has now been greatly improved through the use of commercial collimators at the fiber ends. (The fiber ends are angle polished, anti-reflection coated, and aligned with a collimating lens in a sealed package.) Reliable long-term coupling of the MOPA pump to the WDM fiber may soon be possible through the use of a commercial fiber-coupled MOPA and a simple fusion splice from the MOPA fiber to the WDM coupler.

An unknown in these mode-locked fiber lasers, though, is the stability of the fiber itself. Since the mode-locking mechanism relies on the rotation of the elliptical polarization state in the fiber, the laser will self-start repeatably only if this polarization rotation remains constant over time for a particular input polarization state and intracavity power. Standard single-mode fiber, though, has a small and randomly-oriented birefringence which may change with temperature, stress due to coiling, or when the fiber position is altered. The sensitivity of the P-APM process to linear birefringence (or changing linear birefringence over time) in these fiber lasers has not been evaluated experimentally, and the theory of fiber lasers mode-locked by P-APM has thus far assumed that the fibers were isotropic [82]. Experiments at MIT have shown that if the standard single-mode fiber is coiled too tightly in fiber lasers such as those reported in chapters 3 and 4, mode-locking cannot be obtained, indicating that birefringence in the fiber can have a deleterious effect on the mode-locking process. Proposals for mode-locked fiber lasers which are environmentally stable, though, usually involve schemes that utilize polarization-maintaining (PM) fibers [113,114]. In preparation for the construction of an environmentally stable laser to be discussed

in chapter 6, this chapter includes a description of measurements of the birefringent beat-length both in standard single-mode fiber and in PM fiber in section 5.1 as well as a discussion of measurements of the temperature dependence of the birefringence in both fiber types in section 5.2. The effect of birefringence on P-APM was explored through numerical simulations and is discussed in section 5.3.

## 5.1 Measurement of fiber birefringence

A linearly birefringent fiber has eigenstates which are perpendicular linear polarizations and displays a different index of refraction for light which is polarized along the fast axis versus light polarized along the slow axis. Linearly polarized light along either eigen-axis will travel along the fiber at a speed determined by the index of refraction along that axis and will retain its polarization state. Light which is linearly polarized off-axis or elliptically polarized can be expressed as a sum of the eigenstates. As this light propagates, the eigenstates travel at different speeds and beat, resulting in a periodic change in the polarization state. The birefringent beat-length  $\ell_b$  is defined as this beat period, i.e. the distance over which the phase difference between the two eigenmodes accumulates to  $2\pi$ , and is determined from

$$(k_x - k_y) \ell_b = 2\pi \quad (5.1)$$

where  $k_x$  and  $k_y$  are the propagation constants of the eigenmodes along the slow and fast axes, respectively. With  $k_i = 2\pi n_i/\lambda$  for  $i = x, y$ , the beat-length becomes

$$\ell_b = \frac{\lambda}{(n_x - n_y)} = \frac{\lambda}{\delta n} \quad (5.2)$$

where  $\delta n$  is the index difference  $n_x - n_y$  between the slow and fast axes.

Birefringence in a fiber is caused by manufacturing irregularities such as slight ellipticity of the core or by induced stress on the core. Other causes include application of electric or magnetic fields which cause circular birefringence [115], thermal effects, air drafts, and noise [116]. Birefringence can be created by compressing the fiber which induces a fast axis in the direction perpendicular to the applied force [117]. This technique was used in the fiber laser reported in [113] to induce a slightly birefringent fiber with beat-length  $\approx 10$  cm. Linear birefringence is also induced in coiled fiber, where the bend in the fiber stretches the fiber on the outside of the curve and compresses the fiber on the inside of the curve. The outer layers exert pressure on the inner layers, creating linear birefringence which is proportional to the fiber radius and inversely proportional to the radius of curvature of the coil [118]. The fast axis is in the plane of the loop, while the slow axis is normal to the loop. By employing multiple turns around two or three coils and then twisting the coils, fiber wave-plates and polarization controllers can be formed [119,120].

Polarization-maintaining (PM) fiber has a large induced birefringence (beat-length  $\approx 4$  mm) due to an elliptical core/cladding, stress rods in the fiber cladding (Panda), or stress regions around the core (Bow tie). If light is launched in a single linear

polarization along one of the PM fiber axes, the light will maintain its linear polarization as it travels down the fiber, with cross-coupling to the orthogonal PM axis as low as -30 dB. The birefringence of PM fiber is so large that changes in environmental conditions have no effect on the location of the eigen-axes.

Knowledge of the fiber birefringence is important for understanding the operation of a fiber laser. For standard single-mode fibers, the beat-length is on the order of a meter or more, and so the birefringence can be determined through a simple cutback measurement. The large birefringence of PM fibers, though, implies a beat-length on the order of centimeters or less, and so a different technique must be used to measure the birefringence.

### 5.1.1 Cutback measurement of beat-length for non-PM fiber

The cut-back measurement involves launching circularly polarized light into a short piece of fiber and measuring the output polarization state as a function of the fiber length. Fig. 5-1 shows a diagram of the measurement set-up where a  $1.3 \mu\text{m}$  source was used for doped fibers ( $\text{Er}^{+3}$ -doped and  $\text{Tm}^{+3}$ -doped) so that no absorption occurred. After each cutback the intensity was measured along the semi-major axis ( $I_{max}$ ) and semi-minor axis ( $I_{min}$ ) of the elliptical polarization state. The aspect ratio  $c$  is then defined as

$$c = \frac{I_{max}}{I_{min}} \quad (5.3)$$

where  $c = 1$  for circular polarization and  $c \rightarrow \infty$  for linear polarization. By plotting the aspect ratio  $c$  versus fiber length we should see  $c$  vary periodically between 1 and a large number, where the distance between minimum values of  $c$  corresponds to one-half the beat-length  $\ell_b$  at the wavelength of the source. Fig. 5-2 shows the result of a beat-length measurement on  $\text{Tm}^{+3}$ -doped fiber CTm-158 with the  $1.3 \mu\text{m}$  source. Minima of  $c$  occur at  $\approx 12.5$  cm intervals, indicating a beatlength of  $\approx 25$  cm at  $1.3 \mu\text{m}$ . The index difference  $\delta n$  at  $1.3 \mu\text{m}$  can then be obtained from eqn. (5.2). If we then assume that the index difference does not vary considerably with wavelength, the beat-length at  $1.85 \mu\text{m}$  is estimated to be 35 cm using eqn. (5.2) again. Similar measurements on another  $\text{Tm}^{+3}$ -doped fiber, CTm-119, revealed a beat-length of only 17 cm at  $1.85 \mu\text{m}$ , indicating that the fiber probably had an elliptical core due to the manufacturing process. Measurements of standard telecommunications fiber, SMF-28, were more difficult because the birefringence was so low and the axes could have randomly changed orientation over the length of fiber. Measurements showed the beat-length to be on the order of 4 to 8 meters.

### 5.1.2 Birefringent filter measurement for PM-fiber

In PM fibers, the index difference  $\delta n$  is  $\sim 10^{-4}$ , resulting in a beat-length  $\ell_b \sim 1$  cm at  $1.55 \mu\text{m}$ . The cut-back method described in the previous section cannot be used since it is difficult to cleave less than 1.5 cm from the fiber end, and so aliasing would occur in a cut-back measurement. An alternate method to measure the birefringence is to set up the PM fiber between two polarizers as a birefringent filter (Lyot filter),

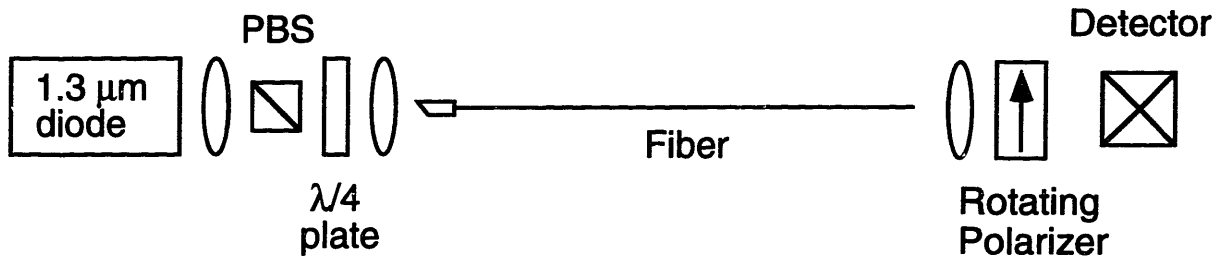


Figure 5-1: Experimental set-up for cut-back measurement of non-PM fibers. A circularly polarized source is launched into the fiber, and the polarization state is monitored at the end of the fiber as a function of fiber length.

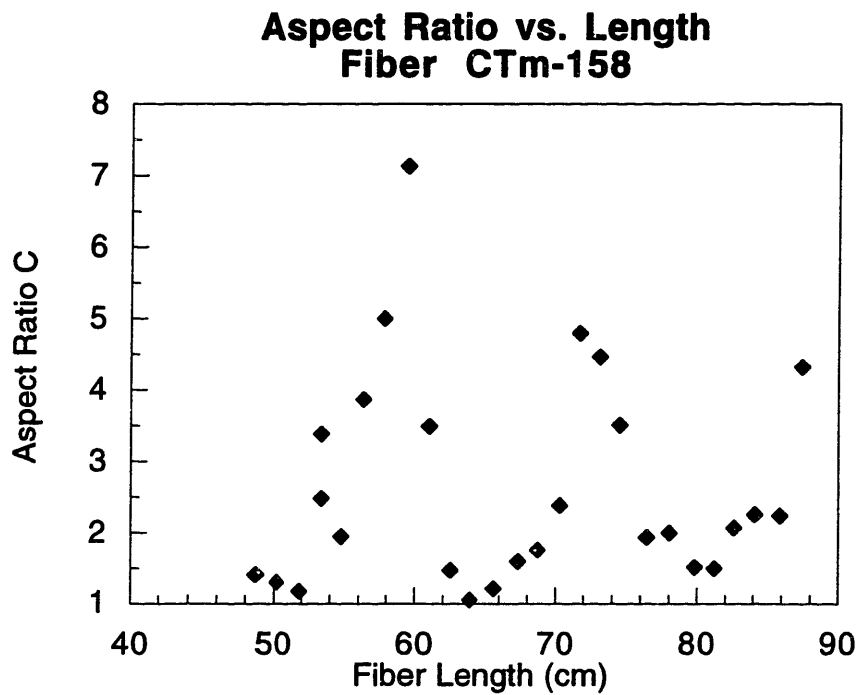


Figure 5-2: Results of cutback measurement for the beat-length of fiber CTm-158 with a launched  $1.3 \mu\text{m}$  source. At  $1.85 \mu\text{m}$  the beat-length is approximately 35 cm.

as shown in Fig. 5-3. A broadband light source is launched at 45 degrees to the birefringent axes of the fiber. The polarization state of the light at the end of the fiber is wavelength-dependent, since the beat-length is wavelength-dependent, as seen from eqn. (5.2), where we again assume that  $\delta n$  is essentially independent of wavelength over the bandwidth of the source. The output polarizer then completes the filter by attenuating all wavelengths except those wavelengths for which the fiber length is exactly an integer number of beat-lengths. Mathematically, the transmission of the filter can be shown to be

$$T(\lambda) = 1 + 2 \cos^2 \theta \sin^2 \theta [\cos(\Delta\phi) - 1] \quad (5.4)$$

where  $\theta$  is the angle between the input polarization and the birefringent axis and is set to  $\pi/2$  for maximum extinction. The phase difference  $\Delta\phi$  is defined as

$$\Delta\phi = \frac{2\pi}{\lambda} (n_x - n_y) L = 2\pi \frac{L}{\ell_b} \quad (5.5)$$

where  $L$  is the fiber length and  $\ell_b$  is the beat-length.

The filter free-spectral range (FSR) is defined as the wavelength separation between two transmission maxima and can be found by setting  $2\pi = \Delta\phi(\lambda_1) - \Delta\phi(\lambda_2)$  and solving for the  $\text{FSR} = \lambda_2 - \lambda_1$ . This yields

$$\text{FSR} = \lambda_2 - \lambda_1 = \frac{\lambda_1 \lambda_2}{(n_x - n_y) L} \quad (5.6)$$

such that by assuming  $\lambda_1 \approx \lambda_2 \approx \lambda$ , the free spectral range becomes

$$\text{FSR} = \frac{\ell_b \lambda}{L}. \quad (5.7)$$

Thus by measuring the FSR formed by the PM-fiber birefringent filter, we can estimate the beat-length of the PM fiber. The measurement can be verified by cutting back the fiber length  $L$  and measuring the change in FSR,

$$\Delta\text{FSR} = \frac{-\lambda^2}{(n_x - n_y) L^2} \Delta L = \frac{-\lambda \ell_b}{L^2} \Delta L. \quad (5.8)$$

With expected beatlengths  $\sim 5$  mm for PM fibers, we must choose the fiber length  $L$  appropriately so that the FSR will be within the range of the resolution of the optical spectrum analyzer. At  $1.55 \mu\text{m}$  this implies that  $L \approx 1$  meter so that the FSR is at least 1 nm.

This method was used to determine the birefringence of a commercial Fujikura Panda fiber where the measured beat-length of 3.7 mm corresponded well with the specified typical value of 3.5 mm. More importantly, the method was used to measure the beat-length of PM  $\text{Er}^{+3}$ -doped fibers when the birefringence was completely unknown. Fig. 5-4 shows the spectrum of a  $1.3 \mu\text{m}$  superfluorescent source after passing through the birefringent filter setup of Fig. 5-3 using 1.157 meters of PM  $\text{Er}^{+3}$ -doped fiber. The FSR at  $1.3 \mu\text{m}$  was 2.90 nm corresponding to a beat-length  $\ell_b = 2.58$  mm

at  $1.3 \mu\text{m}$ . The beat-length at  $1.55 \mu\text{m}$  is estimated to be 3.1 mm. This measurement was also performed with a longer piece of  $\text{Er}^{+3}$ -doped fiber (1.96 meters) which confirmed that  $\ell_b \approx 3.1 \text{ mm}$  at  $1.55 \mu\text{m}$ . Accurate knowledge of the beat-length of PM fibers is important in the design of mode-locked lasers which contain PM fiber, as explained in chapter 6.

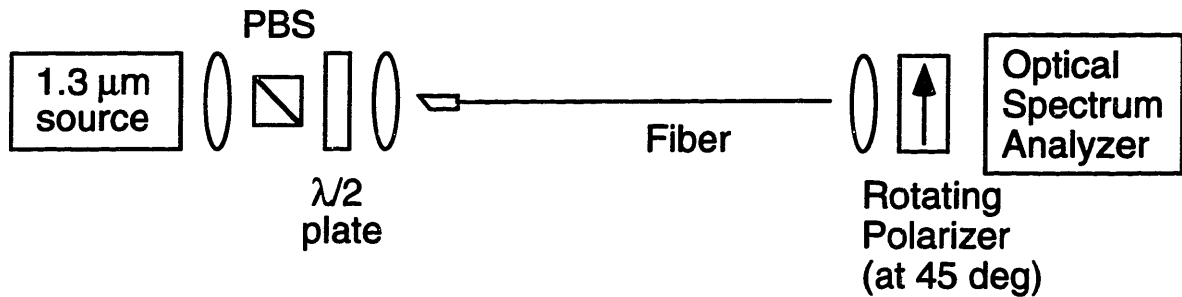


Figure 5-3: Experimental set-up for birefringent filter measurement of the beat-length of a PM fiber. A broadband  $1.3 \mu\text{m}$  source is launched into the fiber at 45 degrees from the birefringent axes, and the output polarizer is also set at 45 degrees to the fiber axes. The optical spectrum of the output then shows the filtering effect and free spectral range from which the beat-length can be determined.

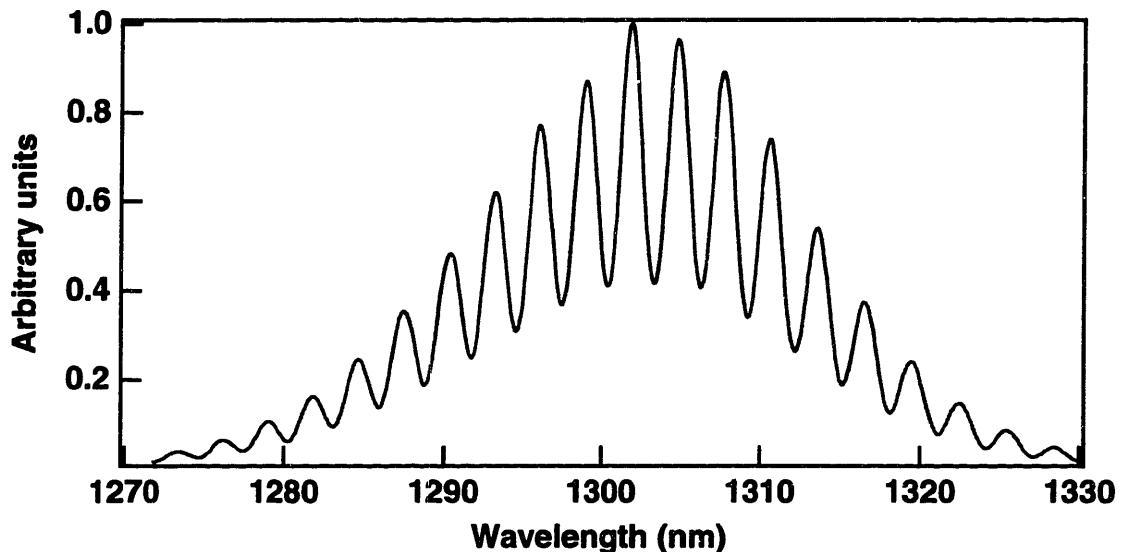


Figure 5-4: Results of a beat-length measurement with 1.157 meters of PM  $\text{Er}^{+3}$ -doped fiber in a birefringent filter configuration with a  $1.3 \mu\text{m}$  broadband source. The free spectral range is 2.90 nm, corresponding to  $\ell_b = 2.6 \text{ mm}$  at  $1.3 \mu\text{m}$  and  $\ell_b \approx 3.1 \text{ mm}$  at  $1.55 \mu\text{m}$ .



## 5.2 Temperature dependence of fiber birefringence

An important consideration for environmental stability is the sensitivity of the fiber laser to temperature changes. Although it may be fairly easy to fix the position of the fiber, assuring that the ambient temperature will not change is much more difficult and costly. Precise temperature control for a fiber laser could be expensive and bulky, and so mode-locked fiber laser schemes which can operate without temperature control would be advantageous. This section contains a discussion of measurements of the temperature stability of the polarization state in standard single-mode fiber (SMF-28) and in Fujikura Panda fiber. The measurements are by no means exhaustive, but do provide some important information about the temperature stability of these fibers.

### 5.2.1 Standard fiber versus PM fiber

In the first set of measurements, the goal was simply to compare the temperature dependence of the output polarization state from a standard SMF-28 fiber with that from a PM Panda fiber. An experimental setup similar to that shown in Fig. 5-1 was used with a 5.1 meter length of SMF fiber and a 1.55  $\mu\text{m}$  source. The fiber was coiled loosely into an aluminum box which was placed on a hot-plate. The output polarization state was monitored by again measuring the intensity along the semi-major axis ( $I_{max}$ ) and semi-minor axis ( $I_{min}$ ) and defining the aspect ratio  $c$  as in eqn. (5.3). As shown in Fig. 5-5 the polarization at the output of the SMF-28 fiber was measured over 150 deg C and did not show dramatic changes in the polarization state. The same length of Fujikura PM Panda fiber was then measured in the same set-up. Fig. 5-6 shows the output polarization state over a temperature range of only 5 deg C, and one can see the large variation over increments as small as 0.2 deg C. An estimate of the birefringence temperature dependence can be made using the plot in Fig. 5-6. The aspect ratio has values near 1 (circular polarization) at intervals of  $\approx 1$  deg C, which implies that for each 2 deg C temperature increase, the birefringence changes such that the fiber length is an integer 1 fewer beat-lengths. This can be expressed mathematically as

$$\frac{L}{\ell_b(T_1)} - \frac{L}{\ell_b(T_2)} = 1 \quad (5.9)$$

where  $L$  is the fiber length and  $T_2 = T_1 + \Delta T$  is the temperature change. Substituting the beat-length  $\ell_b(T) = \lambda/\delta n(T)$ , the temperature dependence of the birefringence is

$$\delta n(T) - \delta n(T + \Delta T) = \frac{\lambda}{L}. \quad (5.10)$$

For the PM fiber of Fig. 5-6,  $\lambda = 1.55\mu\text{m}$ ,  $L = 5.1$  m, and  $\Delta T = 2$  deg C, resulting in a temperature dependence for the birefringence  $\Delta(\delta n)/\Delta T \approx 1.5 \times 10^{-7}/\text{deg C}$ , or a fractional change in birefringence of

$$\frac{d(\delta n)}{dT} \frac{1}{\delta n} \approx 0.036\%/\text{deg C}. \quad (5.11)$$

Although the fractional birefringence change may appear small, the fact that a 2 deg C increase in temperature causes the polarization state to cycle through a beat-length indicates the extreme temperature sensitivity of PM fibers. (PM fibers can be used as temperature sensors.) So, although the positions of the birefringent axes are fixed in a PM fiber and thus environmentally stable (unlike in a standard fiber), schemes for fiber lasers which use PM fibers and light launched off-axis must be designed to compensate for this temperature dependence.

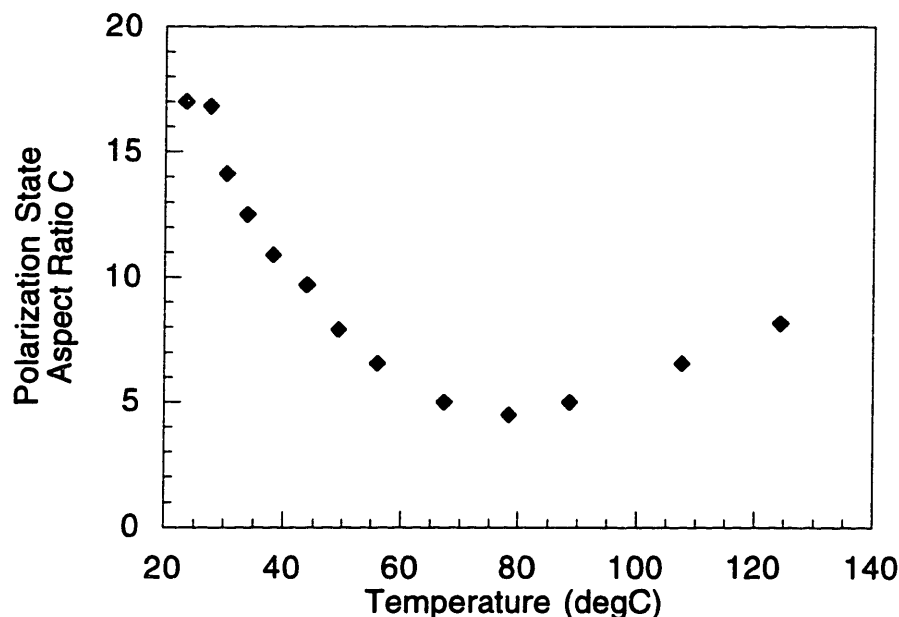


Figure 5-5: Plot of the output polarization state (described in terms of aspect ratio  $c$ ) versus temperature for a 5.1-meter length of SMF-28 fiber with a launched circularly-polarized  $1.55 \mu\text{m}$  source.

### 5.2.2 Measurement of birefringence temperature dependence in Panda fiber

Temperature dependence of birefringence in PM fiber was previously measured for an elliptical-clad fiber by Rashleigh and Marrone [121] over a large temperature range of 1200 deg C. The beat-length change was nonlinear over the whole temperature range, but was nearly linear over the range 0 - 200 deg C with a fractional change in birefringence (defined as in eqn. (5.11)) of  $\approx 0.17\%/ \text{deg C}$ . Barlow and Payne [122] reported measurements on the effect of temperature on fibers with birefringence due to bending. The fractional change in birefringence was measured to be  $0.027\%/ \text{deg C}$ . Also reported was a temperature dependence of  $\sim 0.1\%/ \text{deg C}$  for the birefringence in a linearly birefringent fiber, which corresponded well to the results in [121]. These papers, though, do not report birefringence measurements for current, commercial PM fibers such as Panda or Bowtie which potentially could be used in a fiber

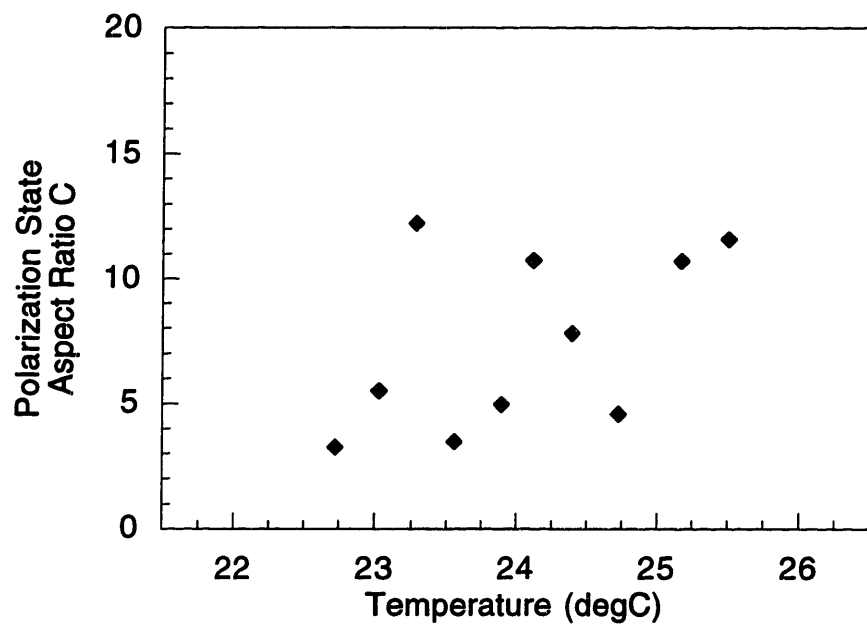


Figure 5-6: Plot of the output polarization state (described in terms of aspect ratio  $c$ ) versus temperature for a 5.1 meter length of PM Panda fiber with a launched circularly-polarized  $1.55 \mu\text{m}$  source. Note that the x-axis range is only 5 deg C compared with 120 deg C in the measurement of the SMF-28 fiber in Fig. 5-5.

laser. In order to verify the estimate of birefringence change with temperature of the Panda fiber from section 5.2.1, a 93-cm length of Panda fiber was again set up as a birefringent filter. The FSR was then monitored as a function of temperature over a range of 300 deg C and is plotted in Fig. 5-7.<sup>1</sup> The temperature dependence of  $\delta n$  can be determined from eqn. (5.6), where the FSR dependence on temperature is

$$\frac{d FSR}{dT} = -\frac{\lambda^2}{(\delta n)^2 L} \frac{d(\delta n)}{dT} - \frac{\lambda^2}{(\delta n) L^2} \frac{dL}{dT}. \quad (5.12)$$

For Panda fiber at 1.55  $\mu\text{m}$  and room temperature,  $\delta n = 4.2 \times 10^{-4}$ , and the linear thermal expansion coefficient for fused silica from [123] is

$$\alpha = \frac{dL}{dT} \frac{1}{L} = 4 \times 10^{-7} / \text{deg C}, \quad (5.13)$$

which implies that for  $L \simeq 1$  meter,

$$\frac{dL}{dT} = 4 \times 10^{-7} \text{m/deg C} \quad (5.14)$$

If we then assume that  $d(\delta n)/dT$  is  $\sim 10^{-7}$  (and significantly less than the index change with temperature for silica fiber,  $dn/dT = 1.2 \times 10^{-5} / \text{deg C}$  [124,61]), this implies that the term proportional to  $dL/dT$  in eqn. (5.12) is negligible for  $L \simeq 1$  m. The measured change in birefringence with temperature is then

$$\frac{d(\delta n)}{dT} \approx -1.3 \times 10^{-7} / \text{deg C} \quad (5.15)$$

from Fig. 5-7 and eqn. (5.12), which agrees well with the estimate in section 5.2.1. The implication of this result will be discussed further in chapter 6.

### 5.3 Simulations of the effect of linear birefringence on P-APM

The theory of fiber lasers mode-locked by nonlinear polarization rotation has thus far assumed that the fibers were isotropic [82]. An important question about these fiber lasers is what effect linear birefringence and beat-length have on the mode-locking mechanism. Based on the operation of various fiber lasers built at MIT and elsewhere, some researchers have hypothesized that birefringence reduces nonlinear polarization rotation and increases the intra-cavity powers required for self-starting to mode-locked operation. It has also been suggested that fiber lasers with lengths which are an integer number of birefringent beat lengths have reduced APM-action because the nonlinear ellipse rotation will reverse and may partially or completely “undo” itself when the polarization state changes handedness due to the linear birefringence. This section discusses the results of numerical simulation and analysis addressing these questions and the role of linear birefringence in mode-locked fiber lasers.

---

<sup>1</sup>This measurement was performed by UROP student Darrin Hsiung.

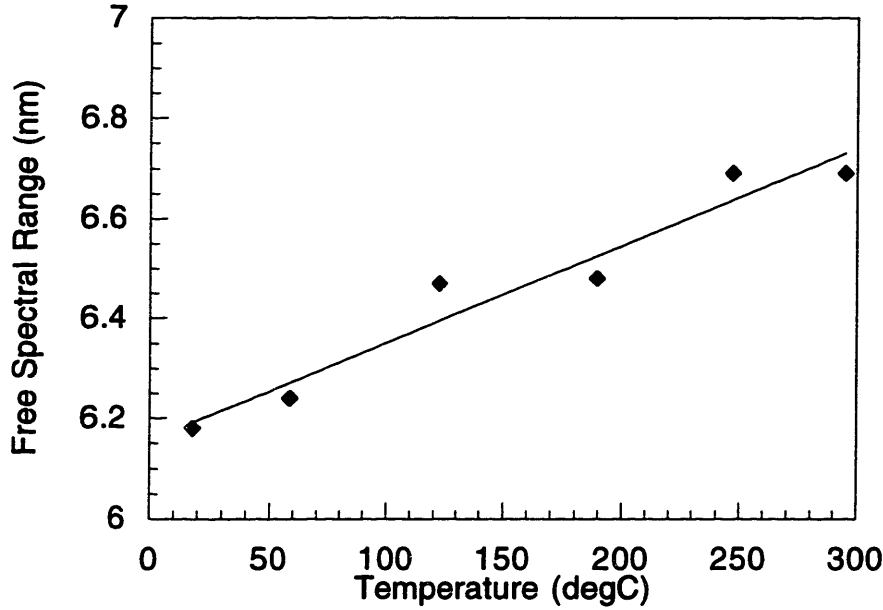


Figure 5-7: Plot of free spectral range versus temperature for the measurement of Panda PM fiber set up as a birefringent filter, as in Fig. 5-3, using a 93-cm fiber length and a  $1.55 \mu\text{m}$  source.

The equations of motion for the electric field propagation down a fiber with linear birefringence and nonlinear polarization rotation can be determined as follows. In the  $x - y$  coordinate frame where  $x$  and  $y$  are the slow and fast axes of the fiber, the linear birefringence gives

$$\frac{dE_x}{dz} = -j \delta E_x \quad (5.16)$$

$$\frac{dE_y}{dz} = +j \delta E_y \quad (5.17)$$

where  $\delta$  is the coefficient for birefringence

$$\delta = \frac{2\pi}{\lambda} \frac{n_x - n_y}{2} \quad (5.18)$$

and the common propagation constant  $k_{xy} = (2\pi(n_x + n_y)/2\lambda)$  has been suppressed. Equations (5.16) and (5.17) can be changed to the circular basis through the unitary transformation

$$E_{\pm} = \frac{E_x \pm jE_y}{\sqrt{2}}. \quad (5.19)$$

The equations for the evolution of the electric field with birefringence then become

$$\frac{dE_+}{dz} = -j \delta E_- \quad (5.20)$$

$$\frac{dE_-}{dz} = -j \delta E_+. \quad (5.21)$$

Next we consider the nonlinear polarization in the circular basis:

$$P_+ = \epsilon_0 \chi^{(3)} [ |E_+|^2 + 2|E_-|^2 ] E_+ \quad (5.22)$$

$$P_- = \epsilon_0 \chi^{(3)} [ 2|E_+|^2 + |E_-|^2 ] E_- . \quad (5.23)$$

Because the linear birefringence is relatively weak ( $n_x - n_y \simeq 10^{-4}$ ), the nonlinear polarization will be approximately the same as in an isotropic medium, at least for effects which are third order in the electric field [125]. Therefore, equations (5.20) to (5.23) can be combined to give

$$\frac{dE_+}{dz} = -j\delta E_- - j\eta [ |E_+|^2 + 2|E_-|^2 ] E_+ \quad (5.24)$$

$$\frac{dE_-}{dz} = -j\delta E_+ - j\eta [ 2|E_+|^2 + |E_-|^2 ] E_- \quad (5.25)$$

where the nonlinear coefficient

$$\eta = \frac{\omega \epsilon_0 n_0 n_2}{3} . \quad (5.26)$$

The preceding set of nonlinear coupled mode equations allow one to study the evolution of a polarization state in an optical fiber with linear birefringence and self-phase modulation. (The equations can be normalized as shown in Appendix B.) In order to study actual pulse propagation in a fiber, we would need to add dispersion and loss for a passive fiber, as well as gain and filtering for a doped fiber. The resulting electric field envelopes would then vary with both time  $t$  and distance  $z$ . Here we are just interested in two effects: linear birefringence and nonlinear polarization rotation, and so for a given intensity, we can solve for the field using equations (5.24) and (5.25). We can determine what happens at different points along the pulse envelope by using different intensities.

Winful [125,126] was the first to use these nonlinear coupled mode equations to study this problem. In [125] he showed that intensity-dependent polarization states are possible even with equal excitation of the fiber's principal axes. (Until this paper, birefringence had been neglected, and so there would be no nonlinear ellipse rotation for an initial linear polarization state.) By assuming that the input state is linear and by changing to dimensionless power variables, Winful solved analytically for the intensities of the right and left-hand circular polarizations in terms of Jacobian elliptic functions and defined a quarter period  $K$  for the circular polarizations. ( $K$  could then be determined through some complicated integrals which were dependent on the initial state.) But the assumption of a linearly polarized input state precludes the application of his analytic expressions to fiber lasers, where in general, the input state is elliptical. Winful also showed that because of the nonlinearity, the evolution of the polarization state is highly dependent on the input state [126].

In order to begin to understand the evolution of the electric field in the fiber, we should review how the linear birefringence and nonlinearity act on the polarization state independently. Birefringence causes the state to oscillate around either the fast axis or the slow axis while changing from elliptical to linear and back to elliptical

and to circular. The electric field amplitudes  $E_x$  and  $E_y$  are constant, while energy is coupled between  $E_+$  and  $E_-$  as shown in Fig. 5-8 (where the equations have been normalized so that  $|E_x|^2 + |E_y|^2 = |E_+|^2 + |E_-|^2 = 1$ ). The relative phase difference  $\phi_x - \phi_y$  accumulates linearly with a  $2\pi$  period equal to the beat-length  $\ell_b$ . Nonlinearity, though, causes a rotation of the polarization state in one direction while maintaining the handedness of the ellipse. Energy is coupled between  $E_x$  and  $E_y$ , while  $E_+$  and  $E_-$  are constant, as shown in Fig. 5-9. The relative phase difference between  $E_+$  and  $E_-$  accumulates linearly with distance, with a  $2\pi$ -period defined by

$$\ell_{npr} = \frac{2\pi}{\eta} \frac{1}{|E_+|^2 - |E_-|^2} \quad (5.27)$$

which will be referred to as the "nonlinear polarization rotation period." Note that the magnitude of  $\ell_{npr}$  is highly dependent on the initial polarization state. (The initial condition for both Fig. 5-8 and Fig. 5-9 is shown in the sample data file in appendix B.)

### 5.3.1 Regimes of birefringence versus nonlinearity

The result of both birefringence and nonlinearity on the polarization state depends, of course, on the relative strengths of the birefringence  $\delta$  and the nonlinearity  $\eta$  in eqns. (5.24) and (5.25). There are essentially three regimes:  $\delta \ll \eta$  where the birefringence is a perturbation to the nonlinear polarization rotation,  $\delta \sim \eta$  where the effects are comparable, and  $\delta \gg \eta$  where nonlinearity is a perturbation to the beat-length. In order to study the polarization evolution in a fiber laser, a fourth-order Runge Kutta program was written to solve equations (5.24) and (5.25).

Fig. 5-10 shows the evolution of an initial elliptically-polarized state for  $\delta = 0.15$  and  $\eta = 1.0$ . (The same initial state was used as in Fig. 5-8 and Fig. 5-9.) We can see that there is some energy transfer between  $E_+$  and  $E_-$ , but the phase difference  $\phi_+ - \phi_-$  still can accumulate to  $2\pi$ , indicating that complete nonlinear polarization rotation can still occur.

To illustrate the second regime, Fig. 5-11 shows the polarization state evolution of the same initial ellipse for  $\delta = 0.25$  and  $\eta = 1.0$ , where the two effects are comparable. Here the nonlinear polarization rotation is reduced by the birefringence such that the phase difference  $\phi_+ - \phi_-$  does not fully accumulate to  $2\pi$ . This phase difference is periodic, but the period is longer than  $\ell_{npr}$  as determined from the initial condition. This behavior agrees with ref. [126] which makes the point that higher powers are required to see changes due to polarization rotation when the birefringence is large. (The nonlinear polarization rotation and existing linear birefringence are competing.) Fig. 5-12 shows the third regime where birefringence dominates the nonlinear polarization rotation. For this case  $\delta = 0.35$  and  $\eta = 1.0$ , and the nonlinearity slightly perturbs the polarization state evolution due to birefringence; the phase shift  $\phi_x - \phi_y$  has a slight ripple, but accumulates almost linearly. The figure indicates that the nonlinear polarization rotation is small, yet this does not mean that there can be no distinction between the polarization states for high and low intensities.

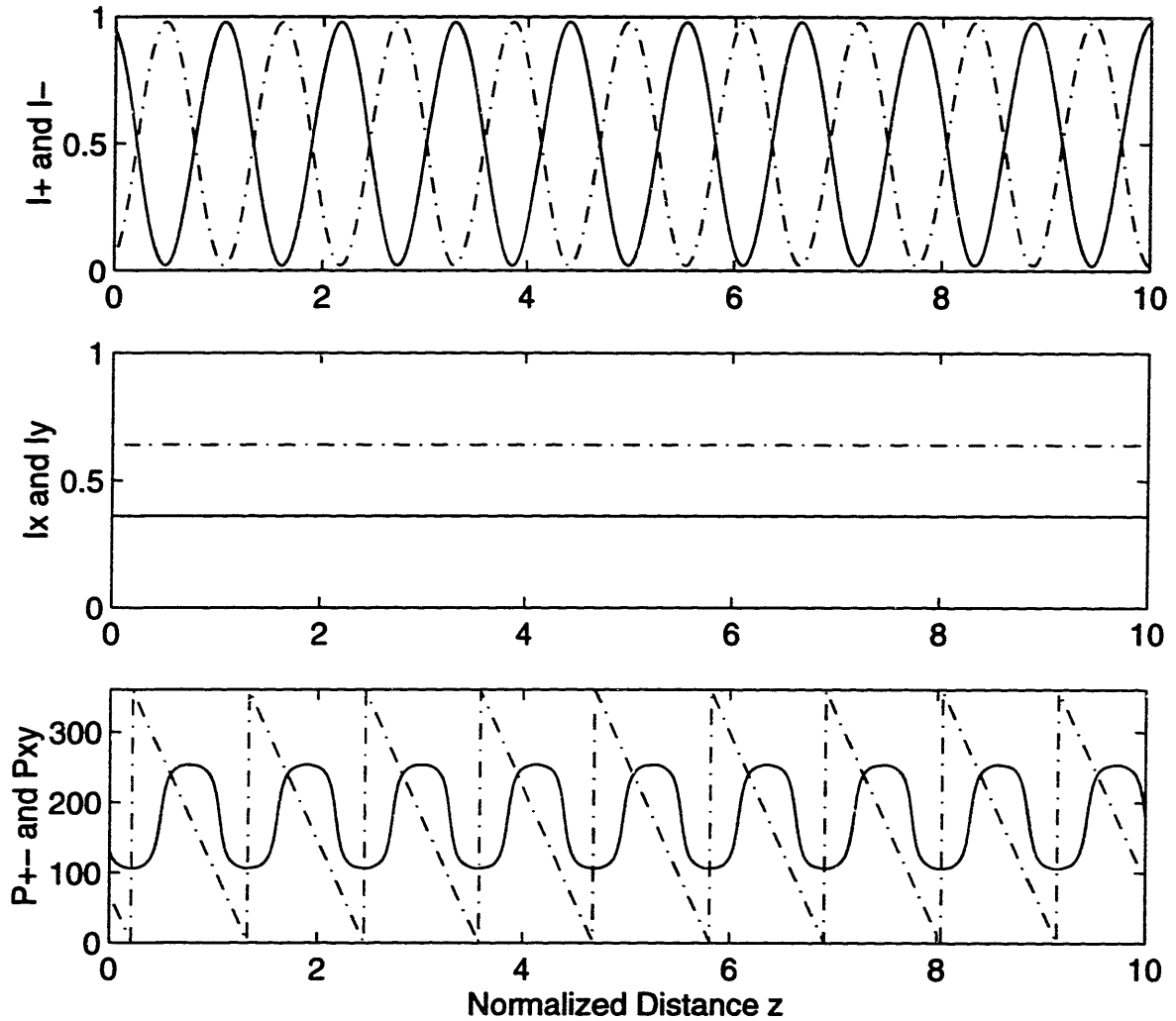


Figure 5-8: Evolution of the polarization state in the presence of only birefringence.  $\ell_b = 8$  meters (normalized  $\ell_b = 1.12$ ) and  $\ell_{npr} = \infty$ . The distance of propagation is  $z$ ,  $I_+ = |E_+|^2$  (solid),  $I_- = |E_-|^2$  (dot-dash),  $I_x = |E_x|^2$  (solid), and  $I_y = |E_y|^2$  (dot-dash). The phase differences are indicated by  $P_{+-} = \phi_+ - \phi_-$  (solid) and  $P_{xy} = \phi_x - \phi_y$  (dot-dash).



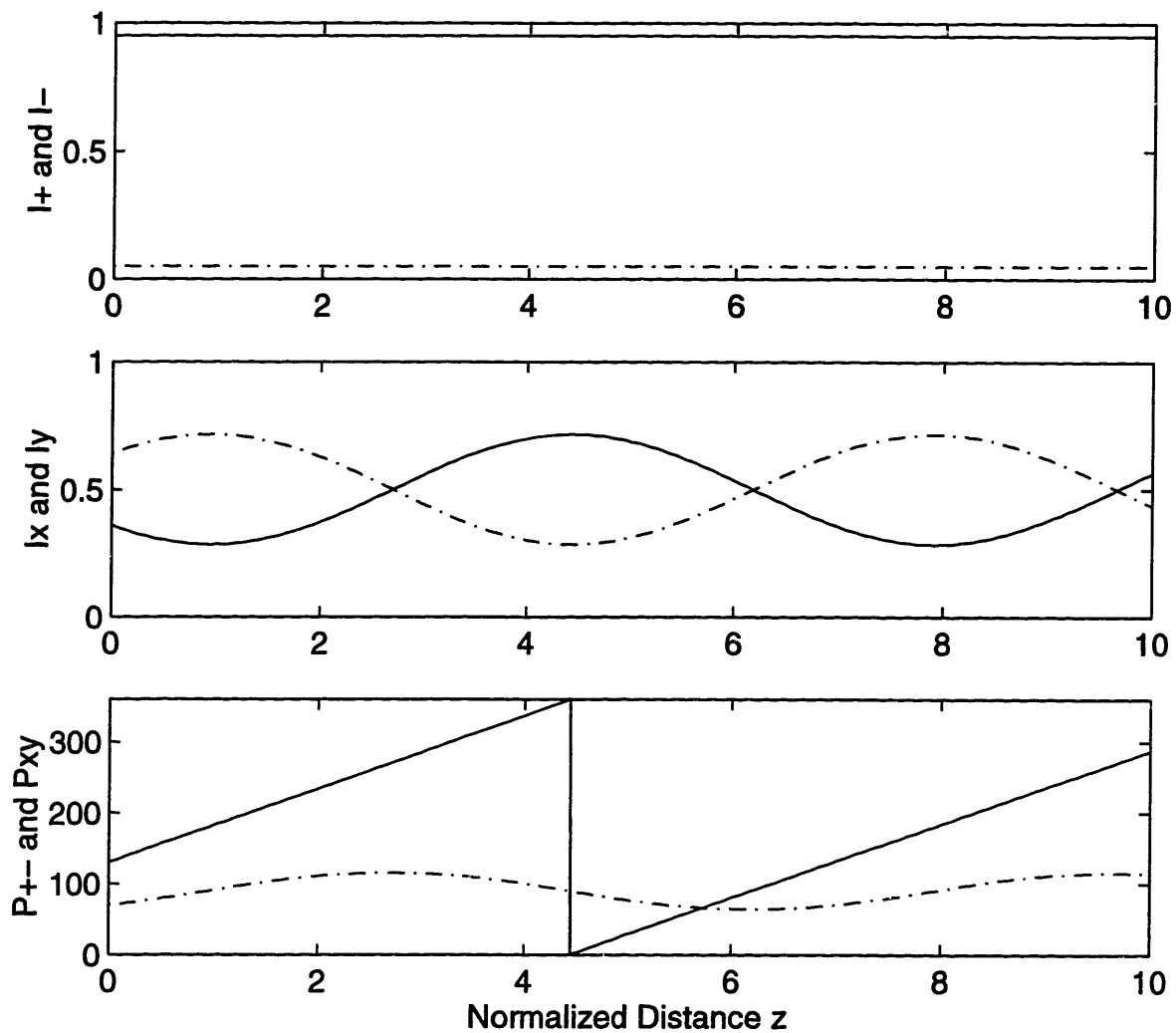


Figure 5-9: Evolution of the polarization state in the presence of only nonlinearity.  $\ell_{npr} = 6.97$  and  $\ell_b = \infty$ . Axis labels are the same as those of Fig. 5-8.

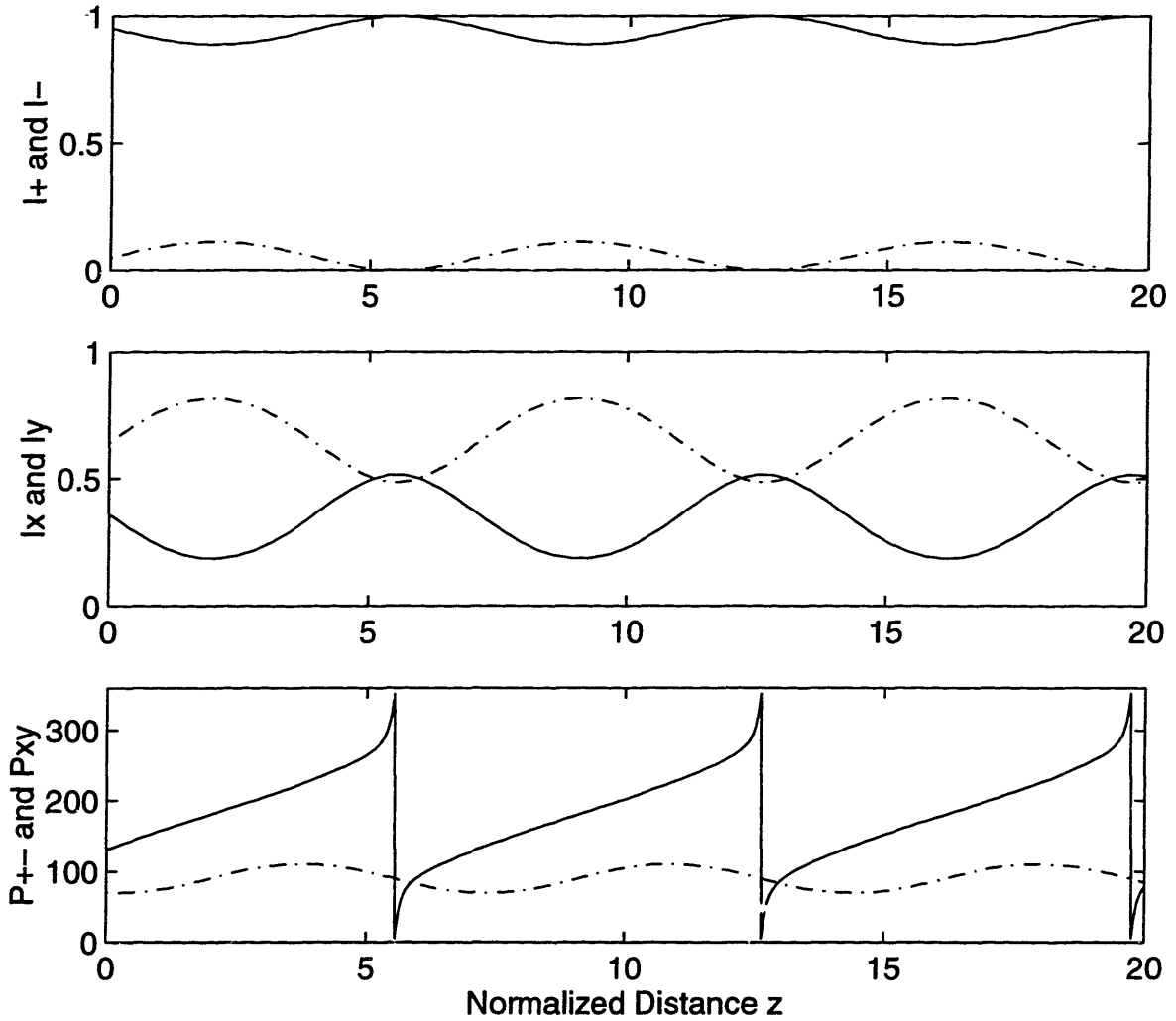


Figure 5-10: Evolution of the polarization state in the presence of nonlinearity  $\eta = 1.0$  and birefringence  $\delta = 0.15$ . ( $\ell_{npr} = 6.97$  and  $\ell_b = 21$ ). Axis labels are the same as those of Fig. 5-8.

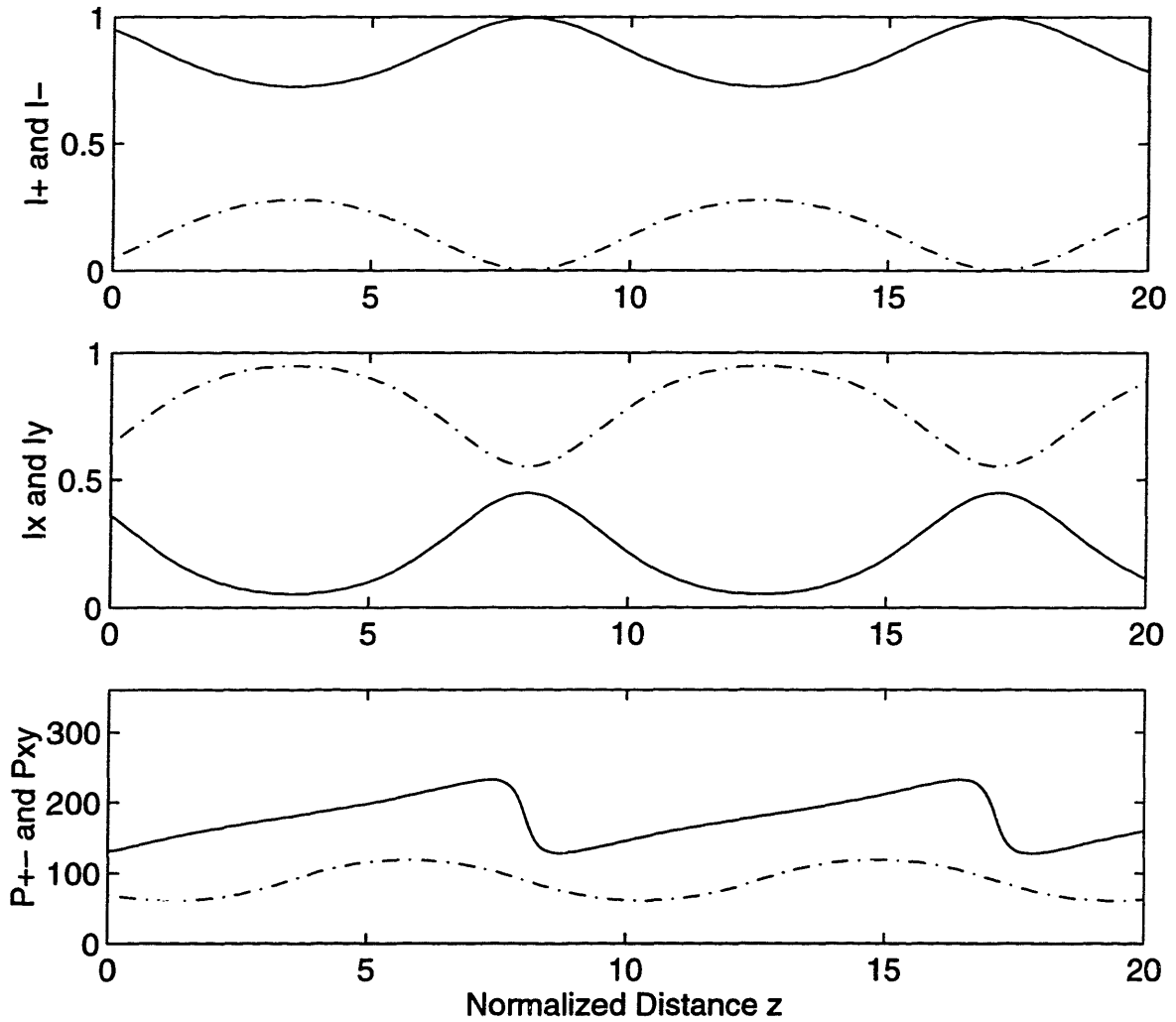


Figure 5-11: Evolution of the polarization state in the presence of nonlinearity  $\eta = 1.0$  and birefringence  $\delta = 0.25$ . ( $l_{npr} = 6.97$  and  $l_b = 12.6$ ). Axis labels are the same as those of Fig. 5-8.

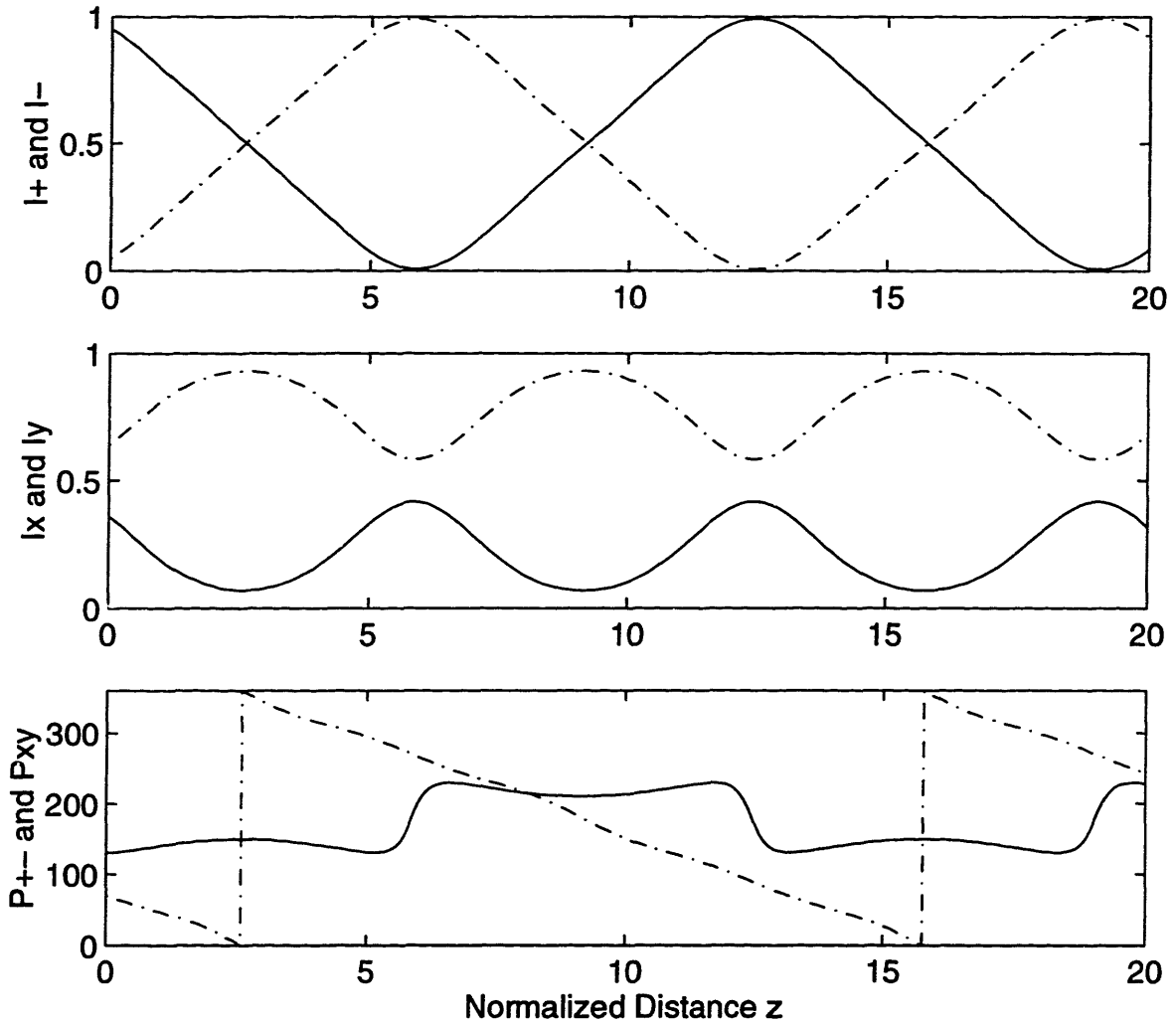


Figure 5-12: Evolution of the polarization state in the presence of nonlinearity  $\eta = 1.0$  and birefringence  $\delta = 0.35$ . ( $l_{npr} = 6.97$  and  $l_b = 8.98$ ). Axis labels are the same as those of Fig. 5-8.

Simulation runs with various initial conditions showed that aligning the initial polarization state close to the fast axis increased the birefringent beat-length, while aligning the initial state closer to the slow axis decreased the beat-length. This result makes sense given that  $\ell_b$  is defined

$$\ell_b = \frac{\lambda}{n_x - n_y} \quad (5.28)$$

where the indices  $n_x$  and  $n_y$  are the slow and fast axes, respectively, and have both linear and nonlinear components ( $n_x = n_{0x} + n_2 I_x$  for polarization along  $x$ ). A given intensity and polarization result in a change in the indices along the  $x$  and  $y$  axes, and thus in a corresponding change in  $\ell_b$ . An important and somewhat more subtle conclusion is that different intensities will have different beat-lengths in the fiber due to the nonlinearity, and so different points along the envelope of a pulse have different beat-lengths. Thus there is dependence of the polarization state on intensity, and so P-APM can be implemented even in a highly birefringent fiber.

### 5.3.2 Does birefringence cause periodicity of P-APM?

The next question to consider is whether there is a periodicity associated with birefringence and nonlinear polarization rotation such that at some distance the polarization rotation will have "undone" itself and no discrimination between the polarization states of different intensities can occur. Fig. 5-13 shows the polarization state evolution for different power levels and the same birefringence. The slightly different beat-lengths for each intensity cause there to be no distance at which all intensities have the same polarization state. This question was also explored in further simulations by considering the case of a mode-locked erbium-doped fiber soliton laser, such as that reported in [21], which had an intracavity peak power of 100 Watts and  $\ell_b = 8$  meters. The normalized value of  $\delta$  was then 2.8 compared with the normalized  $\eta = 1.0$ . This indicates that the birefringence effect is much larger than the nonlinear polarization rotation.

One method of determining how much discrimination there is between the polarization states at different intensities is to propagate the different intensity cases down the fiber (starting with the same initial condition) and then take dot-products of the peak-intensity ellipse with the lower-intensity ellipses. This is analogous to aligning a polarizer to the ellipse at the peak intensity of the pulse and calculating how much relative attenuation the wings of the pulse would experience when passing through this polarizer (analogous to the final polarizer in P-APM as shown in Fig. 2-5). Using the parameters from the erbium-doped fiber laser, Fig. 5-14 shows the calculated dot-product of polarization states at different intensities (80W, 60W, 40W, and 20W) along the pulse with the polarization state at the peak intensity (100W). We see that there is intensity discrimination over the entire 20 meters of simulation with more attenuation for smaller intensities, as expected. The dot-product curves of Fig. 5-14 flatten out in regions of  $z$  during which the polarization state is going through linear. (When the polarization state is linear, nonlinear polarization rotation does not occur, and so there is no more additional intensity discrimination.) The simulation shows

that there is no periodicity and no point at which the discrimination between high and low intensities has been cancelled out.

An interesting comparison can be made between the intensity discrimination which is obtained for fiber with birefringence versus that obtained for fiber without birefringence. A simulation was run using the parameters of [21] where the dot-product was taken between the peak of the pulse (at 100 W) and cw ( $\approx 0$  W). The simulation was also run with the birefringence set to zero ( $\delta = 0$ ). Fig. 5-15 shows a plot of the two dot-product curves as a function of distance. Note that the simulation distance is now considerably longer. As expected, both curves are sinusoidal, although the period of the dot-product with birefringence is longer because the birefringence reduces the nonlinear polarization rotation. The ripples on the dot-product curve with birefringence occur when the polarization state passes through linear due to the birefringence.

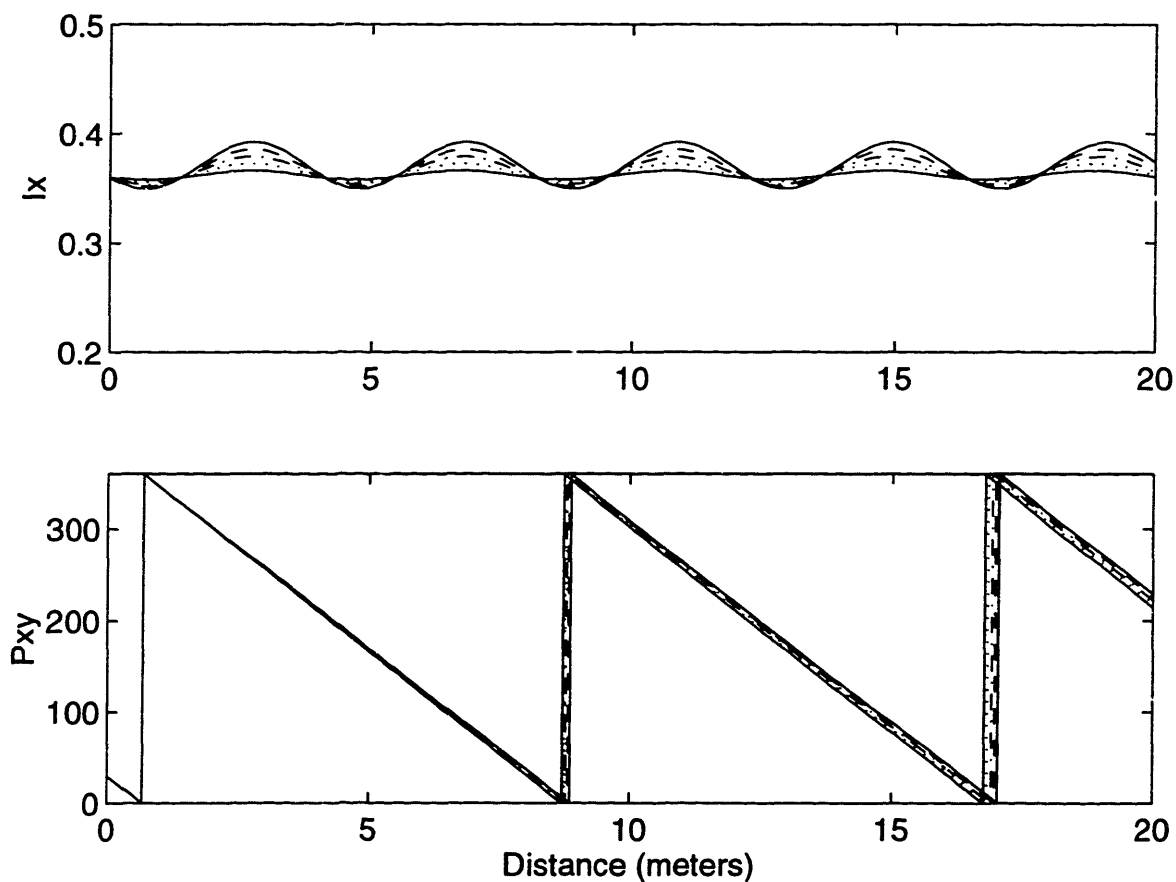


Figure 5-13: Evolution of the polarization state for different intensities: (solid) 100W, (dashed) 80W, (dot-dash) 60W, (dotted) 40W, and (solid) 20W. Parameters are from [21] with normalized  $\eta = 1.0$  and  $\delta = 2.8$  and initial state with  $|E_x|^2 = 0.36$  and  $P_{xy} = \phi_x - \phi_y = 30$  deg. Axis labels are the same as those of Fig. 5-8.

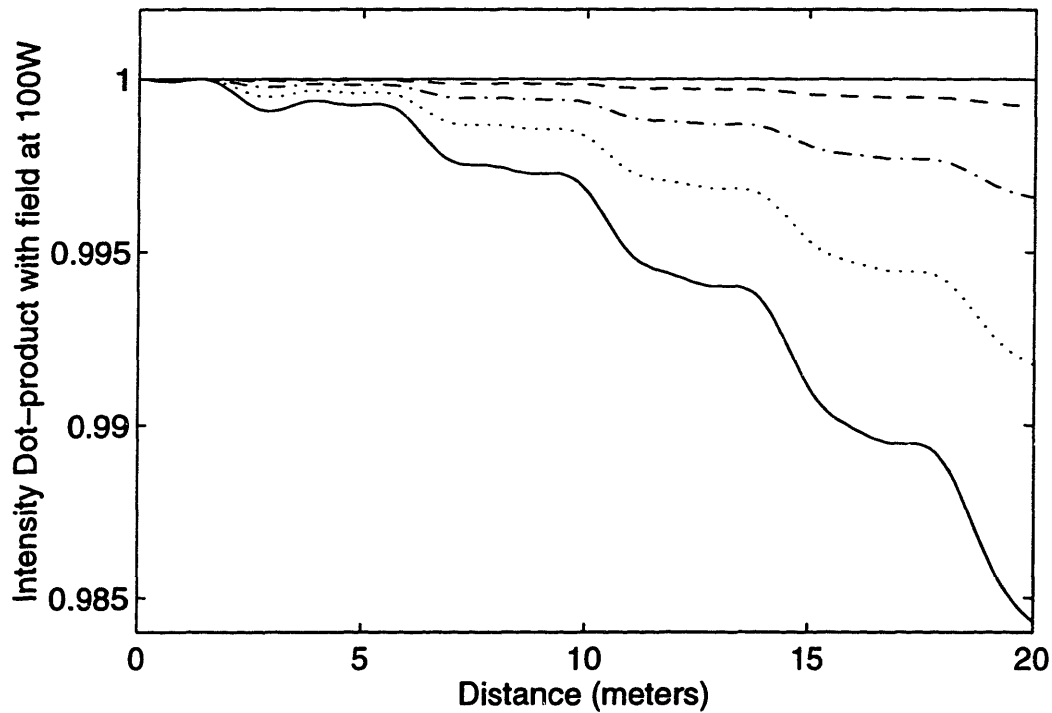


Figure 5-14: Dot-product of polarization states at different intensities with the polarization state at the peak of the pulse. Parameters are from [21] with normalized  $\eta = 1.0$  and  $\delta = 2.8$  and initial state with  $|E_x|^2 = 0.36$  and  $P_{xy} = \phi_x - \phi_y = 30$  deg. Curves: (dashed) dot-product of 80W and 100W, (dot-dash) dot-product of 60W and 100W, (dotted) dot-product of 40W and 100W, and (solid) dot-product of 20W and 100W.

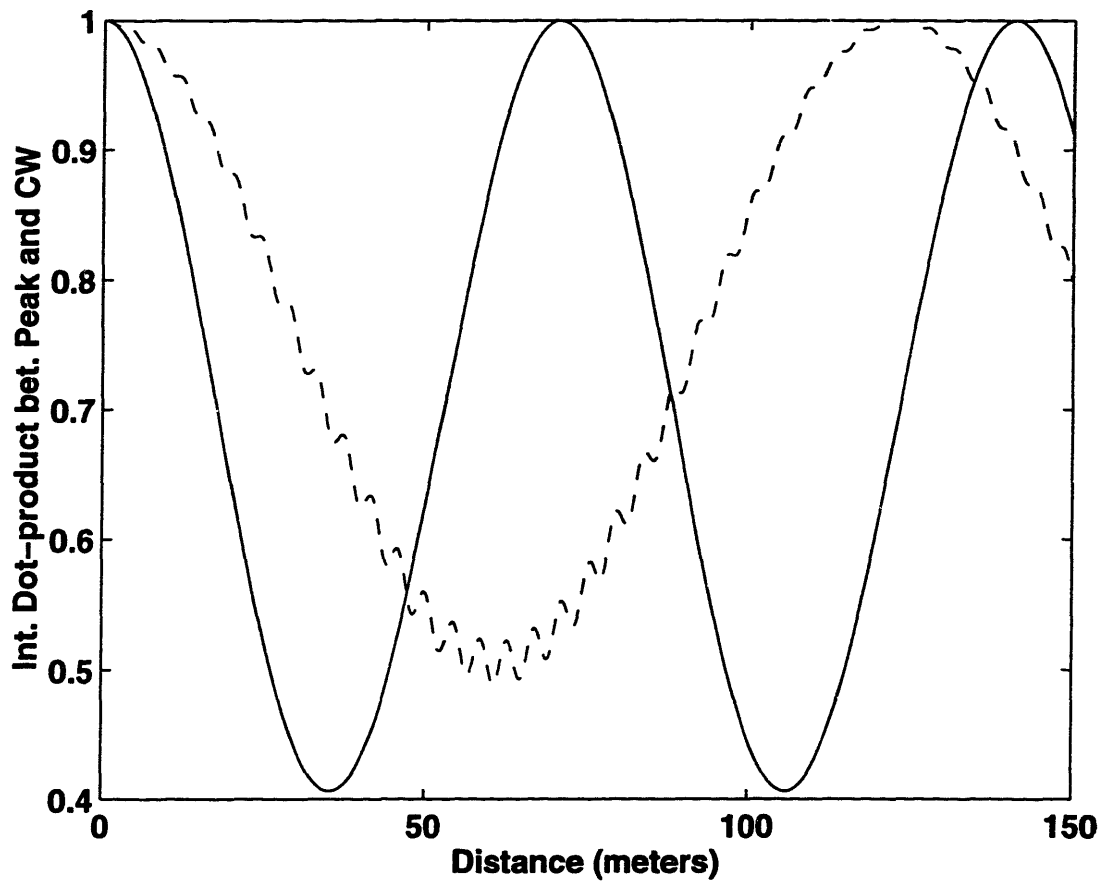


Figure 5-15: Dot-product of polarization state at the peak of the pulse with the polarization state of cw for fiber with birefringence (dashed) and without birefringence (solid). Parameters are from [21] with normalized  $\eta = 1.0$  and  $\delta = 2.8$  for the dashed curve. Both curves are sinusoidal, although the period of the dot-product with birefringence is longer because the birefringence reduces the nonlinear polarization rotation.



### 5.3.3 Optimum starting polarization state for maximum polarization rotation

An additional interesting question to consider: what is the optimum polarization ellipse to launch into the fiber to maximize discrimination between high and low intensities? Using the parameters from [21], simulations were run with all possible starting ellipses. For these simulations the elliptical polarization state was described in terms of ellipticity  $\mathcal{X}$  and azimuthal angle  $\Psi$ , the angle of the major axis of the ellipse from the slow-axis (x-axis), as shown in Fig. 5-16. In terms of the circular basis,

$$\Psi = \frac{\phi_+ - \phi_-}{2} \quad (5.29)$$

and  $-\pi/2 \leq \Psi \leq +\pi/2$  to include all possible polarization states. The ellipticity  $\mathcal{X}$  is defined by

$$\left| \frac{E_+}{E_-} \right|^2 = \left( \frac{1 + \mathcal{X}}{1 - \mathcal{X}} \right)^2 \quad (5.30)$$

so that

$$E_+ = \sqrt{\frac{1 + \mathcal{X}}{1 - \mathcal{X}}}, \quad (5.31)$$

and  $-1 \leq \mathcal{X} \leq +1$ . ( $\mathcal{X} = 0$  is linear polarization,  $\mathcal{X} = +1$  is right-hand circular polarization, and  $\mathcal{X} = -1$  is left-hand circular polarization.)

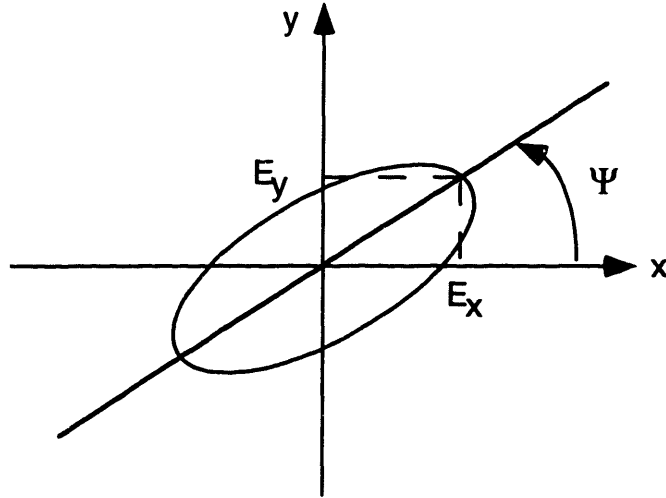


Figure 5-16: Diagram of elliptical polarization state. The azimuthal angle  $\Psi$  is the angle of the major axis of the ellipse from the x-axis (slow-axis) and is defined in eqn. (5.29). The ellipticity of the polarization state is defined by  $\mathcal{X}$  in eqn. (5.30).

The simulation was run similarly to those of section 5.3.2 where, in this case, the dot-product was taken between the polarization state at peak intensity of 100W and the polarization state of the low intensity (cw) which was  $\approx 0W$ . After 10 meters of

simulation length, the dot-product was subtracted from 1.0 to determine which initial polarization states had experienced the most intensity discrimination. Fig. 5-17 shows a contour plot of the intensity discrimination versus azimuthal angle  $\Psi$  and ellipticity  $\mathcal{X}$  where the intensity discrimination has been normalized so that the maximum is set to 1.0. We can see that the maximum discrimination occurs for initial states with  $\mathcal{X} \approx -0.36$  and  $\Psi \approx 80$  deg or with  $\mathcal{X} \approx 0.36$  and  $\Psi \approx -80$  deg. These results makes sense based on the fact that aligning the polarization ellipse closer to the fast axis ( $\Psi \approx \pm 80$  deg) increases the birefringent beat-length, and thus decreases the effect of birefringence on nonlinear polarization rotation. Setting the initial ellipticity to  $\mathcal{X} = \mp 0.36$  must minimize the number of times the polarization state passes through linear ( $\mathcal{X} = 0$ ) within the propagation distance, which again maximizes nonlinear polarization rotation. Knowledge of this optimum initial polarization ellipse could be helpful in mode-locking fiber lasers with birefringent fiber.

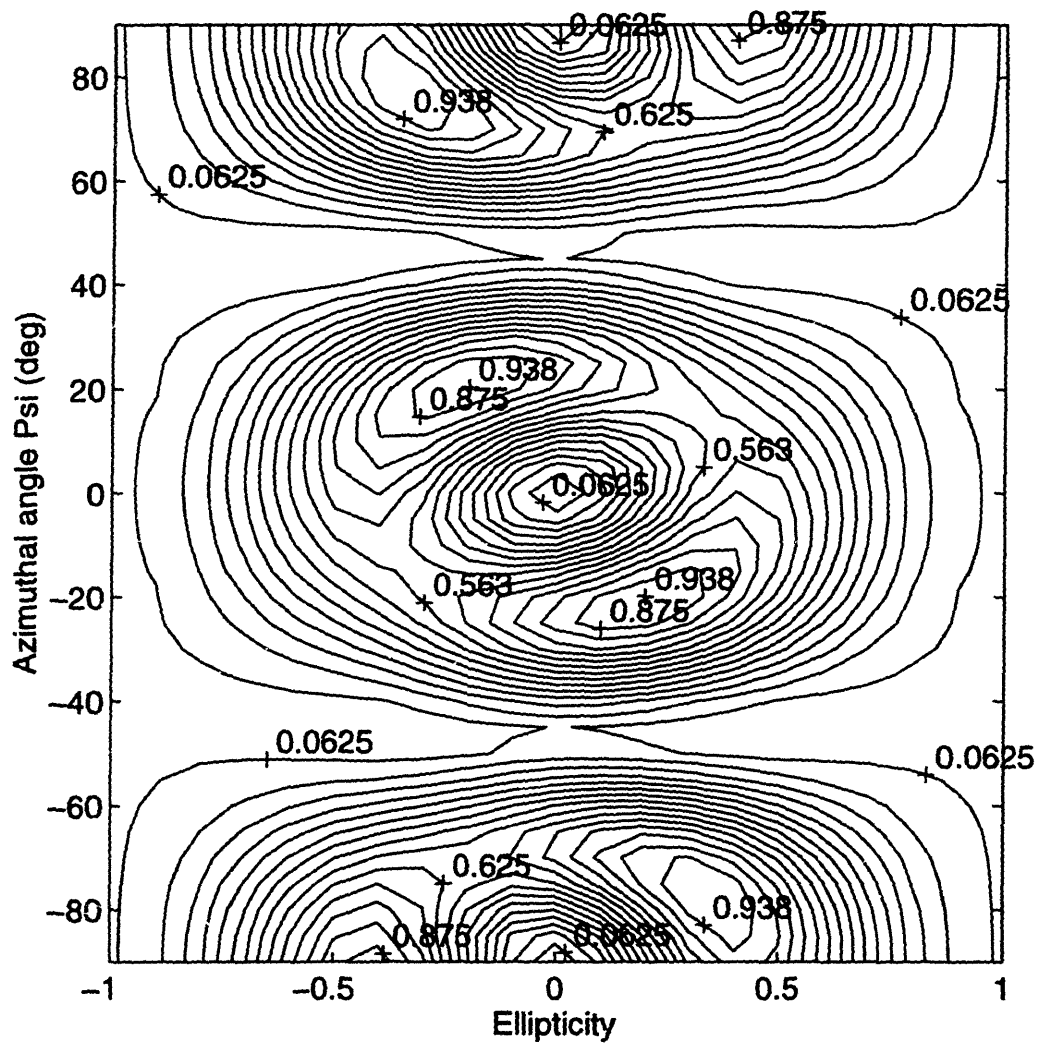


Figure 5-17: Contour plot of intensity discrimination versus azimuthal angle  $\Psi$  and ellipticity  $\mathcal{X}$  which occurs for the simulation length of 10 meters. The optimum initial elliptical states have intensity discriminations which approach 1.0.

## Chapter 6

# Work toward an environmentally stable mode-locked fiber laser

Although fiber lasers have been mode-locked successfully with standard fiber in laboratory settings, environmental stability is an important issue if they are to be used in commercial applications. PM fiber has a large stress-induced birefringence so that the locations of the fast and slow axes are fixed under changing environmental conditions. When linearly polarized light is launched along one of the PM axes, the light will maintain its polarization with cross-coupling to the other PM axis as low as  $-30$  dB. This property of PM fibers points to their use in fiber lasers to ensure environmental stability. Fermann and co-workers have demonstrated a design for mode-locked fiber lasers which uses PM fiber in a linear cavity [113,114,127]. A Faraday rotator mirror at one end of the cavity serves to rotate the polarization of the reflected light by  $90$  deg with respect to the incoming light [128]. The reflected light then travels backward down the fiber in the orthogonal polarization state to the incoming, forward-traveling light. This causes the total linear phase delay between the two polarization eigenmodes to be zero after one round trip and thus compensates any linear phase drifts in the fiber caused by environmental changes. This scheme has been successful in generating  $100$ -fsec,  $100$ -pJ pulses [54] and  $3$ -psec,  $1$ -nJ soliton pulses [54], but there are a number of disadvantages to the scheme. Because the laser has a linear cavity geometry and thus is susceptible to first order spurious reflections, the laser does not self-start to pulsed operation and requires slight detuning of the cavity length or a moving mirror for pulse initiation. In recent experiments, though, a saturable absorber mirror has been used at one end of the cavity to achieve self-starting [127]. Another limitation of this scheme is the requirement for PM  $\text{Er}^{+3}$ -doped fiber which is not yet readily commercially available and is generally designed to have negative GVD. Fiber with negative GVD forces operation in the soliton regime which limits the pulse energy and minimum pulse width with a single pulse per round trip. The goal of the experiments discussed in this chapter was to demonstrate a new environmentally-stable scheme for a mode-locked fiber laser which overcomes the limitations on pulse width and power.

One possible scheme is to use PM fiber in the P-APM fiber ring laser whose operation was described in chapters 3 and 4. An initial polarization ellipse is launched

off-axis, but no transfer of energy between the two PM axes occurs because of the large birefringence. P-APM can still be achieved in PM fiber, though, because the two polarizations along the PM axes have different intensities and thus a differential non-linear phase shift is accumulated. Through experiments with an all-PM laser, it became apparent that the temperature sensitivity of the beat-length in PM fiber (as discussed in section 5.2) is a major problem which motivated work on an alternative cavity design.

This chapter is organized as follows. Section 6.1 outlines a calculation that shows that P-APM is possible in PM fibers and estimates the reduction in the amount of pulse-shortening action compared to non-PM fibers. Section 6.2 discusses an all-PM fiber scheme for a mode-locked fiber laser at  $1.55 \mu\text{m}$ . The performance and problems are identified. The final section discusses a new design for an environmentally-stable mode-locked fiber laser which uses both PM and non-PM fiber.

## 6.1 Comparison of P-APM in PM fiber versus non-PM fiber

An important question is how different the mode-locking mechanism will be in PM fiber versus standard fiber. This issue was addressed by Haus [129]. In a standard non-PM fiber laser, an elliptical polarization is launched into the Kerr medium (i.e. fiber), and this ellipse rotates by an angle which is proportional to the light intensity. As discussed previously and shown in Fig. 5-9, energy is coupled between  $E_x$  and  $E_y$  via the Kerr effect, while  $E_+$  and  $E_-$  are constant. A properly oriented polarizer at the end of the fiber then selects the light with the highest intensity (different intensities have different rotation angles) thus achieving pulse shortening.

In PM fiber, energy transfer between the two PM axes is prevented because the large birefringence changes the phase bias between  $E_x$  and  $E_y$  so rapidly. The propagation equations for  $E_x$  and  $E_y$  in the presence of only the Kerr effect are, following [130]:

$$\frac{dE_x}{dz} = -j\eta [3|E_x|^2 E_x + 2|E_y|^2 E_x + E_y^2 E_x^* \exp(j2\Delta kz)] \quad (6.1)$$

$$\frac{dE_y}{dz} = -j\eta [3|E_y|^2 E_y + 2|E_x|^2 E_y + E_x^2 E_y^* \exp(-j2\Delta kz)] \quad (6.2)$$

where  $\Delta k = k_x - k_y$  is the wave-vector mismatch due to linear birefringence and  $\eta$  is defined in eqn. (5.26). The third term of eqns. (6.1) and (6.2) is the coherence term (a phase-dependent cross modulation term) which essentially averages to zero in the case of PM fiber since  $\Delta k$  is large. With no energy transfer, when a linearly polarized pulse is aligned at some angle to the PM axes of the fiber, the two orthogonal polarizations will have constant (although different) intensities. As the pulse travels in the fiber, the two polarizations will accumulate different nonlinear phase shifts due to the Kerr effect and different linear phase shifts due to birefringence. If the pulses in the orthogonal polarizations are allowed to separate in the fiber due to the linear birefringence, the cross-phase modulation will be greatly reduced and the

pulses will accumulate independent nonlinear phase shifts. This is avoided in the laser by repeatedly cross-splicing the fiber (aligning the fast axis of the first fiber to the slow axis of the second fiber when splicing) to prevent the pulses from separating by more than half the pulse width. Pulse shortening is then achieved by combining the two pulses in a polarizer at the output. With the proper linear phase bias, coherent addition occurs at the peak of the pulse while the wings of the pulse are extinguished.

### 6.1.1 P-APM in PM fiber

When light is launched off-axis into a PM fiber and then combined at the fiber end, the output intensity as a function of intensity and initial angle can be modeled with a nonlinear Mach-Zehnder interferometer as in Fig. 6-1. The two arms of the interferometer correspond to the two polarizations along the fast and slow axes of the fiber. The first beam splitter with reflectance  $r$  determines the initial launch angle, and the output beam splitter (with reflectance  $s$ ) corresponds to the output polarizer which accepts power in one polarization but absorbs power in the orthogonal polarization (the rejection port). In this case, we assume that the fibers are cross-spliced to cancel the linear birefringence so that the pulses from the two arms are overlapped at the output. We also assume that short fiber lengths are cross-spliced so that the pulses in the two orthogonal polarizations remain overlapped and the cross-modulation term is non-zero.

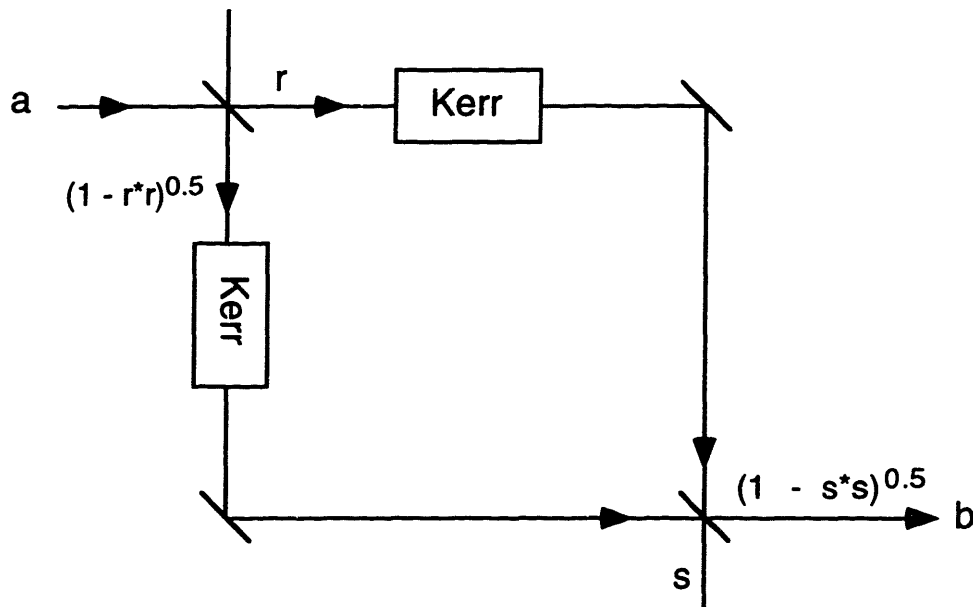


Figure 6-1: Diagram of the nonlinear Mach-Zehnder interferometer which is equivalent to light traveling in two polarizations down a fiber.

After the first beam splitter, representing the input to the PM fiber, the mode

amplitudes along the PM axes of the fiber are

$$a_x = r a \quad (6.3)$$

$$a_y = a \sqrt{1 - r^2} \quad (6.4)$$

where  $x$  and  $y$  indicate the slow and fast axes, respectively. The two "arms" then acquire nonlinear phase shifts as they travel down the fiber:

$$\Phi_x = [3 \kappa |a_x|^2 + 2 \kappa |a_y|^2] = [3 \kappa r^2 + 2 \kappa (1 - r^2)] |a|^2 \quad (6.5)$$

$$\Phi_y = [3 \kappa |a_y|^2 + 2 \kappa |a_x|^2] = [3 \kappa (1 - r^2) + 2 \kappa r^2] |a|^2 \quad (6.6)$$

where  $\kappa$  is proportional to the Kerr coefficient and the length of the fiber. Note that as discussed after eqn. (6.2), the coherence term has been neglected because the fiber is PM and no energy transfer occurs. After traveling through the fiber of length  $L$ , the two mode amplitudes are then

$$a_x(L) = r \exp(+j \Phi_x) a \quad (6.7)$$

$$a_y(L) = \sqrt{1 - r^2} \exp(+j \Phi_y + j \phi) a \quad (6.8)$$

where an additional linear phase shift  $\phi$  is included for proper bias. The two polarizations are then interfered at the output beam splitter (the polarizer) and the output  $b$  is

$$b = \sqrt{1 - s^2} a_x(L) + s a_y(L). \quad (6.9)$$

After substituting eqns. (6.7) and (6.8), the output becomes

$$b = \left[ r \sqrt{1 - s^2} \exp(+j \Phi_x) + s \sqrt{1 - r^2} \exp(+j \Phi_y + j \phi) \right] a. \quad (6.10)$$

The output power is then

$$\begin{aligned} |b|^2 = & \left[ r^2(1 - s^2) + s^2(1 - r^2) \right. \\ & \left. + 2rs \sqrt{(1 - r^2)(1 - s^2)} \cos(\kappa |a|^2(2r^2 - 1) + \phi) \right] |a|^2 \end{aligned} \quad (6.11)$$

We can define an angle  $\theta$  such that

$$s = \sin \theta \quad (6.12)$$

and the output power is then

$$\begin{aligned} |b|^2 = & \left[ \frac{1}{2}(1 - \cos 2\theta) + r^2 \cos 2\theta \right. \\ & \left. + r \sqrt{1 - r^2} \sin 2\theta \cos(\kappa |a|^2(2r^2 - 1) + \phi) \right] |a|^2. \end{aligned} \quad (6.13)$$

We can see that the nonlinearity has maximum effect when  $\sin 2\theta = 1$  and that for  $r^2 = 0.5$  the nonlinear phase is zero.

## 6.1.2 P-APM in non-PM fiber

For non-PM fiber we use the circular basis to describe the polarization state. The coherence terms in the nonlinear phase shift are non-zero in the x-y basis since there is energy transfer in non-PM fiber. But the nonlinear phase shifts in the circular basis do not contain coherence terms, and therefore are more easily manipulated in the calculation. The analysis here closely follows that of section 6.1.1. At the fiber input, the mode amplitude  $a$  is split into the two circular polarizations

$$a_+ = r a \quad (6.14)$$

$$a_- = \exp(+j\phi)\sqrt{1-r^2}a \quad (6.15)$$

The linear and circular polarization bases are related by the unitary transformation shown in eqn. (5.19) such that

$$a_x = \frac{1}{\sqrt{2}}(a_+ + a_-) \quad (6.16)$$

$$a_y = -\frac{1}{\sqrt{2}}(a_+ - a_-) \quad (6.17)$$

The nonlinear phase shifts are then

$$\Phi_+ = 2\kappa [ |a_+|^2 + 2|a_-|^2 ] \quad (6.18)$$

$$\Phi_- = 2\kappa [ 2|a_+|^2 + |a_-|^2 ] \quad (6.19)$$

and after traveling through the fiber of length  $L$ , the two mode amplitudes are

$$a_+(L) = r \exp(+j\Phi_+) a \quad (6.20)$$

$$a_-(L) = \sqrt{1-r^2} \exp(+j\Phi_- + j\phi) a \quad (6.21)$$

Then the output at polarizer b is

$$b = a_x \cos \theta + a_y \sin \theta \quad (6.22)$$

$$= \frac{1}{\sqrt{2}}(a_+ + a_-) \cos \theta + \frac{j}{\sqrt{2}}(-a_+ + a_-) \sin \theta. \quad (6.23)$$

The output power for the non-PM fiber case is then

$$\begin{aligned} |b|^2 &= \frac{1}{2} [ |a_+|^2 + |a_-|^2 + (a_+ a_-^* + a_+^* a_-) (\cos^2 \theta - \sin^2 \theta) \\ &\quad - j(a_+ a_-^* - a_+^* a_-) 2 \sin \theta \cos \theta ] \end{aligned} \quad (6.24)$$

Now we need to recognize that  $(a_+ a_-^* + a_+^* a_-) = 2\text{Re}(a_+ a_-^*)$  and that  $(a_+ a_-^* - a_+^* a_-) = j2\text{Im}(a_+ a_-^*)$ , so that

$$|b|^2 = \frac{1}{2} [ 1 + 2r\sqrt{1-r^2} \cos(2\theta + \phi + \Phi_- - \Phi_+) ] |a|^2 \quad (6.25)$$



And by substituting for the nonlinear phase shifts  $\Psi_+$  and  $\Psi_-$ , the output power is

$$|b|^2 = \left[ \frac{1}{2} + r\sqrt{1-r^2} \cos(2\theta + \phi + 2\kappa|a|^2(2r^2 - 1)) \right] |a|^2 \quad (6.26)$$

This equation is very similar in form to eqn. (6.13) with the nonlinearity appearing in a cosine term. Although the coefficient in front of this cosine term is the same in both cases, the nonlinear phase shift is a factor of 2 larger in the non-PM case. In order to maximize the effect of the nonlinearity, we set  $\sin 2\theta = 1$  in eqn. (6.13), which then results in the same average loss and bias loss for the two cases. Through proper choice of the phase bias  $\phi = \pi$ , eqns. (6.13) and (6.26) are then

$$|b|_{pm}^2 = \left[ \frac{1}{2} + r\sqrt{1-r^2} \sin(\kappa|a|^2(2r^2 - 1)) \right] |a|^2 \quad (6.27)$$

$$|b|_{non-pm}^2 = \left[ \frac{1}{2} + r\sqrt{1-r^2} \sin(2\kappa|a|^2(2r^2 - 1)) \right] |a|^2 \quad (6.28)$$

where the only difference is in the magnitude of the nonlinear modulation. Finally we can choose the value of  $r$  which optimizes the pulse shaping by maximizing the product  $r\sqrt{1-r^2}(2r^2 - 1)$ . Fig. 6-2 shows a plot of this product versus  $r^2$  which indicates that the maximum occurs at  $r^2 = 0.85$ , resulting in

$$r\sqrt{1-r^2} = 0.36 \quad (6.29)$$

$$(2r^2 - 1) = 0.7. \quad (6.30)$$

The difference in nonlinear phase shift indicates the strength of pulse shortening in the lasers, implying that the non-PM-fiber laser should mode-lock more easily. But the random (although small) birefringence of the non-PM fiber also reduces the strength of the pulse-shortening by an amount which cannot be predicted, since the birefringence of the non-PM fiber is in general unknown. The predictable and constant birefringence of PM-fiber should allow precise control of the polarization everywhere in the laser, so that the laser can be designed to operate at a fixed point of maximum possible pulse shortening.

## 6.2 Mode-locking of an all PM-fiber laser

The experimental set-up for an all-PM fiber laser using P-APM<sup>1</sup> is shown in Fig. 6-3. The light exits the isolator linearly polarized, and the first half-wave plate is used to align the linear polarization along one of the axes of the PM-Er<sup>+3</sup>-doped fiber. We did not cross-splice the Er<sup>+3</sup>-doped fiber because we wanted to maximize the gain and had only a limited supply of the fiber. The light is then coupled along one of the PM-axes to avoid walk-off of the pulses due to linear birefringence. A wavelength-division multiplexing (WDM) coupler brings in the 980 nm to backwards pump the Er<sup>+3</sup>-doped fiber and passes the 1550 nm light. The small air gap following the WDM coupler allows variable output coupling by adjustment of the first half-wave plate in

---

<sup>1</sup>The experiment of this section was done with David Jones.

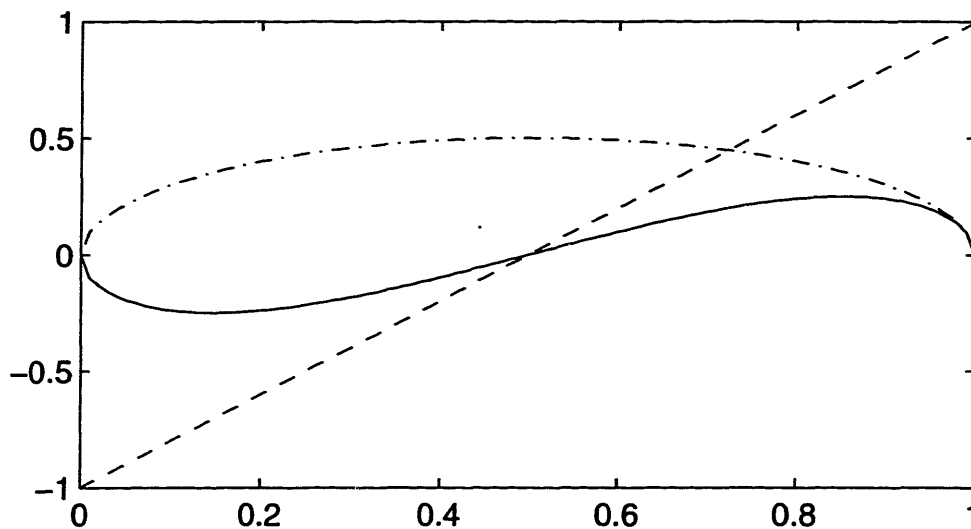


Figure 6-2: Plot of  $r\sqrt{1-r^2}$  (dash-dot),  $(2r^2 - 1)$  (dashed), and  $r\sqrt{1-r^2}(2r^2 - 1)$  (solid) versus  $r^2$ .

front of the polarizing beam splitter (PBS). The second half-wave plate then adjusts the linear polarization so that the linearly polarized light is launched at an angle to the PM axes (and different intensities are coupled onto the orthogonal axes). With these bulk elements the polarization state at the passive PM-fiber input can be determined exactly. The PM-fiber is then cross-spliced every 40 cm to prevent the pulses from separating by more than one pulse width (we assumed a 4 mm beatlength and 500 fsec pulses). The wave-plates after the passive PM-fiber then supply the proper bias for pulse shortening at the PBS. Finally, a birefringent filter provides tuning and bandwidth control.

Although this all-PM laser was designed to operate similarly to other P-APM fiber lasers, this scheme had a number of potential problems due to several differences in the cavity configuration. The additional air-gap should not be a problem in terms of cavity loss, since coupling losses as low -1.5 dB can be achieved and the  $\text{Er}^{+3}$ -doped fiber has high gain. But the additional air gap can be a problem if there are back-reflections from the fiber collimators. Reflections from the  $\text{Er}^{+3}$ -doped fiber end and WDM fiber end can set up a linear cavity in the  $\text{Er}^{+3}$ -doped fiber which would induce spatial hole burning and increase the self-starting threshold. Determining the correct length of passive PM-fiber to use between cross-splices may also be difficult since this calculation depends on the final pulse width, which is unknown before the laser is mode-locked. Additionally, inaccurate cross-splices (offset of the fast axis of the first fiber from the slow axis of the second fiber by some small angle) can cause uncompensated linear birefringence which induces filtering/spectral modulation that looks similar to the effect of an intra-cavity Fabry Perot etalon.

In order to better diagnose and solve these potential problems, the all-PM laser was

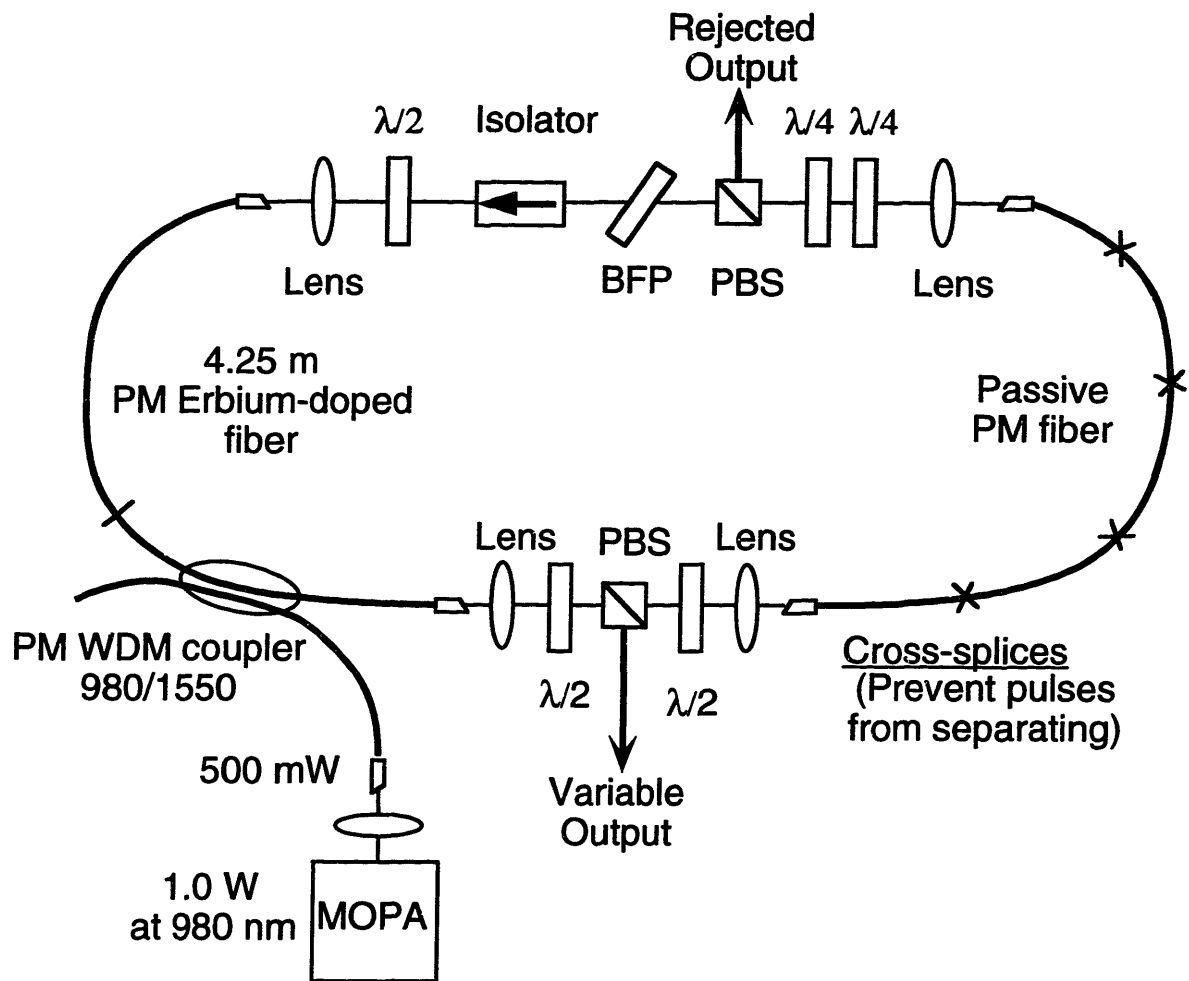


Figure 6-3: Experimental setup of an all-PM Er<sup>3+</sup>-doped fiber laser. WDM: wavelength-division multiplexing coupler, PBS: polarizing beam splitter, and BFP: birefringent tuning plate. In the PM Er-doped fiber section, the light is linearly polarized along one of the PM axes, so no APM action occurs in this fiber. The section of passive PM fiber is repeatedly cross-spliced so that the pulses stay overlapped and both SPM and XPM occur, aiding the pulse shortening.

built in stages starting with the design of Fig.6-3 with standard SMF-28 fiber replacing the PM-cross-spliced fiber. The cavity was composed of 4.3 meters of commercial Fujikura PM Er<sup>+3</sup>-doped fiber with unknown GVD, 0.66 meter of Fujikura Panda PM fiber with GVD of  $-22 \text{ ps}^2/\text{km}$ , 1.1 meters of Bowtie PM fiber with unknown GVD, and 5.5 meters of SMF-28 fiber with GVD of  $-22 \text{ ps}^2/\text{km}$ . The net dispersion of the laser was measured to be  $\approx -0.18 \text{ ps}^2$ , indicating that the pulses should be soliton-like. We were able to achieve self-starting, mode-locked operation with spectra showing typical sidebands due to periodic perturbation of the soliton. With single-pulse operation and 400 fsec pulses, the single-pulse energy should have been 45 pJ with  $\approx 1 \text{ mW}$  intra-cavity power for this net dispersion. The laser, though, tended to operate with multiple pulses. The threshold pump power for mode-locking was very high ( $\approx 250 \text{ mW}$ ), which we believe was due to reflections in the cavity from fiber ends and splice losses. This caused the intra-cavity power at the self-starting point to be higher than the allowable intra-cavity power for single-pulse operation. Thus the laser self-started to multiple pulses. We could reduce the number of pulses in the cavity by attenuating the pump power, but rarely could achieve single-pulses before the laser dropped out of mode-locked operation.

Although achieving controllable single-pulse operation is certainly the goal, we replaced the SMF-28 fiber with cross-spliced PM fiber to try to prove the principle of P-APM and mode-locked operation in this all-PM fiber configuration. Reducing reflections in the cavity could eliminate the high self-starting threshold and eventually allow single-pulse operation. The PM-fiber length between cross-splices can be determined with knowledge of the beat-length and expected pulse width. We calculate what fiber length  $L_s$  is required for two pulses which are launched on the slow and fast axes to separate by a pulse width ( $t_p$ ) due to linear birefringence. (We want to keep the pulses overlapped in the fiber to take advantage of both SPM and XPM for APM action.) This can be expressed by

$$t_p = L_s \left( \frac{1}{v_x} - \frac{1}{v_y} \right) \quad (6.31)$$

where  $t_p$  is the pulse width,  $L_s$  is the fiber length, and  $v_x = c/n_x$  is the velocity on the slow axis while  $v_y = c/n_y$  is the velocity on the fast axis. The fiber length  $L_s$  is then

$$L_s = \frac{ct_p}{\delta n} = \frac{ct_p \lambda}{\ell_b} \quad (6.32)$$

where  $\ell_b$  is the beat length as defined previously. For Panda PM-fiber,  $\ell_b = 3.7 \text{ mm}$  and for a 500 fsec pulse,  $L_s = 38 \text{ cm}$ .

We first tried using 7 meters of PM fiber which was cross-spliced every 50 cm in the cavity. We could not find self-starting mode-locked operation with this configuration and believe that the cross-splices caused the problem. If the cross-splices had high loss or caused reflections in the cavity, self-starting would have been inhibited. Additionally, at each cross-splice an offset angle  $\rho$  between the slow axis of the first fiber and fast axis of the second fiber causes the pulse power along the PM axes to decrease by a factor of  $(\cos \rho)^2$ , as shown in Fig. 6-4. At the cross-splice the light along the slow axis  $E_x$  is divided such that  $E_x \cos \rho$  travels along the fast axis, while

$-E_x \sin \rho$  remains along the slow axis. (And similarly,  $E_y$  on the fast axis is divided after the cross-splice such that  $E_y \cos \rho$  travels along the slow axis and  $E_y \sin \rho$  remains along the fast axis.) The components proportional to  $\sin \rho$  are then essentially lost since they walk off from the  $\cos \rho$  components due to uncompensated linear birefringence. The transmitted power is thus decreased by a factor of  $(\cos \rho)^2$ . For the 7 meters of PM fiber with 13 cross-splices, if the angular offset  $\rho \approx 5$  deg at each splice, the estimated loss would be  $1 - [(\cos \rho)^2]^{13} = 10\%$ . Improvement of the cross-splice quality through use of an auto-aligning PM fusion splicer may result in offsets as small as 0.125 deg and thus may facilitate mode-locked operation.

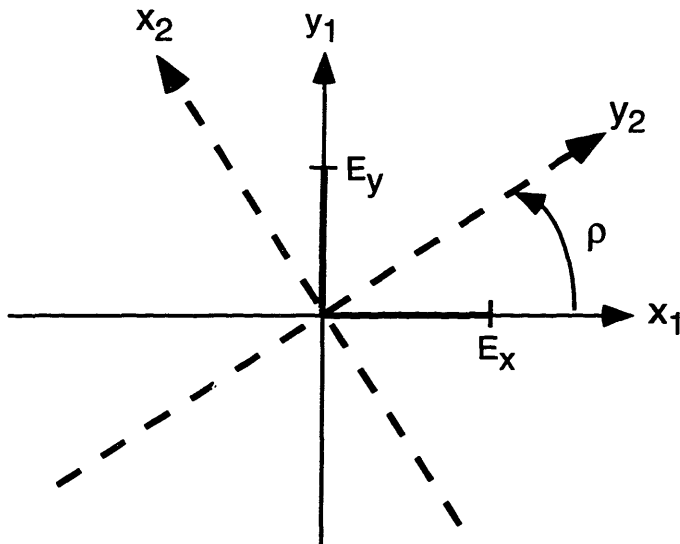


Figure 6-4: Diagram of the offset angle  $\rho$  between fast and slow axes at a cross-splice.  $x_1$  and  $y_1$  are the slow and fast axes, respectively, of the first fiber, while  $x_2$  and  $y_2$  are the slow and fast axes of the second fiber. For an optimum cross-splice,  $y_2$  would overlap  $x_1$ . An offset angle  $\rho$  between  $y_2$  and  $x_1$  decreases the transmitted power by a factor of  $(\cos \rho)^2$  due to walkoff from uncompensated linear birefringence.

Next we simplified the all-PM laser and eliminated some of the cross-splicing problems by using a 6.6 meter length of PM Panda fiber with a single cross-splice in the center. The fast and slow axes were carefully aligned, and the fiber lengths were carefully measured before and after splicing to ensure that they were matched as accurately as possible. With this configuration the pulse would be launched off-axis into the PM-fiber and the two polarizations would completely walk off from each other in the first PM fiber section, and then would walk back together by the end of the second matched PM-fiber section. So the pulses in the two orthogonal polarizations are overlapped for only a segment of the cross-spliced PM-fiber length. Although this pulse separation causes a reduction in the XPM terms of eqns. (6.5) and (6.6), we were able to obtain mode-locked operation with this all-PM configuration with a single cross-splice. Fig. 6-5 is a plot of the spectrum which shows large cw spikes along with the mode-locked spectrum. Mode-locking was difficult to find and required high pump powers ( $< 400$  mW); the pulses were unstable and dropped out completely

after  $\approx 5$  minutes.

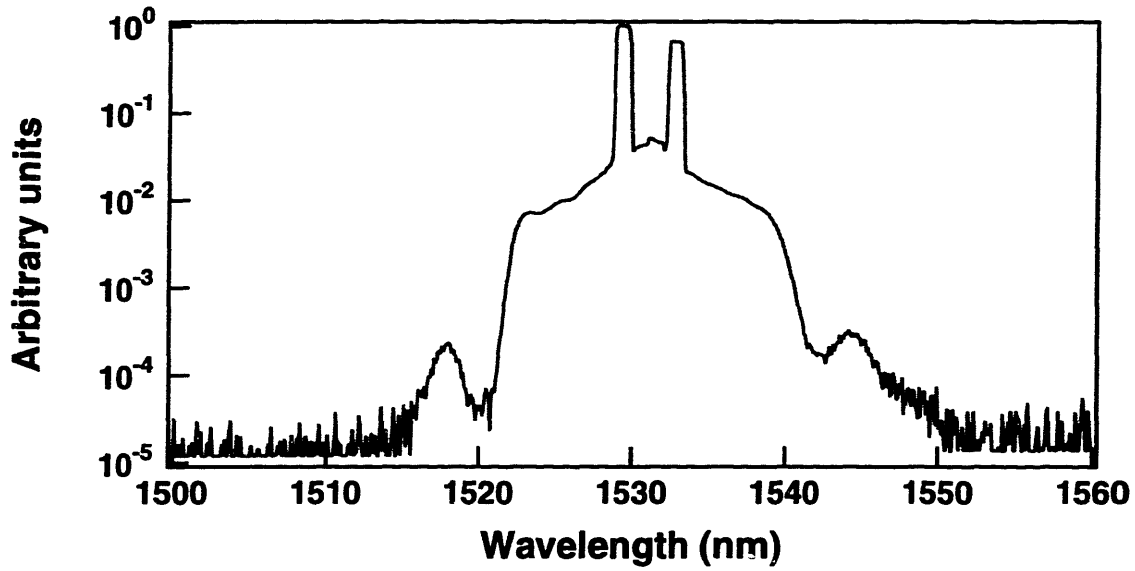


Figure 6-5: Spectrum of pulses from all-PM fiber laser with one cross-splice.

We believe that the instability was due to sensitivity of the fiber birefringence to local temperature changes. (The fiber was simply set out on the optical table; no precautions were taken for temperature stabilization since we were trying to achieve environmental stability.) After placing the fiber in an insulated box, the stability improved and pulses lasted as long as 15 minutes. In chapter 5 the temperature dependence of the birefringence was measured to be  $d(\delta n)/dT \approx -1.3 \times 10^{-7}/\text{deg C}$ . If the temperature effects were global, such that the entire fiber changed temperature by the same amount, the cross-splice would have compensated for the birefringence change as explained by the following. The linear phase bias  $\phi_b$  between the two PM axes at the end of the cross-spliced fiber is

$$\phi_b = \frac{2\pi}{\lambda} (\delta n \Delta L) \quad (6.33)$$

where  $\delta n$  is the fiber birefringence and  $\Delta L$  is the amount by which the cross-spliced fibers are mismatched in length. The temperature dependence is then

$$\frac{d\phi_b}{dT} = \frac{2\pi}{\lambda} \frac{d(\delta n)}{dT} \Delta L + \frac{2\pi}{\lambda} \frac{d\Delta L}{dT} (\delta n) \quad (6.34)$$

where the second term is negligible for  $\Delta L < 5$  mm using eqn. (5.13). The phase bias sensitivity would then be less than  $\pi(8.5 \times 10^{-4})/\text{deg C}$  for a length mismatch  $\Delta L \leq 5$  mm if the temperature effects were global. Such small changes in phase bias with temperature would not have caused the observed unstable mode-locked operation. Local temperature effects, on the other hand, cause larger variations in phase bias. The length mismatch  $\Delta L$  in eqn. (6.34) is now replaced by a length  $L$  which could be on the order of 50 cm or meters. The phase bias sensitivity would then be as much

as  $0.34\pi/\text{deg C}$  for a 2 meter fiber length, which is certainly sufficient to move the laser away from the proper bias point for pulsed operation.

A possible way to reduce the bias temperature sensitivity is to repeatedly cross-slice the PM-fiber with short lengths. If the lengths were 10 cm (the shortest segments that could feasibly be cross-spliced together), the bias temperature dependence would be less than  $0.017\pi/\text{deg C}$ . But if a cross-spliced PM-fiber length of  $> 5$  meters is needed for sufficient P-APM to achieve pulses, performing 50 accurate cross-splices for a single laser would be unreasonable. There may be other methods of reducing or canceling the temperature sensitivity of the birefringence of PM-fiber. Using a fiber with smaller linear birefringence (beat-length  $\sim 10$  cm) should lower the temperature sensitivity by more than an order of magnitude. In the all-PM fiber laser scheme described above, we chose to use the Panda fiber with high birefringence ( $\ell_b = 3.7$  mm) because it was commercially available, and not because the experiment required the short beat-length. Custom PM fibers could be tailored to a variety of beat-lengths by changing the fiber geometry. Secondly, in the fiber sensor field, there have been reports of PM fibers which are constructed to be temperature insensitive. A group at Fujikura developed a PM fiber in which the temperature dependence of the fiber birefringence was cancelled by the thermal stress of a multi-layer plastic jacket [131]. Another method for minimizing the temperature sensitivity involves balancing the built-in stresses of a double-clad, elliptical core fiber with properly-chosen refractive-index differences and core ellipticity [132,133]. The thermal expansion coefficient of the core can be increased by adding dopants such as  $\text{P}_2\text{O}_5$  or  $\text{B}_2\text{O}_3$ , while that of the cladding can be decreased by adding  $\text{TiO}_2$  and  $\text{F}_2$ . Most recently, passive temperature-compensating packages for optical fiber Bragg gratings have been developed which vary the strain in proportion to and opposite to the temperature change [134,135]. The strain compensation is achieved automatically and passively with a mount made of two materials with different thermal-expansion coefficients. The technique possibly could be applied to an all-PM fiber laser to balance the change in birefringence with temperature by a change in length. Closer examination of these schemes would be an interesting subject for additional research on an all-PM fiber ring laser.

If the temperature dependence problem could be solved, we could eventually hope to construct an all-PM fiber laser with only fiber components and no bulk waveplates. This would involve knowing the angle of the linear polarization at the input of the PM fiber relative to the PM-axes of the fiber, which we should be able to determine from the bulk setup. We could then replace the small air gap with an output coupler and a splice between the output coupler and passive PM-fiber with the proper offset angle between the two fast axes. The linear phase bias after the passive PM-fiber could be accomplished by cutting the fiber length to the proper fraction of the birefringent beat length. Many of the other bulk components such as the isolator and output coupling could also be replaced by fiber components, allowing an environmentally stable, all-PM fiber laser.

## 6.3 Stretched-Pulse Sigma Laser

An alternative approach to using PM-fiber for environmental stability is to cancel any changes of the linear bias which occur in non-PM fiber. The work of Fermann and co-workers follows this principle using a linear topology and PM-fiber [113,114,127]. It is apparent, though, that non-PM fiber could be used instead, since the cavity geometry cancels the changes in linear phase bias due to environmental effects [136]. An alternative cavity design to that of Fermann incorporates a non-PM linear section with a ring section constructed of PM-fiber and has been demonstrated by Duling and co-workers [136,137,138]. The laser has been denoted as a "sigma laser" due to its cavity geometry. A modulator in the PM ring section and P-APM in the non-PM branch have generated harmonically mode-locked pulses of 820 fsec at 500 MHz [137] and 1.3 psec at 10 GHz [138]. This section reports work on a stretched-pulse sigma laser operating with significantly higher single-pulse energies. The cavity design is shown in Fig. 6-6 and should be environmentally stable<sup>2</sup>.

The cavity shown in Fig. 6-6 is a traveling-wave cavity, and the path of a pulse is as follows. Light exits the negative dispersion fiber of the ring with linear polarization and passes through the isolator and PBS with no attenuation. The quarter- and half-wave plates set the polarization ellipse followed by the Faraday rotator, which rotates the polarization state by 45 deg. The ellipse then enters the non-PM section consisting of the WDM fiber and Er<sup>+3</sup>-doped fiber where it undergoes nonlinear polarization rotation as well as amplification. A Faraday rotator and mirror at the Er<sup>+3</sup>-doped fiber end flips the polarization state by 90 deg so that the polarization state propagates back through the fiber in the orthogonal polarization state. As explained previously, this causes the total linear phase delay between the two orthogonal polarizations to be zero after a round-trip through the "pigtail" (straight) section and thus compensates any linear phase drifts in the fiber due to environmental effects. Nonlinear phase shifts which are required for pulse-shaping are obviously not compensated. The light then passes back through the first Faraday rotator and back through the waveplates which now provide the proper bias so that the peak of the pulse is reflected by the PBS (P-APM polarizer) and enters the ring section, while the wings of the pulse pass through the PBS and are extinguished in the isolator. A half-wave plate and PBS after the P-APM polarizer serve as a variable output coupler and the filter provides bandwidth control and some tuning. The light enters the negative dispersion fiber with linear polarization. In this first version of the laser, SMF-28 fiber was used in the ring section. This fiber will be replaced by PM-fiber to ensure optimal environmental stability, but we do not expect changes in mode-locked operation since the pulse is linearly polarized in the entire negative dispersion section.

The last element in the ring section is a LiNbO<sub>3</sub> amplitude modulator for pulse start-up. Although the laser is a traveling-wave cavity which should facilitate self-starting, there were numerous possible reflection surfaces on bulk elements in the cavity. A first-order reflection in the pigtail section could form an etalon with the

---

<sup>2</sup>This work was done with D. J. Jones and initial results were submitted to the Conference on Lasers and Electro-Optics, Baltimore, MD, May 18 - 23, 1997.



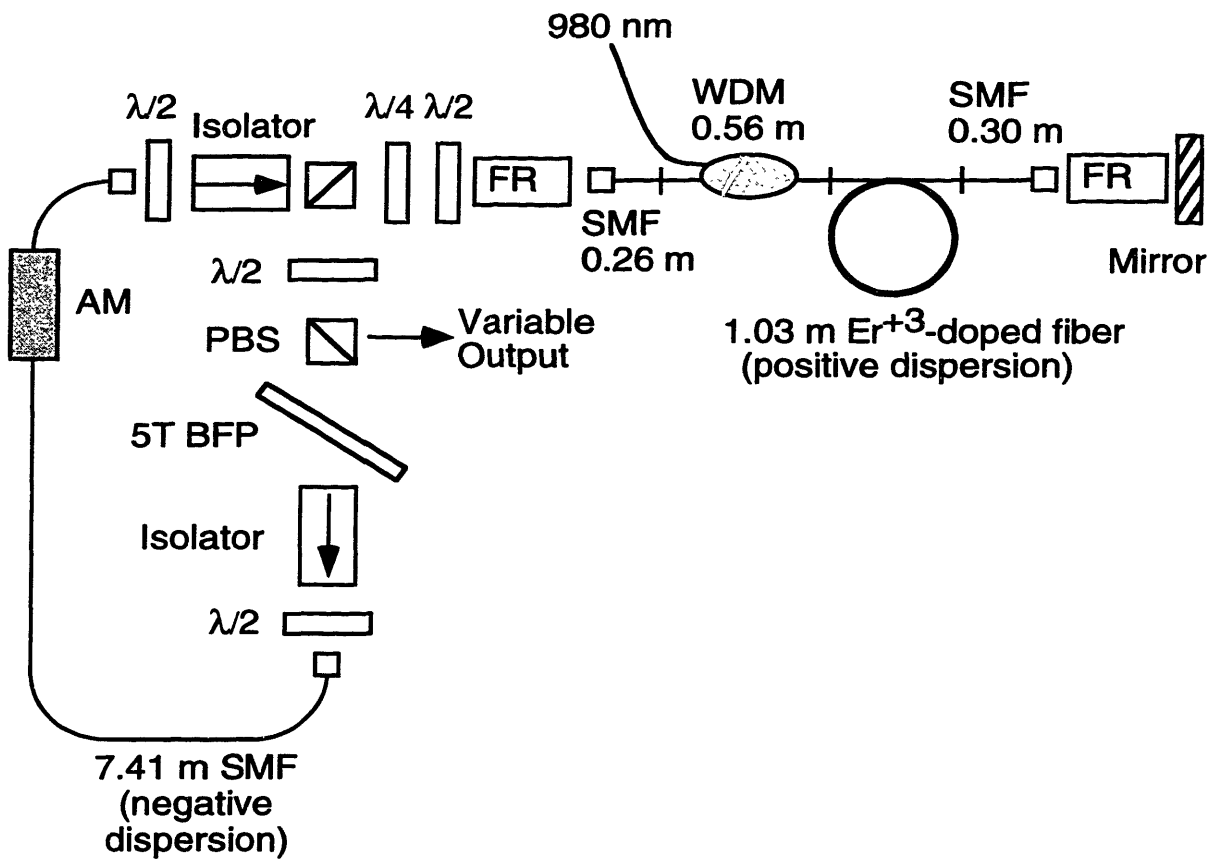


Figure 6-6: Experimental setup for the stretched-pulse sigma laser. FR: Faraday rotator, WDM: wavelength-division-multiplexing coupler, BFP: birefringent tuning plate, and AM: amplitude modulator.

Faraday rotator mirror which would induce mode-pulling and increase the self-starting threshold. After mode-locking was initiated with the modulator and adjustment of the waveplates and filter, the modulator was turned off and single-pulse operation remained. The sigma laser has several advantages over previous schemes which use a Faraday rotator mirror to cancel environmental effects. First, the use of a ring section after the P-APM polarizer instead of a simple mirror provides a unidirectional section which then allows use of a traveling-wave amplitude modulator which is fiber-coupled and easier to synchronize than a standing-wave modulator. The ring-like geometry also reduces spatial-hole burning so that self-starting should be eventually possible. Secondly, using non-PM fiber in the pigtail section allows flexibility in the type of  $\text{Er}^{+3}$ -doped fiber used in the cavity. Instead of being limited to commercially available PM  $\text{Er}^{+3}$ -doped (which tends to have low doping and negative GVD), we were able to use highly-doped, positive-GVD  $\text{Er}^{+3}$ -doped fiber (1128-2). With passive negative dispersion fiber in the ring section, the laser operates in the stretched-pulse regime where higher single-pulse energies and shorter pulses can be achieved than in the soliton regime. The WDM coupler can also be non-PM. Additionally, the output is taken from a variable output coupler which provides a higher quality pulse compared to stretched-pulse lasers which use the rejection port as the output port (as in Chapter 4).

The sigma laser of Fig. 6-6 was optimized for stretched-pulse operation by placing the gain fiber in the pigtail section where nonlinear polarization rotation occurs. The output coupler was placed immediately after the P-APM polarizer (and after the double pass through the gain fiber) in order to maximize the output pulse quality and power. Coupling out a large fraction of the intra-cavity power at this point in the cavity is also important because it decreases the power in the negative GVD fiber and eliminates pulse break-up into multiple pulses due to higher-order soliton formation. In order to minimize losses in mode-locked operation, a pulse minimum should occur near the Faraday rotator mirror at the end of the  $\text{Er}^{+3}$ -doped fiber since this will maximize nonlinear polarization rotation. The second pulse minimum should occur close to the middle of the negative dispersion fiber ring section. With the  $\text{Er}^{+3}$ -doped fiber immediately before the output coupler, the pulse exits the cavity with a large positive frequency chirp which can then be compensated with a grating or prism pair.

With the fiber lengths shown in Fig. 6-6 the net (calculated) cavity dispersion was  $+0.020 \text{ ps}^2$  where the lengths of fiber in the pigtail section must be counted twice. Fig. 6-7 shows a spectrum and autocorrelations when the laser was operating with a single pulse per round trip (and the modulator was turned off). The spectrum was 38 nm wide and centered near 1559 nm. The large spectral spike on the lower wavelength side was caused by third-order dispersion and/or the 1530 nm spike in the ASE spectrum of erbium. Although we are still evaluating this spectral structure, at this point we believe that the gain shaping due to the ASE spectrum is probably the more likely cause, because the spike is persistently located at 1530 nm and shifts only slightly when we try to adjust the wave-plates to find different pulse states. The autocorrelations of Fig. 6-7 show the same output pulse which was compressed to 100 fsec with four reflections from a 150 lines/mm grating and to 140 fsec with a double-passed silicon Brewster prism pair. The time-bandwidth products were then

0.47 and 0.66 for the grating and prism compression, respectively.

We repeatedly were able to obtain better chirp compensation with the grating pair, although measurement of the grating/prism separation and calculation [139] showed that both the gratings and prisms were providing  $\approx -0.035 \text{ ps}^2$  of second-order dispersion (GVD). The difficulty of aligning the prisms due to the large Brewster's angle at  $1.55 \mu\text{m}$  may account for some of the discrepancy. Another possible reason for better compression with gratings is the sign of the third-order dispersion (TOD). Compression with silicon prisms provides negative TOD, while compression with gratings provides positive TOD. Although the net cavity (TOD) was  $\approx +0.70 \times 10^{-3} \text{ ps}^3$  as calculated from the values of Table 2.1, the pulse was coupled out almost immediately after the  $\text{Er}^{+3}$ -doped fiber 1128-2 which has a large negative TOD. (Note that the TOD of  $\text{Er}^{+3}$ -doped fiber 1128-2 is twice as large as that of 1128 which was used in Chapter 4). Since we expect a pulse minimum (near transform-limited) at the Faraday rotator mirror, the pulse which exited the output coupler should then have had negative cubic phase distortion, which was partially compensated by the positive TOD of the grating compressor. The negative TOD of the prism compressor added to the cubic phase distortion of the pulse, resulting in a longer pulse and possibly larger pulse wings.

In mode-locked operation, the output power was 17 mW with coupled pump power of  $\approx 180 \text{ mW}$ , and the repetition rate was 15.67 MHz. Mode-locking was initiated at the same pump power level with a modulation depth of 0.5 dBm at 46.9969 MHz. (The 3-dB points of the RF amplifier gain were at 50 MHz and 1 GHz, so we modulated at the third harmonic for pulse initiation.) The low pump power required for starting and maintaining single-pulse operation points to the eventual use of less expensive 980 nm diodes to replace the MOPA as the pump source. At higher pump powers, multiple-pulse operation was observed which was due to "saturation of the P-APM action." As discussed in section 6.1, P-APM in a fiber laser is analogous to a nonlinear interferometer and has a transmission which is sinusoidal as a function of intensity, as in eqn. (6.28) and shown in Fig. 6-8. As the pulse builds up and grows from zero intensity, the transmission increases. But at larger values of pulse intensity, the nonlinear phase shift is greater than  $\pi/2$  and the transmission rolls over (APM saturates). In the laser, as the pump power is increased, a pulse forms and increases in peak intensity until APM saturation. Then if the pump power is increased further, the pulse must break up into multiple pulses since the intra-cavity power is increasing with pump power. The APM curve can be shifted over so that saturation occurs at higher peak intensity by changing the phase bias  $\phi$ , as shown in Fig. 6-8. But setting the transmission too low for cw can cause difficulties with having sufficient intra-cavity power to obtain mode-locking. A practical way to move the APM saturation point to higher intensities is to decrease the nonlinear coefficient  $\kappa$  by cutting back the fiber in the pigtail section. In the sigma laser, though, this fiber also provides the gain, so the fiber will have to be cut back carefully to balance the increased APM saturation intensity with the decrease in gain.

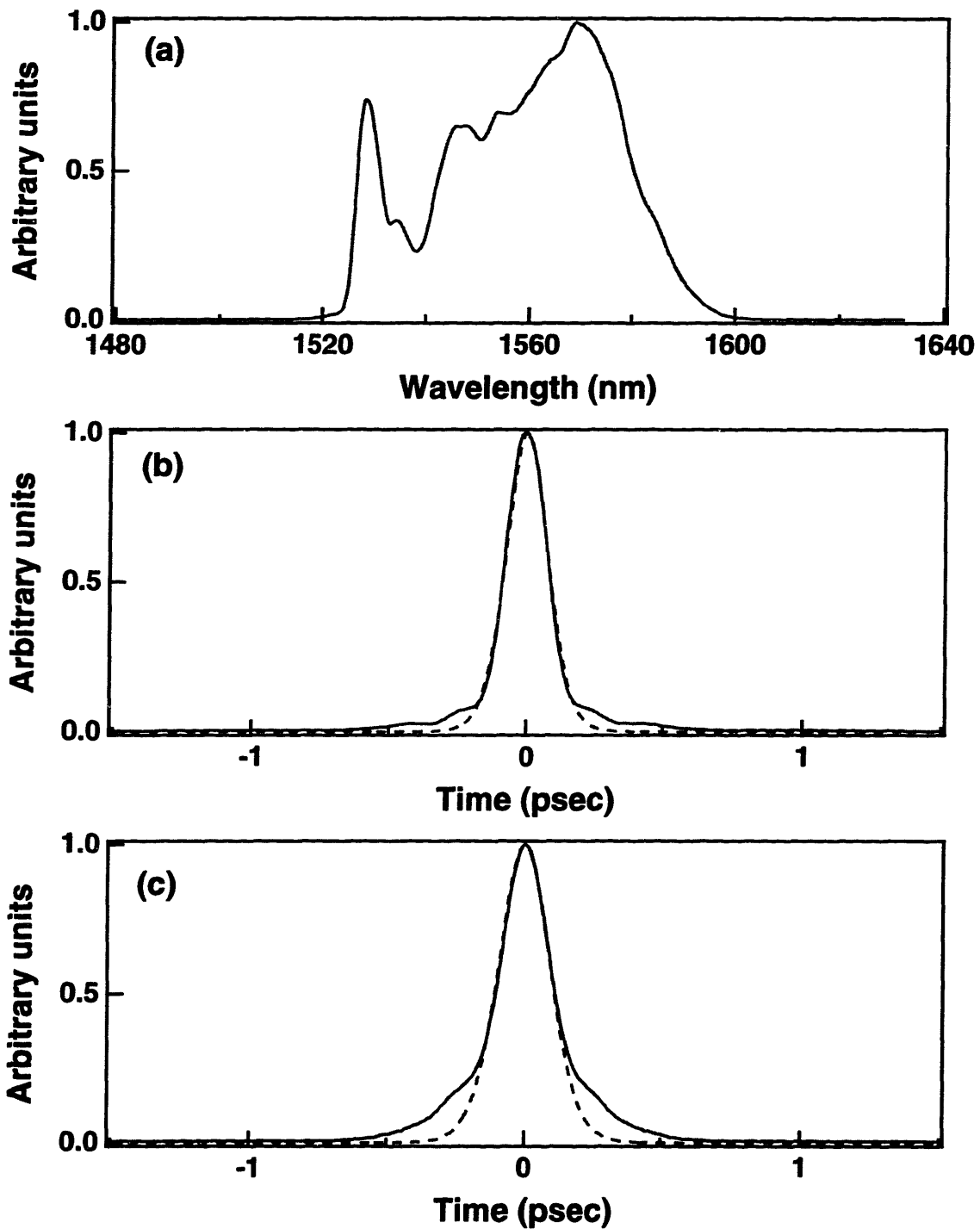


Figure 6-7: Spectrum (a) and autocorrelations of the same pulse from the stretched-pulse sigma laser after compression with gratings (b) or prisms (c). The autocorrelations are fit with a sech (dashed).

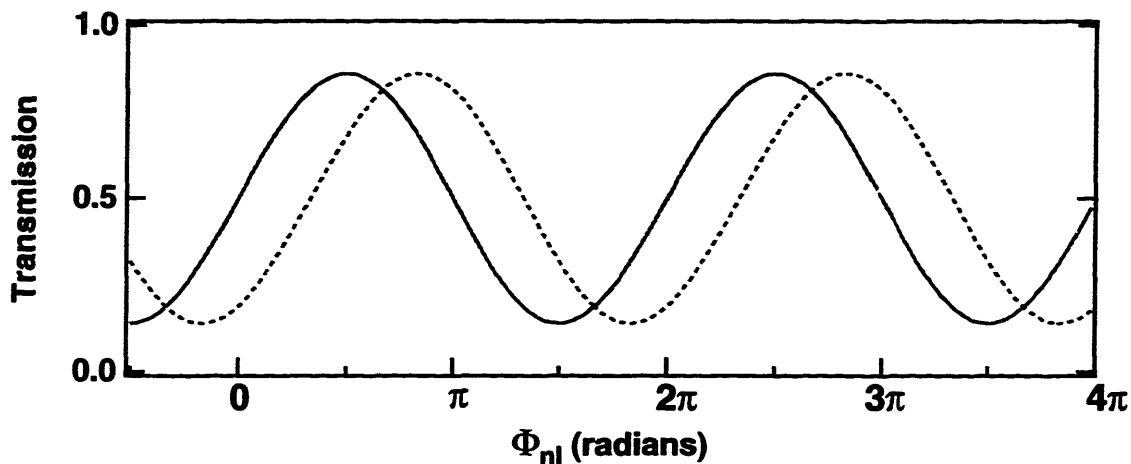


Figure 6-8: Transmission versus nonlinear phase shift  $\phi_{nl}$  for eqn. (6.26) with  $r^2 = 0.85$ ,  $\sin 2\theta = 1$ , and  $\phi_{nl} = 2\kappa|a|^2(2r^2 - 1)$ . For the solid curve, the phase bias  $\phi = \pi$ , while for the dashed curve  $\phi = 2\pi/3$ . Transmission is  $|b|^2/|a|^2$ .

### 6.3.1 Further work on the stretched-pulse sigma laser

There are a number of potential improvements of the sigma laser which would help in approaching our goal of an environmentally stable, high-power laser with short pulses. Working to avoid APM saturation is important for achieving power levels closer to those of the stretched-pulse laser of Chapter 4. Self-starting (without the amplitude modulator) is also an important issue since it would greatly decrease the cost of the laser and complexity of the drive components. (Although reducing reflections is an obvious suggestion, this is not easy to do at this point when all bulk components are AR coated and the fiber ends are angled and also AR coated.) Saturable Bragg reflectors (SBR) have been successfully used to start linear cavity lasers [127], and we are working to obtain an SBR sample to use at the Faraday rotator mirror. The SBR should initiate mode-locking but should not limit the final pulse width because the laser will still use P-APM. In a different direction, the sigma laser could be harmonically mode-locked [138] where modulating at 1 – 10 GHz would set the pulse timing. Pulse shaping in the environmentally stable P-APM section could provide pulse shortening beyond the capability of the modulator. In order to fill all the time slots, the laser would be required to operate in the soliton regime where the soliton fixed-area condition determines the soliton peak power for a given pulse width. Operation in the soliton regime would require a re-design of the fiber dispersion distribution in the cavity.

# Chapter 7

## Conclusions and Suggestions for Future Work

### 7.1 Summary

This thesis reported design and characterization of passively mode-locked  $\text{Tm}^{+3}$ -doped and  $\text{Er}^{+3}$ -doped fiber lasers as well as study of the effect of birefringence on mode-locking. Progress made on each topic is summarized in the following sections.

#### 7.1.1 Mode-locked thulium-doped fiber laser

Tunable, passive mode-locking of a  $\text{Tm}^{+3}$ -doped fiber laser was demonstrated for the first time by extending the use of Polarization Additive Pulse Mode-locking (P-APM) to longer wavelengths [75]. Self-starting pulses of 350 to 500 fsec were generated over a tuning range of 1.8  $\mu\text{m}$  to 1.9  $\mu\text{m}$ . This mode-locked tuning range is the largest reported from rare-earth doped fiber lasers and can be compared with 50 nm of tuning from an  $\text{Er}^{+3}$ -doped fiber laser [140] and 75 nm of tuning from a  $\text{Nd}^{+3}$ -doped fiber laser [141]. This  $\text{Tm}^{+3}$ -doped fiber laser operated in the soliton regime due to the large negative dispersion of the fibers and thus had spectral sidebands due to resonant dispersive radiation generated by perturbations to the soliton. The large net negative dispersion of the laser allowed operation closer to the resonant instability point (where the nonlinear phase shift per pass is  $2\pi$ ) than in previous mode-locked  $\text{Er}^{+3}$ -doped fiber lasers [21]. Operation in the soliton regime, though, still put a limit on the pulse width ( $> 350$  fsec) and pulse energy ( $< 0.6$  nJ intracavity). Average output powers of up to 0.65 mW were obtained from the 5% output coupler, and output powers as high as 5.7 mW were obtained by using the rejected polarization port as the output port. Suggestions for improvements to the  $\text{Tm}^{+3}$ -doped fiber laser were also discussed including using a multiple-plate birefringent filter to obtain larger tuning range and operating in the stretched-pulse regime to obtain higher output powers and shorter pulses. Subsequent to this work, Sharp et. al. [29] reported mode-locking of a  $\text{Tm}^{+3}$ -doped fiber laser with a semiconductor saturable absorber to generate 190-fsec pulses and up to 1 mW of output power, but this laser was not tunable.

Work on the mode-locked  $\text{Tm}^{+3}$ -doped fiber laser at  $1.8 \mu\text{m}$  brought up the interesting prospect of using a  $\text{Tm}^{+3}$ -doped source for optical coherence tomography (OCT) on biological tissues. Areas of current emphasis in OCT include obtaining inexpensive, compact sources and performing multiple wavelength scans on the same tissue. Diode-pumped rare-earth doped fibers operated as either amplified spontaneous emission (ASE) sources or mode-locked sources can potentially fulfill this need. A  $\text{Tm}^{+3}$ -doped fiber ASE source was constructed and optimized to yield output powers as high as 7 mW with bandwidth of 80 nm centered at 1808 nm. This source then had a spatial resolution of  $20 \mu\text{m}$  for OCT. An OCT image of a biological tissue was obtained with this source and compared to the image obtained with a broadband  $1.3 \mu\text{m}$  source of the same spatial resolution. The results were promising; the two images had comparable resolution, with the  $1.8 \mu\text{m}$  image showing a slightly larger penetration depth. Continued examination of the feasibility of using a  $\text{Tm}^{+3}$ -doped fiber source for imaging is currently being done by members of Professor Fujimoto's group at MIT.

### 7.1.2 Stretched-pulse laser and frequency doubling

Extension of previous work on  $\text{Er}^{+3}$ -doped fiber lasers [84,93] was also reported in this thesis and in [92]. A stretched-pulse laser was optimized for the application of frequency doubling through proper choice of the net cavity dispersion and backwards pumping a longer piece of  $\text{Er}^{+3}$ -doped fiber. The laser generated output pulses of 3.0 nJ at 31.8 MHz directly from the cavity, which were then compressed to 100 fsec with 90% transmission through a sequence of four silicon Brewster prisms. These fundamental pulses were frequency doubled with a 1-cm  $\beta\text{-BaB}_2\text{O}_4$  (BBO) crystal to achieve conversion efficiency of up to 10%. The frequency-doubled pulses were near transform-limited with 86-fsec pulse width at 771 nm and with average power of 8.7 mW. Two other nonlinear crystals, 1.5 mm potassium niobate ( $\text{KNbO}_3$ ) and 7.0 mm lithium triborate (LBO), were also used for frequency-doubling. Spectral narrowing occurred in both crystals due to significantly smaller phase-matching bandwidths as compared with BBO.

Frequency-resolved optical gating (FROG) measurements were performed on both the fundamental and frequency-doubled pulses using spectrally resolved autocorrelation. The SHG FROG trace of the  $1.55 \mu\text{m}$  pulses showed that the lower frequency components were contained in the pulse wings, and thus efficient frequency doubling occurred at shorter wavelengths. This explained why the frequency-doubled spectrum was centered at 771 nm rather than at 776 nm as predicted by the first moment of the fundamental spectrum. A low frequency amplitude noise measurement was also performed on the doubled pulses and compared with a commercial argon-ion-pumped mode-locked Ti:Sapphire laser. The amplitude fluctuations on the frequency-doubled pulses were 40 dBc/Hz lower over the range from 3 kHz to 100 kHz. The difference in noise spectra was due to the long, 10-msec upper-state lifetime of  $\text{Er}^{+3}$  and the argon-ion pump of the Ti:Sapphire laser. These experiments showed that the frequency-doubled stretched-pulse fiber laser, producing 270 pJ pulses at 771 nm, could replace the mode-locked Ti:Sapphire laser as the seed for a Ti:Sapphire regen-

erative amplifier, where 100 pJ seed pulses are sufficient for dominance over amplified spontaneous emission [98]. The technology of the stretched-pulse laser was licensed to Clark MXR, Inc. (Dexter, MI) who now have commercial products based on the stretched-pulse laser and frequency-doubled stretched-pulse laser.

### 7.1.3 Linear birefringence on P-APM

Although the stretched-pulse laser operates reliably and has been packaged as a commercial laser for laboratory applications, extending its use to non-laboratory applications requires "turn-key" operation and environmental stability. The standard fiber which comprises the present laser has a small birefringence with beat-length  $\sim 1$  meter which is sensitive to environmental changes. This thesis reported work related to the construction of an environmentally stable mode-locked fiber laser including techniques for measuring the beat-length and temperature sensitivity of both standard and PM-fibers. By setting up a length of PM Panda fiber (with  $\delta n = 4.2 \times 10^{-4}$ ) as a birefringent filter, the temperature dependence of the birefringence was measured to be  $\approx -1.3 \times 10^{-7}/\text{deg C}$ . Simulations of the effect of linear birefringence on P-APM were performed to explore the regime of standard fibers in a soliton laser, where the effects of linear birefringence and nonlinear polarization rotation are of the same order. Birefringence reduces the nonlinear polarization rotation, but discrimination between the peak and wings of the pulse still occurs due to the intensity dependence of the beat-length. The simulations also showed that the fiber beat-length does not cause any inherent periodicity of the pulse-shaping, so there is no particular laser length at which P-APM will be cancelled out due to birefringence.

### 7.1.4 Environmentally stable mode-locked fiber laser

Using PM-fiber in a mode-locked fiber laser may seem to be an obvious means of obtaining environmental stability because the locations of the fast and slow axes are fixed under changing environmental conditions. When linearly polarized light is launched down either PM axis, the polarization state is stable and cross-talk of  $< -30$  dB occurs. But light which is launched off-axis changes polarization state rapidly due to the fiber birefringence. It is not obvious then that APM would work in PM-fibers. An evaluation of the pulse-shaping which can be achieved by APM in PM-fibers was performed and compared with non-PM fibers. The analysis showed that although the nonlinear phase shift per pass was a factor of 2 smaller than in non-PM fibers, pulse shortening could still be achieved in PM-fibers. An all-PM fiber laser was designed and built, but stable mode-locking was not achieved due to the local temperature sensitivity of the PM-fiber birefringence which resulted in a changing phase bias and pulse instability. Possible methods of eliminating this temperature sensitivity include using smaller PM-fiber lengths between cross-splices, PM-fiber with lower birefringence, and PM-fiber which is designed to compensate for its birefringence change with temperature. As an alternative scheme to the all-PM ring laser, the sigma laser used PM-fiber in a unidirectional ring with a non-PM fiber pigtail section. The cavity geometry allows cancellation of changes in the



linear phase bias due to environmental effects. Stretched-pulse operation of the sigma laser was achieved with sub-110 fsec,  $> 1$  nJ pulses of 38-nm bandwidth generated directly from the variable output coupler of the laser with  $< 200$  mW of pump power. Pulses were initiated by an amplitude modulator and then remained stable after the modulator was turned off. Future work on the stretched-pulse sigma laser should include obtaining self-starting and higher output powers as well as simplifying the cavity design.

## 7.2 Further Work

There are a number of additional areas for future work which were not mentioned previously and may be of general interest. One important limitation on the stretched-pulse laser is the high pump power requirement which implies the use of a Master Oscillator/Power Amplifier (MOPA). Although MOPA's are commercially available, their expense, slow delivery time, and unproven reliability over time scales of more than one year make them unattractive pump sources. Typical stretched-pulse lasers, when optimized for output power, require  $> 300$  mW for self-starting mode-locked operation. But we have observed lower self-starting thresholds in recent lasers (and in the sigma laser) with improved coupling across the air gap. With optimization of the cavity and gain fiber length as well as the higher powers now available from 980 nm fiber-coupled diode lasers, it may be possible to pump the stretched-pulse laser with a single 980 nm diode or two polarization-multiplexed diodes.

### 7.2.1 Co-doped and cladding-pumped fibers

Several recent developments in the field of optical fibers could significantly improve the operation of the fiber lasers discussed in this thesis or provide new directions for research. Co-doped fibers (such as Er-Yb) and cladding-pumped fibers increase the number of options for pump wavelengths and pump diode laser types. Although MIT does not have facilities for fabricating fibers, collaborating with other groups to test their new fibers in our lasers might lead to interesting results. Cladding-pumped fibers may be on the verge of having significant impact on mode-locked fiber lasers. Continuous-wave 9.2-W Nd<sup>3+</sup>-doped fiber lasers have been demonstrated at  $1.06 \mu\text{m}$  [142], and output powers as high as 23 W have been obtained from cladding-pumped Yb<sup>3+</sup>-doped fiber lasers at  $1.1 \mu\text{m}$  with 35 W pump at 915 nm [143]. Double-clad Er-Yb fibers have already been mode-locked [54] at  $1.55 \mu\text{m}$ . If high pulse energies ( $\sim$  mJ) could be achieved in mode-locked, cladding-pumped fiber lasers, there could be a new set of high-power applications in laser micro-machining and materials processing with short pulses of femtosecond to nanosecond widths [144,145].

### 7.2.2 Bragg gratings

The technology of forming Bragg gratings in fibers is now so well advanced that the gratings can be custom ordered from commercial manufacturers. Bragg gratings

used in reflection are narrow filters (bandwidth  $\sim 1$  nm) and so are not useful for mode-locked fiber lasers. Chirped gratings, though, can have bandwidths  $\sim 20$  nm and have already been used in fiber lasers to obtain high-power soliton operation [146,147]. Since the gratings must be used in reflection, new cavity designs will have to be developed; designs which do not require fiber-coupled circulators could be especially useful. Significant work has also been done on fiber Bragg gratings with long periods (on the order of hundreds of microns) where the grating performs as a spectrally selective loss element by coupling light from a guided mode into a forward-propagating cladding mode which is lost due to absorption and scattering. Their use has been demonstrated in a variety of applications including gain equalizers in optical amplifiers [148] and filters for ASE in  $\text{Er}^{+3}$ -doped fiber amplifiers [149]. These long-period gratings could possibly be used in a fiber laser to smooth the gain spectrum and achieve larger ranges over which the laser could be continuously tuned. Long period gratings may also be useful in lasers which use co-doped fiber for the gain medium as loss elements for unwanted ASE. For example in Er-Yb co-doped fiber when pumping at 980 nm there is significant ASE at  $1.05 \mu\text{m}$  which is not the transition of interest and could adversely affect elements such as a saturable absorber if left unattenuated in the cavity.

### 7.2.3 Semiconductor saturable absorbers

Semiconductor multiple quantum well saturable absorbers and saturable Bragg reflectors are additional elements which could be incorporated into the laser designs of this thesis to aid in self-starting to mode-locked operation. If we want to use passive mode-locking to obtain  $\approx 100$  fsec pulses, we will want to continue to use P-APM for pulse shaping once the slow time response (interband relaxation time) of the saturable absorber has initiated the pulses. To date semiconductor saturable absorber samples have required complicated growth and post-processing procedures and have been known to suffer optical damage and deterioration. New designs such as the saturable Bragg reflector (SBR), consisting of a quarter-wave stack mirror with thin quantum well(s) in the top layer [150,151], do not require post-processing and allow the effective saturation intensity to be engineered by placement of the quantum well relative to the intensity peaks of the standing wave pattern. There are still a number of interesting questions about these saturable absorbers when applied to fiber lasers. One issue is the wavelength location of the excitonic absorption edge for optimum self-starting and mode-locking. A second issue is understanding exactly how the samples induce mode-locking in a fiber laser. The reported 1% saturated absorption of the SBR is quite small compared to the large cavity losses (3 to 4 dB) which can exist in a mode-locked fiber laser. Finally some mystery still exists about why some samples are successful in mode-locking a laser while other, identically-grown samples are not successful.

Saturable absorbers used in reflection would also require new cavity designs if a traveling-wave cavity was still desired. One such design is shown in Fig. 7-1 which incorporates an SBR into the familiar P-APM ring cavity. The half-wave plate after the isolator allows adjustment of the intensity which impinges upon the SBR so that

the effect of the SBR on the laser's operation can be characterized. For fiber lasers at  $1.55 \mu\text{m}$  it may be possible to grow quantum wells on an InP substrate (which transmits this wavelength) such that saturable absorbers could be used in transmission. Saturable absorbers could then be attached to a fiber end as an inexpensive, compact starting element. It may also be possible to design schemes which use saturable absorbers in transmission to achieve stable passive harmonic mode-locking.

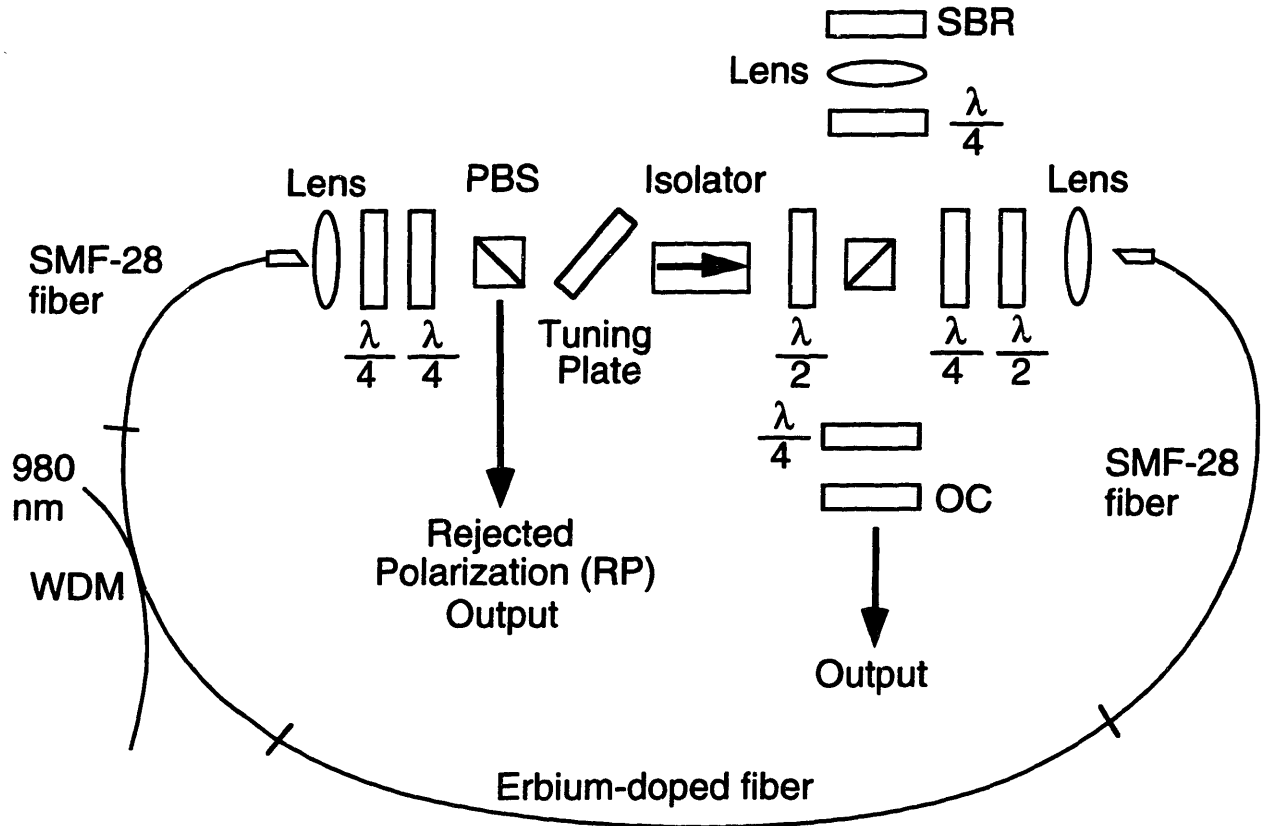


Figure 7-1: Possible design for a mode-locked  $\text{Er}^{+3}$ -doped fiber laser which uses a saturable Bragg reflector and P-APM. The percentage of the intracavity intensity which impinges on the SBR can be adjusted from 0% to 100% so that the effect of the SBR on the mode-locking can be studied.

### 7.2.4 Mode-locked fiber laser applications

Applications of pulsed fiber lasers are the best motivators for areas of continued or new research. The question that should be addressed is, of course, where can ultra-short pulsed fiber lasers make an impact? At the present time there appear to be three main areas of applications for pulsed fiber laser sources: in the laboratory, in optical communications networks, and in medicine. Pulsed fiber lasers have already been

used as seeds for amplifiers [96] and regenerative amplifiers [99,152] in the laboratory. A mode-locked  $\text{Yb}^{+3}$ -doped fiber laser could be used as the seeding source for a Nd:glass amplifier at  $1.053 \mu\text{m}$ . Fiber lasers also have the potential to serve as tunable spectroscopic sources to replace larger color center or Ti:Sapphire laser systems which are costly and difficult to maintain.

In the field of communications there has been recent work on spectrally slicing the broad spectra of a mode-locked fiber laser to form channels for wavelength-division-multiplexing [94,153]. The possibility also exists of using mode-locked fiber lasers at repetition rates  $\sim 300$  MHz for fiber-to-the-home. This application would require that the lasers be constructed very inexpensively and simply. Harmonic mode-locking of fiber lasers to obtain repetition rates of 1 to 10 GHz make them competitive sources for high bit rate time-division-multiplexed communications systems. These lasers have been the focus of much research over the past five years [138,154].

Medicine is an area which also has potential applications for pulsed fiber lasers. As mentioned previously, optical coherence tomography (OCT) would take advantage of the broad bandwidths of mode-locked fiber lasers. Although ASE sources may provide sufficient spectral width for OCT, mode-locked sources are advantageous due to higher powers which allow larger penetration depths and higher signal-to-noise ratios. Tunable fiber lasers could be used in eye surgery, called laser photothermal keratoplasty (LPTK), so that the penetration depth could be matched to the thickness of the cornea, or as seeds for other Q-switched medical lasers. Short pulse fiber lasers may find applications in other types of surgery (orthopedic or dermatology) where the plasma-tissue ablation mechanism can be controlled by adjusting the pulse energy and duration. In medicine as in other areas, communicating with those who could potentially use pulsed fiber laser sources is of vital importance if the sources are to find specific real-world applications outside of the laboratory.

# Appendix A

## Comparison of Forward and Backward Pumping Configurations in Fiber Ring Lasers

Unidirectional fiber ring lasers can be easily pumped in either a forward (co-propagating) or backward (counter-propagating) configuration through the WDM coupler. Within the field of erbium-doped fiber amplifiers, a number of experiments and theoretical analyses have been done to compare the signal gain in the forward and backward pumping configurations [101,155,100]. Generally, the power-conversion efficiency between the pump and signal is higher in the backward-pumping scheme. At first several causes such as fiber excess loss and signal excited-state absorption were proposed to explain the difference in efficiency. But the widely accepted explanation for the pumping difference is that in a saturated erbium-doped fiber amplifier, backward pumping yields higher gains because the pump and signal are both largest at the end of the fiber, and thus the higher pump can counter the larger signal saturation at the fiber end.

Desurvire, though, showed in an analytical paper that in a signal-saturated amplifier the pumping difference is primarily an effect of amplifier "self-saturation" (when the amplified spontaneous emission (ASE) of the fiber is high enough to saturate the gain in the absence of any input signal), which is stronger for forward pumping [100]. The paper reports that in the absence of ASE, there is no discrepancy between the saturated gains obtained in the two pumping configurations *when* the fiber length is optimized for gain for forward pumping. Then when ASE is considered, he claims that in the forward-pumping scheme, there is an important increase in pump absorption due to saturation by the backward ASE, which occurs at the pump input end. This increase in pump absorption where the pump is highest causes decreased gain for forward pumping compared to backward pumping.

The stretched-pulse laser reported in chapter 4 has been pumped in both the forward [84,93] and backward [92] configurations, but the two pumping schemes have not been compared directly with the erbium-doped fiber lengths and pump powers

used in the stretched-pulse laser. There are advantages and disadvantages to both configurations. With a backward-pumping scheme the laser should have more signal gain, but the WDM coupler and a short piece of SMF-28 fiber will be located between the erbium-doped fiber and the air gap where the output is taken at the PBS rejection port. Fusion splices are then required between the gain fiber and the output port, which may cause loss or reflections, thus lowering the output power and/or causing intracavity etalons. The negative dispersion of the WDM and SMF-28 fiber may also cause problems because the high-energy, positively-chirped pulse which exits the erbium-doped fiber starts to compress when it propagates through this length of negative dispersion fiber before the airgap. If this length of negative-dispersion fiber is not sufficiently short, the pulse could break up into a higher-order soliton and seed multiple pulse operation. In the forward-pumping scheme, the erbium-doped fiber can be the last piece of fiber before the airgap thus eliminating problems with fusion splices or negative dispersion. Additionally, the fourth (unused) port of the WDM coupler can be used as an output port ( $\approx 2\%$ ) to monitor the intracavity power and pulse characteristics. But forward-pumping would be expected to result in lower power conversion efficiency.

In order to directly compare the pumping efficiency for the two schemes in the stretched-pulse laser, an erbium-doped ring fiber laser was constructed with essentially the same components as used in chapter 4. As shown in Fig. A-1 the erbium-doped fiber (AT&T 1128-2) was 1.54 meters long and was pumped through the WDM coupler by the 980 nm MOPA. A half-waveplate and PBS were used to create a 50% output coupler in the airgap after the bulk isolator. The coupled pump power was monitored at the fourth port of the WDM, which leaked  $\approx 1.5\%$  of the 980 nm, and the cw output power was measured as a function of input pump power. A fraction ( $\approx 34\%$ ) of the unabsorbed pump power was rejected from the cavity at the opposite PBS port. Measurements were then taken of this unabsorbed pump versus input pump power for both lasing and non-lasing operation (blocking the cavity feedback). The laser was then adjusted to operate in a forward-pumped configuration by simply changing the order of the bulk elements in the air gap and optimizing the laser alignment. Output power versus pump power was again measured, and is shown in Fig. A-2 along with the curve for backward pumping. The pump threshold for lasing was 34 mW for backward pumping versus 38 mW in the forward-pumping case, indicating that the cavity losses were approximately the same for lasers, while the slope efficiencies were 10% and 2.6%, respectively.

An additional PBS was then inserted immediately before the isolator so that the unabsorbed pump power could be measured in the forward-pumping case. The waveplates before this PBS were adjusted to minimize the 1.55  $\mu\text{m}$  power which was rejected, which resulted in a fraction of  $\approx 14\%$  of the unabsorbed 980 nm power rejected. A plot comparing this measurement of unabsorbed pump power versus input pump power for the two pumping schemes is shown in Fig. A-3. (The curves shown are the total unabsorbed pump power, calculated by dividing the measured pump power rejected by the PBS by 0.34 for backward pumping and 0.14 for forward pumping.) In non-lasing operation the unabsorbed pump power was essentially the same for the two schemes, as expected since there was no signal. In lasing operation,

though, the unabsorbed pump power with maximum input pump power was 5.2 mW for backward pumping versus 1.3 mW for forward pumping. This measurement agrees with Desurvire [100] in that there is increased pump absorption in the forward-pumping configuration and less gain. These measurements confirm that backward pumping is advantageous to use in a stretched-pulse laser. Also, with the more efficient power conversion in the backward-pumping configuration, longer erbium-doped fiber lengths can be used for the same available pump powers, resulting in increased gain.

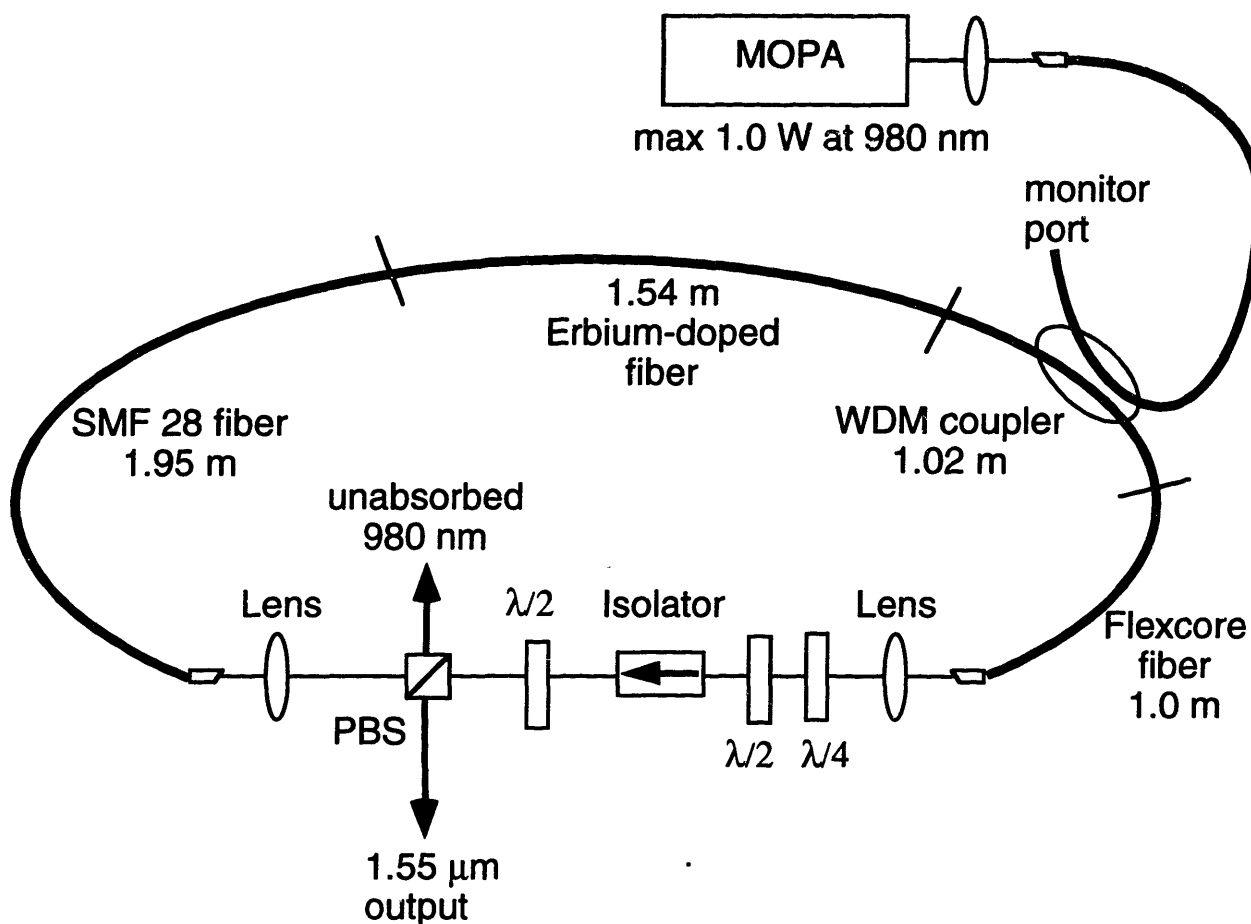


Figure A-1: Experimental setup for measuring output power at 1.55  $\mu\text{m}$  and unabsorbed pump power at 980 nm versus input pump power in the backward-pumping scheme.

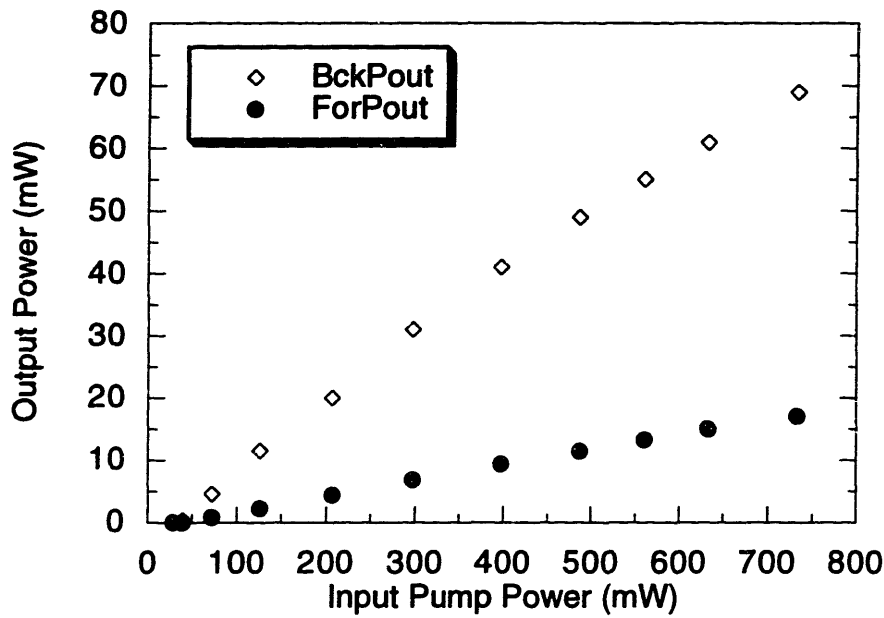


Figure A-2: Plot of output power versus input pump power for backward pumping ( $\diamond$ ) and forward pumping ( $\bullet$ ).

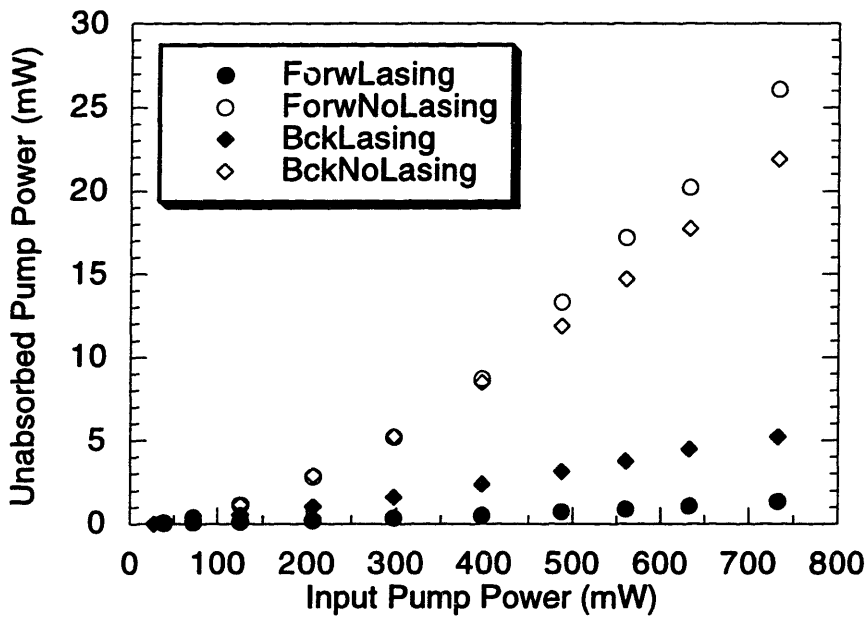


Figure A-3: Plot of unabsorbed pump power versus input pump power for both lasing and non-lasing operation. Backward pumping is indicated by closed and open diamonds for lasing and non-lasing, respectively, while forward pumping is indicated by closed and open circles.



# Appendix B

## Numerical Simulations

This appendix provides greater detail about the numerical simulations used in chapter 5 to explore the effect of linear birefringence on P-APM. First the equation normalization is briefly outlined, and then a sample data file is included which shows the initial polarization state.

### B.1 Normalization of simulation equations

The equations for the evolution of the electric field with birefringence and nonlinear polarization are, from eqns. (5.24) and (5.25),

$$\frac{dE_+}{dz} = -j\delta E_- - j\eta[|E_+|^2 + 2|E_-|^2]E_+ \quad (\text{B.1})$$

$$\frac{dE_-}{dz} = -j\delta E_+ - j\eta[2|E_+|^2 + |E_-|^2]E_-, \quad (\text{B.2})$$

where  $E_+$ ,  $E_-$  are the complex electric field amplitudes of the right-hand circular ( $E_+$ ) and left-hand circular ( $E_-$ ) polarization states,  $z$  is the distance of propagation, and  $\delta = \pi(n_x - n_y)/\lambda$  is the coefficient of birefringence as defined in eqn. (5.18). The coefficient  $\eta$  is the nonlinear coefficient defined as

$$\eta = \frac{\omega \epsilon_0 n_0 n_2}{3} \quad (\text{B.3})$$

where  $\omega$  is the angular frequency,  $\epsilon = 8.85 \times 10^{-12}$  C/V-m is the permittivity of free space,  $n_0$  is the linear refractive index ( $n_0 = 1.44$  for silica fiber at  $1.55 \mu\text{m}$ ), and  $n_2$  is the nonlinear refractive index ( $n_2 = 2.6 \times 10^{-20}$  m<sup>2</sup>/W for silica fibers).

We begin the normalization by recognizing that because  $I = c\epsilon_0 n_0 |E|^2/2$ , the normalized field  $E_{+n}$  can be defined as

$$E_{+n} = E_+ \sqrt{\frac{c\epsilon_0 n_0}{2I}}. \quad (\text{B.4})$$

We then use eqn. (B.4) to substitute for  $E_+$  in eqn. (B.1) and obtain

$$\frac{dE_{+n}}{dz} = -j\delta E_{-n} - j\eta \left( \frac{2I}{c\epsilon_0 n_0} \right) [|E_{+n}|^2 + 2|E_{-n}|^2] E_{+n}. \quad (\text{B.5})$$

Next we divide the entire equation by  $\eta \left( \frac{2I}{c\epsilon_0 n_0} \right)$  to obtain the final normalized evolution equation

$$\frac{dE_{+n}}{dz_n} = -j\delta_n E_{-n} - j\eta_n [|E_{+n}|^2 + 2|E_{-n}|^2] E_{+n}. \quad (\text{B.6})$$

where

$$E_{+n} = E_+ \sqrt{\frac{c\epsilon_0 n_0}{2I}} \quad (\text{B.7})$$

$$z_n = z \eta \left( \frac{2I}{c\epsilon_0 n_0} \right) \quad (\text{B.8})$$

$$\eta_n = 1 \quad (\text{B.9})$$

$$\delta_n = \frac{\delta}{\eta} \left( \frac{c\epsilon_0 n_0}{2I} \right) \quad (\text{B.10})$$

(An analogous equation can be found for  $E_{-n}$  by interchanging  $E_{+n}$  and  $E_{-n}$ .) The strength of the linear birefringence can then be easily compared to the nonlinearity strength by comparing the normalized birefringence coefficient  $\delta_n$  to 1, the normalized coefficient for nonlinearity. (Note that in chapter 5 the subscripts  $n$  were dropped for simplicity.)

## B.2 Sample data file for simulations

File inputdat with parameters from the erbium-doped soliton laser of [21] for running simulation program birefr.f:

```

8.d0          ! beat length in meters
1.34594d-16   ! eta in m/(V*V)
100.d0        ! Peak Power in Watts
8.d-6         ! mode-field diameter in meters
1.4443d0      ! ref. index of fiber at 1.55 um
0             ! idist (flag: 1 = dist (in m), 0 = norm dist)
10.0d0        ! total distance, in m for idist=1, norm for idist=0
0.0001d0      ! step size, in m for idist=1, norm for idist = 0
0.60d0        ! initial amplitude of Ex
70.0d0        ! initial phase difference between Ex and Ey
0.00001d0     ! epsilon, error limit in derivative
1             ! idelta (flag: 1 = use beatlength, 0 = use normdelta)
0.00d0        ! normdelta = deltan when idelta = 0
1             ! ietan (flag: 0 = set etan=0, 1 = use etan=1

```

The following is the output status from program birefr.f which lists the normalized values of the parameters and the initial polarization state:

```

input file          = inputdat
beatlength (m)     = 8.00000000000000

```

eta (m/V <sup>2</sup> )	=	1.345940000000000D-16
total number of steps	=	100000
number of steps between prints	=	100
total norm distance	=	10.000000000000000
total distance (in meters)	=	71.556068316371
conversion: distance	=	7.1556068316371 * norm dist
delta (in 1/m)	=	0.39269908169872
norm. delta	=	2.8100002317810
norm. eta	=	1.000000000000000
Initial values of $E_x$ and $E_y$ :		
Intensity $ E_x ^2$	=	0.360000000000000
Intensity $ E_y ^2$	=	0.640000000000000
$\phi_x - \phi_y$ (in deg)	=	70.0000000000000
Initial values of $E_+$ and $E_-$ :		
$E_+$	=	(0.14510685734529, 0.96436323796421)
$E_-$	=	(0.14510685734529, -0.16700761003579)
$ E_+ ^2$	=	0.95105245478544
$ E_- ^2$	=	4.8947541858493D-02
Normalized values of:		
$\ell_{npr}$	=	6.9650272569665
$\ell_b$	=	1.1180044108390

The important values to note are  $\delta_n = 2.81$  compared to  $\eta_n = 1.0$  resulting in linear birefringence which dominates the nonlinearity. This is also apparent by comparing the normalized values  $\ell_{npr} = 6.97$  to  $\ell_b = 1.12$ , which indicates that the birefringence has a larger effect over a smaller distance.

# Bibliography

- [1] E. Snitzer, "Optical maser action of Neodymium in barium crown glass", *Phys. Rev. Lett.*, vol. 7, pp. 444, 1961.
- [2] E. Snitzer, "Neodymium glass laser", in *Third International Conference on Quantum Electronics*, P. Grivet and N. Bloembergen, Eds. 1963, vol. 1, pp. 999–1019, Columbia University Press.
- [3] C. J. Koester and E. Snitzer, "Amplification in a fiber laser", *Appl. Opt.*, vol. 3, pp. 1182, 1964.
- [4] J. Stone and C. A. Burrus, "Neodymium-doped silica lasers in end-pumped fiber geometry", *Appl. Phys. Lett.*, vol. 23, pp. 388, 1973.
- [5] R. J. Mears, L. Reekie, S. B. Poole, and D. N. Payne, "Low threshold tunable CW and Q-switched fiber laser operating at 1.55  $\mu\text{m}$ ", *Electron. Lett.*, vol. 22, pp. 159, 1986.
- [6] S. B. Poole, D. N. Payne, R. J. Mears, L. Reekie, M. E. Fermann, and R. J. Laming, "Fabrication and characterization of low-loss optical fibers containing rare-earth ions", *J. Lightwave Technol.*, vol. 22, pp. 159, 1986.
- [7] D. C. Hanna, I. M. Jauncey, R. M. Percival, I. R. Perry, R. G. Smart, P. J. Suni, J. E. Townsend, and A. C. Tropper, "Continuous-wave oscillation of a monomode thulium-doped fibre laser", *Electron. Lett.*, vol. 24, pp. 1222–1223, 15 September 1988.
- [8] D. C. Hanna, R. M. Percival, R. G. Smart, and A. C. Tropper, "Efficient and tunable operation of a Tm-doped fibre laser", *Opt. Comm.*, vol. 75, pp. 283–286, 1 March 1990.
- [9] W. L. Barnes and J. E. Townsend, "Highly tunable and efficient diode pumped operation of thulium-doped fibre lasers", *Electron. Lett.*, vol. 26, pp. 746–747, 24 May 1990.
- [10] J. Y. Allain, M. Monerie, and H. Poignant, "Tunable CW lasing around 0.82, 1.48, 1.88, and 2.35  $\mu\text{m}$  in thulium-doped fluorozirconate fiber", *Electron. Lett.*, vol. 25, pp. 1660–1662, 1989.

- [11] J. Y. Allain, M. Monerie, and H. Poignant, "High-efficiency cw thulium-sensitized holmium-doped fluoride fiber laser operating at 2.04  $\mu\text{m}$ ", *Electron. Lett.*, vol. 27, pp. 1513–15, 1991.
- [12] R. M. Percival, D. Szebesta, S. T. Davey, N. A. Swain, and T. A. King, "High-efficiency cw operation of 890 nm pumped holmium fluoride fiber laser", *Electron. Lett.*, vol. 28, pp. 2064–66, October 1992.
- [13] D. C. Hanna, R. M. Percival, I. R. Perry, R. G. Smart, P. J. Suni, J. E. Townsend, and A. C. Tropper, "Continuous-wave oscillation of a monomode ytterbium-doped fibre laser", *Electron. Lett.*, vol. 24, pp. 1111, August 1988.
- [14] H. M. Pask, R. J. Carman, D. C. Hanna, A. C. Tropper, C. J. Mackechnie, P. R. Barber, and J. M. Dawes, "Ytterbium-doped silica fiber lasers: versatile sources for the 1-1.2  $\mu\text{m}$  region", *IEEE J. Selected Topics in Quant. Electron.*, vol. 1, pp. 2–13, April 1995.
- [15] Y. Durteste, M. Monerie, J. Y. Allain, and H. Poignant, "Amplification and lasing at 1.3 microns in praseodymium-doped fluorozirconate fibres", *Electron. Lett.*, vol. 27, pp. 626–628, April 1991.
- [16] T. Whitley, R. Wyatt, D. Szebesta, and S. Davey, "High output power from an efficient praseodymium-doped fluoride fiber amplifier", *IEEE Photon. Tech. Lett.*, vol. 4, pp. 401–403, April 1993.
- [17] I. N. Duling III, "Subpicosecond all-fibre erbium laser", *Electron. Lett.*, vol. 27, pp. 544–545, 14 March 1991.
- [18] D. J. Richardson, R. I. Laming, D. N. Payne, M. W. Phillips, and V. J. Matsas, "320 fs soliton generation with passively mode-locked erbium fibre laser", *Electron. Lett.*, vol. 27, pp. 730–732, 25 April 1991.
- [19] M. Hofer, M. E. Fermann, F. Haberl, M. H. Ober, and A. J. Schmidt, "Mode locking with cross-phase and self-phase modulation", *Opt. Lett.*, vol. 16, pp. 502–504, August 1991.
- [20] V. J. Matsas, T. P. Newson, D. J. Richardson, and D. N. Payne, "Self-starting passively mode-locked fibre ring soliton laser exploiting nonlinear polarization rotation", *Electron. Lett.*, vol. 28, pp. 1391–1392, 16 July 1992.
- [21] K. Tamura, H. A. Haus, and E. P. Ippen, "Self-starting additive pulse mode-locked erbium fibre ring laser", *Electron. Lett.*, vol. 28, pp. 2226–2227, 19 November 1992.
- [22] E. A. DeSouza, C. E. Socolich, W. Pleibel, R. H. Stolen, M. N. Islam, J. R. Simpson, and D. J. DiGiovanni, "Saturable absorber mode-locked polarization maintaining erbium-doped fibre laser", *Electron. Lett.*, vol. 29, pp. 447–449, 4 March 1993.

- [23] M. H. Ober, M. Hofer, and M. E. Fermann, "42-fsec pulse generation from a mode-locked fiber laser started with a moving mirror", *Opt. Lett.*, vol. 18, pp. 367–369, March 1993.
- [24] M. J. Guy, D. U. Noske, A. Boskovic, and J. R. Taylor, "Femtosecond soliton generation in a praseodymium fluoride fiber laser", *Opt. Lett.*, vol. 19, pp. 828–830, June 1994.
- [25] K. Tamura, L. E. Nelson, H. A. Haus, and E. P. Ippen, "Stretched pulse additive pulse mode locking in fiber lasers", in *CLEO 1994 Technical Digest Series*, Baltimore, MD, May 5-13,1994, p. Paper CTuB2.
- [26] D. C. Hanna, I. R. Perry, and J. R. Lincoln, "A 1-Watt thulium-doped cw fibre laser operating at 2  $\mu\text{m}$ ", *Opt. Comm.*, vol. 80, pp. 52–56, 1990.
- [27] R. G. Smart, J. N. Carter, A. C. Tropper, and D. C. Hanna, "Continuous-wave oscillation of thulium-doped fluorozirconate fiber lasers at around 1.47  $\mu\text{m}$ , 1.9  $\mu\text{m}$ , and 2.3  $\mu\text{m}$  when pumped at 790 nm", *Opt. Comm.*, vol. 82, pp. 563–570, 1991.
- [28] N. Kishi, J. N. Carter, R. Mottahedeh, P. R. Morkel, R. G. Smart, A. J. Seeds, J. S. Roberts, C. C. Button D. N. Payne, A. C. Tropper, and D. C. Hanna, "Actively mode-locked and passively Q-switched operation of thulium-doped fibre laser using multiquantum well asymmetric Fabry-Perot modulator", *Electron. Lett.*, vol. 28, pp. 175–177, 16 January 1992.
- [29] R. C. Sharp, D. E. Spock, N. Pan, and J. Elliot, "Mode-locked thulium-doped fiber laser", *Opt. Lett.*, vol. 21, pp. 881–3, June 1996.
- [30] ed. M. J. Digonnet, *Rare-Earth Doped Fiber Lasers and Amplifiers*, Marcel Dekker, Inc., New York, 1993.
- [31] E. Desurvire, *Erbium-doped Fiber Amplifiers*, John Wiley and Sons, Inc., New York, 1994.
- [32] C. Barnard, P. Myslinski, J. Chrostowski, and M. Kavehrad, "Analytical model for rare-earth-doped fiber amplifiers and lasers", *IEEE J. Quantum Electron.*, vol. 30, pp. 1817–1829, August 1994.
- [33] J. Y. Allain, M. Monerie, and H. Poignant, "Lasing at 1.00  $\mu\text{m}$  in erbium-doped fluorozirconate fibres", *Electron. Lett.*, vol. 25, pp. 318, 1989.
- [34] M. C. Brierley and P. W. France, "Continuous wave lasing at 2.7  $\mu\text{m}$  in an erbium-doped fluorozirconate fibre", *Electron. Lett.*, vol. 24, pp. 935, 1988.
- [35] M. Yamada, "Noise characteristics of erbium-doped fiber amplifier pumped by 0.98 and 1.48  $\mu\text{m}$  diode", *IEEE Photon. Tech. Lett.*, vol. 2, pp. 418, 1990.
- [36] A. E. Siegman, *Lasers*, University Science Books, Mill Valley, California, 1986.

- [37] E. Desurvire, J. L. Zyskind, and J. R. Simpson, "Spectral gain hole-burning at 1.53  $\mu\text{m}$  in erbium-doped fiber amplifiers", *IEEE Photon. Tech. Lett.*, vol. 2, pp. 246, 1990.
- [38] E. Desurvire and J. R. Simpson, "Evaluation of  $^4I_{15/2}$  and  $^4I_{13/2}$  Stark-level energies in erbium-doped aluminosilicate glass fibers", *Opt. Lett.*, vol. 15, pp. 547, 1990.
- [39] E. Desurvire, J. W. Sulhoff, J. L. Zyskind, and J. R. Simpson, "Study of spectral dependence of gain saturation and effect of inhomogeneous broadening in erbium-doped aluminosilicate fiber amplifiers", *IEEE Photon. Tech. Lett.*, vol. 2, pp. 653, 1990.
- [40] W. L. Barnes, R. I. Laming, E. J. Tarbox, and P. R. Morkel, "Absorption and emission cross-section of erbium-doped silica fibers", *IEEE J. Quantum Electron.*, vol. QE-27, pp. 1004–10, 1991.
- [41] H. W. Gandy, R. J. Ginther, and J. F. Weller, "Stimulated emission of  $\text{tm}^{+3}$  radiation in silicate glass", *J. Appl. Phys.*, vol. 38, pp. 3030, 1967.
- [42] D. C. Hanna, M. J. McCarthy, I. R. Perry, and P. J. Suni, "Efficient high-power continuous-wave operation of monomode  $\text{tm}$ -doped fibre laser at 2  $\mu\text{m}$  pumped by  $\text{nd}:\text{YAG}$  laser at 1.064  $\mu\text{m}$ ", *Electron. Lett.*, vol. 25, pp. 1365, 28 September 1989.
- [43] R. M. Percival, S. F. Carter, K. Szebesta, S. T. Davey, and W. A. Stallard, "Thulium-doped monomode fluoride fibre laser broadly tunable from 2.25 to 2.5  $\mu\text{m}$ ", *Electron. Lett.*, vol. 27, pp. 1912–1913, 10 October 1991.
- [44] D. C. Hanna, R. M. Percival, I. R. Perry, R. G. Smart, J. E. Townsend, and A. C. Tropper, "Frequency upconversion in  $\text{tm}$ - and  $\text{yb}:\text{tm}$ -doped silica fibers", *Opt. Comm.*, vol. 78, pp. 187–94, 15 August 1990.
- [45] L. J. Poyntz-Wright, M. E. Fermann, and P. St. J. Russell, "Nonlinear transmission and color-center dynamics in germanosilicate fibers at 420-540  $\text{nm}$ ", *Opt. Lett.*, vol. 13, pp. 1023, 1988.
- [46] M. M. Broer, D. M. Krol, and D. J. DiGiovanni, "Highly nonlinear near-resonant photodarkening in a thulium-doped aluminosilicate glass fiber", *Opt. Lett.*, vol. 18, pp. 799, 1993.
- [47] D. M. Krol, D. J. DiGiovanni, W. Pleibel, and R. H. Stolen, "Observation of resonant enhancement of photoinduced second-harmonic generation in  $\text{Tm}$ -doped aluminosilicate glass fibers", *Opt. Lett.*, vol. 18, pp. 1220, 1993.
- [48] M. H. Muendel, Polaroid Corporation, Private communication.
- [49] D. J. DiGiovanni, Lucent Technologies/Bell Laboratories, Private communication.

- [50] M. H. Muendel, "Optimal inner cladding shapes for double-clad fiber lasers", in *CLEO 1996 Technical Digest Series*, Santa Monica, CA, June 1 - 7, 1996, p. Paper CTuU2.
- [51] E. Snitzer, H. Po, F. Hakimi, R. Tumminelli, and B. C. McCollum, "Double-clad, offset core Nd fiber laser", in *Proceedings of Optical Fiber Sensors '88*, New Orleans, 1988, p. Postdeadline paper PD5.
- [52] H. Po, J. D. Cao, B. M. Laliberte, R. A. Minns, R. F. Robinson, B. H. Rockney, R. R. Tricca, and Y. H. Zhang, "High power neodymium-doped single transverse mode fibre laser", *Electron. Lett.*, vol. 29, pp. 1500, 1993.
- [53] J. D. Minelly, W. L. Barnes, R. I. Laming, P. R. Morkel, J. E. Townsend, S. G. Grubb, and D. N. Payne, "Diode-array pumping of  $\text{Er}^{+3}/\text{Yb}^{+3}$  co-doped fiber lasers and amplifiers", *IEEE Photon. Tech. Lett.*, vol. 5, pp. 301, 1993.
- [54] M. E. Fermann, D. Harter, J. D. Minelly, and G. G. Vienne, "Cladding-pumped passively mode-locked fiber laser generating femtosecond and picosecond pulses", *Opt. Lett.*, vol. 21, pp. 967, 1996.
- [55] M. E. Fermann and J. D. Minelly, "Cladding-pumped passive harmonically mode-locked fiber laser", *Opt. Lett.*, vol. 21, pp. 970, 1996.
- [56] A. Galvanauskas, M. E. Fermann, D. Harter, J. D. Minelly, G. G. Vienne, and J. E. Caplen, "Broad-area diode-pumped 1W femtosecond fiber system", in *CLEO 1996 Technical Digest Series*, Santa Monica, CA, June 1 - 7, 1996, p. Paper CFD4.
- [57] B. Bouma and G. J. Tearney, MIT, Private communication.
- [58] K. S. Kim, R. H. Stolen, W. A. Reed, and K. W. Quoi, "Measurement of the nonlinear index of silica-core and dispersion-shifted fibers", *Opt. Lett.*, vol. 19, pp. 257, 1994.
- [59] A. Yariv, *Optical Electronics*, Holt, Rinehart, and Winston, Inc., New York, 1985.
- [60] W. H. Knox, "In situ measurement of complete intracavity dispersion in an operating Ti:sapphire femtosecond laser", *Opt. Lett.*, vol. 17, pp. 514-516, 1 April 1992.
- [61] T. Izawa and S. Sudo, *Optical fibers: materials and fabrication*, KTK Scientific Publishers, Tokyo, 1987.
- [62] J. Mark, L. Y. Liu, K. L. Hall, H. A. Haus, and E. P. Ippen, "Femtosecond pulse generation in a laser with a nonlinear external resonator", *Opt. Lett.*, vol. 14, pp. 48, 1989.
- [63] E. P. Ippen, H. A. Haus, and L. Y. Liu, "Additive pulse mode-locking", *J. Opt. Soc. Amer. B*, vol. 6, pp. 1736-45, September 1989.



- [64] H. A. Haus, J. G. Fujimoto, and E. P. Ippen, "Structures for additive pulse mode locking", *J. Opt. Soc. Amer. B*, vol. 8, no. 10, pp. 2068–76, October 1991.
- [65] P. D. Maker, R. W. Terhune, and C. M. Savage, "Intensity-dependent changes in the refractive index of liquids", *Phys. Rev. Lett.*, vol. 12, pp. 507, 1964.
- [66] D. U. Noske, N. Pandit, and J. R. Taylor, "Subpicosecond soliton pulse formation from self-mode-locked erbium fibre laser using intensity dependent polarization rotation", *Electron. Lett.*, vol. 92, pp. 2185–6, November 1992.
- [67] L. F. Mollenauer, J. P. Gordon, and M. N. Islam, "Soliton propagation in long fibers with periodically compensated loss", *IEEE J. Quantum Electron.*, vol. QE-22, no. 1, pp. 157–73, January 1986.
- [68] L. F. Mollenauer, Jr. S. G. Evangelides, and H. A. Haus, "Long-distance soliton propagation using lumped amplifiers and dispersion shifted fiber", *J. Lightwave Technol.*, vol. 9, no. 2, pp. 194–6, February 1991.
- [69] H. A. Haus, E. P. Ippen, and K. Tamura, "Additive-pulse modelocking in fiber lasers", *IEEE J. Quantum Electron.*, vol. 30, no. 1, pp. 200–208, January 1994.
- [70] K. Tamura, *Additive Pulse Mode-locked Erbium-doped Fiber Lasers*, PhD thesis, MIT, October 1994.
- [71] E. P. Ippen, "Modelocking, stabilizing, and starting ultrashort pulse lasers", in *Ultrafast Phenomena VIII*, J. L. Martin, A. Migus, G. A. Mourou, and A. H. Zewail, Eds., number 55 in Springer Series in Chemical Physics, chapter 4, pp. 155–59. Springer-Verlag, Berlin, 1993.
- [72] F. Krausz, T. Brabec, and Ch. Spielmann, "Self-starting passive mode locking", *Opt. Lett.*, vol. 16, no. 4, pp. 235–237, 15 February 1991.
- [73] K. Tamura, J. Jacobson, E. P. Ippen, H. A. Haus, and J. G. Fujimoto, "Unidirectional ring resonators for self-starting passively mode-locked lasers", *Opt. Lett.*, vol. 18, no. 3, pp. 220–222, 1st February 1993.
- [74] F. Krausz and T. Brabec, "Passive mode locking in standing-wave laser resonators", *Opt. Lett.*, vol. 18, no. 11, pp. 888–890, 1st June 1993.
- [75] L. E. Nelson, E. P. Ippen, and H. A. Haus, "Broadly tunable sub-500 fs pulses from an additive-pulse mode-locked thulium-doped fiber ring laser", *Appl. Phys. Lett.*, vol. 67, pp. 19–21, 1995.
- [76] R. G. Smart, J. N. Carter, A. C. Tropper, and D. C. Hanna, "Continuous-wave oscillation on thulium-doped fluorozirconate fibre lasers at around 1.47  $\mu\text{m}$ , 1.9  $\mu\text{m}$  and 2.3  $\mu\text{m}$  when pumped at 790 nm", *Opt. Comm.*, vol. 82, pp. 563–570, 1 May 1991.

- [77] A. Hasegawa, "Numerical study of optical soliton transmission amplified periodically by the stimulated raman process", *Appl. Opt.*, vol. 23, no. 19, pp. 3302–9, 1st October 1984.
- [78] S. M. J. Kelly, K. Smith, K. J. Blow, and N. J. Doran, "Average soliton dynamics of a high-gain erbium fiber laser", *Opt. Lett.*, vol. 16, no. 17, pp. 1337–9, 1st September 1991.
- [79] J. P. Gordon, "Dispersive perturbations of solitons of the nonlinear Schroedinger equation", *J. Opt. Soc. Amer. B*, vol. 9, no. 1, pp. 91–97, January 1992.
- [80] N. Pandit, D. U. Noske, S. M. J. Kelly, and J. R. Taylor, "Characteristic instability of fibre loop soliton lasers", *Electron. Lett.*, vol. 28, no. 5, pp. 455–7, 27th February 1992.
- [81] S. M. J. Kelly, "Characteristic sideband instability of periodically amplified average soliton", *Electron. Lett.*, vol. 28, pp. 806–7, 9th April 1992.
- [82] H. A. Haus, E. P. Ippen, and K. Tamura, "Additive-pulse modelocking in fiber lasers", *IEEE J. Quantum Electron.*, vol. 30, pp. 200–208, 1994.
- [83] K. Tamura, C. R. Doerr, H. A. Haus, and E. P. Ippen, "Soliton fiber ring laser stabilization and tuning with a broad intracavity filter", *IEEE Photon. Tech. Lett.*, vol. 6, pp. 697–699, 1994.
- [84] K. Tamura, C. R. Doerr, L. E. Nelson, E. P. Ippen, and H. A. Haus, "Technique for obtaining high-energy ultrashort pulses from an additive-pulse mode-locked erbium-doped fiber ring laser", *Opt. Lett.*, vol. 19, pp. 46–48, 1994.
- [85] K. Tamura, E. P. Ippen, H. A. Haus, and L. E. Nelson, "77-fsec pulse generation from a stretched-pulse mode-locked all-fiber ring laser", *Opt. Lett.*, vol. 18, pp. 1080–82, 1993.
- [86] K. Tamura, L. E. Nelson, H. A. Haus, and E. P. Ippen, "Soliton versus non-soliton operation of fiber ring lasers", *Appl. Phys. Lett.*, vol. 64, pp. 149–151, 1994.
- [87] D. Huang, E. A. Swanson, C. P. Lin, J. S. Schuman, W. G. Stinson, W. Chang, M. R. Hee, T. Flotte, K. Gregory, C. A. Puliafito, and J. G. Fujimoto, "Optical coherence tomography", *Science*, vol. 254, pp. 1178–1181, 22 November 1991.
- [88] J. A. Izatt, M. R. Hee, D. Huang, J. G. Fujimoto, E. A. Swanson, C. P. Lin, J. S. Schuman, and C. A. Puliafito, "Optical coherence tomography for medical diagnostics", in *SPIE Medical Optical Tomography: Functional Imaging and Monitoring*, Bellingham, Washington, 1993, vol. IS11, pp. 450–472.

- [89] B. Bouma, G. J. Tearney, S. A. Boppart, M. R. Hee, M. E. Brezinski, and J. G. Fujimoto, "High-resolution optical coherence tomographic imaging using a mode-locked Ti:Sapphire laser source", *Opt. Lett.*, vol. 20, no. 13, pp. 1486, 1 July 1995.
- [90] B. E. Bouma, G. J. Tearney, B. Golubovic, and J. G. Fujimoto, "Optical coherence tomographic imaging using a mode-locked Chromium:Fosterite laser source", in *Ultrafast Phenomena X*, P. F. Barbara, J. G. Fujimoto, W. H. Knox, and W. Zinth, Eds., number 62 in Springer Series in Chemical Physics, chapter 6, pp. 143–4. Springer, Berlin, 1996.
- [91] H. A. Haus, K. Tamura, L. E. Nelson, and E. P. Ippen, "Stretched-pulse additive pulse mode-locking in fiber ring lasers: theory and experiment", *IEEE J. Quantum Electron.*, vol. 31, no. 3, pp. 591–598, March 1995.
- [92] L. E. Nelson, S. B. Fleischer, G. Lenz, and E. P. Ippen, "Efficient frequency doubling of a femtosecond fiber laser", *Opt. Lett.*, vol. 21, no. 21, pp. 1759, 1 November 1996.
- [93] G. Lenz, K. Tamura, H. A. Haus, and E. P. Ippen, "All-solid-state femtosecond source at 1.55  $\mu\text{m}$ ", *Opt. Lett.*, vol. 20, pp. 1289–91, 1995.
- [94] M. C. Nuss, W. H. Knox, J. B. Stark, S. Cundiff, D. A. B. Miller, and U. Koren, "Femtosecond chirped-pulse multifrequency sources", in *Ultrafast Phenomena X*, P. F. Barbara, J. G. Fujimoto, W. H. Knox, and W. Zinth, Eds., number 62 in Springer Series in Chemical Physics, chapter 1, pp. 22–23. Springer, Berlin, 1996.
- [95] S. M. Lepage, K. L. Hall, G. Lenz, and E. P. Ippen, "Widely tunable source generating sub-picosecond pulses at 1550 nm", in *SPIE All-Optical Communication Systems: Architecture, Control, and Network Issues*, Philadelphia, PA, 25-26 October, 1995.
- [96] G. Lenz, W. Gellermann, D. J. Dougherty, K. Tamura, and E. P. Ippen, "Femtosecond fiber laser pulses amplified by a KCl:Tl<sup>+</sup> color-center amplifier for continuum generation in the 1.55 micron region", *Opt. Lett.*, vol. 21, no. 2, pp. 137, 15 January 1996.
- [97] D. Huang, J. Wang, C. P. Lin, C. A. Puliafito, and J. G. Fujimoto, "Micron-resolution ranging of cornea anterior chamber by optical reflectometry", *Las. Surg. Med.*, vol. 11, pp. 419, 1991.
- [98] T. B. Norris, "Femtosecond pulse amplification at 250 kHz with a Ti:Sapphire regenerative amplifier and application to continuum generation", *Opt. Lett.*, vol. 17, pp. 1009, 1992.
- [99] A. Hariharan, M. E. Fermann, M. L. Stock, D. J. Harter, and J. Squier, "Alexandrite-pumped alexandrite regenerative amplifier for femtosecond pulse amplification", *Opt. Lett.*, vol. 21, pp. 128, 1996.

- [100] E. Desurvire, "Analysis of gain difference between forward- and backward-pumped erbium-doped fiber amplifiers in the saturation regime", *IEEE Photon. Tech. Lett.*, vol. 4, pp. 711, 1992.
- [101] R. I. Laming, J. E. Townsend, D. N. Payne, F. Meli, G. Grasso, and E. J. Tarbox, "High-power erbium-doped-fiber amplifiers operating in the saturated regime", *IEEE Photon. Tech. Lett.*, vol. 4, pp. 711, 1992.
- [102] D. Eimerl, L. Davis, S. Velsko, E. K. Graham, and A. Zalkin, "Optical, mechanical, and thermal properties of barium borate", *J. Appl. Phys.*, vol. 62, pp. 1968, 1987.
- [103] B. Zysset, I. Biaggio, and P. Gunter, "Refractive indices of orthorhombic  $\text{KNbO}_3$ . I. dispersion and temperature dependence", *J. Opt. Soc. Amer. B*, vol. 9, pp. 380, 1992.
- [104] I. Gontijo, "Determination of important parameters for second harmonic generation in LBO", *Opt. Comm.*, vol. 108, pp. 324, 1994.
- [105] D. J. Kane and R. Trebino, "Characterization of arbitrary femtosecond pulses using frequency-resolved optical gating", *IEEE J. Quantum Electron.*, vol. 29, pp. 571-8, 1993.
- [106] J. Paye, M. Ramaswamy, J. G. Fujimoto, and E. P. Ippen, "Measurement of the amplitude and phase of ultrashort light pulses from spectrally resolved autocorrelation", *Opt. Lett.*, vol. 18, pp. 1946-8, 1993.
- [107] R. Trebino and D. J. Kane, "Using phase retrieval to measure the intensity and phase of ultrashort pulses: frequency-resolved optical gating", *J. Opt. Soc. Amer. A*, vol. 10, pp. 1101, 1993.
- [108] K. W. DeLong, R. Trebino, J. Hunter, and W. E. White, "Frequency-resolved optical gating using second-harmonic generation", *J. Opt. Soc. Amer. B*, vol. 11, pp. 2206, 1994.
- [109] K. W. DeLong, D. N. Fittinghoff, and R. Trebino, "Pulse retrieval in frequency-resolved optical gating based on the method of generalized projections", *Opt. Lett.*, vol. 19, pp. 2152, 1994.
- [110] D. von der Linde, "Characterization of the noise in continuously operating mode-locked lasers", *Appl. Phys. B*, vol. 39, pp. 201, 1986.
- [111] J. Son, J. V. Rudd, and J. F. Whitaker, "Noise characterization of a self-mode-locked ti:sapphire laser", *Opt. Lett.*, vol. 17, pp. 733, 1992.
- [112] C. X. Yu, S. Namiki, W. S. Wong, and H. A. Haus, "Noise of stretched pulse fiber lasers", in *CLEO 1996 Technical Digest Series*, Santa Monica, CA, June 1 - 7, 1996, p. Paper CFD6.

- [113] M. E. Fermann, M. J. Andrejco, Y. Silberberg, and M. L. Stock, "Passive mode locking by using nonlinear polarization evolution in a polarization-maintaining erbium-doped fiber", *Opt. Lett.*, vol. 18, pp. 894, 1993.
- [114] M. E. Fermann, L. M. Yang, M. L. Stock, and M. J. Andrejco, "Environmentally stable kerr-type mode-locked erbium fiber laser producing 360-fs pulses", *Opt. Lett.*, vol. 19, pp. 43, 1994.
- [115] R. Ulrich and A. Simon, "Polarization optics of twisted single-mode fibers", *Appl. Opt.*, vol. 18, pp. 2241, 1979.
- [116] N. Chinone and R. Ulrich, "Elasto-optic polarization measurement in optical fiber", *Opt. Lett.*, vol. 6, pp. 16, 1981.
- [117] M. Johnson, "In-line fiber-optical polarization transformer", *Appl. Opt.*, vol. 18, pp. 1288, 1979.
- [118] R. Ulrich, S. C. Rashleigh, and W. Eickoff, "Bending-induced birefringence in single-mode fibers", *Opt. Lett.*, vol. 5, pp. 273, 1980.
- [119] H. C. Lefevre, "Single-mode fibre fractional wave devices and polarisation controllers", *Electron. Lett.*, vol. 16, pp. 778, 1980.
- [120] B. G. Koehler and J. E. Bowers, "In-line single-mode fiber polarization controllers at 1.55, 1.30, and 0.63  $\mu\text{m}$ ", *Appl. Opt.*, vol. 24, pp. 349, 1985.
- [121] S. C. Rashleigh and M. J. Marrone, "Temperature dependence of stress birefringence in an elliptically clad fiber", *Opt. Lett.*, vol. 8, pp. 127, 1983.
- [122] A. J. Barlow and D. N. Payne, "The stress-optic effect in optical fibers", *IEEE J. Quantum Electron.*, vol. QE-19, pp. 834, 1983.
- [123] Y. S. Touloukian, R. D. Kirby, R. E. Taylor, and T. Y. R. Lee, *Thermal Expansion - Nonmetallic Solids*, vol. 13 of *Thermophysical Properties of Matter*, p. 359, Plenum, New York, 1977.
- [124] D. E. Gray, Ed., *American Institute of Physics Handbook*, pp. 6-29, *Thermophysical Properties of Matter*. American Institute of Physics, New York, 3rd edition, 1972.
- [125] H. G. Winful, "Self-induced polarization changes in birefringent optical fibers", *Appl. Phys. Lett.*, vol. 47, pp. 213, 1985.
- [126] H. G. Winful, "Polarization instabilities in birefringent nonlinear media: application to fiber-optic devices", *Opt. Lett.*, vol. 11, pp. 33, 1986.
- [127] M. E. Fermann, K. Sugden, and I. Bennion, "Environmentally stable high-power soliton fiber lasers that use chirped fiber bragg gratings", *Opt. Lett.*, vol. 20, pp. 1625, 1995.

- [128] M. Martinelli, "A universal compensator for polarization changes induced by birefringence on a retracing beam", *Opt. Comm.*, vol. 72, pp. 341, 1989.
- [129] H. A. Haus and L. E. Nelson, "Additive pulse mode-locking with non-birefringent and pm fibers", 1996, *Quantum Electronics and Femtosecond Optics*, Memo No. 72.
- [130] G. P. Agrawal, *Nonlinear Fiber Optics*, pp. 177–179, Academic Press, Inc., San Diego, CA, 1989.
- [131] Y. Kikuchi, R. Yamauchi, M. Akiyama, O. Fukuda, and K. Inada, "Polarimetric strain and pressure sensors using temperature-independent polarization maintaining optical fiber", in *Proc. of SPIE, 2nd International Conference on Optica Fiber Sensors*, Stuttgart, West Germany, September 5 - 7, 1984, pp. 395–8.
- [132] F. Zhang and J. W. Y. Lit, "Temperature and strain sensitivities of high-birefringent elliptical fibers", *Appl. Opt.*, vol. 31, pp. 1239–43, 1992.
- [133] F. Zhang and J. W. Y. Lit, "Minimization of temperature effects of high-birefringent elliptical fibers for polarimetric optical-fiber sensors", *Appl. Opt.*, vol. 33, pp. 3604–10, 1994.
- [134] G. W. Yoffe, P. A. Krug, F. Ouellette, and D. A. Thorncraft, "Temperature-compensated optical fiber bragg gratings", in *Optical Fiber Communications*, Washington, DC, 1995, p. 134, Optical Society of America.
- [135] G. W. Yoffe, P. A. Krug, F. Ouellette, and D. A. Thorncraft, "Passive temperature-compensating package for optical fiber gratings", *Appl. Opt.*, vol. 34, pp. 6859–61, 1995.
- [136] I. N. Duling III and R. D. Esman, "Single-polarisation fibre amplifier", *Electron. Lett.*, vol. 28, pp. 1126, 1992.
- [137] T. F. Carruthers, I. N. Duling III, and M. L. Dennis, "Active-passive mode-locking in a single-polarisation erbium fibre laser", *Electron. Lett.*, vol. 30, pp. 1051, 1994.
- [138] T. F. Carruthers and I. N. Duling III, "10-GHz, 1.3-ps erbium fiber laser employing soliton pulse shortening", *Opt. Lett.*, vol. 21, pp. 1927, 1996.
- [139] R. L. Fork, C. H. Brito Cruz, P. C. Becker, and C. V. Shank, "Compression of optical pulses to six femtoseconds by using cubic phase compensation", *Opt. Lett.*, vol. 12, pp. 483, 1987.
- [140] K. Tamura, E. P. Ippen, and H. A. Haus, "Optimization of filtering in soliton fiber lasers", *IEEE Photon. Tech. Lett.*, vol. 6, pp. 1433, 1994.

- [141] M. H. Ober, M. Hofer, R. Hofer, G. A. Reider, G. D. Sucha, M. E. Fermann, D. Harter, C. A. C. Mendonca, and T. H. Chiu, "Widely tunable femtosecond neodymium fiber laser", *Opt. Lett.*, vol. 20, pp. 2303-05, 1995.
- [142] H. Zellmer, U. Willamowski, A. Tünnermann, H. Willing, S. Unger, V. Reichel, H. R. Müller, J. Kirchhof, and P. Albers, "High-power cw neodymium-doped fiber laser operating at 9.2 W with high beam quality", *Opt. Lett.*, vol. 20, pp. 578, 1995.
- [143] M. H. Muendel, Polaroid Corporation, Private communication.
- [144] C. Momma, B. N. Chichkov, , S. Nolte, F. von Alvensleben, A. Tuennermann, H. Welling, and B. Wellegehausen, "Short-pulse laser ablation of solid targets", *Opt. Comm.*, vol. 129, pp. 134, 1996.
- [145] B. N. Chichkov, C. Momma, S. Nolte, F. von Alvensleben, and A. Tuennermann, "Femtosecond, picosecond, and nanosecond laser ablation of solids", *Appl. Phys. A*, vol. 63, pp. 109, 1996.
- [146] M. E. Fermann, K. Sugden, and I. Bennion, "High-power soliton fiber laser based on pulse width control with chirped fiber bragg gratings", *Opt. Lett.*, vol. 20, pp. 172, 1995.
- [147] K. Tamura, T. Komukai, and M. Nakazawa, "Optimization of power extraction in a high-power soliton fiber ring laser containing a chirped fiber grating", *Appl. Phys. Lett.*, vol. 69, pp. 1535, 1996.
- [148] A. M. Vengsarkar, J. R. Pedrazzani, J. B. Judkins, P. J. Lemaire, N. S. Bergano, and C. R. Davidson, "Long-period fiber-grating-based gain equalizers", *Opt. Lett.*, vol. 21, pp. 336, 1996.
- [149] A. M. Vengsarkar, P. J. Lemaire, J. B. Judkins, , V. Bhatia, T. Erdogan, and J. E. Sipe, "Long-period fiber gratings as band-rejection filters", *J. Lightwave Technol.*, vol. 14, pp. 58, 1996.
- [150] S. Tsuda, W. H. Knox, E. A. de Souza, W. Y. Jan, and J. E. Cunningham, "Low-loss intracavity AlAs/AlGaAs saturable bragg reflector for femtosecond mode locking in solid-state lasers", *Opt. Lett.*, vol. 20, pp. 1406, 1995.
- [151] S. Tsuda, W. H. Knox, J. L. Zyskind, J. E. Cunningham, J. Y. Pan, and R. Pathak, "Broadband compact mode-locked er/yb fiber laser", in *CLEO 1996 Technical Digest Series*, Santa Monica, CA, June 1 - 7, 1996, p. Paper CFD2.
- [152] P. Bado and D. Walker, Clark MXR, Inc., have demonstrated seeding of a commercial Ti:Sapphire regenerative amplifier system with the frequency-doubled stretched-pulse fiber laser.

- [153] K. Tamura, E. Yoshida, and M. Nakazawa, "Generation of 10GHz pulse trains at 10 wavelengths by spectrally slicing a high power femtosecond source", *Electron. Lett.*, vol. 32, pp. 1691, 1996.
- [154] K. Tamura, E. Yoshida, E. Yamada, and M. Nakazawa, "Generation of 0.5 W average power train of femtosecond pulses at 10 GHz in the 1.55  $\mu\text{m}$  region", *Electron. Lett.*, vol. 32, pp. 835, 1996.
- [155] M. Suyama, I. Yokota, S. Watanabe, and H. Kuwahara, in *Proc. Optical Amplifiers Appl.*, Washington, DC, 1991, p. Paper ThE4, Optical Society of America.



# THESIS PROCESSING SLIP

FIXED FIELD: ill. \_\_\_\_\_ name \_\_\_\_\_

index \_\_\_\_\_ biblio \_\_\_\_\_

▶ COPIES: Archives Aero Dewey Eng Hum  
Lindgren Music Rotch Science

TITLE VARIES: ▶  \_\_\_\_\_

NAME VARIES: ▶  \_\_\_\_\_

IMPRINT: (COPYRIGHT) \_\_\_\_\_

▶ COLLATION: 1521

▶ ADD. DEGREE: \_\_\_\_\_ ▶ DEPT.: \_\_\_\_\_

SUPERVISORS: \_\_\_\_\_

NOTES:

cat'r:

date:

▶ DEPT: E.E. page:  
▶ J171

▶ YEAR: 1997 ▶ DEGREE: Ph.D.

▶ NAME: NELSON, Lynn Elizabeth